Approaches to Passive Operation of a Direct Methanol Fuel Cell

Zur Erlangung des akademischen Grades eines

Doktor-Ingenieurs

von der Fakultät für Elektrotechnik und Informationstechnik
der Universität Karlsruhe (TH) genehmigte

Dissertation

von

Dipl.-Ing. Steffen Eccarius

geb. in Friedrichshafen

Tag der mündlichen Prüfung:	19.07.2007
Hauptreferent:	Prof. Dr.-Ing. Ellen Ivers-Tiffée
Korreferent:	Prof. Dr.-Ing. Jürgen Garche

Contents

Glossary

Variables

ΔG	Gibbs free energy change $(\mathrm{kJ/mol})$
ΔH	Enthalpy change $(\mathrm{kJ/mol})$
ΔS	Entropy change $(\mathrm{J/(mol\,K)})$
$\dot{m}$	Mass flow $(\mathrm{cm^3/s})$
ϵ	Porosity
η	Losses (V)
γ	Surface tension $(\mathrm{N/cm})$
γ_i	Activity coefficient of species i
λ	Stoichiometry
Φ	Potential (V)
σ	Conductivity $(\mathrm{S/cm})$
τ	Tortuosity
$\vec{n}$	Outward–pointing normal vector
A	Area $(\mathrm{cm^2})$
a	Activity, Inner surface $(\mathrm{cm^2/cm^3})$
$A_{i,j}$	Species–specific parameters
c	Concentration $(\mathrm{mol/cm^3})$
D	Diffusion coefficient $(\mathrm{cm^2/s})$
d	thickness $(\mathrm{cm^3})$
F	Faraday constant $(9.648 \cdot 10^4\,\mathrm{C/mol})$
f	Fugacity (Pa)
I	Current (A)
i	Current density $(\mathrm{A/cm^2})$
i_0	Exchange current density $(\mathrm{A/cm^2})$
k	Mass transfer coefficient $(\mathrm{cm^2/s})$
$M_{i,amu}$	Molar mass of species i $(\mathrm{g/mol})$
N	Flux $(\mathrm{mol/(cm^2\,s)})$
n	Number of electrons
P	Total pressure (Pa)
p	Partial pressure (Pa)
$Perm_i$	Permeability of species i $\left((\mathrm{cm^2\,mol}) / (\mathrm{J\,s})\right)$

Q	Sink or source term
q	Heat flux ($\mathrm{W/cm^2}$)
R	Universal gas constant ($8.314472\ \mathrm{J/(K\,mol)}$)
r	Radius (cm)
R_x	Resistance of x (Ω)
U	Voltage (V)
V_m	Standard molar volume of an ideal gas ($22.414 \cdot 10^3\ \mathrm{cm^3/mol}$)
x_i	Mole fraction of species i (liquid)
y_i	Mole fraction of species i (gaseous)

Indices

A	Activation
an	Anode
aq	Aqueous
ca	Cathode
cap	Capillary
$chem$	Chemical
CO_2	Carbon dioxide
el	Electronic
eq	Equilibrium
G	Galvani
g	Gaseous
hc	half–cell
l	Liquid
$leak$	Leakage
mem	Membrane
O_2	Oxygen
ohm	Ohmic
ox	Oxidant
p	Protonic
red	Reductant
ref	Reference electrode
rev	Reversible
th	Thermo neutral, thermodynamic
$therm$	Thermal
vap	Vapor
we	Working electrode

Abbreviations

ACL	Anode catalyst layer
CCL	Cathode catalyst layer
CCM	Catalyst–coated membrane
DEFC	Direct ethanol fuel cell

DMFC	Direct methanol fuel cell
FR-4	Flame resistant 4
laser	Light amplification by stimulated emission of radiation
LDMFC	liquid-fed DMFC
MAF	Misalignment factor
MEA	Membrane electrode assembly
MeOH	Methanol, Methyl alcohol
MOR	MeOH oxidation reaction
MPP	Maximum power point
NHE	Normal hydrogen electrode
OCV	Open circuit voltage
ORR	Oxygen reduction reaction
PCB	Printed circuit board
PDMS	Polydimethyl siloxane
PEM	Polymer electrolyte membrane
PEMFC	Polymer electrolyte membrane fuel cell
PTFE	Polytetrafluorethylene
VDMFC	Vapor-fed direct methanol fuel cell
VLE	Vapor–liquid equilibrium

Acknowledgments

This thesis was written during time with the Department of Energy Technology at the Fraunhofer Institute for Solar Energy Systems ISE in Freiburg, Germany.

I would like to thank Prof. Ellen Ivers-Tiffée, Ordinariat and Head of the Institute of Materials for Electrical Engineering at the Universität Karlsruhe, for supervising this thesis and being the first reviewer. Also, I would like to thank Prof. Jürgen Garche, Universität Ulm, for his contribution as the second reviewer.

The encouragement and support of Dr. Christopher Hebling, Head of the Department of Energy Technology, during my stay is greatly appreciated. Special thanks are due to Dr Carsten Agert, Leader of the Fuel Cell Systems Group, for many fruitful discussions and for nurturing a creative work environment. I would like to thank all my colleagues at Fraunhofer ISE who helped me at many stages during my stay.

The collaboration with the Department of Microsystem Engineering (IMTEK), Universiät Freiburg, in particular with Dipl.-Ing. Christian Litterst and Dr Peter Koltay, is gratefully acknowledged.

Especially, I would like to thank my former colleagues Dipl.-Ing. Natsuki Miyakawa, Dipl.-Ing. Julia Melke, M.Sc. Timbul Hapataran Manurung, Dipl.-Ing. Manuel Morcos, Dipl.-Ing. Falko Krause and B.Sc. Kevin Beard, for their invaluable work.

Finally, I sincerely thank all those people who accompanied, encouraged and helped me during this phase of my life — in particular my parents and my girlfriend Daniela.

Freiburg, 19.07.2007 Steffen Eccarius

Chapter 1

Introduction

The portable electronic device market is quickly outgrowing the capabilities of existing battery technology. A need for higher capacities to power new functions and enhanced features of consumer electronics is growing faster than battery energy densities can increase. Portable fuel cells are believed to be one possible solution which allows longer intervals between refueling [1]. Energy densities of various electrochemical battery and fuel cell systems are given in Table 1.1. These theoretical values are based on the active anode and cathode materials only. Other materials that may be involved in the reaction are neglected in the calculation. It should be noted that the theoretical energy densities for liquids or gases used in fuel cells exceed actual electrochemical systems of batteries by more than one order of magnitude.

Unlike a battery that incorporates its reactants as intrinsic component of the device, fuel cells require a continuous supply of reactants from a storage reservoir. The advantage of separating storage from electrochemical conversion is twofold. First, a separate reservoir allows for instantaneous refueling that can be repeated many times. Batteries require several minutes to hours for recharging and degrade seriously when subjected to frequent charging cycles. Second, the lifespan of the storage reservoir is not linked to the energy converter. Effects that are common in battery technology, like self–discharging, can be overcome by new design and operating protocols. In addition, the feature of separating storage from electrochemical conversion offers a variety of customized applications.

In the power range of several watts and less, the fuel cell has to meet challenging specifications. Fuel cell units must be small in order to fit into portable devices. A planar serial connection of fuel cells is favored over the classical stack design. The flat design offers easy integration into the housing [2,3]. Furthermore passive approaches like air breathing cathodes, passive cooling/heating or a passive fuel supply, are needed to minimize energy losses of a fuel cell system. Peripheral components like pumps, fans, valves or humidity regulators reduce the total efficiency of a fuel cell system, which is significant for low power fuel cells. Passive approaches also imply fewer parts, which increases the durability and the reliability of the fuel cell components. Energy densities of up to $1000\,\mathrm{Wh/l}$, a durability of at least $1000\,\mathrm{h}$ and costs below $5\,€/\mathrm{W}$ are current bench marks [4].

System	**Anode**	**Cathode**	**Reaction mechanism**	**Voltage** V	**Energy** Wh/kg
`Primary batteries:`					
Mercury	Zn	HgO	$Zn + HgO \rightarrow ZnO + Hg$	1.34	255
Alkaline	Zn	MnO_2	$Zn + 2MnO_2 \rightarrow ZnO + Mn_2O_3$	1.5	358
Zn/air	Zn	air	$Zn + \frac{1}{2}O_2 \rightarrow ZnO$	1.65	1353
`Secondary batteries:`					
Ni/Cd	Cd	Ni oxide	$Cd + 2NiOOH + 2H_2O \rightarrow 2Ni(OH)_2 + Cd(OH)_2$	1.35	244
Ni/MH	MH	Ni oxide	$MH + NiOOH \rightarrow M + Ni(OH)_2$	1.35	240
Li–ion	Li_xC_6	$Li_{1-x}CoO_2$	$Li_xC_6 + Li_{1-x}CoO_2 \rightarrow LiCoO_2 + C_6$	4.1	410
`Fuel cells:`					
H_2/air	H_2	O_2	$H_2 + \frac{1}{2}O_2 \rightarrow H_2O$	1.23	39306
DMFC	CH_4O	O_2	$CH_3OH + \frac{3}{2}O_2 \rightarrow CO_2 + 2H_2O$	1.21	6086
DEFC	C_2H_6O	O_2	$C_2H_5OH + 3O_2 \rightarrow 2CO_2 + 3H_2O$	1.15	7992

Table 1.1: Theoretical voltages and energy densities for different electrochemical systems. Data for batteries is taken from [5], data for fuel cells calculated from Gibbs free energies [6]. Values are based on active anode and cathode materials (electrolyte is not included).

Efficient storage of gases like hydrogen is still a major obstacle in terms of weight, size and safety. Accordingly, low power fuel cells for portable applications usually operate with liquid fuels. Liquid fuels, mostly hydrocarbons like methanol, ethanol or formic acid, are either reformed to hydrogen–rich gas or directly converted into electricity. Direct conversion is advantageous for low power systems, as it eliminates the need for complicated fuel reforming and simplifies the system considerably. Furthermore, it is convenient to combine solid polymer electrolytes like Nafion® with liquid fuel instead of hydrogen, as complex humidification and thermal management can be avoided [7].

Direct methanol fuel cells, operated with methanol in the liquid phase, have received by far the most extensive attention and efforts compared to other liquid fuels and comprehensive reviews can be found in the literature [7–10]. A direct methanol fuel cell shows good electrochemical activity and a high energy density. Methanol itself as a fuel is readily available with a global production capacity of 34 Mt/a in 1999 [11]. It is mainly produced using synthesis gas derived from methane components in natural gas. Nevertheless, it can also be produced from biomass, like biodegradable waste or wood–chips. Another option is a heterogeneous catalysis of CO_2 and renewable hydrogen [12]. One great disadvantage of methanol is its toxicity. Methanol is not directly poisonous, but toxicity occurs when enzymes in the liver decompose it to formic acid and formaldehyde. Thus safeguards and safety regulations are needed.

Despite the fact that various prototypes of direct methanol fuel cells have been constructed and demonstrated, there are still some major drawbacks that hinder commercialization of the direct methanol fuel cell, such as slow anode kinetics and fuel crossover. A complex reaction pathway of the methanol oxidation reaction leads to noticeable polarization losses at the anode, unlike a hydrogen-fed fuel cell, which are in the same range as cathodic losses for the oxygen reduction reaction. Methanol crossover across the membrane causes two detrimental effects. First, the parasitic oxidation of methanol at the cathode produces heat and additional water, which increases flooding. The Faradaic efficiency of the system is lowered due to the parasitic fuel loss. Second, a mixed potential of oxygen reduction reaction and methanol oxidation reaction at the cathode electrode drastically increases cathode losses. Many new or altered membrane materials have been studied and are currently under investigation to decrease methanol crossover [13–21].

A conventional hybrid design of a direct methanol fuel cell/battery system consists of a fuel storage reservoir of diluted methanol, a methanol pump, an air pump or fan, the fuel cell, an electronic controller and a battery for peak power demands [22]. Diluted methanol is used to minimize fuel losses and mixed potentials at the cathode because of crossover. The fuel cell is operated at a point that can be optimized with respect to e.g. power density or lifetime. These systems suffer the major disadvantages of large volumes, increased weight and, especially, a low system efficiency because of high parasitic energy consumption of the auxiliary devices. In addition the theoretical energy density of methanol is drastically reduced using 1 M solutions of methanol diluted in water.

Several approaches have been discussed to decrease the complexity of direct methanol fuel cell systems for portable applications. The use of pure methanol in the storage tank, that is then diluted within the direct methanol fuel cell system has been successfully demonstrated [23–26]. Other approaches have combined high molarities with a rate–controlling diffusion layer [27–29], which reduced methanol crossover. Air–breathing cathodes that use atmospheric oxygen to feed the oxygen reduction reaction have been developed [25, 26, 30–33]. A great risk of flooding at the cathode because of limited water evaporation into the surrounding atmosphere, especially at increased crossover, is one major difficulty of this approach. Oxygen access to the cathode catalyst layer is impeded by blocked pores and the overall performance decreases. Various concepts based on MEMS technology, mainly using silicon technology [34–38], with reduced size and weight have been reported.

Completely passive operation with a liquid methanol solution at the anode has been studied [31, 39, 40]. One difficulty of passive operation of a direct methanol fuel cell is the formation of gaseous CO_2 in the liquid fuel at the anode. For pumped systems the convective flow of fuel is used to flush out dissolved CO_2 before bubbles can block channels or pores of the gas diffusion layer and catalyst layer. For passive operation the bubbles become immobile, block fuel access to anode catalyst sites and thus decrease the overall performance. Innovative designs that use natural circulation [41] or a combination of hydrophobic and hydrophilic layers [42] have been introduced to overcome this obstacle.

The object of this thesis is to investigate new approaches to passively operate direct methanol fuel cells and compare these passive concepts to existing technology. Two different technological concepts will be pursued. One concept includes diluted liquid methanol that is fed to a micro–

structured anode to facilitate bubble removal of gaseous CO_2. The other concept utilizes a passive evaporation of highly concentrated methanol which feeds the anode compartment with methanol in the vapor-phase. Finally, the two concepts will be compared and evaluated with respect to the electric performance and methanol crossover from anode to cathode. Various effects such as e.g. mass transport problems or slow kinetics lead to voltage losses at the electrodes of a fuel cell. A reference electrode will be used as a tool to distinguish between voltage losses occurring at the anode and cathode electrode. Measurements including a reference electrode are fault–prone and subject to large measurement errors. Thus, the reliability of the reference electrode will be studied and optimization measures obtained.

Chapter 2

Fundamentals of a DMFC

A fuel cell converts chemical energy directly into electricity without intermediate thermal steps. An electrolyte separates reactants of the electrochemical reaction to eliminate direct combustion of fuels. Thus, efficiency is not limited to the Carnot efficiency which is especially advantageous at low temperatures. Principles of various fuel cells are extensively discussed in the literature [43–45].

In this chapter, the fundamentals of a direct methanol fuel cell (DMFC) are discussed. Besides introducing typical configurations, thermodynamics and kinetics of the electrochemical methanol oxidation reaction (MOR) and oxygen reduction reaction (ORR) are clarified and loss mechanisms are given. Several efficiencies with respect to different loss mechanism are defined. Finally, the methods for single electrode measurements are looked at.

2.1 Functionality and configuration

In DMFCs, methanol (MeOH) is oxidized at the anode electrode. Protons originating from this reaction migrate through the electrolyte to the cathode electrode. Here, oxygen is reduced and water is produced. The electrochemical reaction mechanism can be described as followed.

$$\text{MOR (Anode):} \qquad \mathrm{CH_3OH_{(l)} + H_2O_{(l)} \longleftrightarrow CO_{2(g)} + 6H^+ + 6e^-} \tag{2.1}$$

$$\text{ORR (Cathode):} \qquad \mathrm{\frac{3}{2}O_{2(g)} + 6H^+ + 6e^- \longleftrightarrow 3H_2O_{(l)}} \tag{2.2}$$

$$\text{Total cell reaction:} \qquad \mathrm{CH_3OH_{(l)} + \frac{3}{2}O_{2(g)} \longleftrightarrow CO_{2(g)} + 2H_2O_{(l)}} \tag{2.3}$$

The reaction is driven by a negative Gibbs free energy change. While protons migrate through the electrolyte, electrons are consumed within an external electric circuit. The electronically isolating electrolyte, which is a solid polymer electrolyte membrane, physically separates MeOH and oxygen at the anode and cathode and prevents direct combustion. For Nafion®, a commonly

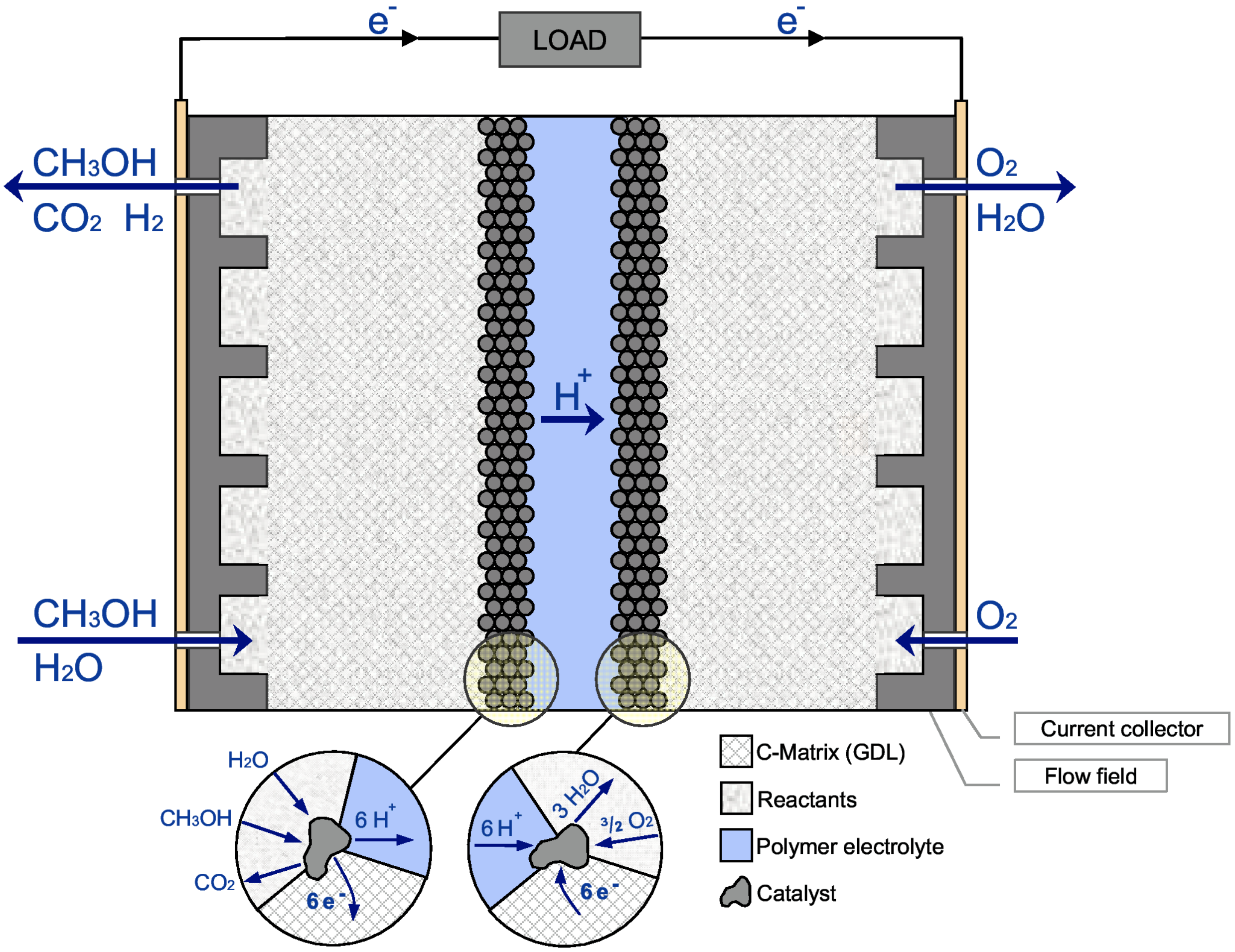

Figure 2.1: Principal assembly of a DMFC. Reaction is taking place at the triple–phase boundary within the catalyst layers.

used polymer electrolyte membrane developed by DuPont[1], protonic conductivity is ensured by sulfonic acid groups that are chemically bonded to a fluor carbon polymer backbone. In combination with water hydrogen bonds of the acid groups are split, allowing protons to migrate freely through the electrolyte. Thus, conductivity is directly correlated to water uptake of the membrane. One problem in using Nafion® as an electrolyte for DMFCs is the physical similarity of water and MeOH, resulting in an uptake of MeOH as well as water. A flux of MeOH across the membrane to the cathode, the so–called MeOH crossover, reduces performance and efficiency of a DMFC significantly. Because of a parasitic MeOH oxidation at the cathode, a mixed potential between the equilibrium potentials of the MOR and ORR is formed and voltage efficiency as well as Faradaic efficiency is lowered. As a consequence, highly diluted MeOH in deionized water (typically between $0.5\,\mathrm{M}$ and $2\,\mathrm{M}$) is used instead of the stoichiometric 1:1 molar ratio.

---

[1] http://www.dupont.com/

A schematic drawing of a DMFC single cell is shown in Fig. 2.1. Diluted MeOH is typically pumped into flow channels of the anode flowfield. Diffusion and convection transport both reactants through the gas diffusion layer (GDL) to the reaction zone of the anode catalyst layer (ACL). Electrochemical oxidation of MeOH takes place at the triple–phase boundary of the anode electrode, where the proton–conductive polymer, the electron–conductive GDL and the fuel are linked to a catalyst site. As already mentioned, protons are transported to the reaction zone of the cathode electrode. Electrons migrate through the GDL and the anode flowfield to a current collector. CO_2, a product of the MOR at the anode electrode, is either diluted in the liquid fuel or forms gas bubbles and leaves the anode flowfield because of forced convection. It is necessary to ensure a design where gas bubbles cannot become stationary and block reactant access to the ACL. Therefore, pumped operation with single serpentine flow channels is frequently used.

In general, a stream of oxygen or air is supplied to the flow channels of the cathode flowfield. It is transported to the reaction zone of the cathode catalyst layer (CCL) by diffusion and convection through the GDL. Oxygen is electrochemically reduced at the triple–phase boundary using protons that migrated through the electrolyte and electrons from the external circuit. Water is produced during the ORR. In the system investigated here, it is believed that this water is in the liquid phase initially and than evaporates into the gas stream. Additional water is produced at the cathode because of the parasitic oxidation of crossover MeOH. If the saturation vapor pressure of water in the gas stream is reached, droplets of water form. These are either driven out by convection or fill some pores of the CCL or GDL, a phenomena called flooding. When this happens, oxygen transport to the catalyst is hindered and the ORR is slowed down, resulting in reduced performance of the fuel cell. Specially treated GDLs (e.g. having an additional microporous layer) are used to minimize flooding of the CCL.

For DMFCs, mostly carbon–supported PtRu for the MOR and carbon–supported Pt for the ORR are utilized for the porous electrodes. Small catalyst particles between $1-5\,\mathrm{nm}$ are placed on the surface of carbon particles and mixed with a proton–conductive electrolyte (e.g. impregnation with Nafion® solution) to increase the active sites along the triple–phase boundary. The catalysts can be applied directly to the membrane, which is then called a catalyst–coated membrane (CCM) or 3-layer membrane electrode assembly (MEA). If the catalyst is applied to the GDL, the terminology of catalyst–coated backing or 5-layer MEA is used. Besides being the support for catalysts for 5-layer MEAs, GDLs are employed to distribute reactants homogeneously to the electrodes, reduce damage to the membrane by mechanical forces and electronically connect the electrodes and the flowfields. Commonly used materials are carbon cloth, carbon papers or metal meshes.

It is usually advantageous to increase the single cell voltage for a DMFC system and adapt the system voltage to the characteristics of the connected load. This is realized by a serial connection of several single cells. Two different concepts are currently being pursued. A pile of single cells is called a stack, and electric connection is realized by a conductive material (bipolar plate) which is sandwiched between two singles cells. When space is limited, the serial connection is realized in a single plane. The term "planar fuel cell" is often used for this concept.

2.2 Operation at open circuit

The voltage of a DMFC reaches its maximum when the external circuit is disconnected and no current is drawn from the fuel cell. This condition is called open circuit voltage (OCV).

2.2.1 Thermodynamic OCV

The change of enthalpy ΔH of the electrochemical reaction describes the maximum work that can be obtained at a constant temperature and pressure. If the complete change in enthalpy were transformed into electric work, a potential difference called U_{th} would be achieved.

$$U_{th} = -\frac{\Delta H}{nF} \tag{2.4}$$

Here n describes the numbers of electrons involved in the electrochemical reaction, which would be 6 for the given case, and F is the Faraday constant. The change of entropy ΔS of the system cannot be converted into electric work according to the second law of thermodynamics. Only the part that is called Gibbs free energy ΔG can be converted and the reversible cell voltage is gained. It equals the potential difference between reversible cathode potential $\Phi_{rev,ca}$ and the reversible anode potential $\Phi_{rev,an}$.

$$U_{rev} = -\frac{\Delta G}{nF} = -\frac{\Delta H - T\Delta S}{nF} = \Phi_{rev,ca} - \Phi_{rev,an} \tag{2.5}$$

Thermodynamic data for a DMFC are given in Table 2.1. According to eq. (2.3), a thermo neutral voltage of $U^0_{th} = 1.255\,\mathrm{V}$ and a reversible voltage of $U^0_{rev} = 1.213\,\mathrm{V}$ can be calculated for standard conditions. It is assumed that CO_2 at the ACL is in the gas phase and water at the CCL is in the liquid phase. These assumptions hold true if the anode liquid phase is saturated with CO_2 and the cathode gas phase is saturated with water vapor.

	$\mathbf{CH_3OH_{(l)}}$	$\mathbf{H_2O_{(l)}}$	$\mathbf{CO_{2(g)}}$	$\mathbf{O_{2(g)}}$
$\Delta H^0/kJ\,mol^{-1}$	-238.66	-285.83	-393.51	0
$S^0/J\,mol^{-1}\,K^{-1}$	126.8	69.91	213.74	205.14
$\Delta G^0/kJ\,mol^{-1}$	-166.27	-237.13	-394.36	0

Table 2.1: Thermodynamic data of reactants involved in the electrochemical reactions within a DMFC under standard conditions at 298.15 K and $1.013 \cdot 10^5$ Pa [6].

A thermodynamic conversion efficiency η_{th} is defined as the ratio of the maximal electric work that can be extracted from the system to the change of enthalpy of the electrochemical reaction ΔH. Using eq. (2.4) and eq. (2.5) it can be further defined as the ratio of reversible to thermo neutral voltage.

$$\eta_{th} = \frac{\Delta G}{\Delta H} = \frac{U_{rev}}{U_{th}} \tag{2.6}$$

The thermodynamic efficiency η_{th}^{0} for a DMFC reaches a high value of $97\,\%$ under standard conditions for the values of Table 2.1 because of low reaction entropies ($\eta_{th}^{0} = 83\,\%$ for a H_2/O_2 fuel cell [46]).

As long as the overall pressure remains constant and no phase changes occur for any involved species, the Gibbs free energy is lowered with increasing temperature.

$$U_{rev}^{T} = U_{rev}^{0}(T_0, P_0) + \frac{\Delta S}{nF}\,(T - T_0)\bigg|_{P=P_0} \tag{2.7}$$

Variation in values for the potential can be very small within the operation conditions of a DMFC. An increase from $30\,^{\circ}\mathrm{C}$ to $80\,^{\circ}\mathrm{C}$ lowers U_{rev} of the electrochemical reaction of eq. (2.3) by only $19\,\mathrm{mV}$. The dependence of U_{rev} on pressure is well described in [43,44] and is of no importance to this work as the pressure is kept constant at ambient values.

2.2.2 Experimental OCV

The OCV that can be measured across a DMFC is much lower than the value of $1.23\,\mathrm{V}$ that can be calculated by thermodynamics. Various effects reduce the OCV for real systems, a voltage loss labeled η_{OCV} occurs.

The electrochemical equilibrium of the electrodes describes the dependence of the reversible cell voltage on the activity a of each species. The Nernst equation is used to describe these dependences [6] and can be determined according to eq. (2.3).

$$U_{rev} = U_{rev}^{T} + \frac{RT}{nF}\left(\ln\frac{a_{ca,ox}^{x_i}}{a_{ca,red}^{x_j}} - \ln\frac{a_{an,ox}^{x_k}}{a_{an,red}^{x_l}}\right) = U_{rev}^{T} + \frac{RT}{nF}\ln\left(\frac{a_{O_2}^{1.5}\cdot a_{MeOH}}{a_{H_2O}^{2}\cdot a_{CO_2}}\right) \tag{2.8}$$

Stoichiometric factors x of the electrochemical reaction are used as exponents of the activity for each species. It can be noted that the reversible cell voltage is dependent on the activity of the reactants. The activities for the different species depend on many factors such as morphology, material properties, reaction paths, concentrations, partial pressures, etc. For instance, in DMFCs the OCV is greatly reduced because of CO poisoning of anode catalyst sites at low anode potentials with reference to the normal hydrogen electrode (NHE) [47]. Contamination of the catalyst sites with organic or inorganic substances, caused during production, assembly or operation, or gas permeation from cathode to anode, decrease catalyst activity.

Although the conductivity of the electrolyte is mainly protonic, still a slight electronic conductivity remains. Thus electrons migrate from the anode to the cathode, causing an internal short circuit. Even if no electrons are transported within the external circuit, the internal circuit causes the OCV to decrease.

MeOH crossover causes an electrochemical MeOH oxidation with oxygen at the cathode, especially at OCV when cathode potentials versus NHE are high. This generation and consumption of electrons and protons under open circuit conditions can be regarded as an internal short circuit that decreases the cathode potential because of polarization losses. The amount of MeOH permeating to the cathode greatly depends on operating conditions (such as temperature, pressure, methanol concentration, cathodic gas stream, etc.) as well as structural parameters (membrane thickness, morphology and thickness of the catalyst layer, etc.).

2.3 Operation under load

When a fuel cell powers an electric device, a current has to be drawn from the fuel cell. Typically fuel cells are operated at a designated working point galvanostatically, when the current is controlled, or potentiostatically, when the voltage is controlled. The voltage and current change at different working points according to the IV characteristics of the fuel cell.

2.3.1 Methanol oxidation

The basic MOR, as given in eq. (2.1), has been studied by many researchers [48–50]. Compared to the rapid oxidation of hydrogen in polymer electrolyte fuel cells (PEMFC), it is a complex reaction with a large number of reaction steps involved and intermediates formed. A basic reaction scheme is given in Fig. 2.2 in the form of squares.

PtRu catalyst are commonly used to shift the MOR to lower anode potentials. Although various parallel reactions paths are possible, a reaction mechanism as shown below is most likely [50, 52, 53].

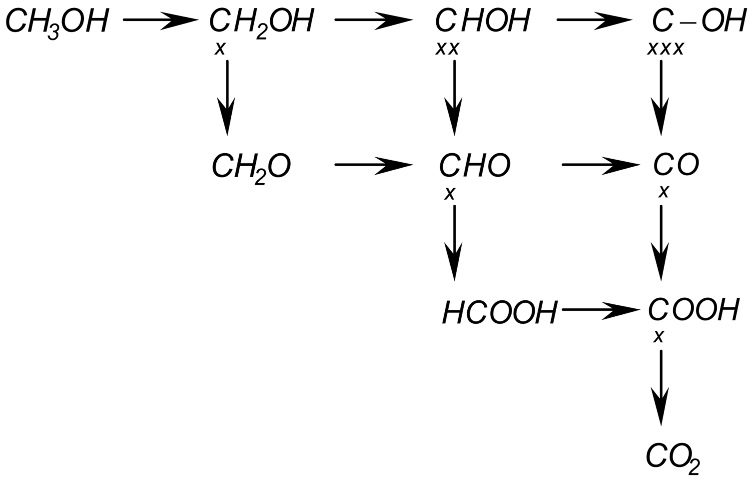

Figure 2.2: Oxidation reaction of methanol depicted as a reaction scheme in the form of squares [51]. A Pt-C bond is symbolized by x.

$$\mathrm{CH_3OH + Pt} \longrightarrow \mathrm{Pt - CH_2OH + H^+ + e^-} \tag{2.9}$$
$$\mathrm{Pt - CH_2OH + Pt} \longrightarrow \mathrm{Pt_2 - CHOH + H^+ + e^-} \tag{2.10}$$
$$\mathrm{Pt_2 - CHOH + Pt} \longrightarrow \mathrm{Pt_3 - COH + H^+ + e^-} \tag{2.11}$$
$$\mathrm{Pt_3 - COH + Pt} \longrightarrow \mathrm{Pt - CO + 2Pt + H^+ + e^-} \tag{2.12}$$

Methanol is adsorbed on a platinum site, followed by a stepwise stripping of protons and electrons to CO. Strong adsorbents like CO on Pt sites reduce the activity of the catalyst. The terminology of CO poisoning is often used. Oxidation of an adsorbent is facilitated by adding Ru to the catalyst.

$$\mathrm{H_2O + Ru} \longrightarrow \mathrm{Ru - OH + H^+ + e^-} \tag{2.13}$$
$$\mathrm{Pt - CO + Ru - OH} \longrightarrow \mathrm{Pt + Ru + CO_2 + H^+ + e^-} \tag{2.14}$$

Formation of $\mathrm{Ru - OH}$ takes place at much lower potentials than formation of $\mathrm{Pt - OH}$. Thus the impact of CO poisoning at high cell voltages, when anode potentials are low, can be lowered by adding Ru, typically in a 1:1 atomic ratio.

When the oxidation of MeOH is incomplete, intermediate products (e.g. formaldehyde, formic acid) can be found at the anode outlet. In this case, the energy density of MeOH is only partially utilized and Faradaic efficiency decreases. Several groups have reported intermediate products in the anode outlet stream [49,54].

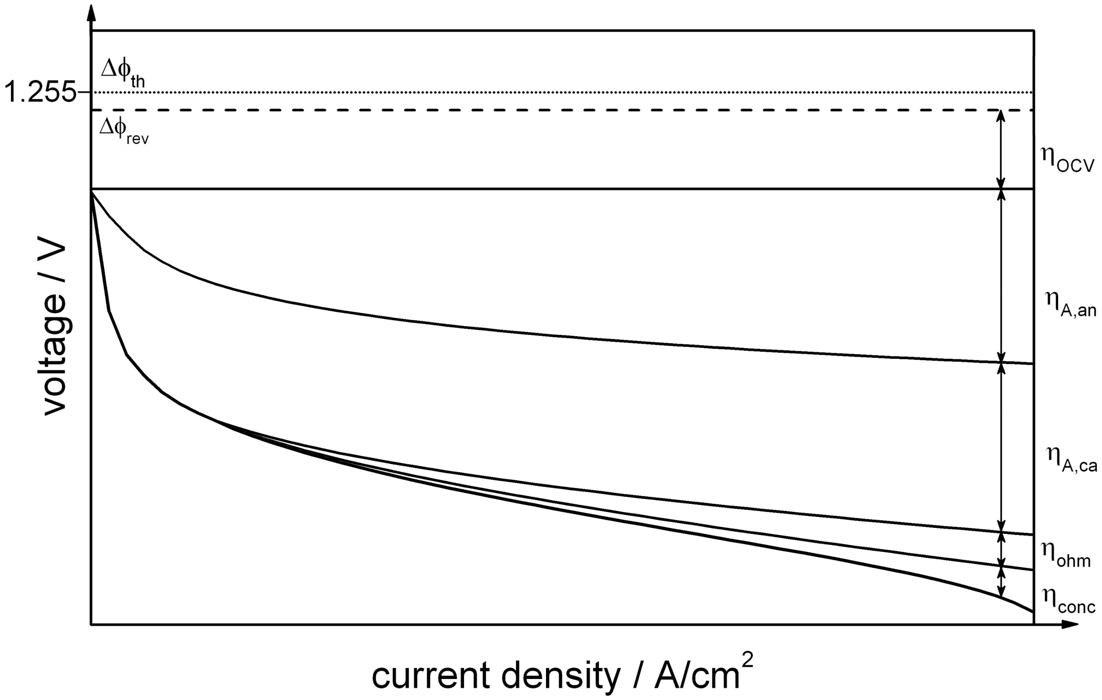

Figure 2.3: Polarization plot of a DMFC. Different loss mechanisms are illustrated that cause irreversible voltage losses in the fuel cell. See section 2.3.2 for an explanation of the symbols.

2.3.2 Loss mechanisms

At OCV, a dynamic equilibrium is established at the electrodes of the fuel cell. This equilibrium is disturbed when a current is drawn from the cell and a new electrode potential is established. The deviation of the electrode potential under load $\Phi(i)$ from the reversible electrode potential Φ_{rev} is defined as the overpotential or polarization loss η.

$$\eta = \Phi\left(i\right) - \Phi_{rev} \tag{2.15}$$

The total loss can be split into activation losses, ohmic losses and concentration losses. The impact of the different loss mechanisms on the IV characteristic of a DMFC is schematically illustrated in Fig. 2.3. The contribution of each mechanism changes with current density as can be seen in the graph. The voltage can be split into the reversible cell voltage and different loss mechanisms.

$$U = U_{rev} - \eta_{OCV} - |\eta_{A,an}| - |\eta_{A,ca}| - \eta_{ohm} - \eta_{conc} \tag{2.16}$$

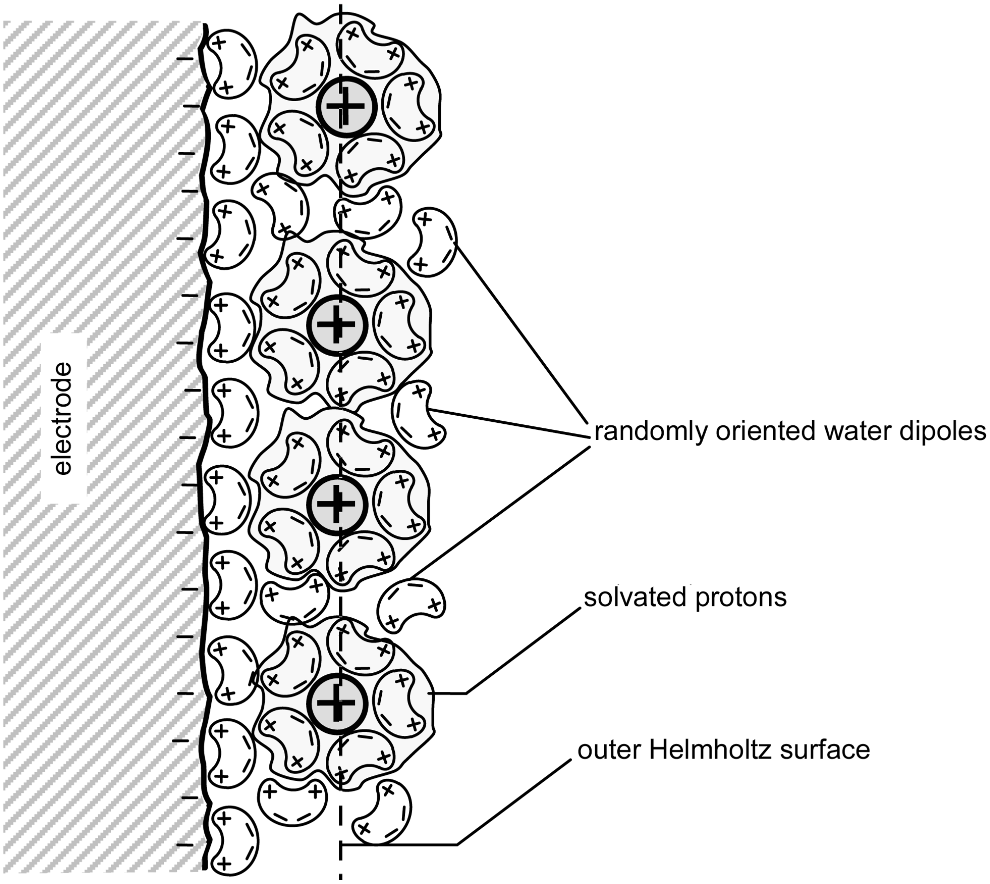

Figure 2.4: Helmholtz model of an electric double layer between the electrode and solvated ions within the electrolyte.

Activation losses η_A

A finite charge transfer through the phase boundary between the protonic and the electronic phase, which is typical for electrochemical reactions, causes the activation losses. In general, a reversible electrochemical reaction between an electrode and a species in an electrolyte involving n electrons can be formulated as

$$\mathrm{S_{ox}} + \mathrm{ne}^- \longleftrightarrow \mathrm{S_{red}} \tag{2.17}$$

where $\mathrm{S_{ox}}$ is the oxidized form and $\mathrm{S_{red}}$ the reduced form of species S. A simple model that describes the separation of charges between the electrode and the electrolyte is the Helmholtz model that is depicted in Fig. 2.4.

It describes the formation of an electric double layer due to solvated ions and neglects thermal movements of the molecules [55]. The solvated ions approach the surface of the electrode as closely as possible (called the outer Helmholtz surface) and the double layer acts as a capacitor. The double layer causes a potential difference between the electrode and electrolyte. The forward respectively reverse reaction of eq. (2.17) is favored until an electrochemical equilibrium is established at the phase boundary between the electrode and the electrolyte [55]. The difference between the protonic potential in the electrolyte Φ_p and the electronic potential in the electrode Φ_{el} is called the Galvani potential difference $\Delta\Phi^G$.

$$\Delta\Phi^G = \Phi_{el} - \Phi_p \tag{2.18}$$

The equilibrium is disturbed when a current is forced through the system and the charge of the capacitor is changed. The Galvani potential difference changes from its equilibrium value $\Delta\Phi_0^G$ to its value under load $\Delta\Phi^G$. The protonic charge has to move across the double layer which occurs during a quantum mechanical tunneling process. Therefore an activation loss η_A occurs that can be defined as

$$\eta_A = \Delta\Phi^G - \Delta\Phi_0^G \tag{2.19}$$

The Butler–Volmer equation couples η_A and the cell current density i.

$$i = i_0 \cdot \left[\underbrace{\exp\left(\frac{(1-\alpha)\,nF}{RT}\cdot\eta_A\right)}_{Oxidation} - \underbrace{\exp\left(\frac{-\alpha nF}{RT}\cdot\eta_A\right)}_{Reduction} \right] \tag{2.20}$$

Both the anodic oxidation reaction and the cathodic reduction reaction of eq. (2.17) are summed up in one equation. At equilibrium, when η_A is zero, no net current is produced at the electrodes and the oxidation and reduction current densities of eq. (2.20) are equal. The modulus of the anodic and the cathodic current density in equilibrium is called the exchange current density i_0, a measure for the rate of electron transfer at equilibrium. It depends, besides many other factors, on the concentration of the oxidized and reduced species respectively. The parameter α is called the transfer coefficient and is in the range between 0 and 1 and n is the number of electrons involved in the electrochemical reaction. A detailed derivation of the Butler–Volmer equation can be found in [6,43,55].

In the case of high anodic activation losses ($\eta_A \gg \frac{RT}{nF}$), the reduction current is negligible. Therefore eq. (2.20) can be simplified to the Tafel approximation.

$$i = i_0 \cdot \exp\left(\frac{(1-\alpha)\,nF}{RT} \cdot \eta_A\right) \tag{2.21}$$

Analogously, at high cathodic activation losses the oxidation current can be neglected.

$$i = -i_0 \cdot \exp\left(\frac{-\alpha nF}{RT} \cdot \eta_A\right) \tag{2.22}$$

Besides activation losses further kinetic losses occur when the coupled chemical reactions cannot keep pace with a quicker electron transfer step. Dissociation, adsorption or desorption of reactants as rate limiting steps cause a change in the Galvani potential difference. These losses are called **reaction losses** and are attributed to the activation losses in this thesis.

Ohmic losses η_{ohm}

Electronic and protonic currents in the fuel cell lead to a voltage drop due to finite resistances of the components. According to Ohm's law, these losses are summed up into the ohmic losses.

$$\eta_{ohm} = I \cdot R_x \tag{2.23}$$

In this case, the ohmic resistance R_x contains all resistivities and contact resistances of the fuel cell. The contact resistance depends on the clamping pressure of the fuel cell sandwich. In addition, the ionic resistance of the membrane, which gives a high contribution to the overall resistance, is also included in R_x. The ionic resistance is highly dependent on the humidification of the membrane and thus on the operating conditions of the fuel cell. Thicker membranes are used for DMFCs compared to hydrogen–fed PEMFCs. Hence, in most cases, the ionic resistance is the major contributor to the overall ohmic resistance.

As a consequence, the ohmic resistance is a good parameter to characterize the water content of the membrane. For convenience it is typically normalized to the active area of the fuel cell.

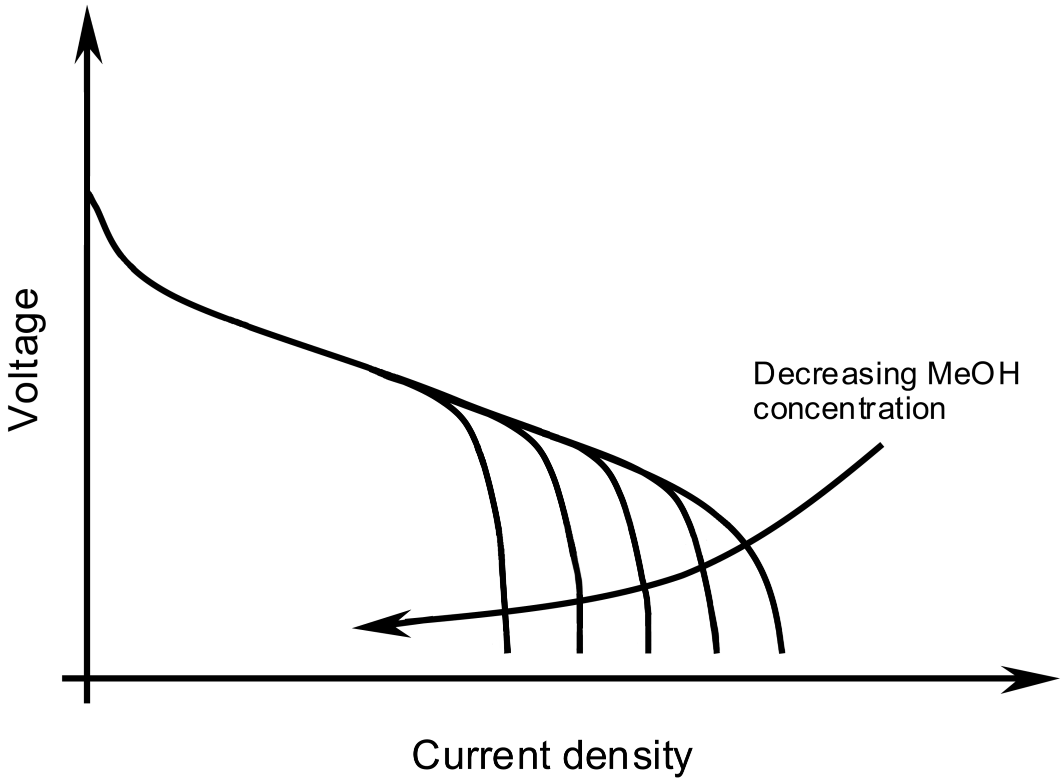

Figure 2.5: Influence of a decreasing MeOH feed concentration on the IV characteristics of a DMFC that results in smaller limiting current densities.

Concentration losses η_{conc}

Mass transport losses arise at higher current densities as a result of insufficient transport of reactants to the electrode. For instance, the oxidation of MeOH at the anode electrode of a DMFC cannot be faster than the supply of MeOH to the anode electrode. Current generation diminishes with decreasing MeOH concentration at the anode and consequently the cell voltage has to be lowered to maintain current density. The additional term that decreases cell voltage is labeled concentration loss.

At the anode electrode, MeOH consumption increases with current density. Assuming that the MeOH concentration at the electrode is limiting performance, the cell voltage decreases rapidly as the concentration of MeOH approaches zero. A maximum current density called *limiting current density* is reached when the supply of MeOH limits the electrochemical reaction. Polarization plots for decreasing methanol feed concentrations and limiting current densities are shown in Fig. 2.5.

At the cathode electrode, decreasing partial pressures of oxygen can cause a concentration loss as well. For a liquid-fed DMFC, a common problem is the flooding of the porous cathode electrode or the GDL due to water and MeOH crossover across the membrane. Large amounts of water block the oxygen access to the catalyst sites, which causes a high concentration loss.

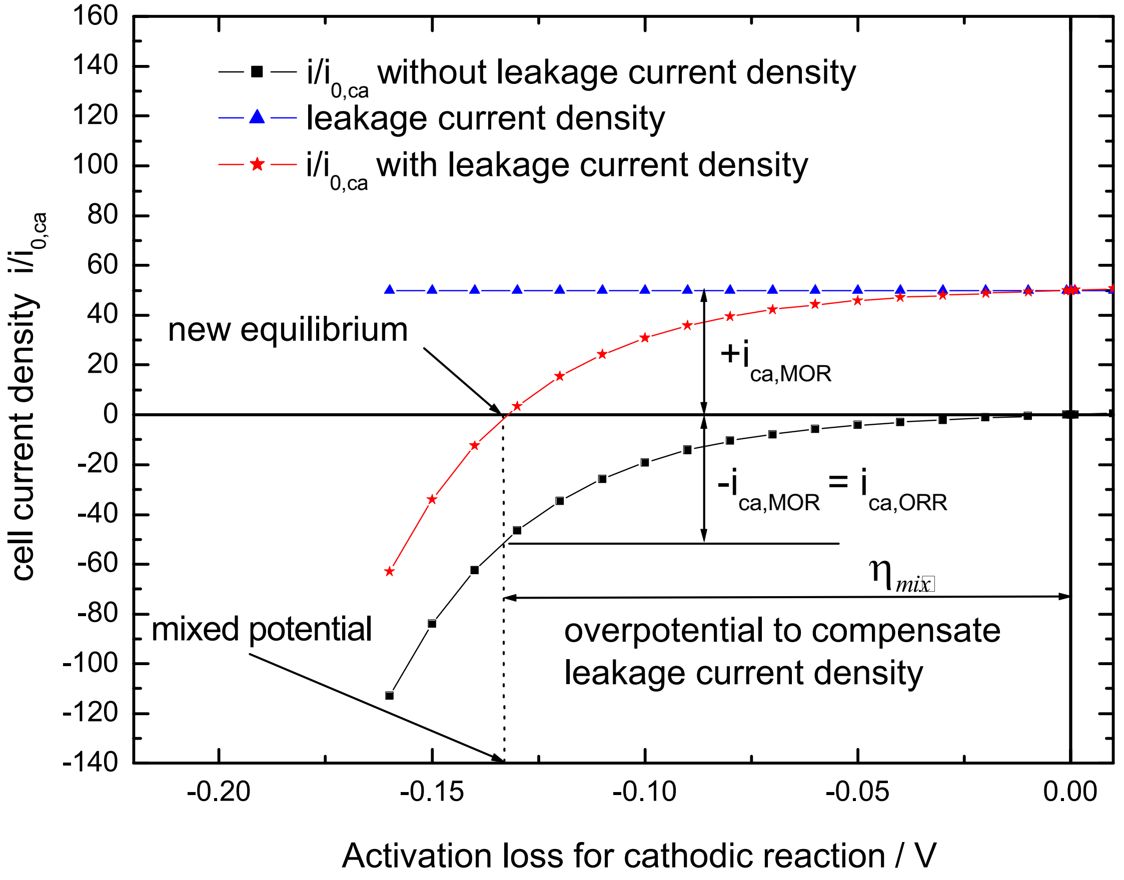

Figure 2.6: Influence of the cathodic activation losses with and without a leakage current density on the cell current density of the DMFC [56].

2.3.3 Methanol crossover

As already mentioned above, protonic conductivity at acidic solid polymer electrolytes like Nafion® is established by an uptake of water into the membrane. High water contents have to be maintained during fuel cell operation to guarantee good protonic conductivity of the membrane. Due to its similarity to water, MeOH is easily taken up by the membrane as well.

Two different transport mechanism cause a MeOH crossover from the anode to the cathode side across the membrane, diffusion and active transport together with protons and their solvation shell water called electroosmotic drag. For a better comparison the crossover flux of MeOH is commonly converted into an equivalent current density using Faraday's law. This crossover current is labeled the leakage current density i_{leak}. If all MeOH is oxidized at the cathode electrode, one obtains

$$i_{leak} = nF\left(\frac{c_{MeOH,an}}{\delta_{mem}} \cdot D_{MeOH,mem} + \frac{c_{MeOH,an}}{c_{H_2O,an}} \cdot \xi \cdot \frac{i}{F}\right) \tag{2.24}$$

where δ_{mem} is the thickness of the membrane and n the number of electrons. The MeOH concentration $c_{MeOH,an}$ and the water concentration $c_{H_2O,an}$ is applied at the anode electrode. $D_{MeOH,mem}$ is the effective diffusion coefficient of the membrane. The electroosmotic drag factor ξ describes the number of molecules that are dragged along with each proton. Thus the electroosmotic drag depends on the current density i of the fuel cell.

In a DMFC, MeOH reaching the cathode electrode is oxidized at the Pt catalyst sites due to high cathode potentials. Oxygen is reduced during this reaction and CO_2, water and heat are produced. This parasitic reaction causes an internal short circuit of the fuel cell. It occurs even under open circuit conditions as long as enough oxygen is present at the cathode electrode. Under load, the leakage current density has to be generated additionally to the cell current density.

Electrons and protons that are generated by the parasitic MOR influence the potential of the double layer between the cathode electrode and the electrolyte. The disturbance results in a new potential, a so called mixed potential. Its value is located between the potential of the MOR and the ORR [57]. For this work a superposition of the two reactions is assumed that is coupled by the Galvani potential difference. Qualitatively the formation of a mixed potential can be explained using Fig. 2.6. The system reaches equilibrium when the leakage current density is compensated by the ORR.

2.4 Efficiencies

A fuel cell converts chemical energy directly into electric energy and thus is not subject to the Carnot efficiency of a heat engine. In general the total efficiency can be defined as the ratio of the electric energy E_{el} and thermal energy E_{therm} that is derived from the system to the chemical energy E_{chem} that is stored within the system.

$$\eta = \frac{E_{el} + E_{therm}}{E_{chem}} \tag{2.25}$$

Gibbs free energy ΔG defines the maximum energy and consequently also U_{rev}, as derived in eq. (2.5), the maximum potential that can be extracted from the electrochemical system. The *thermodynamic efficiency* η_{th} was already defined above in eq. (2.6).

In reality, the operating potential U of a fuel cell is much lower than the maximum value U_{rev} derived from Gibbs free energy. The *voltage efficiency* η_u, which is also termed electrochemical efficiency, can be defined accordingly.

$$\eta_u = -\frac{nFU}{\Delta G} = \frac{U}{U_{rev}} \tag{2.26}$$

The *Faradaic efficiency* η_i compares the actual cell current I to the theoretically expected cell current I_{tot}, when all reactants are consumed in the overall reaction of the fuel cell and electrochemical conversion is complete.

$$\eta_i = \frac{I}{I_{tot}} = \frac{m}{m_{tot}} \tag{2.27}$$

A convenient way to determine η_i is to compare the total mass of fuel m_{tot} at the beginning of an experiment and compare it to the mass of fuel m at a designated point of time. For a DMFC, η_i is much less than $100\,\%$, which is mainly caused by the MeOH crossover to the cathode electrode.

The total efficiency derived in eq. (2.25) can now be rewritten as

$$\eta = \eta_i \cdot \eta_u \cdot \eta_{th} \tag{2.28}$$

2.5 Single electrode measurements

Reference electrodes are used to measure potentials of single electrodes in an electrochemical system. This method can determine the losses of anode potential and cathode potential separately in a fuel cell. If additionally the ohmic resistance is known, the total loss of a fuel cell η_{tot} can be devided into its components.

$$\eta_{tot} = \eta_{an} + \eta_{ohm} + \eta_{ca} = U_{rev} - U \tag{2.29}$$

Here η_{an} and η_{ca} stand for the anode and cathode electrode polarization losses, which will also be named anode loss and cathode loss throughout this thesis. Furthermore, η_{ohm} stands for the ohmic losses and U for the actual voltage of the fuel cell. The standard or normal hydrogen electrode (NHE) is commonly used as a reference electrode and its equilibrium potential is defined to be zero. It consists of a platinum sheet immersed into an aqueous solution in contact with gaseous hydrogen [55]. The potential–determining reaction has the form

$$2\mathrm{H}^+_{(\mathrm{aq})} + 2\mathrm{e}^- \longleftrightarrow \mathrm{H}_2 \tag{2.30}$$

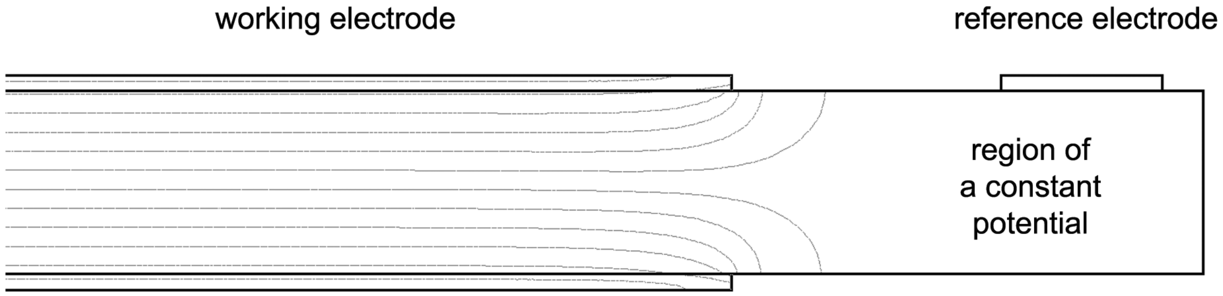

Figure 2.7: Schematic diagram of an equipotential line distribution throughout the membrane. For this symmetric case the membrane losses are equally distributed between anode and cathode electrodes. A region of constant potential exists far away from the working electrode.

For a DMFC, it is of great interest to distinguish between cathode and anode losses to gain enhanced knowledge of the electrode processes and consequently improve structural parameters and operating conditions. Effects like flooding of the cathode, MeOH depletion at the anode or the temperature dependence of the MOR have a strong influence on the overall performance of a DMFC. Therefore, single electrode data provides valuable information and helps to characterize loss mechanisms such as activation losses due to kinetics or concentration losses due to mass transfer limitations.

Data of single electrode potentials can be obtained by using a reference cell that is either connected directly to the same substrate as the working electrode or attached to the membrane by using a salt bridge. Another method to reveal a single electrode potential is half–cell operation of the fuel cell, where one of the working electrodes acts as a NHE.

2.5.1 Reference cell

Several concepts of reference cells, including a dynamic hydrogen electrode (DHE) [58–60] and a normal hydrogen electrode [61, 62], have been reported on both PEMFC and solid oxide fuel cells. In a DHE, hydrogen is usually produced by placing a Pt working electrode on both sides of the membrane and applying a small cathodic current. One major advantage is assumed to be the constant coverage of hydrogen at the working electrode, resulting in a stable potential [60]. Conversely, the induced current leads to polarization resistances that can influence the reference cell measurement. Also a drift of the DHE has been reported by Küver et al. [58]. The concept of a NHE provides an electronically separated electrode on the same substrate as the working electrodes. Hydrogen is typically provided to the NHE due to its high reversibility in order to stabilize the reference potential. As no current is drawn from the reference electrode, no polarization losses occur.

It is necessary to know the contributions of the ohmic drop across the fuel cell to deduct the correct fraction of the ohmic losses from the respective electrode potential that is gained by the reference cell. Thus, it is necessary either to identify the ohmic contributions of the fuel cell that affect the reference readings for both the anode and the cathode or to guarantee a known position of the equipotential line inside the membrane that is sensed by the reference cell. If the potential U_{ref} between the reference electrode and the working electrode, the ohmic loss R_{ohm}, and the contribution of the ohmic losses to the electrode polarization losses are known, the anode losses η_{an} and the cathode losses η_{ca} can be calculated.

A schematic diagram of equipotential lines inside the membrane is shown in Fig. 2.7. The case is depicted where the potential that the reference cell senses is located exactly in the center of the membrane – resulting in symmetric equipotential lines. In this case, an equal distribution of the ohmic loss between anode and cathode losses occurs and the following equations can be obtained [59,60].

$$\eta_{an} = U_{ref} - \frac{R_{ohm} \cdot I}{2} \tag{2.31}$$

$$\eta_{ca} = U_{rev} - U - U_{ref} - \frac{R_{ohm} \cdot I}{2} \tag{2.32}$$

Here I stands for the actual current of the fuel cell. R_{ohm} denotes the ohmic impedances such as flowfield and contact resistances, electrode resistances and the membrane resistance. Slight deviations of the symmetric potential distribution can lead to significant different contributions to the membrane loss for the reference readings, as will be discussed in Appendix A. Therefore great experimental care must be taken to guarantee that the assumption of an even distribution of the membrane loss throughout the ionomer is correct.

2.5.2 Half–cell operation

Half–cell operation can be achieved by filling the cathode compartment with hydrogen [63], nitrogen [64] or an inert gas such as argon [65]. Instead of the cell voltage resulting from an electrochemical potential gradient, an intermediate voltage is imposed between the anode and cathode that forces the electrochemical reactions. When the voltage of the power supply is adjusted, the current changes and the balance of the oxidation reaction at the anode can be shifted. For DMFCs, it is important that the voltage does not exceed a value of $0.6\,\mathrm{V}$; otherwise, degradation effects such as irreversible ruthenium oxidation of the PtRu catalyst occur [66]. At the same time, hydrogen is produced at the cathode electrode according to the imposed current density.

$$6\mathrm{H}^+ + 6\mathrm{e}^- \longleftrightarrow 3\mathrm{H}_2 \tag{2.33}$$

The imposed current causes a constant coverage of the electrode with H_2 and the cathode acts as a DHE. Due to fast kinetics, the cathodic hydrogen evolution reaction experiences only a small overvoltage compared to the large anode overvoltage because of the MOR. Thus, the losses due to hydrogen evolution are usually neglected [67,68].

The anode losses can be determined by correcting the impressed cell voltage U_{hc} between the anode and cathode for the ohmic drop of the fuel cell.

$$\eta_{an} = U_{hc} - R_{ohm} \cdot I \tag{2.34}$$

Chapter 3

Experimental Details

3.1 MEA preparation

Two differently prepared MEAs were used throughout this work. As the catalyst was applied directly onto the membrane the terminology of catalyst coated membrane (CCM) will be used in this thesis. CCMs used for investigations about MeOH crossover in Chapter 4 were transferred from a decal film whereas all other experiments were carried out with screen–printed CCMs.

3.1.1 CCM production by “decal transfer”

Nafion® was used as the ionomer for the CCMs. The catalyst layers of the CCM’s were prepared in two steps [69]:

1. knife coating of the catalyst ink onto a decal film.
2. transfer from the decal film to either a Nafion® 117 or Nafion® 1135 membrane by hot-pressing.

The anode catalyst consists of $60\,\mathrm{wt\%}$ Pt/Ru and $40\,\mathrm{wt\%}$ carbon (Johnson Matthey[1] HiSpec10000). The Pt/Ru loading of the anodes was 1.5 and $2.5\,\mathrm{mg/cm^2}$ respectively. The cathode catalyst has a composition of $60\,\mathrm{wt\%}$ Pt and $40\,\mathrm{wt.\%}$ carbon (Johnson Matthey HiSpec9000), with a Pt loading of either 1.5 or $2.5\,\mathrm{mg/cm^2}$. All catalyst layers were prepared with a Nafion® content of $20\,\mathrm{wt\%}$. The hot–pressing temperature was $130\,^{\circ}\mathrm{C}$ and the pressure was $0.5\,\mathrm{kN/cm^2}$. The reference electrodes had the same composition as the respective electrode, i.e. working anode or cathode, on the same side of the membrane.

---

[1] http://www.jmfuelcells.com/

3.1.2 CCM production by “screen–printing”

Nafion® was used as the ionomer for the CCMs. During pre–treatment of the membranes, a tempering step was performed at $150\,^\circ\mathrm{C}$ for 30 minutes. DMFC membranes were screen printed on an EKRA E1 semi–automatic screen printer, equipped with a screen having the working electrode and reference electrode design. The anode side of the membrane was printed two, three or four times, depending on the loading required, using a screen–printing paste based on PtRu black and Nafion® ionomer. After drying overnight, the anode loading was determined gravimetrically. The cathode side was printed with the same procedure, using an electrode paste based on high surface–area, carbon–supported Pt and Nafion® ionomer. After drying for another night, the loading of the cathode was determined.

For post treatment of the CCMs, the air–dried CCMs were tempered at $145\,^\circ\mathrm{C}$ for 30 minutes and slowly cooled down. After tempering, the CCMs were placed in boiling $5\,\mathrm{wt\%}$ nitric acid for 30 minutes, then placed in boiling demineralised water twice for 30 minutes each, and after cooling down put in cold water, also for 30 minutes. The CCMs were then dried between lint–free paper, pressed between wooden plates. Unless stated otherwise in the text CCMs of Nafion® 1135 that had been screen–printed 3-times with Johnson Matthey’s HiSPEC11100 (resulting in $1\,\mathrm{mg/cm^2}$ Pt) at the cathode electrode and that had been screen–printed 3-times with Johnson Matthey’s HiSPEC6000 (resulting in $3\,\mathrm{mg/cm^2}$ Pt/Ru) at the anode electrode, were used. The reference electrodes had the same composition as the respective electrode, i.e. working anode or cathode, on the same side of the membrane.

3.2 MEA post–processing

A misalignment of the electrodes during the preparation step, as shown in Fig. 3.1a, is inevitable for the given methods. The purpose of post–processing is to improve the alignment of the two electrodes. High geometric resolution is needed as the ionomer is very thin and therefore only slight geometric deviations between anode and cathode electrode result in large misalignment factors [70]. Using a laser ablation process is a convenient way to fulfill two goals, segmentation of the catalyst layer combined with high spatial resolution.

Two different membranes, Nafion® 117 and Nafion® 1135 with a thickness of $90\,\mu\mathrm{m}$ and $180\,\mu\mathrm{m}$ respectively were used to evaluate the effect of membrane thickness on the ablation process. The distance between the two electrodes was $30\,\mathrm{mm}$. To minimize the misalignment of the working electrodes δ, the catalyst layer was ablated by a laser beam on both the cathode and the anode side, as depicted in Fig. 3.1b. Since the catalyst was removed in one step on both sides, a minimal value of δ could be achieved.

The laser ablation was performed using a Nd:YAG laser that was working at a wavelength of $1064\,\mathrm{nm}$ (near infrared). In the focus of the fixed laser optics was a probe chuck that could be moved in the xy–plane by a micro–stepping motor. The chuck could be positioned with an ac-

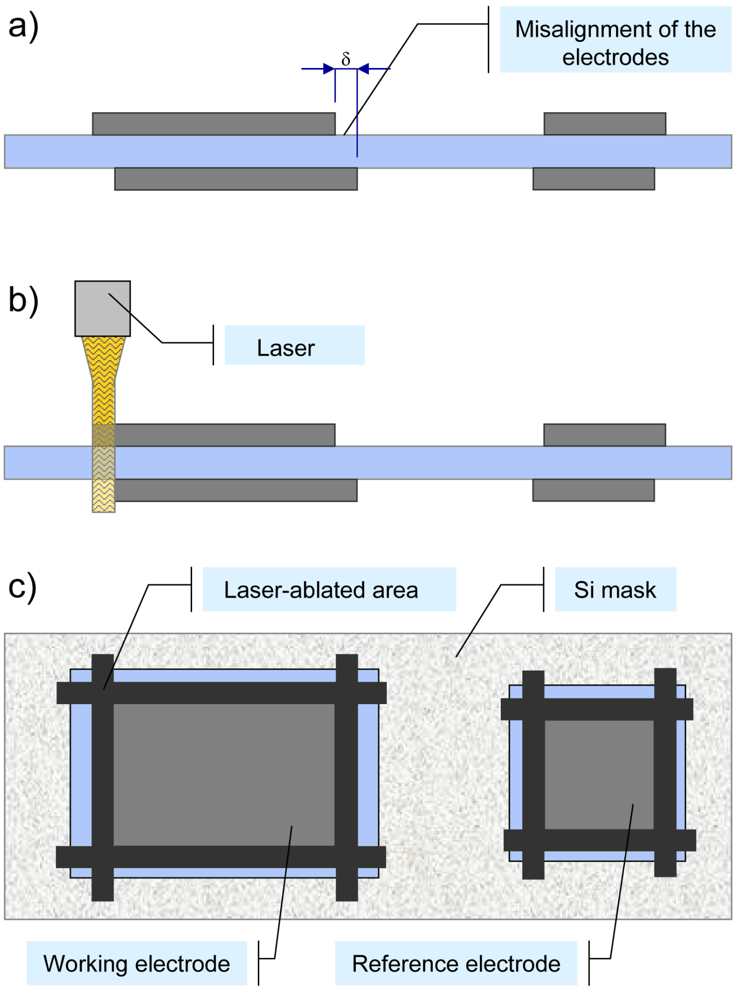

Figure 3.1: a) Misalignment of the electrodes after preparation. b) Single–step laser segmentation of both electrodes decreased misalignment. c) Silicon blend used for the laser ablation process to absorb initial higher energies. The laser beam started and stopped on the mask.

curacy of $1\,\mu\mathrm{m}$ at a speed of $200\,\mathrm{mm/s}$. The beam itself had a diameter of approximately $30\,\mu\mathrm{m}$. In order to avoid local overheating of the membrane, the lowest possible pulse energy density of $0.25\,\mathrm{J\,cm^{-2}}$ with a high pulse frequency of $20\,\mathrm{kHz}$ was selected. One severe risk was self–ignition of the MEA, since catalyst and oxygen were present during the ablation process. Because the process area could not be flooded with an inert gas due to limitations of the laser system, the MEA was covered with a highly transparent glass substrate. Another problem appeared when the shutter of the beam was opened. The laser pulses used for segmentation initially had higher energy densities than later during stable operation. Thus, it burnt holes into the ionomer at the point the laser started. To prevent this, a Si–mask (Fig. 3.1c) absorbing the initial energy was used on top of the glass substrate. The laser started and stopped on the Si–mask.

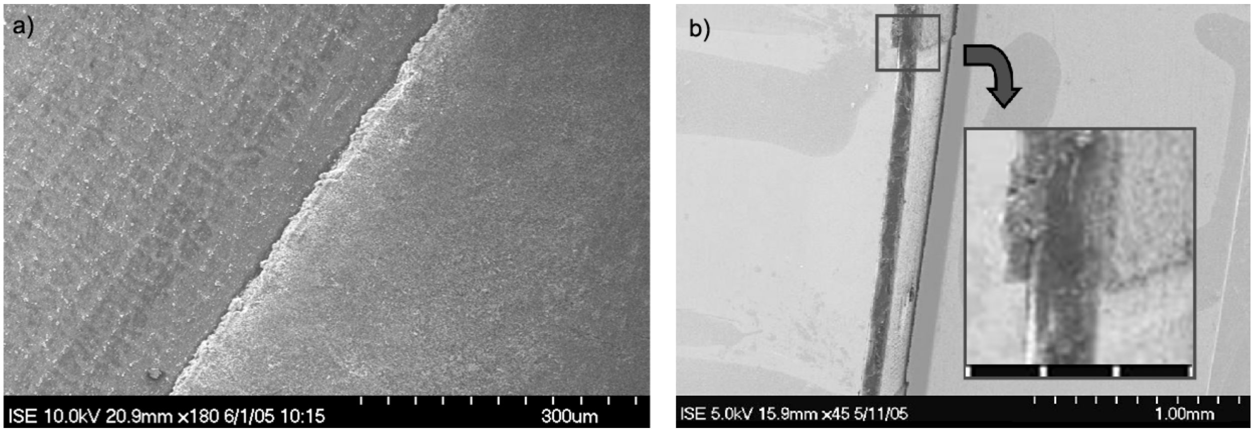

Figure 3.2: a) Top view of a segmented MEA showing the interface between the catalyst layer and the pure ionomer at the ablated area. The beam width of the laser ablation process can be seen as lines in the ionomer. b) Cross–section through the MEA with segmented catalyst layers. The electrode ablation was processed in one step because of the transparency of the ionomer to the laser radiation so the two catalyst layers were well aligned above each other.

During the ablation process, the chuck was moved and the laser beam scanned in lines over the MEA. After each line, the chuck was shifted $30\,\mu\mathrm{m}$, the diameter of the laser beam. These "lines" can also be seen on the ionomer, as illustrated in Fig. 3.2a on the left side. They had a thickness of approximately $30\,\mu\mathrm{m}$ that indicated that the ionomer was not totally transparent to the laser light. During the ablation process the catalyst layer was either evaporated or the adhesion to the substrate is lost. Remaining particles could easily be removed using an air jet. Structuring larger areas was a time–consuming process. In order to ablate an area with a width of $2\,\mathrm{mm}$, the beam had to be moved and shifted more than 60 times over the MEA.

Fig. 3.2b shows a cross section through a MEA with segmented catalyst layers. The "lines" seen in the top view a) do not appear to penetrate deep into the ionomer. Therefore, it can be concluded that the membrane, in this case Nafion® 1135, was not damaged structurally. It can be seen in the magnification on the right that the catalyst layers on the cathode and anode side were aligned precisely above each other. This was due to the one–step ablation process. The laser energy was adsorbed on both electrodes at the same time as the beam passed through the partially transparent ionomer.

Additional experiments to study the transmission of Nafion® 117 and Nafion® 1135 were performed, using a *Cary 500i* from Varian. A light source (a tungsten halogen lamp in the near infrared) was followed by two grating monochromators to select the desired wavelength. A chopper split the beam into the beam that was transmitted by the sample and a reference beam. Both beams were directed into an integrating sphere, where multiple diffuse reflection distributed the flux of light homogeneously throughout the sphere. Detectors measured the total intensity at the given wavelength. A transmission of $95\,\%$ at the given wavelength of the laser was determined for both membranes as shown in Fig. 3.3.

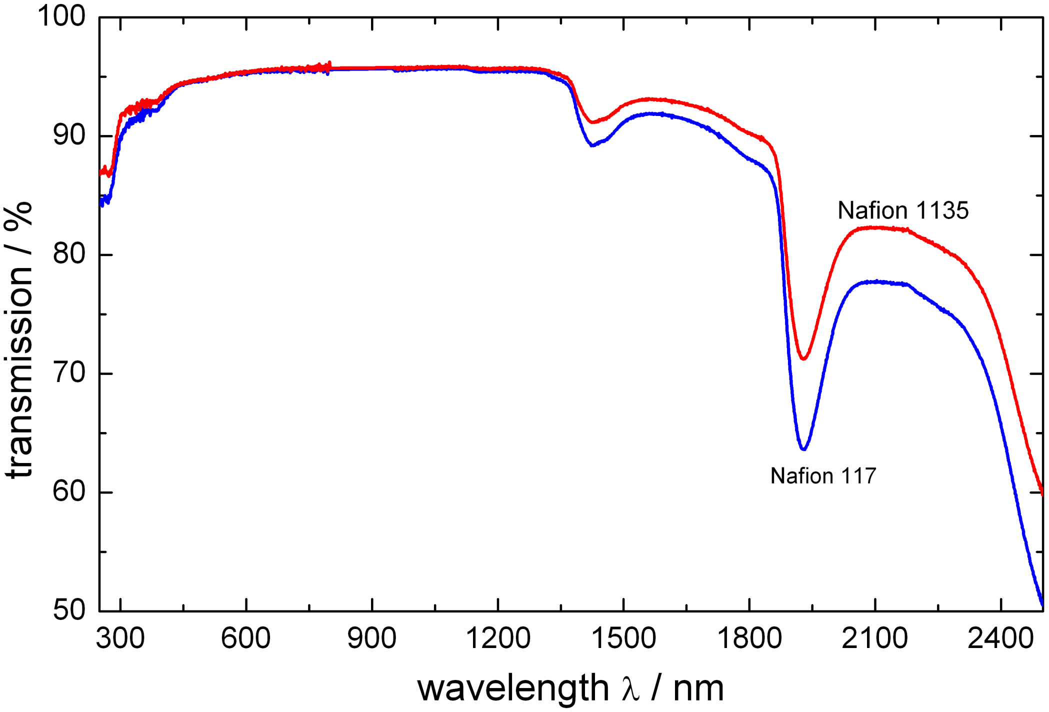

Figure 3.3: Transmittance spectra of Nafion® 1135 and Nafion® 117. At 1064 nm, the wavelength of the laser beam for post–processing, the transmittance is greater than 95 % for both materials.

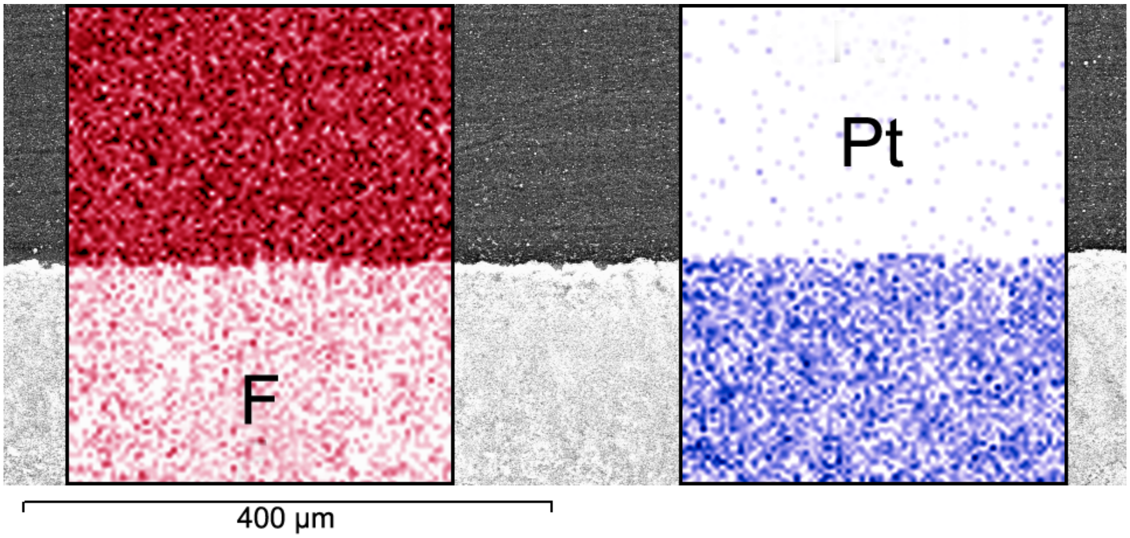

Figure 3.4: Energy dispersive x-ray analysis of the segmented areas, showing the amount of fluorine on the left and platinum on the right according to their element density on the investigated area. The scanning electron microscopy image in the background of the same investigated area shows the ablated area on the upper half and the electrode on the lower half of the image (top view).

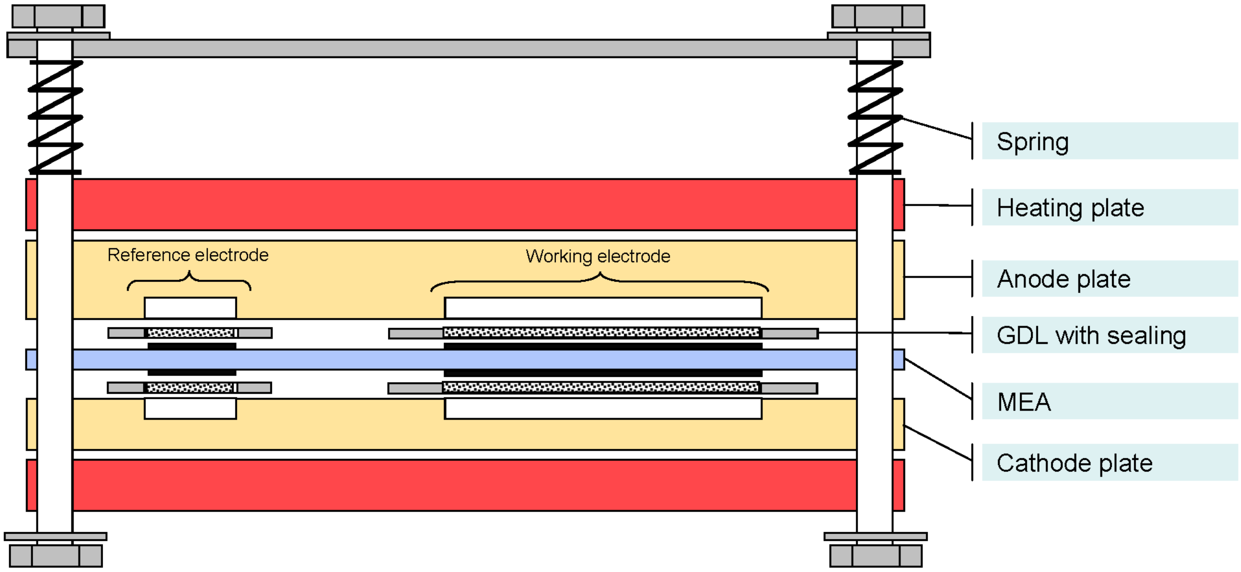

Figure 3.5: Schematic drawing of DMFCs under investigation. The MEA including the GDL and sealing was sandwiched between anode and cathode plates. A reference electrode was located adjacent to the working electrodes. Thick metal heating plates at the anode and cathode were kept at a controlled temperature by an external cryostat. The clamping force was applied with four springs.

Finally energy dispersive x-ray analysis of the interface between the catalyst layer and the ionomer was performed. Fig. 3.4 depicts the results of element mapping of the MEA. In the background, the scanning electron microscopy image of this area can be seen. The foreground shows the element density images for platinum and fluorine. Whenever an element was detected on a specific position, a pixel was printed at the same point in the element picture. Therefore, many pixels represent a high concentration of this particular element at this position. As can be seen, nearly all of the platinum is removed on the ablated area whereas high concentrations can be found, as expected, on the catalyst layer. The interface can also be seen as a clear line. The element picture for fluorine reveals a high concentration on the ionomer and a lower concentration inside the catalyst layer. This indicates that the catalyst layer was treated with a Nafion® suspension, as mentioned earlier in the MEA preparation section.

3.3 Fuel cell assembly

The test cell that is schematically shown in Fig. 3.5 consisted of several components that could be modularly assembled. Cathode plates were constructed from SIGRACET® [2] BMA5, a graphite compound material with both the working electrode flowfield and the isolated reference electrode flowfield milled 0.8 mm deep into the material. Anode plates are described in detail in Chapter

---

[2] http://www.sglcarbon.com/sgl_t/fuelcell/index.html

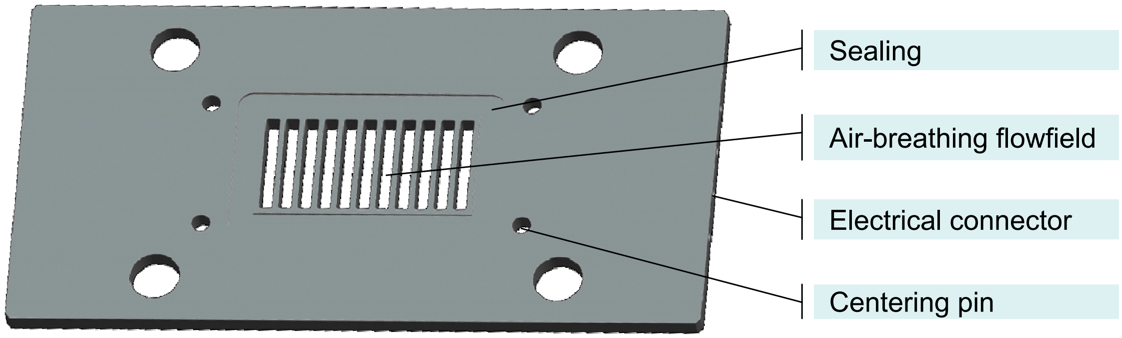

Figure 3.6: Open cathode plate used for the air–breathing operation in both the liquid-fed and the vapor-fed DMFC.

4 and Chapter 5. The cathode plate was identical to the anode plate used for the liquid-phase operation, except when the cathode was operated at air–breathing conditions. In this case open structures in an additional cathode plate allowed surrounding air to diffuse into the cathode as depicted in Fig. 3.6. Connectors allowing direct measurement of the voltage without measuring at the current collectors were attached to the graphite material. A thermo–couple was placed directly at the center of the working electrode on the back of each graphite plate. The working electrode had an area of $10\,\mathrm{cm}^2$. The reference electrode, which was offset $30\,\mathrm{mm}$ to one side of the working electrode, had an area of $1\,\mathrm{cm}^2$ and a $1\,\mathrm{mm}$ serpentine flowfield. The large distance between the working electrode and the reference electrode was chosen to guarantee that no methanol could diffuse in–plane between the working and the reference electrode. If methanol diffuses from the working anode electrode to the reference electrode the reference potential of the NHE could change during operation, leading to additional errors in the measurement.

Different SIGRACET® GDLs that were produced by SGL Technologies GmbH could be used by varying the thickness of the gaskets. Viton sealing rings were used for both the anode and cathode sides. The post–processed MEA was sandwiched between with four centering pins to obtain precise alignment. Two copper plates were used as current collectors on the anode and cathode, followed by two thick end plates made of stainless steel. The steel plates could be temperature–controlled by an external cryostat and were effective in distributing temperature and contact pressure homogeneously over the whole assembly. Four springs were used to adjust the desired pressure on the MEA.

Homogeneous contact pressure is very important to guarantee a symmetric potential distribution inside the membrane, as will be shown in Appendix A. Therefore, several experiments were performed to study the impact of different sealing materials and thicknesses on the pressure inside the cell. A force transducer was placed within a hollow metal block that covered the gaskets of the working electrode. Freely moving plates within the block adjusted the height of the transducer to the height of the metal block and guaranteed a homogeneous pressure distribution between the GDL and transducer. Both anode and cathode GDLs were compressed when a force was applied by compressing the springs.

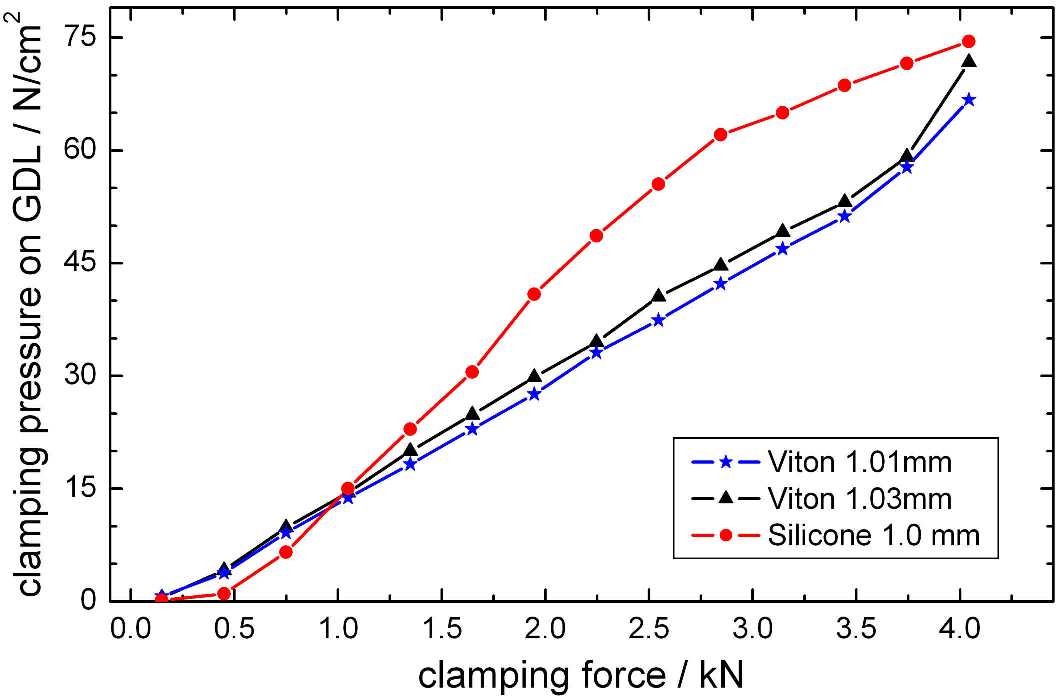

Figure 3.7: Pressure on the GDL at different compressions of the springs. Viton and silicone with different thicknesses were used as sealing materials for the active area.

Results of the force transducer measurement can be seen in Fig. 3.7. Silicone as a sealing material displayed a noticeable nonlinear effect whereas Viton had a linear dependence up to 3.5 kN total clamping force. In addition, slight deviations of the thickness of this material did not considerably affect the pressure on the GDL. Uncertainty about the nonlinear effect of silicone on the pressure distribution determined the choice of Viton as the sealing material.

3.4 Fuel cell operation

The fuel cell was connected to external devices within the test rig for operation. Methanol was supplied using a pulse–free *Cat Microdosing Pump HPLH 200-PF*. The gas flow for the cathode was adjusted by a *MKS Multi Gas Controller 647C*. The reference cell could be operated by two extra mass flow controllers with N_2, H_2, O_2 or air. A *Fisherbrand FBC 735* cryostat controlled the cell temperature, making isothermal measurement possible.

Current was drawn by *Höcherl&Hackl Electronic Load ZS512*, which could be operated in constant current or constant voltage mode and had the capability to force a closed circuit. Currents and voltages were recorded every 100 ms using an *Agilent Data Acquisition System N6700A*. The actual cell resistance was obtained using an *Agilent Milliohmmeter 4338B* which recorded the real part of the impedance at 1 kHz and sent averaged data to the PC every 2 s. It is important to be very careful with this data as the internal resistance of the attached devices can influence the measurement significantly. Therefore, the influence of such parasitic effects (e.g. internal resistance of the power supply) were deducted when necessary. Half–cell experiments were performed using a *Steiber High Precision Power Supply PNG-202*.

The whole measurement sequence was automated and controlled using a computer that also saved the results of the experiment. Stoichiometric control of the cathode flow rate was implemented according to Faraday's law.

$$\dot{m}_{Ca} = \lambda_{Ca} \cdot V_m \cdot \frac{I_{cell}}{y_{O_2} \cdot 4F} \tag{3.1}$$

The cathodic mass flow $\dot{m}_{Ca}$ in units of sccm is dependent on the cathode stoichiometry λ_{Ca}, molar mass V_m, total cell current I_{cell} and molar fraction of oxygen y_{O_2}.

3.4.1 MEA activation

After each new fuel cell had been assembled, a conditioning procedure was applied. The cell was flooded with distilled water overnight. Then humidified H_2 was supplied to the anode and humidified O_2 to the cathode flowfield at $60\,^\circ\mathrm{C}$. Under these conditions the electrodes were activated much faster than if the cell were operated with methanol. A current of $0.05\ \mathrm{A/cm^2}$ was drawn from the cell to humidify the membrane until a reasonable membrane resistance was reached. Cell voltage was cycled four times from $0.9\ \mathrm{V}$ down to $0.05\ \mathrm{V}$ and up to $0.9\ \mathrm{V}$ again in $50\ \mathrm{mV}$ steps, each step lasting $30\ \mathrm{s}$. This procedure was repeated using methanol at the anode and air at the cathode instead of hydrogen and oxygen, starting at $0.6\ \mathrm{V}$. The reference electrodes were activated as well to clean the catalyst surface. Reference electrodes were printed on both sides of the membrane. Thus, the reference cell was operated like a PEMFC, with hydrogen on one side and oxygen on the other. The cell voltage was kept constant at $0.1\ \mathrm{V}$ for $30\ \mathrm{min}$.

3.4.2 Electric measurements

In addition to initial treatment of a new MEA, the fuel cell was preconditioned before each experiment. Therefore, the cell voltage was cycled four times from $0.6\ \mathrm{V}$ down to $0.05\ \mathrm{V}$ and up to $0.6\ \mathrm{V}$ again in $50\ \mathrm{mV}$ steps, each step lasting $10\ \mathrm{s}$. This procedure was repeated if a strong hysteresis was detected between the third and fourth cycle. Polarization measurements started at the OCV. The voltage was decreased in $25\ \mathrm{mV}$-steps to short circuit or voltages slightly above short circuit with each step lasting $20\ \mathrm{s}$. This measurement was repeated in order to study hysteresis effects.

Fig. 3.8 depicts an equivalent circuit of the fuel cell with its losses under load. Polarization losses of anode and cathode occur in addition to pure ohmic losses of the membrane and the flowfield.

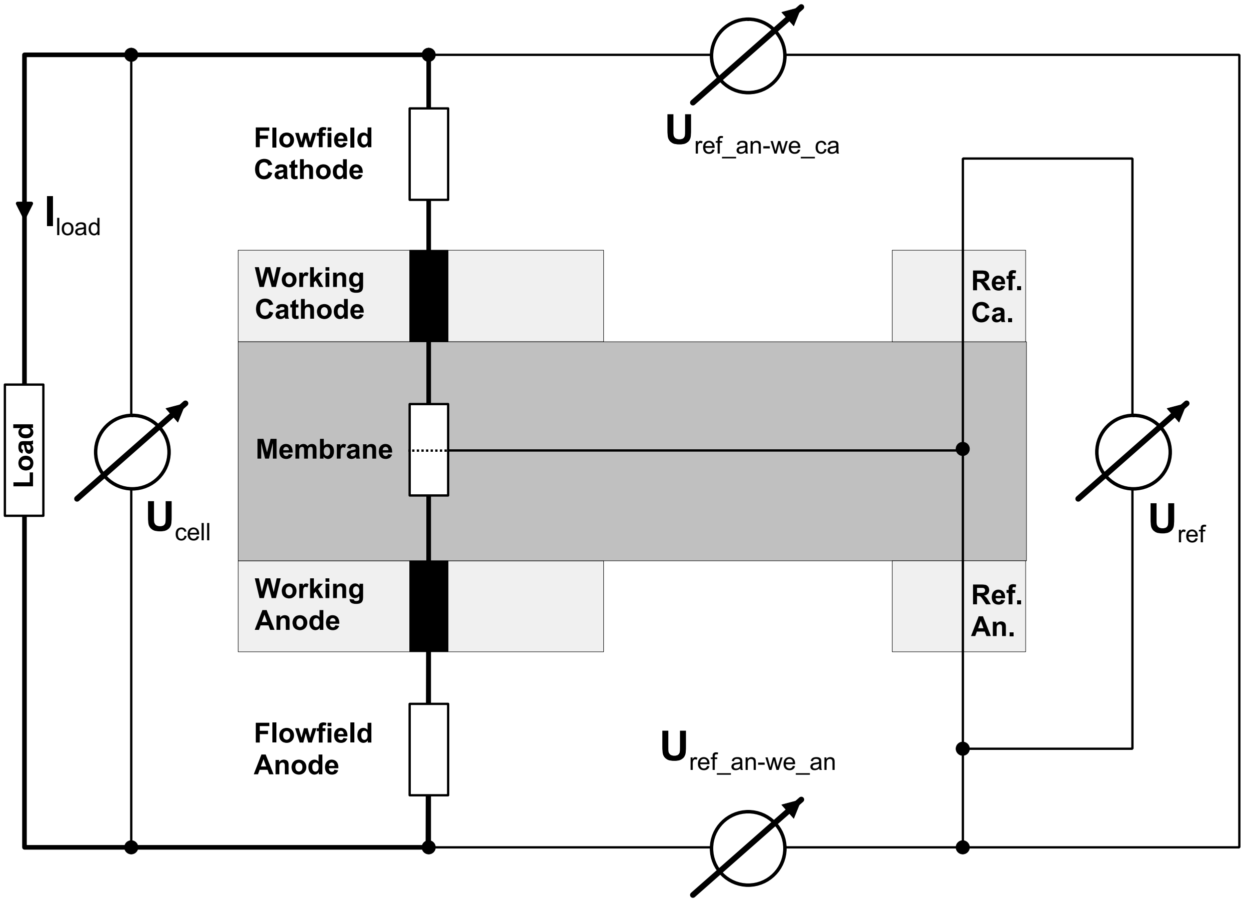

Figure 3.8: Equivalent circuit of a fuel cell including a reference cell. The current path is displayed with bold lines, voltage readings with thin lines. The fuel cell set–up is displayed schematically. Resistances shown in white denote ohmic impedances, resistances in black are complex impedances.

All ohmic losses are summed up in the cell resistance which is measured by the milliohmmeter. Several voltages were recorded during experiments. In addition to the cell potential U_{cell}, the potential of the reference cell U_{ref}, the potential of the reference anode relative to the working electrode anode $U_{ref\_an-we\_an}$ and the potential of the reference anode relative to the working electrode cathode $U_{ref\_an-we\_ca}$ were logged. Polarization plots were extracted by averaging the sampled data of each operating point. Effects of the transient change between operating conditions were eliminated by neglecting the initial ten measurements. The standard deviation of the averaging procedure is displayed as error bars in each measurement.

3.4.3 Crossover measurements

Crossover measurements were performed by sampling the cathode exit gas each second using a mass spectrometer (*MKS Mini-Lab*). Before the experiments started, the mass spectrometer was calibrated with gas mixtures similar to those expected. Compressed air was analyzed in order to get the baseline for differential measurements.

The CO_2 crossover from the anode to the cathode was determined in half–cell operation of the DMFC [71]. During half–cell experiments, the cell was potentiostated with hydrogen supplied to the cathode at a flow rate of $15\,\mathrm{sccm}$. The absence of oxygen prevented methanol on the cathode side from being oxidized. For this case, all of the CO_2 measured in the cathode outlet stream must have crossed the membrane from the anode.

In full–cell operation, air or oxygen is provided to the cathode electrode. In addition to CO_2 crossing over from the anode, CO_2 is formed by the parasitic oxidation of methanol at the cathode. If not all of the methanol is oxidised inside the CCL, methanol should be present inside the cathode flowfield. Thus both the CO_2 and the methanol concentrations were measured inside the cathode outlet stream during functional DMFC operation. An equivalent current density was calculated from the mass flow for better comparison to the cell current.

$$i_{leak} = \frac{N_{MeOH,ca}}{6F} \tag{3.2}$$

Faraday's law is applied to calculate the leakage current density i_{leak}. Electrochemical oxidation of MeOH as shown in Chapter 2 as a 6-electron transfer process is assumed. Vielstich et al. [72] suggested that parallel chemical oxidation of MeOH occurs at high cathode potentials ($> 0.5\,\mathrm{V}$ vs. NHE). Nevertheless for simplicity eq. (3.2) is commonly used in the literature [73,74] and is also applied in this thesis.

Chapter 4

Liquid-Phase Operation

DMFCs are most commonly operated with a liquid fuel at present. Many researchers have studied the influence of operating conditions, crossover and structural parameters on the performance of the cell. So far, only a few have used reference electrodes to gain knowledge about individual electrode processes [59,75,76]. Difficulties in handling and high potential errors are probably one reason for the infrequent use of this powerful method. It is demonstrated in Appendix A that a reliable measurement with a connected NHE can be performed when several aspects are considered and measures to minimize measurement errors are taken. Distinguishing between anode and cathode losses is especially important for passive operation, as many effects are superimposed in the IV characteristic.

Different anode and cathode flowfield geometries, catalysts, catalyst loadings, MEA preparation techniques and structural parameters such as clamping pressure considerably affect the performance as well as activation and concentration losses of a liquid-fed DMFC (LDMFC), so comparison to literature values is difficult. Furthermore, literature data for single electrode losses are limited, as stated above. Thus a thorough parameter study was performed. A DMFC cell configuration as described in Chapter 3 was used for all experiments. The anode plate was machined as illustrated in Fig. 4.1 with its integrated reference electrode.

MeOH crossover from the anode to the cathode across the membrane is still a major issue for LDMFCs. Parasitic MeOH oxidation at the cathode results not only in a mixed potential but also in a high water production rate within the CCL, which causes flooding effects within the pores of the CCL and the GDL. This is especially severe for air–breathing cathodes, as water removal is limited to evaporation into the surrounding air. Furthermore, voltage efficiency and Faradaic efficiency are decreased. The impact of operating conditions and structural parameters on MeOH crossover has to be known to optimize efficiency. Therefore, experiments including crossover measurements analyzing the cathode outlet stream were performed. A crossover model was fitted to experimental results and revealed contributions of diffusion and electroosmotic drag. Additionally, conclusions about temperature, membrane thickness, molarity and anode flow rate were drawn from the model.

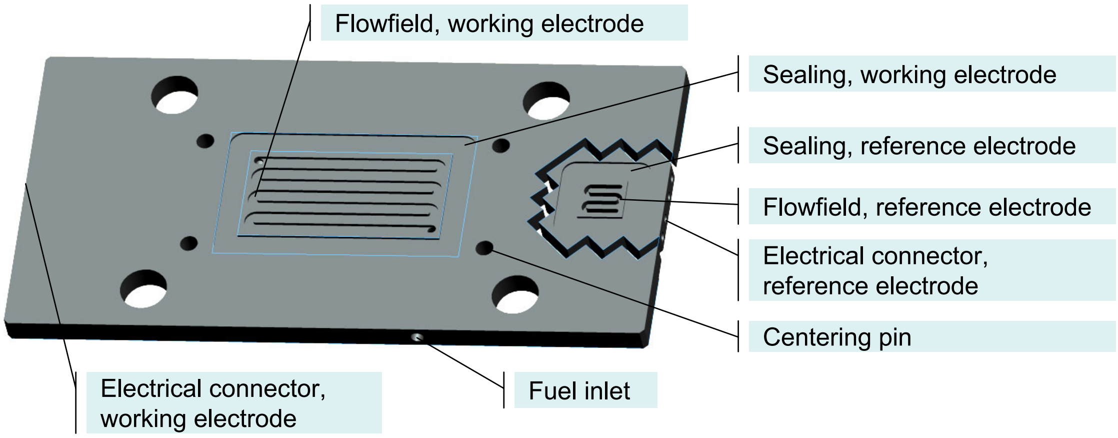

Figure 4.1: Anode with a 1 mm serpentine flowfield that was used throughout LDMFC experiments unless stated otherwise. The reference electrode was electrically insulated and mechanically fixed using synthetic resin.

One of the problems concerning passive operation of a LDMFC is caused by the production of CO_2 during the oxidation of MeOH on the anode side of the fuel cell. This reaction results in two–phase flow of the liquid fuel and the gaseous CO_2. The gas bubbles reduce efficiency since they block parts of the MEA as they become immobile or even block a flow channel completely, a problem that is well known in microfluidics [77]. Another obstacle toward passive operation is the supply of MeOH to the anode compartment. Typically, the MeOH supply is implemented as a continuous flow forced by pumps. Convective flow is also used to flush out dissolved CO_2 before bubbles can block the channels and reactant access to the MEA. However, continuous pumping is not consistent with passive concepts, as it consumes a non–negligible amount of energy. Due to this, it is favorable to reduce the pumping energy or even to completely eliminate pumps from a LDMFC system. This is only possible if the gas bubbles are removed passively from the liquid MeOH. A flowfield layout was developed that removed the gas bubbles by capillary forces only and thus improved system efficiency, since continuous convective flow was not required for operation.

4.1 Parameter study

The impact of operating conditions and structural parameters on performance as well as activation and concentration losses of a LDMFC was studied and compared to literature data. The connected NHE was used to assess polarization losses of anode and cathode individually. A $0.5\,\mathrm{M}$ solution of MeOH dissolved in deionized water was used and pumped into the anode flow channel at a flow rate of $1.5\,\mathrm{ml/min}$. Dry air was supplied to the cathode flow channel. A minimum air flow rate of $30\,\mathrm{sccm}$ was set before switching to a stoichiometry of 6 at a current density of $0.03\,\mathrm{A/cm^2}$. Hydrogen, which was humidified inside a washing bottle at ambient conditions, was fed to one electrode of the reference electrode. The other electrode was flooded with deionized water to

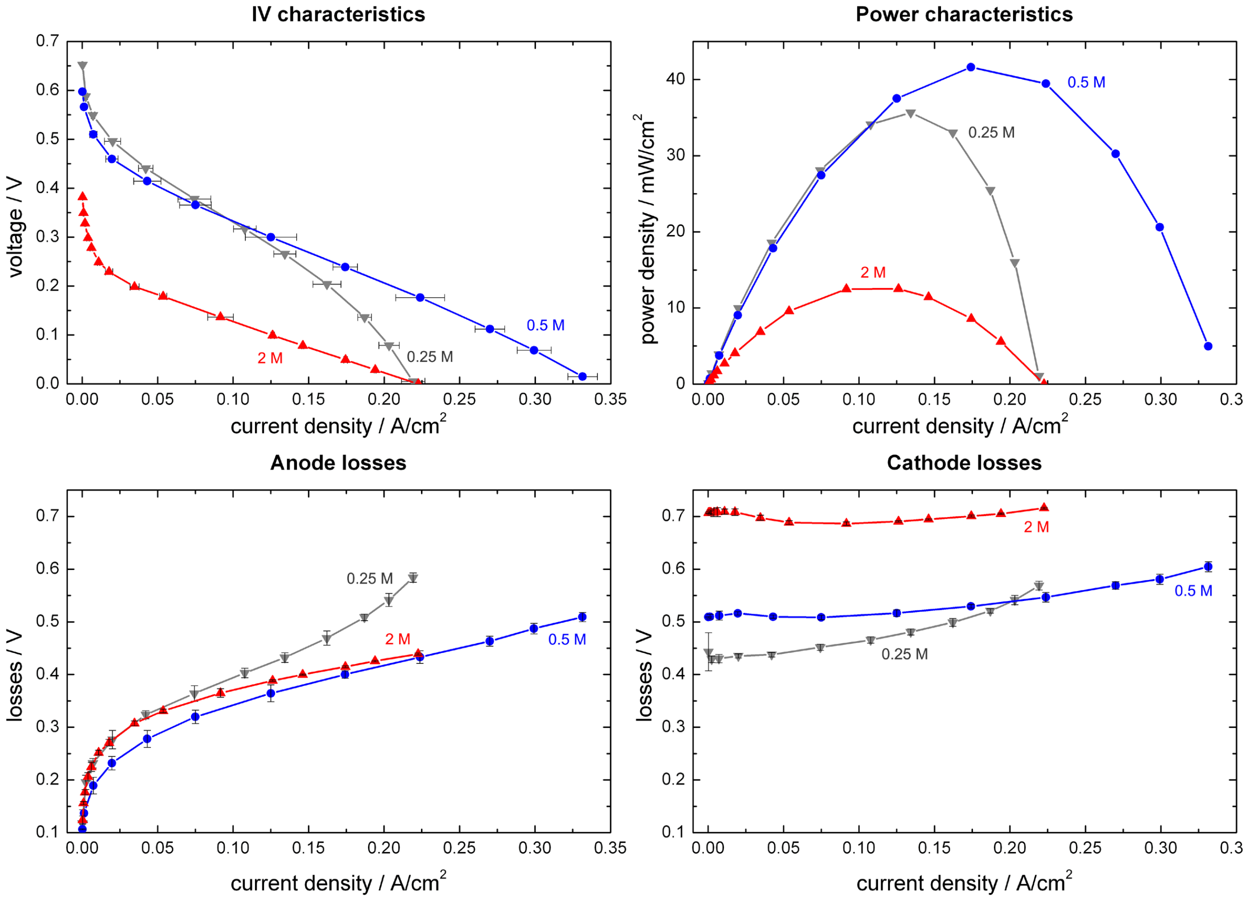

Figure 4.2: Electric properties of a LDMFC at different MeOH molarities. Anode and cathode polarization losses were calculated using a connected reference NHE. The temperature was 50 °C, the cathode air stream 30 sccm/λ 6 and the anode flow rate 1.5 ml/min.

guarantee a stable reference potential as mentioned in Appendix A. The temperature of the cell was kept constant at $50\,^\circ\mathrm{C}$. SIGRACET® GDL 35AA was used on both the anode and cathode sides. For the CCM, Nafion® 1135 was used with $3\,\mathrm{mg/cm^2}$ Pt/Ru at the anode and $1\,\mathrm{mg/cm^2}$ Pt at the cathode ("screen–printing"). A total clamping force of $2850\,\mathrm{N}$ was applied, which creates a pressure of $285\,\mathrm{kPa}$ on the GDL. These standard conditions were applied unless stated otherwise in the text.

4.1.1 Methanol concentration

The MeOH molarity was varied between $0.25\,\mathrm{M}$ and $2\,\mathrm{M}$ to investigate concentration effects on the LDMFC. Results are depicted in Fig. 4.2. The $0.5\,\mathrm{M}$ solution of MeOH displayed the best performance for the given operating conditions. Improved performance with molarity and a decrease from a certain concentration on is reported in the literature, with values depending on structural parameters and operating conditions [76,78,79].

At $0.25\,\mathrm{M}$, a lack of MeOH inside the ACL could be assumed as the anode losses rose significantly at high current densities. A high MeOH concentration of $2\,\mathrm{M}$, which did not display any mass transport problem at the anode, turned out to have only one quarter of the peak power density compared to $0.5\,\mathrm{M}$. High cathode losses of $700\,\mathrm{mV}$ caused a shift of the IV characteristics of about $250\,\mathrm{mV}$ toward zero. Crossover of MeOH across the membrane caused a mixed potential at the cathode as MeOH oxidizes parasitically at the CCL. Catalyst sites were blocked by strong CO bonds that occurred during the MOR (eq. (2.3)) and flooding effects due to excess water reduced the active area. The exponential rise of the electrochemical reaction following Butler–Volmer characteristics, that is apparent for the anode losses, cannot be found for the cathode losses due to internal currents. This was reported by Ren et al. [59] and Paganin et al. [80] as well using an internal DHE to assess losses separately. Increased losses at the cathode at higher MeOH concentrations were also found by Oedegaard [68] during half–cell experiments. Cathode losses increased slightly with current density, which probably can be attributed to a superposition of increased losses of the ORR and a decrease in MeOH crossover. A systematic analysis of phenomena related to crossover is presented in the **Methanol crossover** section of this chapter.

4.1.2 Cathode stoichiometry

Cathode flow rates can influence the performance of a LDMFC. Ge et al. [79] has stated that air flow plays a critical role in preventing flooding effects by removing liquid water from the GDL and from the cathode flow channels. Improved performance at high cathode air flow rates has been reported by Cowart [81] and Nakagawa et al. [27]. Nakagawa found that by replacing air with oxygen, performance did not change for different flow rates, which was probably due to the high initial flow rate of oxygen he used in his experiments. He has also mentioned unstable operation at low cathode flow rates. As these experiments were performed without a reference electrode or half–cell operation, no conclusion about individual losses were drawn.

Fig. 4.3 describes results of an experiment at different air stoichiometries. A large error bar reflects the unstable behavior of the cell, which is especially apparent for a low stoichiometry of 2. At a current density of $0.09\,\mathrm{A/cm^2}$, the voltage drops significantly compared to the other experiments. At this point, the cathode flow was switched from a constant flow rate of $30\,\mathrm{sccm}$ to a stoichiometrically controlled flow of 2. A significant increase of the cathode losses appeared while anode losses remained relatively stable. Partial flooding of the cathode caused this steep rise in losses, as access of oxygen to the catalyst sites was severely hindered. This is also indicated by the unstable operation reflected by high standard deviations. For stoichiometries of 4 and 6, the cathode losses decreased with increasing stoichiometry, in particular at high current densities. The partial pressure of oxygen inside the CCL increases and partial flooding is minimized. The MeOH concentration at the cathode decreases at higher partial pressures of oxygen as more MeOH is oxidized. From a particular air flow rate on, the MeOH concentration inside the CCL equals zero and cathode losses do not improve further. This phenomenon is described in detail in the following section about **Methanol crossover** of this chapter.

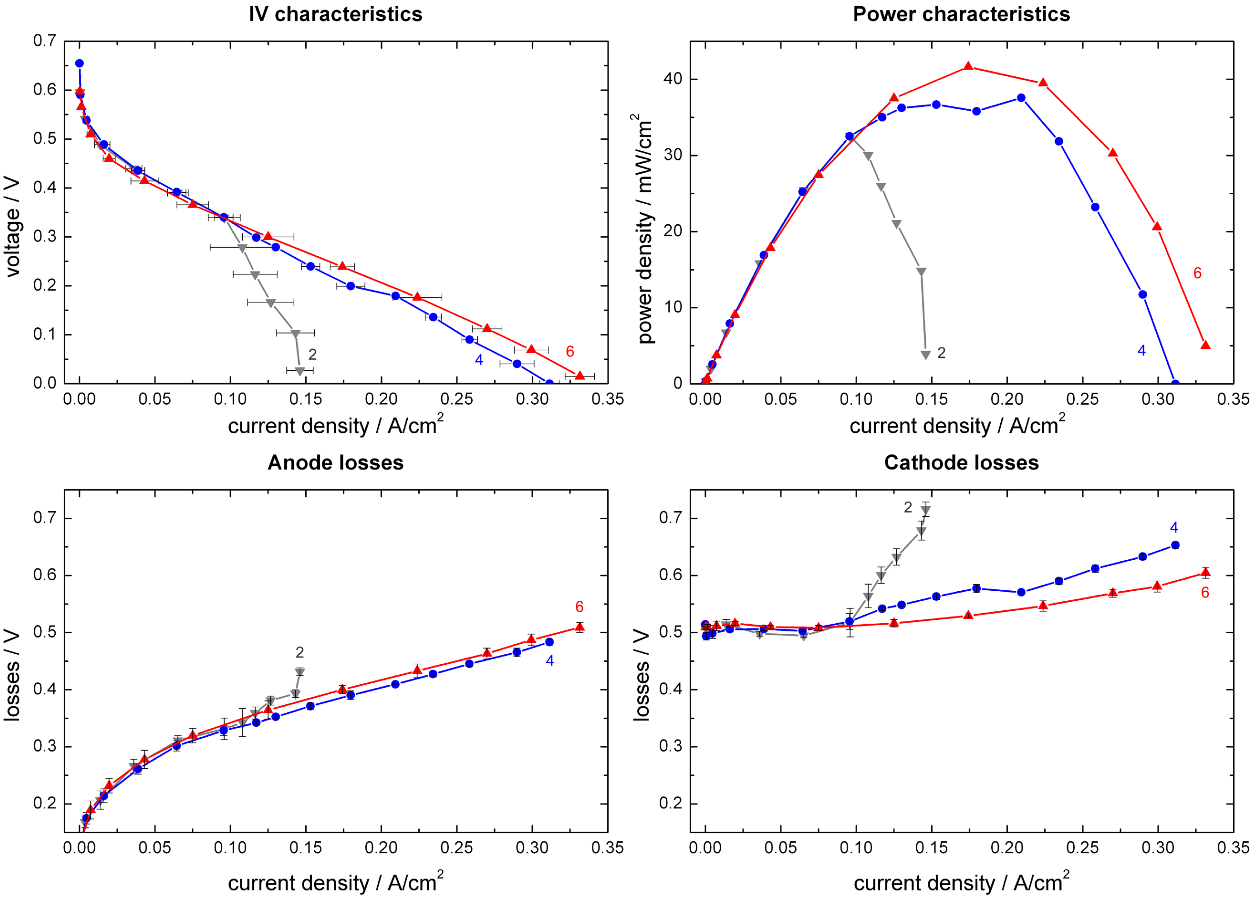

Figure 4.3: Electric properties of a LDMFC at different cathode stoichiometries. Anode and cathode polarization losses were calculated using a connected reference NHE. The temperature was 50 °C, minimum cathode air stream was 30 sccm. A 0.5 M MeOH solutions was fed to the anode at a flow rate of 1.5 ml/min.

4.1.3 Anode flow rate

Different phenomena of a LDMFC are affected by anode flow rate. On the one hand, anode flow is one parameter that affects mass transport of MeOH to the ACL. High concentration losses have been reported when the flow rate was too low [63,78,79,81]. On the other hand, CO_2 is formed in the vicinity of the ACL as a product of the MOR. At higher flow rates, more gaseous CO_2 can be dissolved in the liquid and blocking of pores in the catalyst or within the GDL can be minimized. Furthermore, the anode flow rate should be higher than the CO_2 generation rate to prevent clogging by gaseous CO_2 in the anode flow channels. Cowart stated [81] that this can be caused by the volumetric dominance of CO_2 relative to the base liquid methanol–water reactant. Finally, higher MeOH concentrations within the ACL at higher anode flow rates will increase crossover of MeOH across the membrane and lower the overall performance.

Results for different anode flow rates of 0.225, 1.5 and $5\,\mathrm{ml/min}$ are presented in Fig. 4.4. High concentration losses for the lowest flow rate are apparent, starting at a current density of $0.06\,\mathrm{A/cm^2}$.

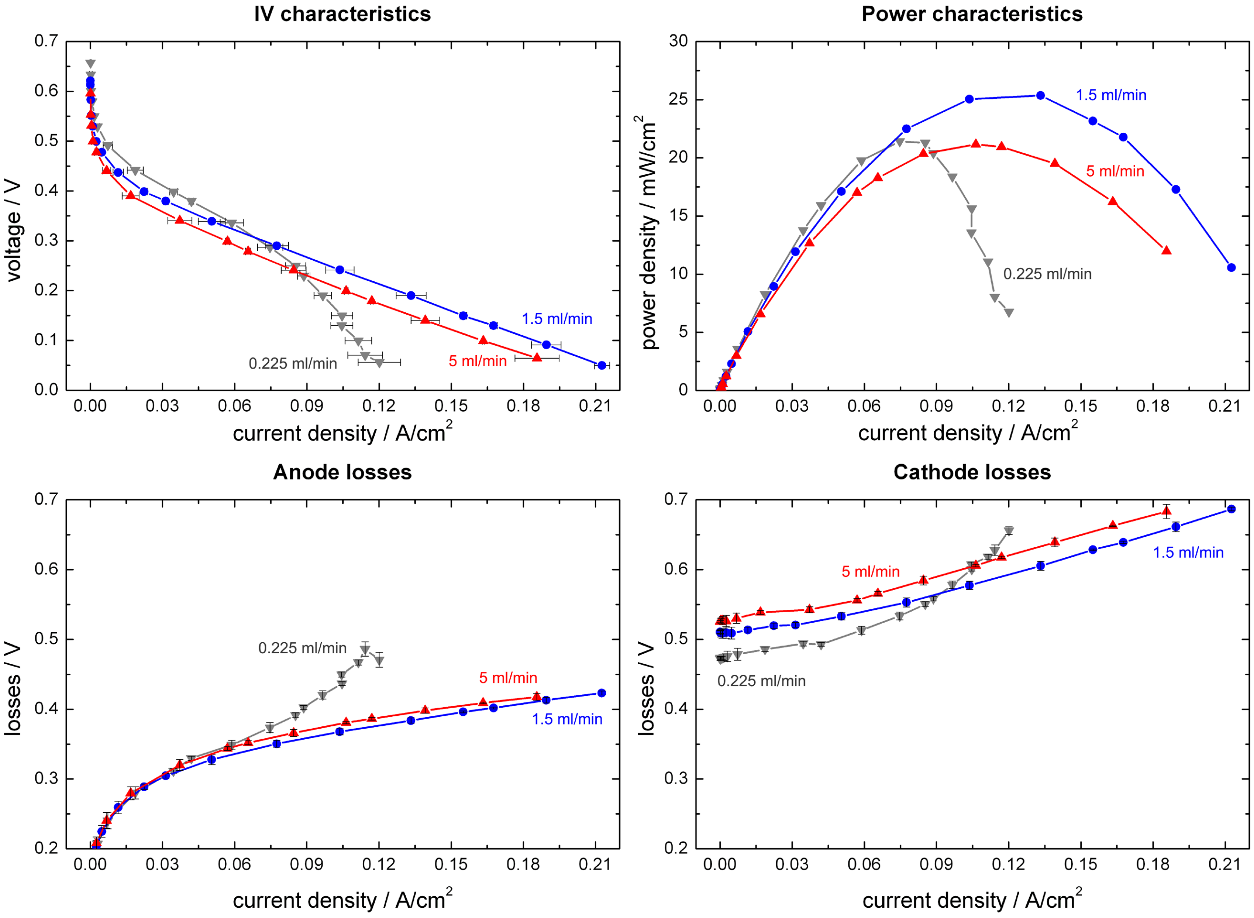

Figure 4.4: Electric properties of a LDMFC at different anode flow rates. Anode and cathode polarization losses were calculated using a connected reference NHE. The temperature was 50 °C, the cathode air stream 30 sccm/λ 6. A 0.5 M MeOH solutions was fed to the anode.

This cannot be found for the other two flow rates, where anode losses increased much slower with current density. Cathode losses close to OCV increased with flow rate. As mentioned before, high MeOH concentrations inside the ACL lead to enhanced crossover, which is reflected by the cathode losses. An anode flow rate of $1.5\,\mathrm{ml/min}$ resulted in the best performance of $25\,\mathrm{mW/cm^2}$, which was a result of low crossover at a flow rate where no mass transport problems occurred. Similar results have been reported by Gurau et al. [63] using consecutive half–cell and full–cell experiments. Structural parameters as well as operating conditions will influence phenomena which depend on the the flow rate. Thus the anode flow rate has to be optimized for different types of DMFCs.

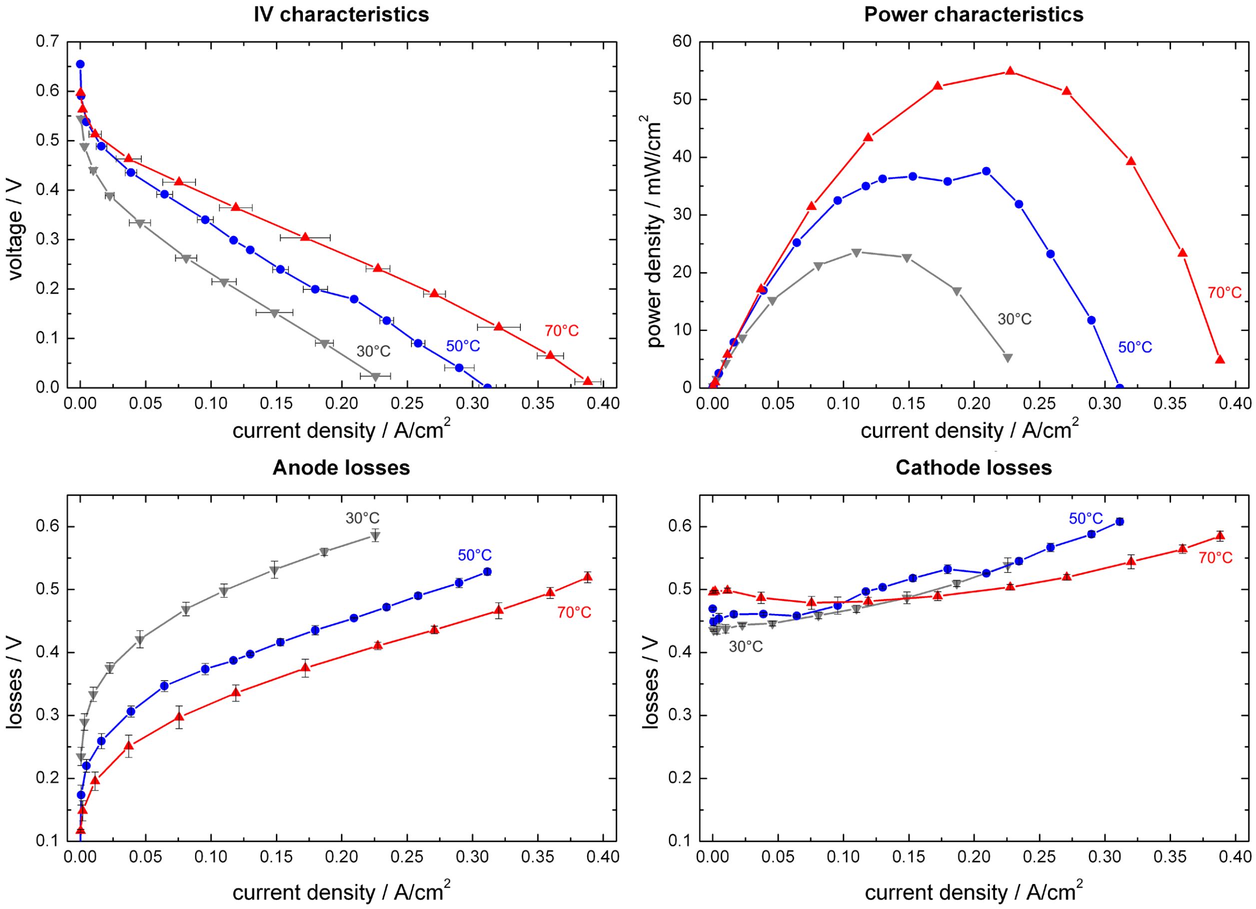

Figure 4.5: Electric properties of a LDMFC at different cell temperatures. Anode and cathode polarization losses were calculated using a connected reference NHE. The cathode air stream was 30 sccm/λ 6. A 0.5 M MeOH solutions was fed to the anode at a flow rate of 1.5 ml/min.

4.1.4 Temperature

The influence of temperature on a LDMFC has been studied by many researchers, often in the integrated form of IV plots [27,30,34,64,78] or consecutive half–cell and full–cell experiments [63, 68]. A connected DHE to distinguish between anode and cathode losses at different temperatures has been used as well [59,75,76]. The kinetics of the MOR, which is considered to be a slow reaction with a strongly adsorbed intermediate, increase significantly with temperature. Some researchers [27, 68] have stated that performance of the fuel cell increased up to a certain temperature and leveled or decreased as the temperature rose further. Nakagawa et al. [27] has concluded that performance reached its maximum just before boiling point. Gurau et al. [63] has shown that the anode losses display Arrhenius behavior while total losses do not. Cathode losses are influenced by crossover of MeOH across the membrane. The water uptake of the membrane is higher at high temperatures [82]. Elevated temperatures increase both the electroosmotic drag and diffusion of MeOH and water, which leads to enhanced flooding and a mixed potential at the cathode. In conclusion the overall performance of a LDMFC depends on a superposition of anode, cathode and membrane losses and changes for different types and operating conditions.

The results for temperatures between ambient conditions of 30 °C and 70 °C are depicted in Fig. 4.5. Improvement of performance is obvious, with the power densities at the maximum power point (MPP) nearly tripling between 30 °C and 70 °C. This was caused by a significant decrease in anode losses in accordance with the theory stated above. The impact of crossover can be noted in the cathode losses. At OCV, cathode overvoltages were higher for elevated temperatures, indicating increased crossover. This finding will be verified in the **Methanol crossover** section later. The impact of crossover diminishes at higher current densities, when more MeOH is consumed during MOR and the MeOH concentration inside the ACL decreases.

4.1.5 Air–breathing cathode

With the need to reduce complexity, size and weight of a fuel cell system, especially for portable applications, a concept of "air–breathing" cathodes has been introduced for hydrogen–fed PEMFCs [3, 83–85]. Instead of a forced flow of oxygen or air inside the cathodic flow channels an open design that allowed diffusive supply of oxygen to the CCL from surrounding air has been implemented at the cathode. Later, this concept was transferred to DMFCs [30, 31, 37, 40, 86–89]. While PEMFCs that have been supplied with dry hydrogen suffer simultaneously from drying effects and flooding effects of the membrane [3, 84], flooding is much more pronounced for a LDMFC, as water accumulates at the cathode [30, 40, 87]. In addition to a higher uptake of water in Nafion® within the liquid phase [90] and thus increased water transport across the membrane, crossover MeOH that is oxidized at the cathode produces additional water at the CCL. Water production at the cathode increases with MeOH molarity due to elevated crossover [59].

A comparison between forced flow through a closed cathode and diffusive supply of oxygen at an air–breathing cathode is depicted in Fig. 4.6. Instead of Nafion® 1135 the thicker Nafion® 117 was used to minimize MeOH crossover. As expected, the cathode losses of the air–breathing cell start higher and rise much faster with increasing current density. More molecules of water are produced at high current densities and accumulation of water leads to the predicted flooding of the cathode.

4.2 Methanol crossover

Major efforts have been made to investigate and understand MeOH crossover from the anode to the cathode in DMFCs. Measurements of CO_2 in the cathode outlet stream have been made by mass spectroscopy, infrared spectroscopy or gas chromatography. However, the majority of this work has been done at elevated temperatures and/or pressures. In a first approach Fuller et al. [91] and Zawodzinski et al. [92] studied the water uptake and transport through Nafion® 117. MeOH crossover has been studied by Wang et al. [93] and Cruickshank et al. [94]. They

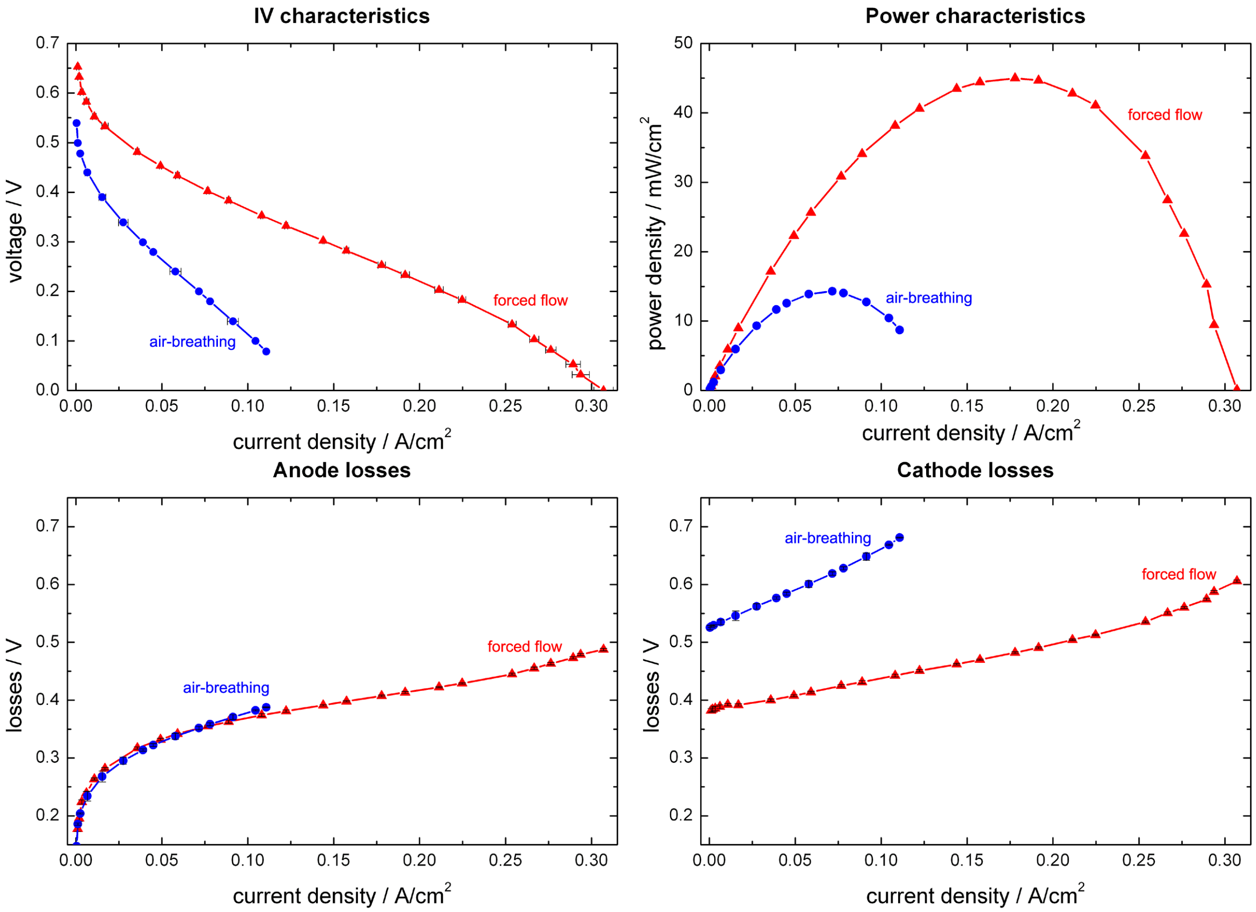

Figure 4.6: Electric properties of a LDMFC with Nafion® 117 using an air–breathing cathode and forced flow through a closed cathode. Anode and cathode polarization losses were calculated using a connected reference NHE. The temperature was 50 °C, the cathode air stream 30 sccm/λ 6. A 0.5 M MeOH solutions was fed to the anode at a flow rate of 1.5 ml/min.

assumed complete conversion of cathodic MeOH to CO_2 and neglected CO_2 crossover from the anode to the cathode. Heinzel et al. [95] summarized the research on crossover in DMFCs in 1999. Dohle et al. [73] found that MeOH was not completely oxidized at the cathode and used a catalytic burner before measuring. He also found CO_2 crossover from the anode to the cathode to be non–negligible. Meier et al. [71] has compared MeOH crossover and electrode polarization, Gogel et al. [96] has compared MeOH crossover and cell voltages at temperatures greater than $60\,^{\circ}C$. Recently some research has been done at near–ambient conditions [68,76].

In this section MeOH crossover is investigated at ambient and near–ambient conditions, which is favorable for passive operation. By applying an experimental design approach, the number of experiments could be reduced from 256 to 64. These experiments included crossover measurements and were performed with changing parameters. The independent variables which were

Parameter	Value	Unit
MeOH concentration	$0.5\,/\,1.5$	M
Temperature	$30\,/\,50$	$^\circ\mathrm{C}$
Cathode stoichiometry	$3\,/\,6$	
MeOH flow rate	$1\,/\,3$	$\mathrm{ml\,min^{-1}}$
Clamping force	$2\,/\,3.5$	kN
Anode catalyst loading	$1.5\,/\,2.5$	$\mathrm{mg\,cm^{-2}}$
Cathode catalyst loading	$1.5\,/\,2.5$	$\mathrm{mg\,cm^{-2}}$
Membrane thickness	$90\,/\,180$	$\mu\mathrm{m}$

Table 4.1: Parameters and their two values that were varied during the series of crossover experiments.

varied through the series of experiments are specified in Table 4.1. A one–dimensional model was utilized and enhanced to assess contributions of diffusion and electroosmotic drag.

4.2.1 Crossover experiments

Fig. 4.7 depicts one result of a cell operating at $30\,^\circ\mathrm{C}$ and a $1.5\,\mathrm{M}$ solution of MeOH at a high air stoichiometry of 6. SIGRACET® GDL 35AA was used on both the anode and cathode sides. A total clamping force of $2850\,\mathrm{N}$ was applied, which creates a pressure of $285\,\mathrm{kPa}$ on the GDL. Nafion® 1135 was used with a catalyst loading of $2.5\,\mathrm{mg/cm^2}$ on both electrodes (prepared by the decal transfer method). The equivalent current density of the $\mathrm{CO_2}$ crossover from the anode to the cathode $i_{CO2,crossover}$ was determined in half–cell experiments as described in the measurement section. In addition to $\mathrm{CO_2}$, unreacted MeOH $i_{MeOH,unreacted}$ was found in the cathode outlet stream. The right axis refers to $i_{CO2,crossover}$ and $i_{MeOH,unreacted}$ while $(i_{leak} + i_{CO2,crossover})$, the total amount of $\mathrm{CO_2}$ measured in the cathode outlet stream, is plotted using the scale of the left axis. The MeOH oxidation current that originates at the cathode during full–cell operation can be calculated by subtracting $i_{CO2,crossover}$ from the total $\mathrm{CO_2}$ measurement.

$$i_{leak} = (i_{leak} + i_{CO2,crossover}) - i_{CO2,crossover} \tag{4.1}$$

It is shown in Fig. 4.7 that the MeOH on the cathode side is not completely oxidized, as MeOH is detected in small amounts in the mass spectrometer. The amount of MeOH exiting the cathode flux increases with increasing current. The $\mathrm{CO_2}$ crossover measured during half–cell experiments and depicted as $i_{CO2,crossover}$ stabilizes at a certain value and does not change significantly further on. It slightly changes the value of the leakage current density i_{leak} for a given cell current density. A relative error of $4\,\%$ at a current density of $0.2\,\mathrm{A/cm^2}$, caused by neglecting $\mathrm{CO_2}$ crossover was calculated. In other experiments, relative errors up to $20\,\%$ were found.

Fig. 4.8 illustrates another result with different operating conditions. The cell was operated at $50\,^\circ\mathrm{C}$ with a $0.5\,\mathrm{M}$ solution of MeOH concentration and at a low air stoichiometry of 2. Again Naf-

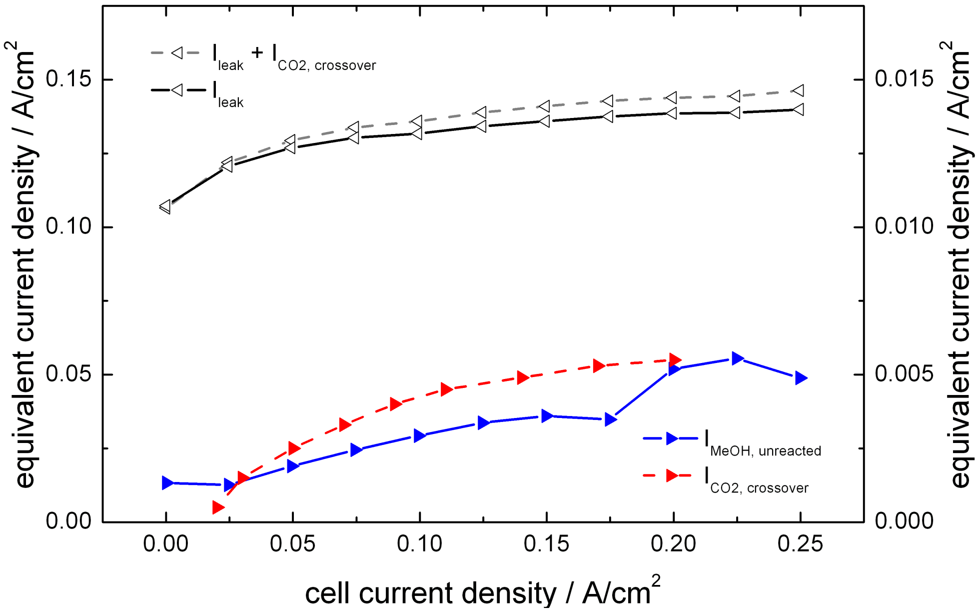

Figure 4.7: Mass spectrometric measurements of the cathode outlet stream at a cell temperature of 30 °C, a 1.5 M MeOH solution, air stoichiometry 6, Nafion® 1135 and a catalyst loading of 2.5 mg/cm^2 on both electrodes. The crossover of CO$_2$ from the anode to the cathode determined in half–cell experiments is labeled as $i_{CO2,crossover}$, unreacted MeOH in full–cell operation as $i_{MeOH,unreacted}$.

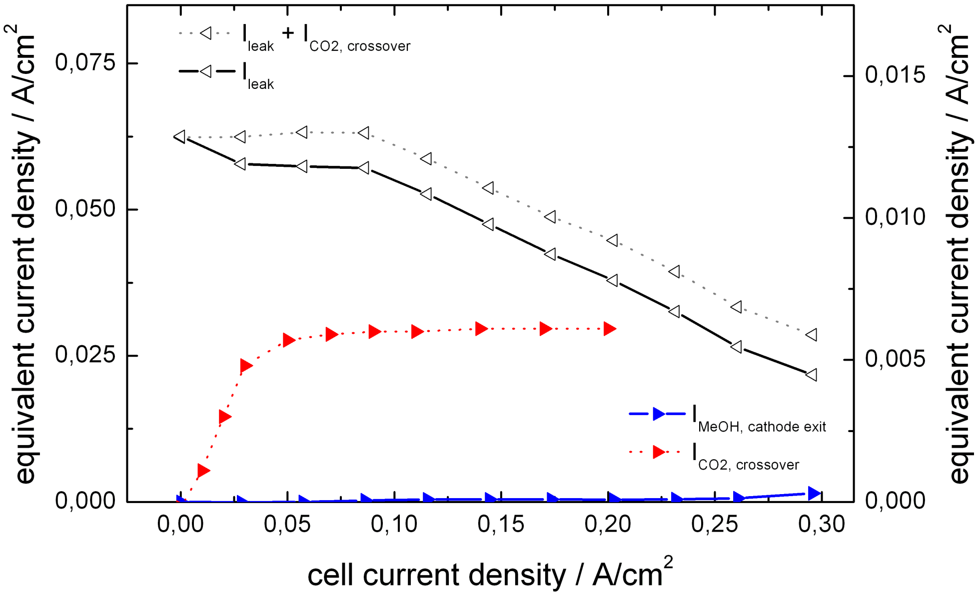

Figure 4.8: Mass spectrometric measurements of the cathode outlet stream at a cell temperature of 50 °C, a 0.5 M MeOH solution, air stoichiometry 2, Nafion® 1135 and a catalyst loading of 2.5 mg/cm^2 on both electrodes. The crossover of CO$_2$ from the anode to the cathode determined in half–cell experiments is labeled as $i_{CO2,crossover}$, unreacted MeOH for full–cell operation as $i_{MeOH,unreacted}$.

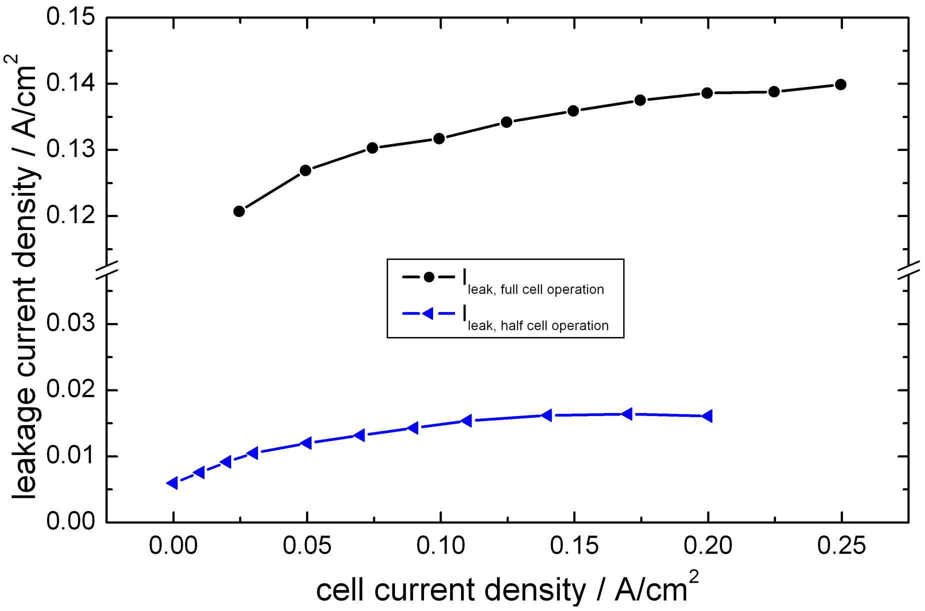

Figure 4.9: Comparison of the equivalent MeOH crossover current density in half–cell and full–cell experiments. The cell had a temperature of 30 °C, a 1.5 M MeOH solution, air stoichiometry of 6 for full–cell operation or a H_2 flow rate of 15 sccm for half–cell operation. Nafion® 1135 and a catalyst loading of 2.5 mg/cm^2 on both electrodes was used.

ion® 1135 was used with a catalyst loading of $2.5\,\mathrm{mg/cm^2}$ on both electrodes. No MeOH could be detected in the cathode outlet stream for this measurement. The CO_2 crossover stabilizes at about $6\,\mathrm{mA/cm^2}$. The relative error due to this can be calculated to be $18.5\,\%$ at $0.2\,\mathrm{A/cm^2}$. Thus, the impact of CO_2 crossover from the anode to the cathode should not be neglected in the evaluation of the measurement data [73,97].

A comparison between MeOH crossover in a full–cell experiment and a half–cell experiment is depicted in Fig. 4.9. The same operating conditions as in Fig. 4.7 were applied. It can be seen that the crossover current density in the cathode outlet for the half–cell experiment is one order of magnitude lower than for the full–cell experiment. Nevertheless, the slope of the two curves shows similar behavior. The crossover current density for the half–cell experiment starts close to zero and it can be concluded that the diffusive term of the crossover nearly vanishes. Therefore the gradient of the MeOH concentration between anode and cathode has to decrease. One phenomenon that could cause this is the formation of diluted MeOH, creating a liquid film on the pore walls of the CCL [98]. If a liquid film containing MeOH is formed on the cathode, the concentration gradient between ACL and CCL will decrease for all currents, thus reducing diffusion. The concentrations can equilibrate as the reductive hydrogen atmosphere at the cathode prevents MeOH from being oxidised and thus from being consumed. Evaporation of MeOH was low in this experiment because of a temperature of $30\,^\circ\mathrm{C}$ and a low cathode flow rate of $15\,\mathrm{sccm}$.

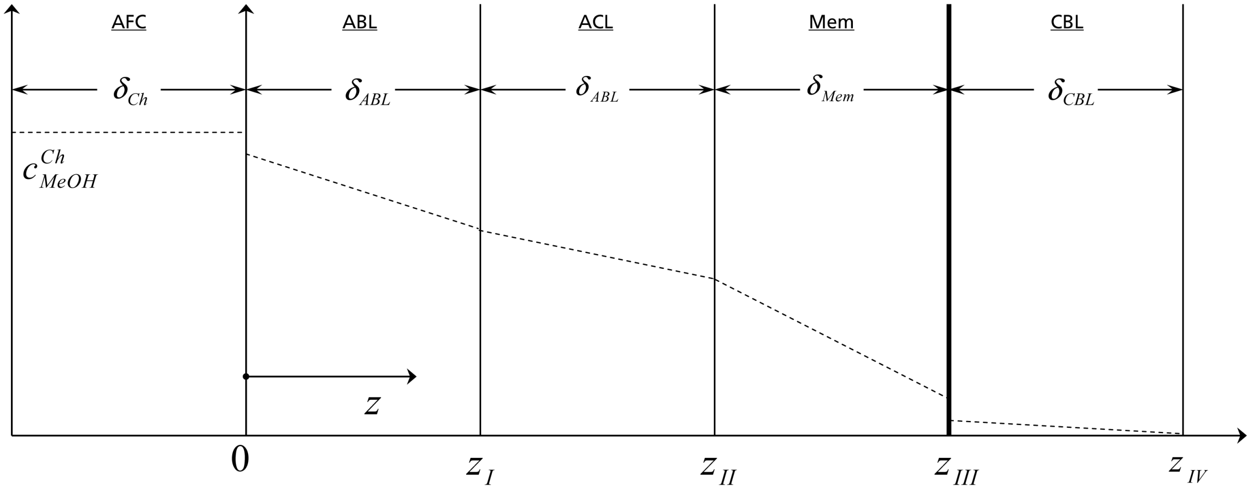

Figure 4.10: Model domains that were used in the model. The CCL was modeled as an interface at z_{III}. An example for the relative MeOH concentration in the different model domains is shown.

4.2.2 Crossover Model

The mathematical model developed by Garcia et al. [99,100] is extended to include oxygen diffusion through the cathode backing layer (CBL) to enable the experimental data to be fitted data with the model. Also, the assumption that all the MeOH that crosses to the cathode is completely oxidized at the CCL is relaxed such that some MeOH may pass through the cathode unoxidized. The CCL is modeled as an interface between the membrane and the CBL. Fig. 4.10 shows a schematic drawing of the different model domains.

The model includes a mass transfer resistance between the anode flow channel (AFC) and the anode backing layer (ABL) as described in [100]. It is an isothermal, steady–state model with variations only in one coordinate. Convective transport of MeOH is neglected and CO_2 is assumed to be dissolved in solution. The anode kinetic expression is taken from [101] assuming a homogeneous reaction in the ACL.

Methanol transport in the cathode

As shown before, a small concentration of MeOH was measured in the cathode outlet stream, even under open circuit conditions during some experiments. This led to the conclusion that MeOH is not completely oxidized in the CCL but a small fraction leaves the CCL unreacted. In this work, it is therefore assumed that there can be transport of MeOH through the cathode, resulting in a MeOH concentration greater than zero within the CCL. This transport is described by a mass transfer coefficient in the CBL.

$$N_{MeOH,zIV} = k_{MeOH,CBL} \cdot c_{zIII} \tag{4.2}$$

Consequently the flux of MeOH through the membrane in [99] is rewritten with the term c_{zIII} for the MeOH concentration in the CCL.

$$N_{MeOH,zIII} = \frac{(c_{zII} - c_{zIII}) D_{MeOH,mem}}{\delta_{mem}} + \frac{c_{MeOH,zII}}{c_{H2O,zII}} \cdot \xi \cdot \frac{i_{cell}}{F} \tag{4.3}$$

The flux of MeOH at position z_{III} is described by $N_{MeOH,zIII}$. $D_{MeOH,mem}$ denotes the MeOH diffusion coefficient in the membrane, δ_{mem} the thickness of the membrane and i_{cell} the cell current density, and ξ the electroosmotic drag coefficient. In addition to the diffusion term the electroosmotic drag with its coefficient ξ and the actual cell current i_{cell} is taken into account as well. The pressure on both sides of the fuel cell throughout experiments equaled atmospheric pressure. Thus this equation neglects the transport of MeOH across the membrane due to convection.

The leakage current density can be calculated according to Faraday's law via eq. (4.3).

$$i_{leak} = 6F \left(N_{MeOH,zIII} - N_{MeOH,zIV} \right) \tag{4.4}$$

Oxygen transport in the cathode

Oxygen flux through the CBL to the CCL is modeled as a diffusion process through the CBL. The mass balance in the CBL is described as

$$\frac{dN_{Ox,CBL}}{d(z_{IV} - z)} = 0 \tag{4.5}$$

The flux of oxygen through the membrane is assumed to be negligible. Oxygen is consumed inside the CCL according to the cell current density and the crossover current density.

$$N_{Ox,zIII} = \frac{i_{cell} + i_{leak}}{4F} \tag{4.6}$$

Solving eq. (4.5) for the CBL, one obtains

$$N_{Ox,zIII} = \frac{\left(c_{Ox,zIII} - c_{Ox,zIV} \right) D_{Ox,CBL}}{\delta_{CBL}} \tag{4.7}$$

Here $c_{Ox,zIV}$ is the concentration of oxygen in the cathode flow channel. Using eq. (4.6) and eq. (4.7) the concentration of oxygen inside the CCL can be determined. Knowing the oxygen concentration at the CCL a concentration term can be added to the Tafel equation for the oxygen reduction reaction (ORR).

$$i_{cell} + i_{leak} = i_{Ox,0} \cdot \frac{c_{Ox,zIII}}{c_{Ox,zIV}} exp\left(-\frac{\alpha_{Ca} F \eta_{Ca}}{RT}\right) \tag{4.8}$$

Losses occurring due to parasitic oxidation at the cathode are accounted for by i_{leak} from eq. (4.4).

4.2.3 Model validation

The assumption that all MeOH is oxidized at the Mem-CCL interface is often applied in DMFC modeling [94, 102–105]. Even models that include a term for a MeOH transport concentration within the CCL in the cathode [106, 107] assume the MeOH to be rapidly oxidized under given operating conditions and thus set the MeOH concentration at z_{III} to zero.

Due to the findings of MeOH in the cathode outlet stream, additional experiments were performed to study for which operating conditions the MeOH concentration at z_{III} was zero. In these experiments, the fuel cell was operated at OCV while the MeOH concentration inside the AFC and the flow rate in the cathode flow channel were varied. These experiments were conducted using different concentrations between $0.2\,\mathrm{M}$ and $2\,\mathrm{M}$ in the anode. At OCV, the electroosmotic drag in eq. (4.3) is zero. If the air or oxygen stream at the cathode inlet is high enough, then all the MeOH concentration at the CCL should go to zero as all of the liquid MeOH is either oxidized, evaporated or driven out by convection. Thus, at OCV and a high cathode flow rate, the crossover reaches a maximal flux and eq. (4.3) can be reduced to

$$N_{MeOH,zIII,max} = \frac{(c_{zII} - 0) D_{MeOH,mem}}{\delta_{mem}} \tag{4.9}$$

The limiting parameters are the MeOH concentration at z_{II}, the diffusion coefficient within the membrane $D_{MeOH,mem}$ and the thickness of the membrane δ_{mem}.

Results from these experiments can be seen in Fig. 4.11. Nafion® 117 was used at a cell temperature of $70\,^{\circ}\mathrm{C}$. Air was supplied to the cathode at a back pressure of $2\,\mathrm{bar}$. At lower cathode flow rates a strong increase of the leakage current density can be seen. At cathode flow rates above approximately $200\,\mathrm{sccm}$, the MeOH flux from the anode to the cathode levels out at a certain value and depends only on the MeOH concentration within the AFC. This behavior at high flow rates is predicted by eq. (4.9) assuming a well hydrated membrane with the same diffusion coefficient for all molarities. Thus, this method of MeOH crossover measurements at OCV with different MeOH

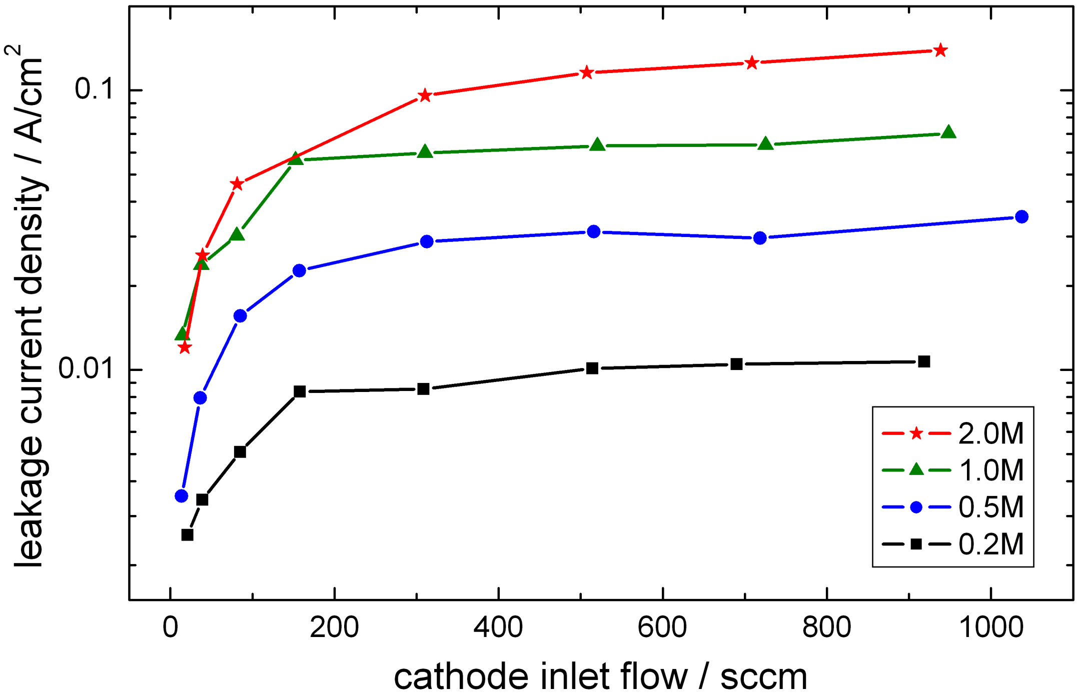

Figure 4.11: Dependence of the flux of CO_2 *in the cathode outlet stream on the cathode inlet flow for different MeOH solutions. No current was drawn from the fuel cell. The cell temperature was 70 °C and the cathode back pressure was 2 bar. Methanol was supplied at* $2\,\mathrm{ml/min}$ *to the anode.*

concentrations can be used to determine the effective diffusion coefficient for MeOH crossing over from the ACL to the CCL in the Nafion® membrane. At cathode flow rates lower than $200\,\mathrm{sccm}$, the crossover current density depends strongly on the air flow rate in the cathode. The formation of a liquid film on the cathode may explain the dependence of MeOH crossover on cathode flow rate at low current densities. A MeOH and water film on the cathode reduced the concentration gradients of MeOH and water across the membrane, thus reducing crossover. The MeOH concentration c_{zIII} inside the CCL varied depending on the mass transfer coefficient in the cathode. The mass transfer coefficient itself depended strongly on the cathode flow rate and becomes large at higher flow rates.

The MeOH concentration at the Mem-CCL interface is not zero for all operating conditions. Model parameters for the diffusion coefficients can be found in Table 4.2. Values for the ACL and the membrane were taken from findings of Scott et al. [108]. The experimentally fitted value for the diffusion coefficient at the ABL was one order of magnitude higher than the values for pure diffusion in water. Thus it can be concluded that not only diffusional but also convectional forces were present inside the ABL throughout the experiments.

The dependence of the MeOH mass transfer coefficient in the cathode on the cell current density and the concentration of liquid MeOH inside the CCL has not been clarified yet. Furthermore, the flux of MeOH into the cathode outlet stream arbitrarily depended on structural parameters as well

Parameter	Value	Source
$D_{MeOH,ABL}$	$3.0 \cdot 10^{-4}\,\mathrm{cm^2\,s^{-1}}$	fitted
$D_{MeOH,ACL}$	$2.8 \cdot 10^{-5} \exp(2436\,(1/353 - 1/T))\ \mathrm{cm^2\,s^{-1}}$	[108]
$D_{MeOH,mem}$	$4.9 \cdot 10^{-6} \exp(2436\,(1/333 - 1/T))\ \mathrm{cm^2\,s^{-1}}$	[108]
$k_{MeOH,CBL}$	$2 \cdot 10^{-7}\,\mathrm{cm^2\,s^{-1}}$	assumed
δ_{AFC}	$0.1\,\mathrm{cm}$	measured
δ_{ABL}	$0.028\,\mathrm{cm}$	measured
δ_{ACL}	$0.002\,\mathrm{cm}$	measured
δ_{mem}	$0.018\,\mathrm{cm}$	measured
δ_{CBL}	$0.03\,\mathrm{cm}$	measured

Table 4.2: Model parameters used for the simulation results that are depicted in Fig. 4.12.

as operation conditions. Therefore, a constant concentration of MeOH inside the CCL at c_{zIII} and a constant MeOH mass transfer coefficient for all cell current densities was assumed in the model. Introducing these terms into the model, simulation results agreed well with experiments as shown in Fig. 4.12. During operation of the fuel cell, electroosmotic drag causes crossover of MeOH besides diffusion. The cathode MeOH mass transfer coefficient at z_{III} and the electroosmotic drag coefficient were used as model parameters to fit measurement results to the model. The flux of MeOH at OCV where no electroosmotic drag occurred was used to fit c_{zIII} the cathode MeOH mass transfer coefficient, to experimental values. The electroosmotic drag coefficient was changed to fit the shape of the leakage current density as a function of different cell current densities data to experimental values.

One result of the fitting procedure can be seen in Fig. 4.12. The cell had a high catalyst loading of $2.5\,\mathrm{mg/cm^2}$ on both sides, Nafion® 117, a temperature of $50\,^\circ\mathrm{C}$ and a $1.5\,\mathrm{M}$ solution of MeOH was pumped at $3\,\mathrm{ml/min}$ to the anode. The cathode stoichiometry was 6. Experimental values of the leakage current density are displayed as dots. Fitting the proposed model to these data an electroosmotic drag coefficient of 2.2 was determined, which is in accordance with literature values [109]. The concentration of MeOH inside the CCL was found to be $0.56\,\mathrm{M}$ $(37\,\%)$. Once these values had been determined, the different contributions of diffusion through the membrane, labeled as “diffusive flux”, and the electroosmotic drag, labeled as “electroosmotic flux” of MeOH through the membrane, could be extracted from model results.

Table 4.3 documents mean values for experiments having the same operation conditions, specified in column two, and their standard deviation for the electroosmotic drag coefficient ξ and the concentration within the CCL c_{zIII}. The electrode catalyst loadings were equal for both sides, and the molarity and temperature were as specified in the operation condition column. The electroosmotic drag coefficient was found to be independent of all parameters except the temperature. The MeOH concentration inside the CCL depended on the molarity of the MeOH solution and the loading of the ACL.

A thicker ACL decreases the MeOH concentration at the interface z_{II} between the anode electrode and the membrane and hence reduces the MeOH concentration gradient between z_{II} and z_{III}.

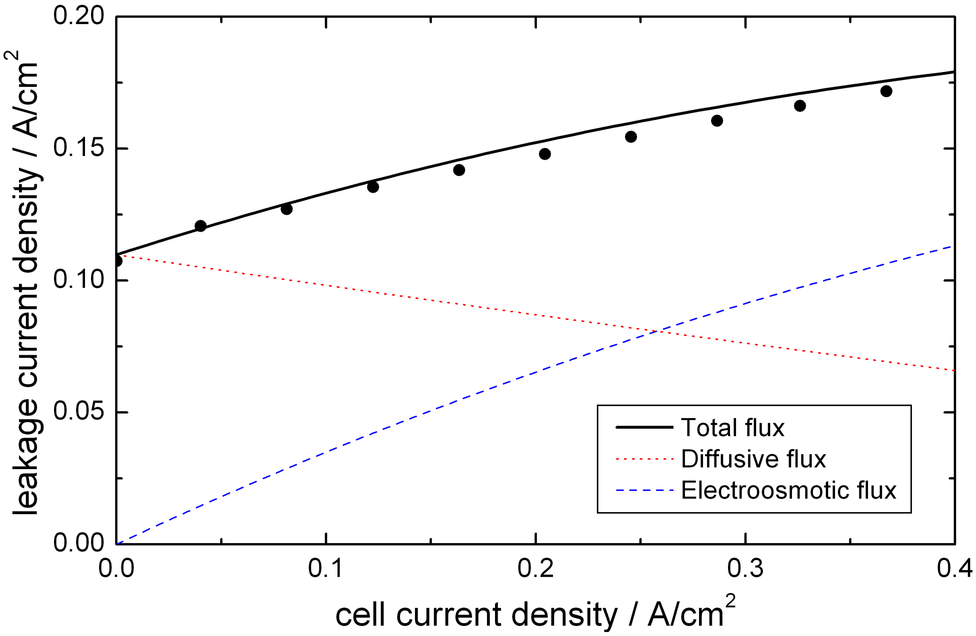

Figure 4.12: Experimental and model results of the leakage current density and the contribution of diffusion and electro-osmosis. Nafion® 117 with a catalyst loading of 2.5 mg/cm^2 on both sides, 50 °C and a 1.5 M solution of MeOH was used. The anode flow rate was 3 ml/min, cathode stoichiometry was 6.

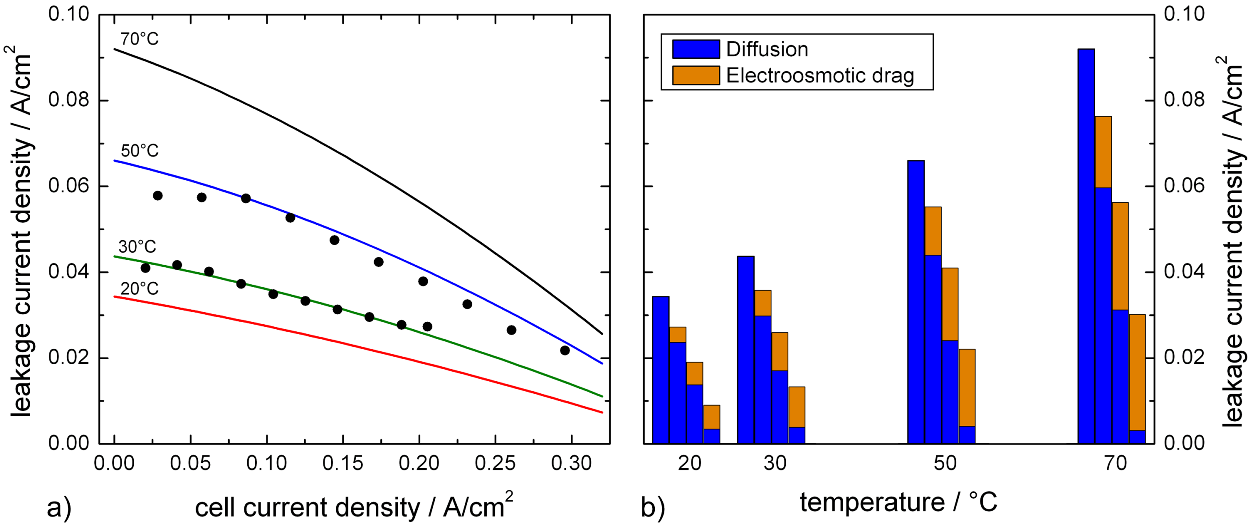

Figure 4.13: a) Simulation results for the leakage current density and experimental validation for Nafion® 1135 with a catalyst loading of 2.5 mg/cm^2 on both electrodes, a 0.5 M solution of MeOH flowing at 1 ml/min and an air stoichiometry of 2 at different temperatures. b) Contributions of the electroosmotic drag and diffusion on the leakage current density. For each temperature, the values at OCV, 0.1, 0.2 and 0.3 A/cm^2 are displayed from left to right.

Parameter	Operating conditions	Fitted value	Standard deviation
ξ	$30\,^\circ\mathrm{C}$	1.2	0.133
ξ	$50\,^\circ\mathrm{C}$	2.3	0.197
c_{zIII}	$1.5\,\mathrm{mg\,cm^{-2}}$, $0.5\,\mathrm{M}$	$0.37\,\mathrm{M}$ $(74\,\%)$	$0.029\,\mathrm{M}$
c_{zIII}	$1.5\,\mathrm{mg\,cm^{-2}}$, $1.5\,\mathrm{M}$	$1.20\,\mathrm{M}$ $(80\,\%)$	$0.188\,\mathrm{M}$
c_{zIII}	$2.5\,\mathrm{mg\,cm^{-2}}$, $0.5\,\mathrm{M}$	$0.19\,\mathrm{M}$ $(38\,\%)$	$0.021\,\mathrm{M}$
c_{zIII}	$2.5\,\mathrm{mg\,cm^{-2}}$, $1.5\,\mathrm{M}$	$0.56\,\mathrm{M}$ $(37\,\%)$	$0.050\,\mathrm{M}$

Table 4.3: Values for the electroosmotic drag coefficient and the MeOH concentration inside the CCL with respect to feed concentration. Values were determined by fitting and averaging measurement results to the proposed model and only changed with given operating conditions. Standard deviations from the averaging procedure are also presented.

Experimental results support this conclusion. At a high catalyst loading of $2.5\,\mathrm{mg/cm^2}$ (which equals a thickness of the ACL of $20\,\mu\mathrm{m}$), the extracted values of c_{zIII} were half of values calculated for a catalyst loading of $1.5\,\mathrm{mg/cm^2}$ (which equals a thickness of the ACL of $10\,\mu\mathrm{m}$) for both the high and the low MeOH concentrations.

4.2.4 Influence of temperature

During the experiments, the leakage current density was measured at $30\,^\circ\mathrm{C}$ and $50\,^\circ\mathrm{C}$. The results indicated that the electroosmotic drag was only a function of the temperature and no structural parameters, e.g. membrane thickness, showed an influence on the electroosmotic drag. The electroosmotic drag coefficient could be gained from model results as documented in Table 4.3. Extracted values are in good agreement with literature values [92,108,110]. The membrane model of Meyers et al. [101] predicts more open pores for liquid transport within the membrane at higher temperatures, which can be one cause for a higher drag coefficient at elevated temperatures. Ge et al. [111] has reviewed the literature from 4 different sources on the effect of temperature on the electroosmotic drag coefficient at different temperatures. He has shown that the electroosmotic drag coefficient increases linearly with temperature in a temperature range between $20\,^\circ\mathrm{C}$ and $70\,^\circ\mathrm{C}$. He has also shown that the drag coefficient is independent of the cell current density.

Consequently, in this work the drag was assumed to increase linearly with temperature at the given temperature between $30\,^\circ\mathrm{C}$ and $50\,^\circ\mathrm{C}$. A linear extrapolation of the drag coefficient values at $30\,^\circ\mathrm{C}$ and $50\,^\circ\mathrm{C}$ was used in the model.

The predicted leakage current density at different temperatures can be seen in Fig. 4.13a. The leakage current densities increased significantly with temperature, up to $0.1\ A/cm^2$ were predicted with the maximum value at OCV and $70\,^\circ\mathrm{C}$. Black dots represent experimental values of the experiments at $30\,^\circ\mathrm{C}$ and $50\,^\circ\mathrm{C}$. It can be noted that the increase of the leakage current density at small cell current densities is much higher compared to large cell current densities. Simulation results for the electroosmotic and diffusion parts of the leakage current density at OCV, 0.1, 0.2 and $0.3\,\mathrm{A/cm^2}$ can be seen in Fig. 4.13b for a selection of temperatures.

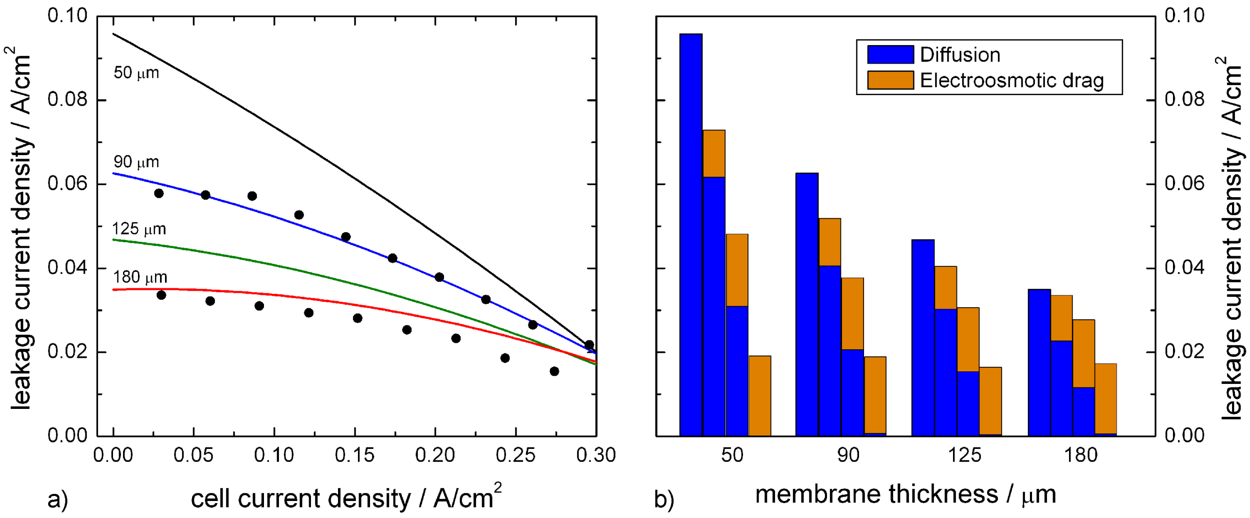

Figure 4.14: a) Simulation results for the leakage current density and experimental validation at a catalyst loading of 2.5 mg/cm^2 on both electrodes, 50 °C, a MeOH concentration of 0.5 M at an anode flow rate of 1 ml/min and an air stoichiometry of 6 for different membrane thicknesses. b) Contributions of the electroosmotic drag and diffusion on the leakage current density. For each membrane thickness the values at OCV, 0.1, 0.2 and 0.3 A/cm^2 are displayed from left to right.

Obviously diffusion is the only driving force for the MeOH crossover at OCV. At $0.3\,\mathrm{A/cm^2}$, the diffusion part of the leakage current density nearly vanishes and the leakage current density is dominated by the electroosmotic drag. At this current density, the MeOH concentration at z_{II} is nearly equal to the film concentration inside the CCL. The leakage current density at $0.3\,\mathrm{A/cm^2}$ is only one third of the leakage current density at OCV. Thus, fuel cell operation at high cell current densities at near–ambient temperatures is favorable in terms of fuel economy.

4.2.5 Influence of membrane thickness

The thickness of the membrane influences crossover of MeOH to the cathode. The leakage current density for different membrane thicknesses can be seen in Fig. 4.14a. Experimental values derived from the experiments for Nafion® 117 ($180\,\mu\mathrm{m}$) and Nafion® 1135 ($90\,\mu\mathrm{m}$) are depicted as dots and validate the model.

The different contributions of electroosmotic drag and diffusion are shown in Fig. 4.14b. According to eq. (4.3), the flux of MeOH at z_{III} at OCV is reciprocally proportional to the membrane thickness δ_{mem}. When a current is applied to the cell, the flux of MeOH to the cathode side increases due to electroosmotic drag and thus the MeOH concentration at z_{II} is lowered. In consequence, the concentration gradient of MeOH across the membrane between the ACL-Mem and CCL-Mem interfaces is lowered and the contribution of diffusion to the leakage current den-

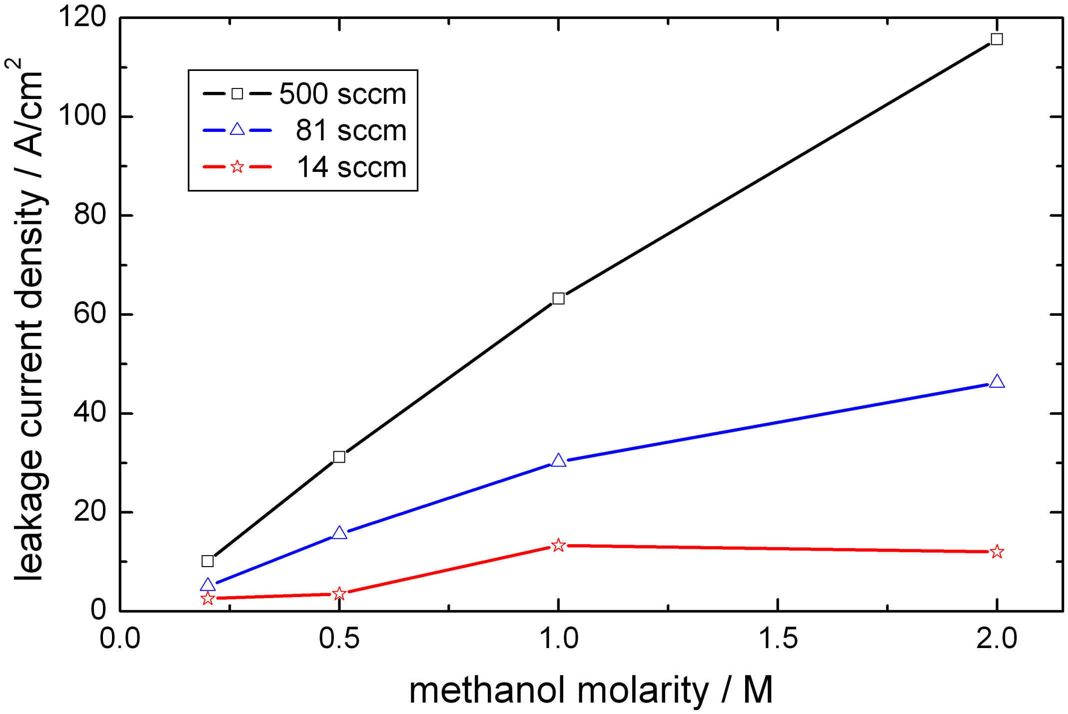

Figure 4.15: Influence of the molarity on the leakage current density at different cathode flow rates and OCV. The operating conditions are as specified for Fig. 4.11.

sity decreases. It can be seen that for the given operating conditions, the diffusional part totally vanished at cell current densities of $0.3\ \mathrm{A/cm^2}$.

It can be concluded that fuel losses can be minimized by using thicker membranes. Especially at OCV or low current densities, the parasitic losses due to crossover of MeOH to the cathode can be minimized, optimizing the Faradaic efficiency.

4.2.6 Influence of molarity

While the electroosmotic drag coefficient changed the form of the function relating the leakage current density i_{leak} to the current density, the MeOH concentration inside the CCL c_{zIII} determined the value of i_{leak} at OCV. Besides the thickness of the ACL the MeOH concentration significantly influenced c_{zIII} in the cathode, as shown in Table 4.3.

If no MeOH is consumed or evaporated inside the CCL and no current is drawn from the fuel cell, c_{zIII} should equilibrate with the MeOH concentration of the AFC for the OCV. Thus for this limiting case, a strong dependence of the MeOH concentration of the AFC is expected. For the other limiting case, when all MeOH is consumed inside the CCL, only mass transfer resistances control the flux. Therefore a thicker ACL acts as a larger barrier for MeOH to cross to the CCL and decreases the flux of MeOH.

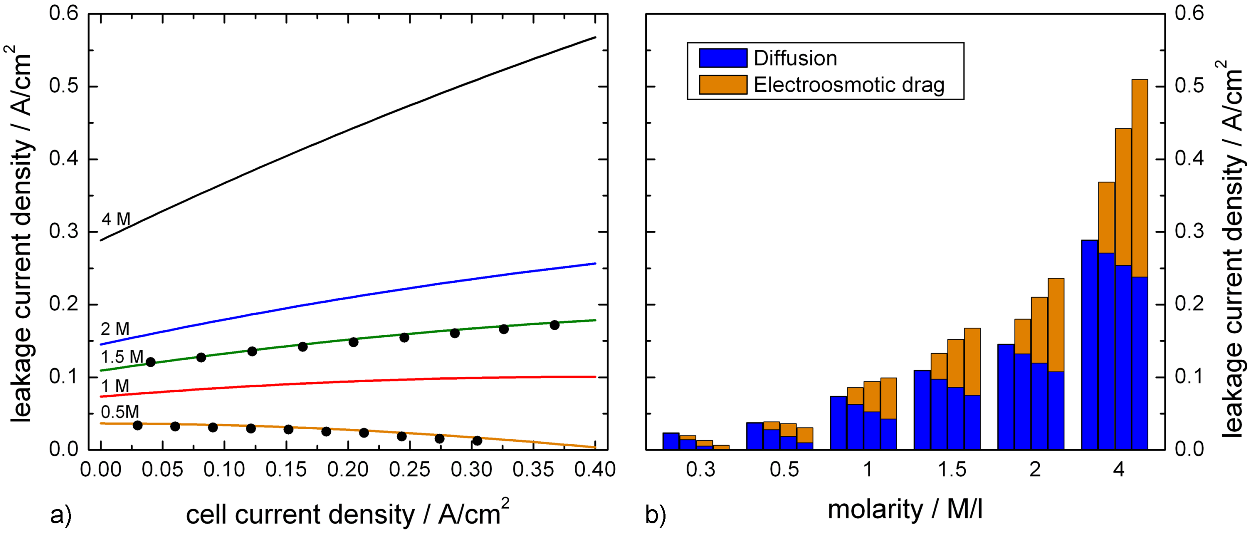

Figure 4.16: a) Simulation results for the leakage current density and experimental validation for Nafion® 117 with a catalyst loading of 2.5 mg/cm^2 on both electrodes, 50 °C, an anode flow rate of 1 ml/min and an air stoichiometry of 6 at different molarities. b) Contributions of the electroosmotic drag and diffusion on the leakage current density. For each molarity the values at OCV, 0.1, 0.2 and 0.3 A/cm^2 are displayed from left to right.

As the electroosmotic drag vanishes at OCV, MeOH permeates through the membrane only by diffusion. Fig. 4.15 shows the leakage current density for different molarities and cathode air flow rates. The leakage current density showed a linear behavior on the MeOH concentration in the feed and declined with the cathode flow rate. A linear dependence between MeOH concentration in the feed and MeOH concentration at z_{III} is assumed in the given range, an assumption that holds true if consumption of MeOH at z_{III} is constant for different molarities. Values extracted from experimental results at $0.5\,\mathrm{M}$ and $1.5\,\mathrm{M}$ are extrapolated and introduced into the model.

Simulation results for the leakage current density at various MeOH concentrations can be seen in Fig. 4.16a. At $0.5\,\mathrm{M}$ and $1.5\,\mathrm{M}$ it was validated using experimental values. Simulation results at a MeOH concentration of $4\,M$ have to be regarded as a qualitative projection as the linear dependence was not verified for concentrations greater than $2\,\mathrm{M}$. The molarity has a much higher impact on the leakage current density than the temperature (Fig. 4.13) or the membrane thickness (Fig. 4.14). It also changes the gradient from a decrease with cell current density at lower MeOH concentrations to rising values at higher concentrations. The cause can be seen in Fig. 4.16b. Although the diffusion part of the leakage current density is decreasing with increasing cell current density at MeOH concentrations greater than $0.5\,\mathrm{M}$, the superposition of diffusion and electroosmotic drag is increasing.

In conclusion, it is favorable to operate a LDMFC at lower MeOH concentrations, especially at the interface between ACL and membrane, to keep crossover small. For higher MeOH concentrations,

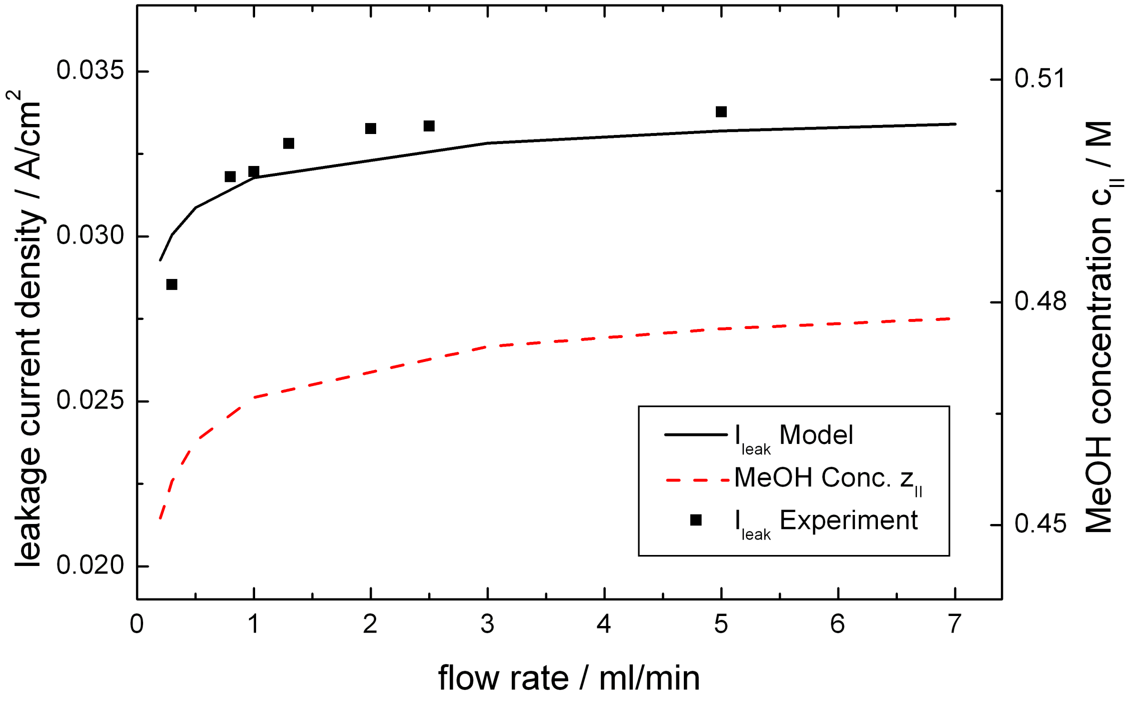

Figure 4.17: Simulation results and experimental values for the total leakage current density and the MeOH concentration at z_{II} at OCV and varying flow rates. A 0.5 M solution of MeOH and Nafion® 1135 having a catalyst loading at each electrode of 2.5 mg/cm^2 at 30 °C was used. Air was supplied to the cathode at a constant flow rate of 20 sccm.

the crossover even increases with cell current density. At $4\,\mathrm{M}$ and $0.3\,\mathrm{A/cm^2}$ the leakage current density exceeds the cell current density by a factor of almost two.

4.2.7 Influence of anode flow rate

Experiments were performed at a flow rate of $1\,\mathrm{ml/min}$ and $3\,\mathrm{ml/min}$ to study the influence of anodic flow. Results indicated that the flow rate of MeOH at the anode had an noticeable impact on the crossover. This was introduced as a dependence on flow rate for the mass transfer between the anode flow channel and the backing. The model was tested with parameters fixed to a $0.5\,\mathrm{M}$ solution of MeOH at $30\,^\circ\mathrm{C}$ and a thickness of $90\,\mu\mathrm{m}$. The flow rate was parameterized between $0.5\,\mathrm{ml/min}$ and $7\,\mathrm{ml/min}$.

To verify the model predictions, additional experiments were performed at OCV and different anode flow rates. Fig. 4.17 shows experimental values for Nafion® 1135 having a catalyst loading at each electrode of $2.5\,\mathrm{mg/cm^2}$, the same operating conditions as for the simulation. Air was supplied to the cathode at a constant flow rate of $20\,\mathrm{sccm}$. The model agreed well with the experimental values. As can be seen in the model predictions, the leakage current density at OCV increases sharply near OCV at first an then goes into saturation as the cell current density is increased.

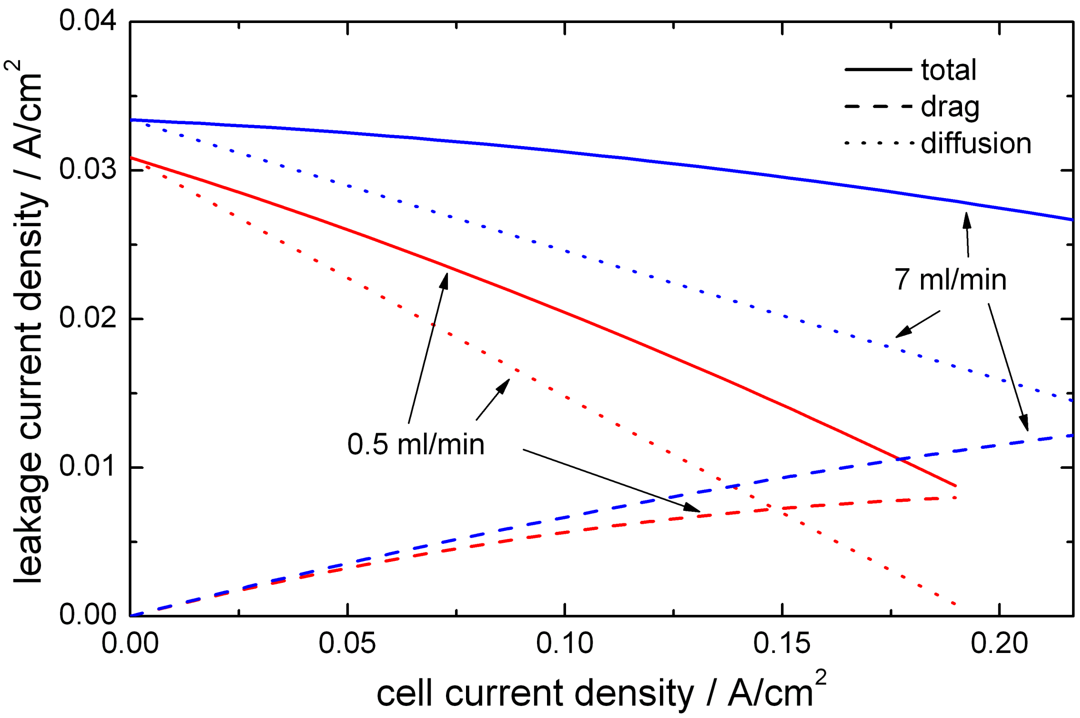

Figure 4.18: Simulation results for the leakage current density at 30 °C and a membrane thickness of 90 μm. The shape of the total leakage current density changes significantly between 0.5 ml/min and 7 ml/min due to much lower MeOH concentrations at z_{II} for low flow rates.

On examining the modeled MeOH concentrations at the ACL-Mem interface, it is obvious that a decreases at low flow rates in the MeOH concentration at z_{II} is the cause for the lower leakage current densities at low flow rates.

Changing the anode flow rate lead to a significant change in the shape of the total leakage current density on the cell current density as model predictions indicate in Fig. 4.18. Here the total crossover density and the contributions of electroosmotic drag and diffusion are plotted for a MeOH flow rate of $0.5\,\mathrm{ml/min}$ and $7\,\mathrm{ml/min}$ respectively. It is obvious that the superposition of drag and diffusion leads to totally different behavior on the leakage current density, depending on which process dominates. For a high anode flow rate, the crossover increases with increasing current density, whereas it decreases for the lower flow rates. A high flow rate of MeOH also reduces the performance of the fuel cell. Therefore, one can conclude that for high power densities or high current densities, a low MeOH flow rate is preferable with respect to the crossover.

In addition to the model results, it is possible that a pressure difference between the anode and cathode compartment, which was neglected in the model, is more pronounced at higher flow rates and consequently causes higher leakage current densities [112, 113].

4.3 Structures for passive CO_2 removal

If operation of a LDMFC is to be completely passive, no external devices can be used. This includes the fuel pump, which continuously supplies new fuel to the anode and drives out the product CO_2 of the MOR. Operating a fuel cell without any flow would yield a power breakdown if the whole electrochemically active surface of the anode were blocked by CO_2 bubbles or after all the MeOH had been oxidized.

Concerning CO_2 bubbles, passive structures could aid bubble removal and thus might ensure that electrochemically active surface was sufficient for the MOR. Special micro–channel designs, for example, have been reported to increase the mobility of gas bubbles trapped in liquid–filled channels [114, 115]. The channel geometry and the capillary forces can be used to shape bubbles and increase their mobility. A further improvement of the micro–channel design allows passive CO_2 gas bubble removal from the anode flowfield of a LDMFC as described in the following section.

To overcome the problem of MeOH depletion, a possible solution is to pump fuel into the system at certain intervals to replace the reaction volume and to increase the MeOH concentration again. Regarding the efficiency of the fuel cell system, the benefit is twofold. As will be shown the fuel cell efficiency itself is higher than for a continuously pumped system. Additionally, there is no continuous energy demand for the pump as it is idle most of the time and the system efficiency is increased.

4.3.1 Flowfield concept

In brief, the working principle of the flowfield layout is based on the non–uniform capillary pressure $\left(P_{cap} = \gamma\left(r_x^{-1} + r_y^{-1}\right)\right)$ exerted by a tapered channel. The considered situation is sketched in Fig. 4.19. The two ends of an elongated gas bubble exhibit different curvatures r and thus experience different capillary pressures P_{cap}. The pressure difference forces the bubble to move toward the wider channel part until both capillary pressures are in equilibrium as sketched Fig. 4.19c. In this case, the bubble takes on a spherical form and the movement stops. In the fuel cell application, the bubble might even increase in size during its movement along the channel. This

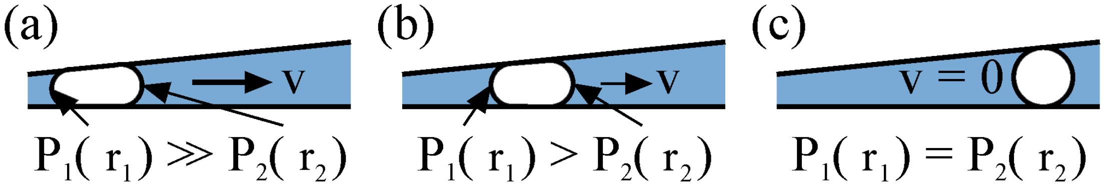

Figure 4.19: a) and b) Two-dimensional representation of gas bubble movement in a tapered channel, driven by different capillary pressures. c) Equilibrium state with no bubble movement.

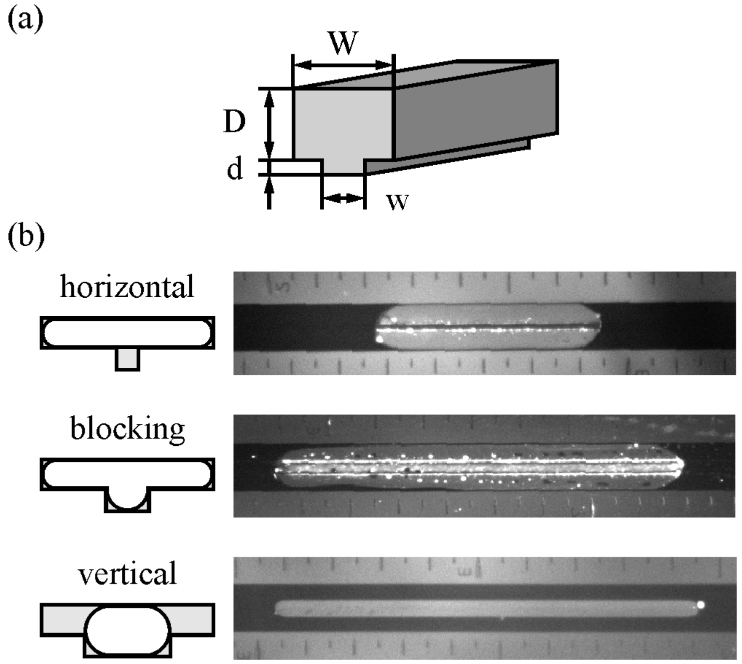

Figure 4.20: a) Sketch of the original T-shaped channel design [114]. b) Photographs of the three possible gas bubble positions in a T-shaped channel [115] filled with liquid (dark gray).

happens, if one wall is formed by the MEA and other bubbles growing there are wiped off and merge with the passing bubble.

A prerequisite for sufficiently fast bubble movement is a channel design which allows liquid to bypass the gas bubble. A design that provides such a bypass is a channel with a T-shaped cross section as shown in Fig. 4.20a. This channel design has already been presented by Kohnle et al. [114] together with an analytical model describing the movement of a gas bubble in this specific geometry. Based on this work and the study of geometric variations of the T-shaped cross–section, Litterst et al. presented a model to determine the bubble position in channels with this cross–sectional layout [115]. Depending on the geometrical parameters (W,w,D,d) shown in Fig. 4.20a, any one of the three stable bubble positions referred to as "horizontal", "blocking" and "vertical" can be adopted as shown in Fig. 4.20b.

Since the T-shaped cross section itself only influences the bubble position inside the channel but does not provide the necessary capillary forces to move the gas bubble passively, tapered channel walls have been added to the basic T-shaped channel design as shown in Fig. 4.21a. However, the channel dimensions have been chosen to guarantee a vertical bubble position by assuming the worst case at the shallowest part of the central channel. To form a flowfield for the fuel cell, the T-shaped tapered channels are arranged as two parallel rows connected to a central supply channel. The other side of the channel is connected to an outlet channel placed on the outer side of the flowfield. In each of the two rows, 18 T-shaped channels are placed with a spacing of $0.3\,mm$ between each other as indicated in Fig. 4.21b. The T-shaped channels are tapered in two

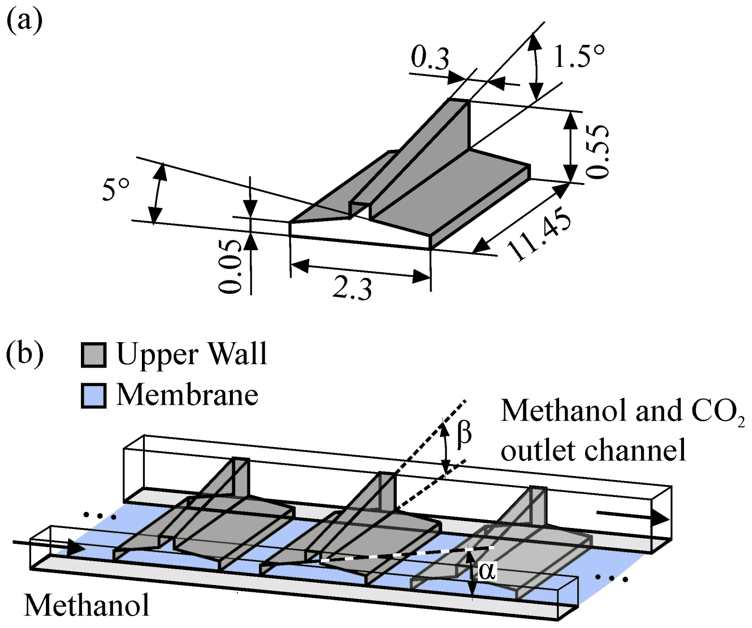

Figure 4.21: a) Sketch of the channel dimensions of the test samples in millimeters (not to scale). b) Plan of one side of the flowfield indicating the supply and the outlet channel as well as the T-shaped parallel channels with their taper angles, α and β.

dimensions: first symmetrically by a tapering angle $\alpha = 5°$ across their profile and by an angle $\beta = 1.5°$ along their longitudinal section opening toward the outlet channel.

As shown in Fig. 4.21b, the CCM or GDL (e.g. carbon paper or metal mesh) forms the bottom of the parallel channels while the remaining channel walls are formed by the substrate. Since the MEA covers the whole bottom of the T-channels, the largest possible area is used for fuel cell operation. The bubbles can grow on that surface and as soon as a bubble comes into contact with the upper wall, capillary action starts to move it toward the larger cross–section of the channel. Due to the ongoing reaction, the bubble size increases continually, so the bubble is forced to deform its spherical shape into a stretched oval shape as already sketched in Fig. 4.19. The pressure gradient created by the unbalanced capillary forces causes a bubble movement toward the central part of the T-shaped channel. This motion continues toward the central channel as already described above for tapered channels. Once the central part has been reached, the bubble takes on a shape that only fills the central part due to the T-shaped design. When the bubble is inside the central channel, the tapering again makes the bubble move to the final outlet.

4.3.2 Sample preparation

In the preparation of experiments, a negative of the flowfield design with the dimensions given in Fig. 4.21 was milled into a brass plate to form a hot embossing tool. The embossing tool was placed into a frame to prevent polymer spilling out sideways during the embossing process.

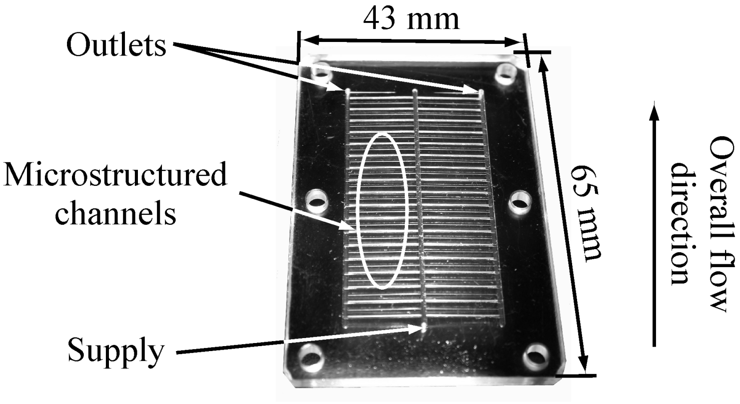

Figure 4.22: Photograph of one of the transparent test samples illustrating the fuel supply and the outlet channels at the edges of the micro–structured array of channels.

Two different polymers were chosen as substrates for the test samples: PMMA and a conductive graphite-filled polymer SIGRACET®[1] PPG86 (SGL Technologies GmbH). The two polymers were chosen to serve for two kinds of experiments: the transparent PMMA for experiments where the bubble development and movement were observed by a camera and the opaque, conductive graphite–filled polymer to assemble a fully functional LDMFC. After the hot embossing process, the mounting holes and the fluid interconnections were drilled in a second step to complete the sample as shown in Fig. 4.22. The samples were supplied with fuel through a channel along the central axis. CO_2 was removed through the outlet channels on the edges of the flowfield.

4.3.3 Visual experiments

To study the bubble behavior the configuration shown in Fig. 4.23 was assembled. The setup consisted of a lower mounting frame, two sheets of metal mesh sandwiching the MEA, the PMMA sample and finally an upper mounting frame. In this frame, a notch was milled to allow a direct view of the PMMA sample. To avoid MeOH leakage, the stack was sealed with silicone and then tightly screwed together.

For the experiment, the metal meshes were electrically connected and the system was primed with a $2\,\mathrm{M}$ MeOH solution that had been dyed with red ink to achieve higher contrast. The evolution of gas bubbles was forced by applying a current of $50\,\mathrm{mA/cm^2}$ at a voltage of about $0.2\,\mathrm{V}$ between the metal meshes. A fuel cartridge was connected to the supply channel during the experiments to allow passive refueling of the flowfield. The CO_2 bubbles could be released through the outlet channel located at the left edge of the photos in Fig. 4.24 that show a detail of the flowfield. During the experiment, a video camera was used to observe the bubble behavior. The bubbles first had to pass through the metal mesh before they moved toward the central part of the micro–structured channel. Since the mesh used is rather coarse, some bubbles were trapped inside the mesh until

---

[1] http://www.sglcarbon.com/sgl_t/fuelcell/index.html

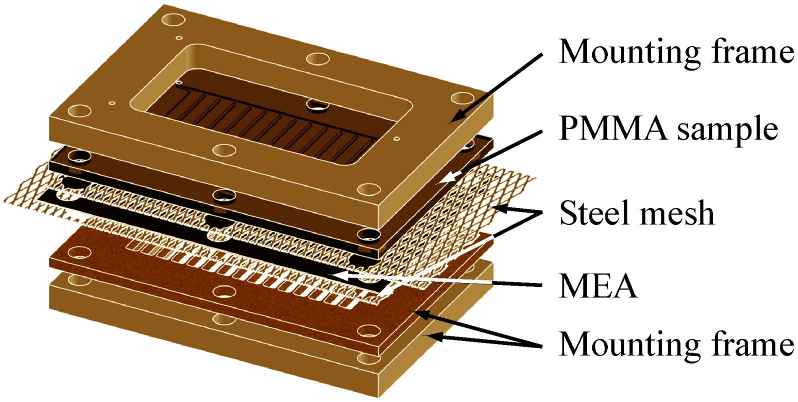

Figure 4.23: Assembly of the test cell for visual studies of the bubble behavior inside the flowfield.

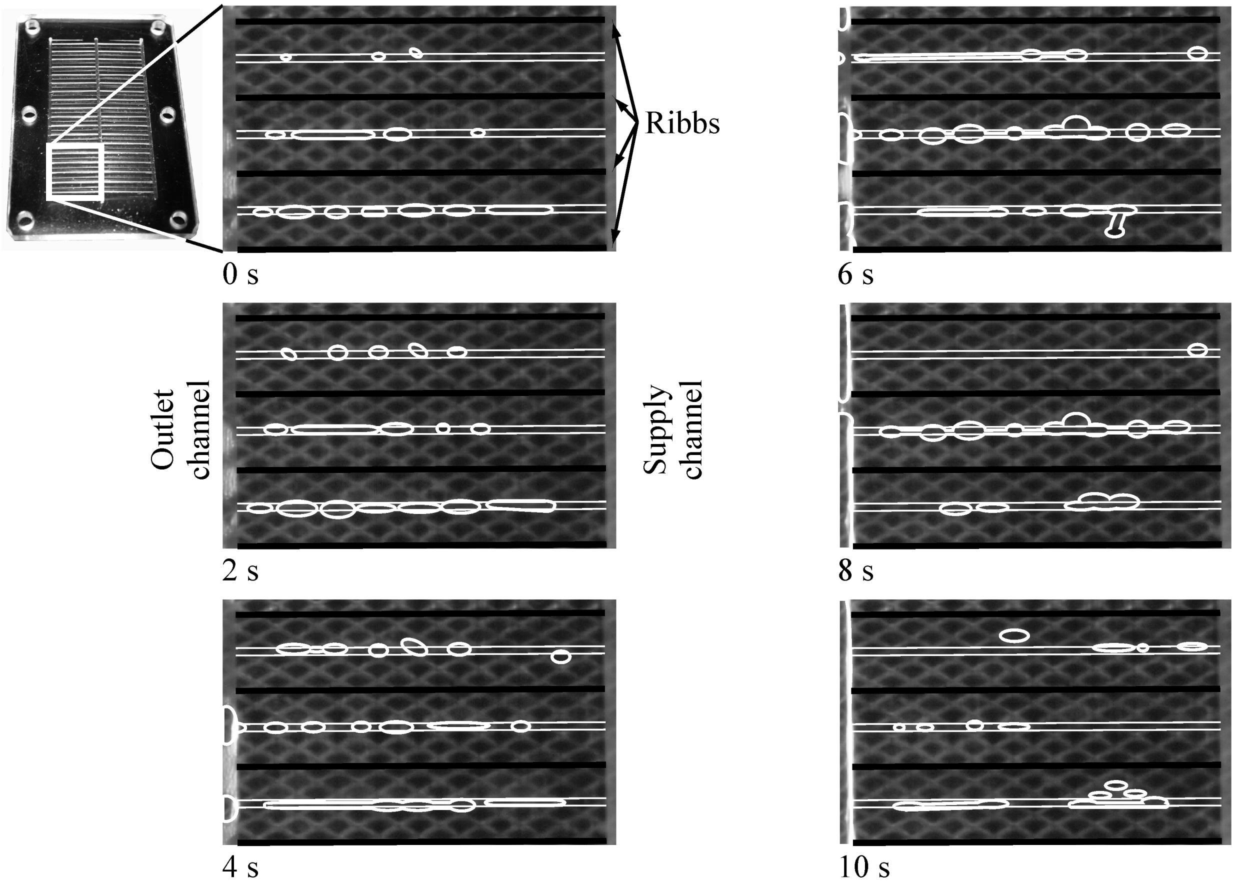

Figure 4.24: Picture sequence of the developing gas bubbles and their movement inside one test sample with a 2 M MeOH solution. To improve visibility, the spaces between each particular micro–channel (ribs) have been marked as black bars, while the edges of the central part of the channel and the bubbles have been marked in white.

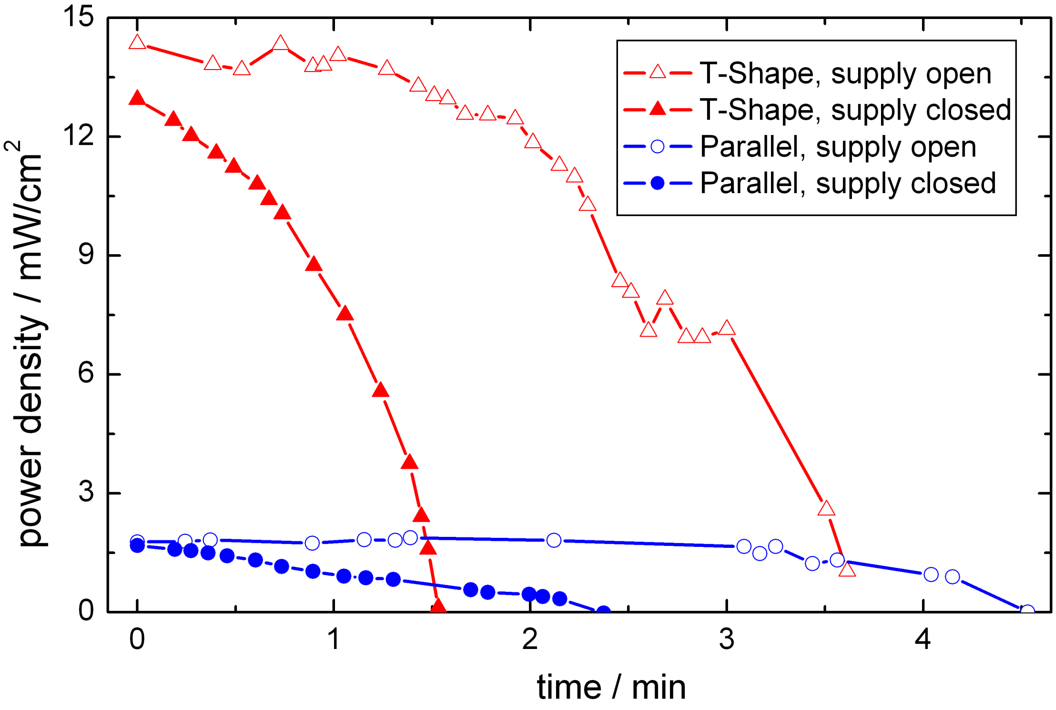

Figure 4.25: Power densities of a T-shaped micro–structured flowfield and a parallel flowfield at no–flow conditions. The MeOH supply tube was either mechanically open or closed.

they got wiped off by another bubble or had grown to a sufficient size to detach. The bubbles first moved toward the central channel and once there grew further until they started to move again. This time their movement was directed toward the outlet channel as anticipated.

4.3.4 Electric experiments

As well as the visual proof of concept for the micro–structure, electric measurements were performed under no–flow conditions. Isothermal experiments were conducted using the test cell that is described in Chapter 3. Instead of the anode flowfield that was used for the **Parameter study** and the **Methanol crossover** section of this chapter (Fig. 4.1), the anode flowfield used here incorporated the micro–structure given in Fig. 4.20b. An additional flowfield with parallel channels served as a reference.

A $0.5\,\mathrm{M}$ solution of MeOH was fed to the anode. The cathodic air flow was set to $100\,\mathrm{ml/min}$. The temperature was kept constant at $50\,^\circ\mathrm{C}$. Two different configurations at the anode were chosen for the experiments. For one, the pump was stopped and closed the supply tube mechanically. For the other, hydrostatic pressure because of an elevated supply tube fed the anode and was kept open throughout the experiment. The MPP was determined for both the parallel and the micro–structured flowfield. Therefore the fuel cell could be operated galvanostatically at MPP, which was $80\,\mathrm{mA/cm^2}$ for the T-shaped structure and $30\,\mathrm{mA/cm^2}$ for the parallel channels. Each measurement was stopped when the cell voltage reached zero.

Although a reference electrode was attached to the setup, bubbles close to the reference electrode disturbed the symmetric potential within the membrane and reference readings were heavily biased. Experimental errors in performing reference electrode measurements are discussed in detail in Appendix A. As a result, the anode and cathode losses could not be determined individually. Nevertheless, the cathode losses should have remained stable, as the cell was operated galvanostatically and the operating conditions for the cathode were not altered. Hence all changes in cell voltage should have been caused by effects taking place on the anode side.

Results of these measurements can be found in Fig. 4.25. It is obvious that the T-shape micro–structure outperforms the parallel flowfield by far. Probably several channels of the parallel flowfield were blocked by $\mathrm{CO_2}$ bubbles so that the active area was drastically reduced. The slight changes at the beginning of the measurements between "open" and "closed" for both flowfields can be explained by bubbles that remained immobile within the GDL. Reproducibility was especially difficult to achieve for the T-shaped flowfield. The area below the curves reflects the total energy density for the given systems. It can be noted that it is higher for the open supply tube, which means that MeOH is transported into the flowfield as gas bubbles leave the anode.

4.3.5 Prototype cell

The massive endplates and the thick flowfields of the test cell caused a high thermal mass for the setup. In order to study the impact of non–isothermal operation, a planar prototype cell was built as illustrated in Fig. 4.26, including the micro–structured flowfield. The assembly differs from the cell for visual experiments although the same flowfield design has been used. In this assembly, the cathode was made of an ordinary printed circuit board (PCB). The PCB is a laminate of glass fiber and epoxy sandwiched between two copper layers of $35\,\mu\mathrm{m}$ thickness. In the cathode, parallel rectangular openings of $3\,\mathrm{mm} \times 21\,\mathrm{mm}$ with a spacing of $1\,\mathrm{mm}$ were milled to form the cathode flowfield to allow for air–breathing operation. The electrochemically active area of the fuel cell was $2\,\mathrm{mm} \times 43\,\mathrm{mm}$. The copper layer of the PCB was used as the current collector and electrical contact to the outside of the fuel cell. A hot embossed and drilled graphite plate of PPG86 with the flowfield structure described above was used as the fuel cell's anode. For the electrical contact, a copper plate was placed on top of the graphite plate. CCMs produced by the "decal transfer" method, consisting of Nafion® 117 with catalyst loadings of $2.5\,\mathrm{mg/cm^2}$, and $350\,\mu\mathrm{m}$ thick Toray carbon paper, were stacked together as the MEA. To avoid short circuits between the electrodes, the MEA was sandwiched between two polymer films with a thickness of $100\,\mu\mathrm{m}$. The whole assembly was pressed together by six M3 screws with a torque of $0.5\,\mathrm{Nm}$ each. To ensure sufficient contact pressure between the plates, an adhesive was applied onto the edges and pressed together while curing. Furthermore, the adhesive was used to prevent leakage.

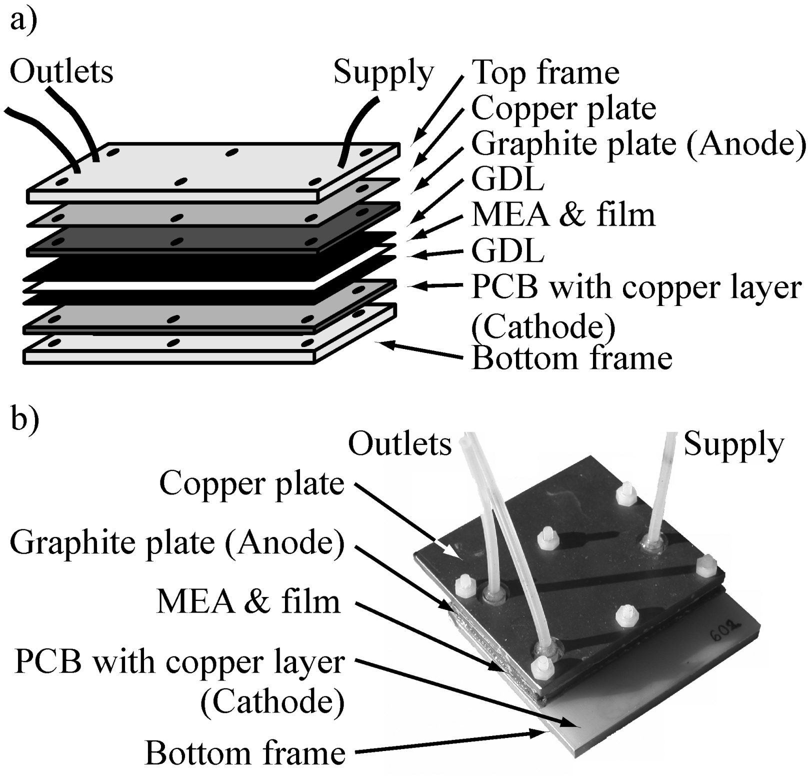

Figure 4.26: a) Draft of the prototype fuel cell assembly (not to scale). b) Photograph of the assembled prototype fuel cell.

Extended–duration potentiostatic measurements at $0.25\,\mathrm{V}$ with a $4\,\mathrm{M}$ MeOH solution were performed at ambient temperatures. The cathode was passively operated under air–breathing conditions. The micro–structured anode flowfield layout was designed for totally passive as well as for active, pump–assisted operation. Thus a direct comparison of the experimental results in the active and passive modes could be made. Three set of conditions at the anode were chosen for the experiments: pumping continuous ($0.225\,\mathrm{ml/min}$), pumping at the same flow rate but in intervals and an open cartridge without any pump.

In the configuration refueled by pumping at intervals the fuel cell was operated for approximately $23\,\mathrm{min}$ and then new fuel was pumped into the system for $15\,\mathrm{s}$. During the time that the pump was switched off, the connection between the fuel cartridge and the cell was mechanically interrupted. Thus no gas or liquid could enter or leave the cell at the supply port during this time. In the last configuration, the connection between the reservoir and the fuel cell was mechanically open during the whole operating time. Due to a small hydrostatic height difference (about $10\,\mathrm{mm}$) between the cartridge and the fuel cell, MeOH was allowed to enter the cell by diffusion and convection during the whole measurement. After about $25\,\mathrm{min}$ the hydrostatic height of the cartridge was increased for a few seconds to flush new fuel into the flowfield by hydrostatic pressure.

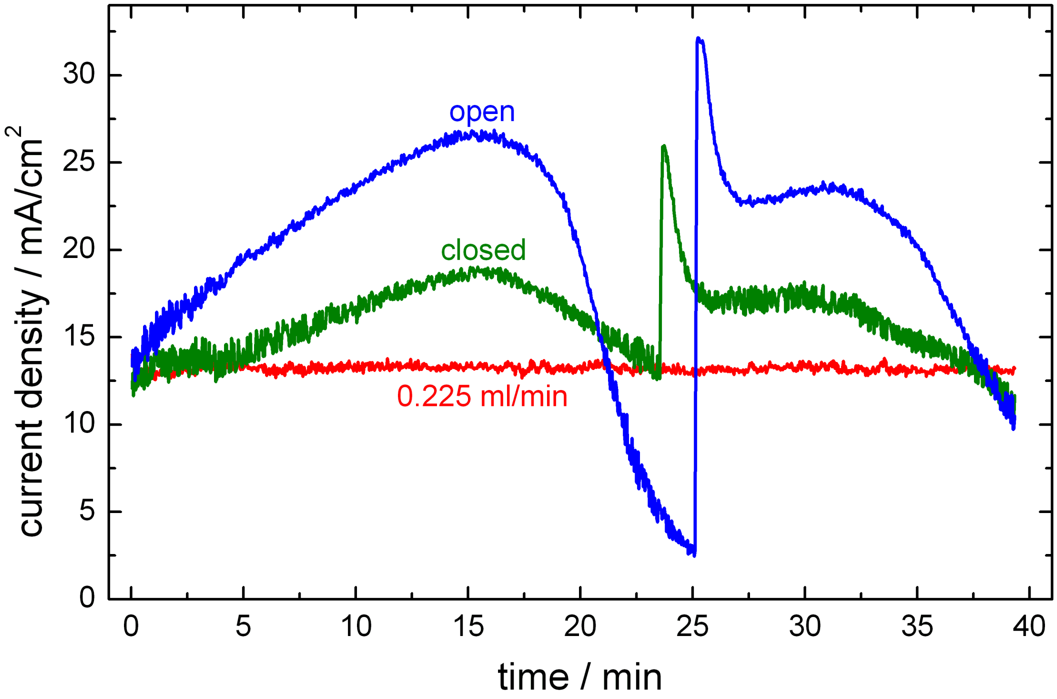

Figure 4.27: Long–time measurements with a 4 M MeOH solution at 0.25 V. Continuously pumped ("0.225 ml/min"), pumping at intervals ("closed", 23 min pause and 15 s pumping) and passive with refueling by hydrostatic pressure after 25 min ("open").

The results of all three configurations are given in Fig. 4.27. In the case of continuously pumped fuel cell operation, a stable current of about $14.5\,\mathrm{mA/cm^2}$ was reached. The results for the other two configurations did not show a stable current level during the extended operation as anticipated. The current density increased significantly until depletion of MeOH caused a decline in current density. Without any convective flow the temperature inside the fuel cell increased in contrast to the continuously flushed fuel cell where the flow also continually cooled the cell. The increased temperature led to better kinetics and consequently higher current densities in the cell. This phenomenon, which is especially significant for the MOR at the anode, was studied and discussed in detail in the **Parameter study** section of this chapter. The current densities for the LDMFC fed by hydrostatic pressure exceeded the current densities for the configuration with intermittent pumping. Higher energy densities for mechanically open connections between the fuel reservoir and the fuel cell were also found for isothermal operation as shown in Fig. 4.25. Therefore it can be concluded that for a micro–structured LDMFC system a pump should be used that does not interrupt the connection and allows passive MeOH supply from the reservoir either by diffusion or by convection.

Chapter 5

Vapor-Phase Operation

Two–phase problems, like CO_2 bubble removal, can be avoided if methanol is delivered in the vapor phase to the anode electrode. The first papers on vapor-fed DMFCs (VDMFC), which were published in the 1990s, reported using a vaporizer at high temperatures between $130\,^\circ\mathrm{C}$ and $200\,^\circ\mathrm{C}$ [116–118]. The fuel cell itself was kept well above the boiling point of methanol at around $100\,^\circ\mathrm{C}$. Hogarth et al. [118] stated that the performance of their vapor-fed system exceeded by some margin performance of their liquid-fed systems. Power densities up to $0.22\,\mathrm{W/cm^2}$ using air at the cathode were achieved. The impedance of VDMFCs has been studied by Fukunaga et al. [119] and Furukawa et al. [120]. Kallo et al. [121] found that membrane conductivity is an important parameter for a VDMFC and that MeOH crossover is lowered for vapor-phase operation and decreases with increasing temperature. He also studied the transient behavior of a VDMFC [47].

Vapor-phase operation at high temperatures is incompatible with the need for passive approaches for portable DMFCs. In addition, the vaporizer has a high energy consumption, and thus decreases the system efficiency. Recently, much has been published on MeOH mass transfer resistances at the anode, e.g. by using a microporous plate, to lessen the impact of methanol crossover for liquid-fed DMFCs [28,122,123]. W.-J. Kim et al. [29] used hydrogels in a methanol fuel cartridge as a diffusion–rate–controlling agent that suppressed methanol crossover in passively operated LDMFCs. Although he did not specify vapor-phase operation, probably most of the liquid MeOH that had soaked into the hydrogel he used during his experiments was in vapor-liquid equilibrium inside the anode chamber, as similar OCVs for the $4\,\mathrm{M}$ and $8\,\mathrm{M}$ MeOH solution indicate.

Thermodynamically driven evaporation of MeOH at ambient temperatures was utilized for this work. Instead of hydrogels, membranes were used as phase barriers between the liquid and the gaseous methanol. Usually phase separation membranes are used to separate mixtures of liquids by partial vaporization through the dense membrane, a process called pervaporation [124]. One side is kept at ambient pressures while the other side is under vacuum to increase the driving force, the chemical potential difference. For the vapor-phase operation, these membranes were used as an evaporator under ambient conditions. The chemical potential difference in this case

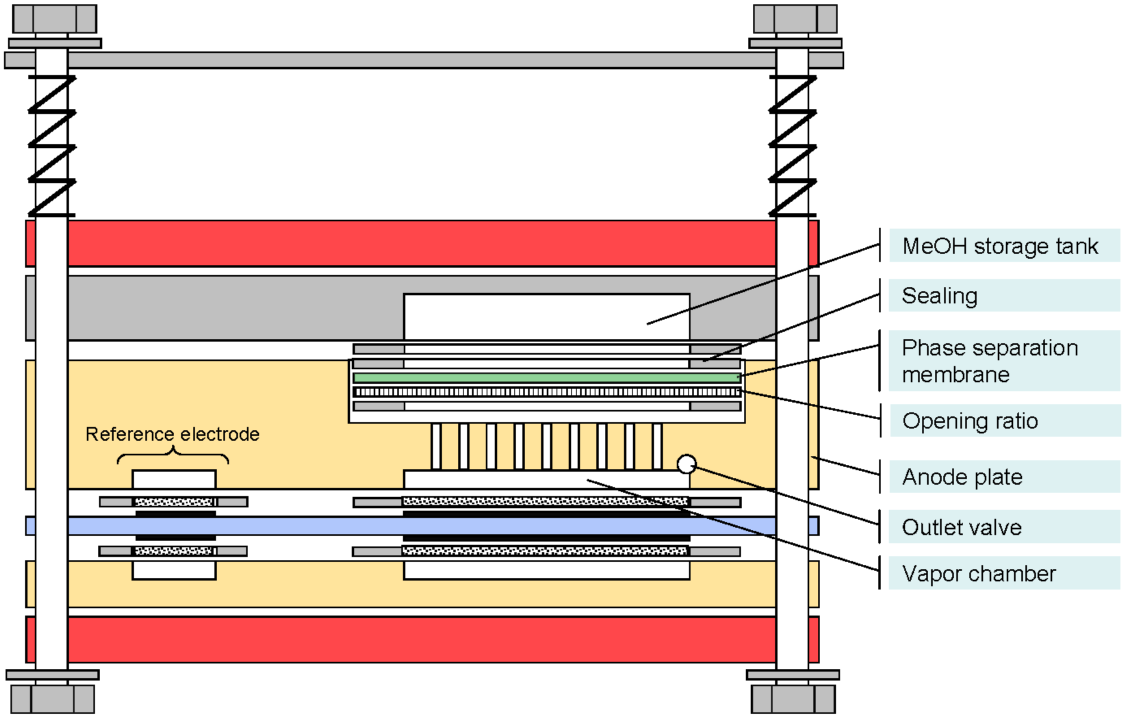

Figure 5.1: Test cell used for experiments with the vapor-fed DMFC. Liquid methanol is stored in the tank and is evaporated into the vapor chamber using the phase separation membrane. The vapor chamber has one outlet to release CO_2 *into the atmosphere.*

was created by consumption of MeOH during the anodic MOR that disturbed the thermodynamic equilibrium and forced MeOH to diffuse from the storage tank into the anode chamber. As experimental data are difficult to gain due to the small volume of the vapor chamber, a one–dimensional model of the evaporator was developed to study gas composition and its transient behavior inside the vapor chamber. Just recently a similar concept has been published by H. Kim [125].

The design of the evaporator and the anode that were used throughout vapor-phase operation experiments is shown in Fig. 5.1. A complete description of the test cell is given in Chapter 3. Liquid MeOH was stored in a temperature–controlled storage tank and a needle valve was used to equalize the pressure between the tank and the surroundings. A plate of FR-4, a material used for making printed circuit boards, was used to change opening ratios. This plate and the phase separation membrane were attached between VITON sealing rings. The anode plate was used to give mechanical strength as well as to collect current. Vaporized MeOH diffused into the anodic vapor chamber and was oxidized at the ACL. Atmospheric pressure was maintained through an outlet, where in particular CO_2 could leave the vapor chamber.

The impact of structural parameters and operating conditions has not been researched yet for vapor-fed operation of a DMFC at near–ambient conditions. Thus a detailed parameter study that included reference cell measurements to assess anode losses and cathode losses separately was performed. Among other parameters, different opening ratios that controlled evaporation of MeOH into the vapor chamber were examined. Experimental results were compared to the evaporator model.

Water management was found to be a critical parameter for a VDMFC. Depletion of water inside the ACL, especially at higher current densities, decreased performance of the fuel cell substantially. Back diffusion of water from the cathode to the anode was examined. A micro–structured cathode electrode that increased water back diffusion due to a reduced mass transfer resistance was developed and investigated. Finally, efficiencies and heat losses of a VDMFC were determined.

5.1 Evaporator

Vapor-phase operation of a DMFC greatly depends on the properties of the evaporator and the vapor chamber. Transient experimental characterization of evaporation is difficult to perform inside a working DMFC, as the fluxes of the reactants, MeOH, water and CO_2, are very small. Thus an approach utilizing a bulk and membrane evaporation model was chosen and parameters were determined by additional experiments. Two different methods were considered, bulk evaporation and evaporation through a dense membrane. Simulation results at equilibrium and pseudo–equilibrium revealed partial pressures of the reactants at steady state as well as transient changes inside the vapor chamber.

5.1.1 Vapor chamber model

This section concerns the evaporation and behavior of MeOH and water vapor in a vapor chamber which is separated from the liquid reservoir by one of two means. These two methods of separation have been labeled “Bulk Evaporation” and “Dense Membrane”.

- **Bulk Evaporation**: This geometry refers to the lack of any physical separation between the liquid reservoir and the vapor chamber, with only a stagnant film present to resist mass transfer [126]. Equilibrium is assumed at the liquid–vapor interface. This model was created as a first example to develop equations of interest. It might be inapplicable to actual applications as the fuel cell system would be highly position–dependent. The variable parameter is the thickness of the stagnant layer.

- **Dense Membrane**: This configuration uses a polymer membrane to separate phases and transport MeOH and water from the liquid reservoir to the vapor chamber. This model assumes that transport through the membrane is the limiting process and that equilibrium between the gas phase and the solvated liquid phase is established at the surface of the membrane. The variable parameter is the permeability of species diffusing through the membrane.

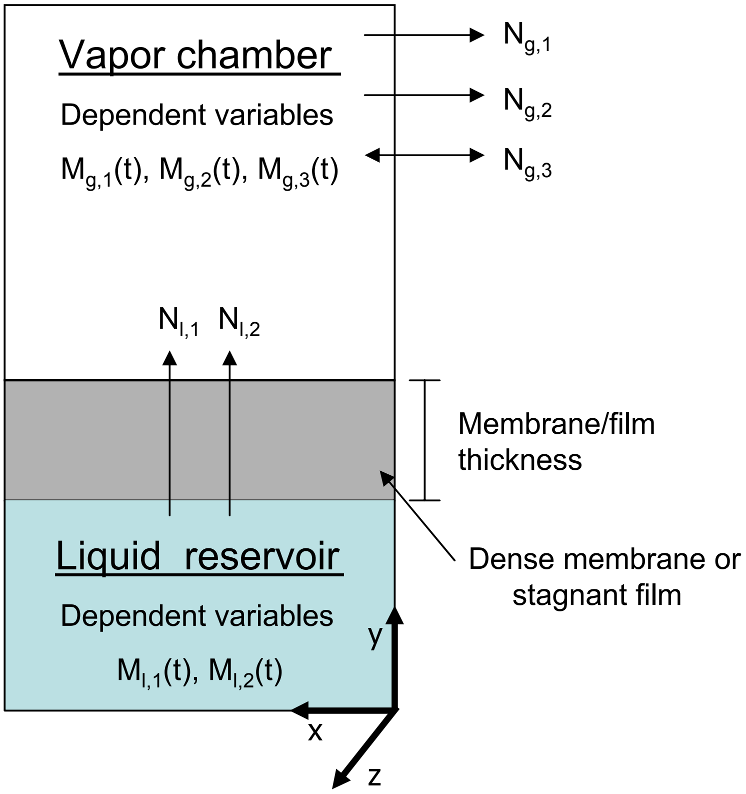

Figure 5.2: Geometry of the one–dimensional evaporator model for bulk evaporation and dense membrane evaporation. Water and MeOH are denoted as species 1 and 2, CO_2 *as species 3.*

Vapor Chamber and Model Geometry

A model of a vapor chamber from which the fuel cell draws MeOH and water vapor by a given current was developed. Because the vapor chamber is the focus of the model, its structure and geometry are important considerations. Fig. 5.2 shows the basic geometry for the model of bulk evaporation and the dense membrane.

The two subdomains considered are the liquid reservoir and the vapor chamber with both the fuel cell and phase boundary represented as two boundaries straddling the vapor chamber. The liquid reservoir has two variables for masses of MeOH and water, while the vapor chamber is characterized by the mass of MeOH and water vapor and CO_2. Finally, both subdomains are considered to be well mixed due to strong intermolecular forces in the liquid phase and turbulence in the gas phase.

In the proposed scheme, MeOH and water are evaporated from the liquid reservoir into the vapor chamber while passing through the vapor–liquid barrier which offers resistance to transport. The fuel cell consumes the MeOH and water vapor while releasing heat into the vapor chamber which is then transported to the liquid reservoir. The fuel cell also releases CO_2 into the vapor chamber with CO_2 leaving or entering to maintain atmospheric pressure within the vapor chamber.

Thermodynamics

While evaporation is a mass transport phenomena, thermodynamics must be considered for at least two reasons: first, thermodynamics defines what is feasible and unfeasible and second, thermodynamics determines the driving force behind evaporation and mass transport. In the proposed system for fuel (MeOH and/or water) delivery, vapor and liquid phases are in equilibrium whenever no current is drawn from the cell. In this equilibrated state, the fugacities of each phase and species are equal and a system of equations describing the equilibrium can be written as a result. The vapor phase fugacity is described as follows.

$$f_g = y_i \gamma_i P \tag{5.1}$$

Here, y_i refers to the vapor mole fraction, γ_i the activity coefficient which is a measure of the interspecies molecular interactions, and P the total system pressure. Since operating pressures for passive VDMFCs should not exceed atmospheric pressure, it is a common and correct simplification to ignore the activity coefficient and to describe the fugacity by the ideal gas law [127]. The liquid phase fugacity is described in a similar fashion.

$$f_l = x_i \gamma_i P_{i,vap} \tag{5.2}$$

Here, x_i refers to the liquid phase mole fraction, γ_i the activity coefficient, and $P_{i,vap}$ the liquid vapor pressure. Unlike the vapor phase, the activity coefficient cannot be ignored in the liquid phase as the intermolecular interactions are much greater than in the low pressure vapor chamber.

To evaluate values for γ_i and $P_{i,vap}$, one can refer to an excess Gibbs energy function and the Antoine equation, respectively. Examples of excess Gibbs energy functions for binary species include the two–suffix Margules, Van Larr, Wilson, and NRTL equations, which can be found in Perry's Chemical Engineering Handbook [128]. In the models presented here, the two–suffix Margules equation was chosen because the parameters were readily available.

$$\ln \gamma_1 = x_2^2 (A_{12} + 2x_1(A_{21} - A_{12})) \tag{5.3}$$

Here $A_{i,j}$ are the species specific parameters for the two–suffix Margules equation, x_1 and x_2 the molar fractions of species 1 and 2. The Antoine equation is the standard equation to relate a liquid's vapor pressure to its temperature.

$$\log P_{vap} = a - \frac{b}{T + c} \tag{5.4}$$

Both of these equations require constants for their usage. Antoine constants can be found in Perry's [128]. The excess Gibbs energy constants require a more specialized reference and will vary based on the species in the system. An excellent reference for these constants is the Dechema Data Series [129].

These thermodynamic expressions are used twice in the following models. First, solving these thermodynamic expressions for a binary system where the temperature and liquid phase compositions are known provides the gas phase composition and pressure. The initial condition for each model is solved using this technique. Second, the driving force is based on these thermodynamic expressions. The driving force represents how far the system is removed from equilibrium and is expressed as the difference between the partial pressures of the liquid and gas phase for a particular species. This driving force Δf is the difference in fugacities between the liquid fugacity of eq. (5.2) and the gas phase fugacity of eq. (5.1).

$$\Delta f = x_i \gamma_i P_{i,vap} - y_i P \tag{5.5}$$

Thus, the maximum driving force for MeOH evaporation is realized when there is no MeOH in the vapor phase ($y_{MeOH} = 0$). Conversely, when in equilibrium, the driving force is zero and no net evaporation occurs.

Kinetics

Although thermodynamics determines what is and is not possible, it is the kinetics of the system which describes the actual rates of evaporation and mass transport. Because it is assumed that the only resistance to mass transport is a stagnant layer or a dense membrane, the definition of mass transfer can be refined to include only diffusion and not convection. Fickian diffusion was used for this model.

$$N_i = D_{i,j} \nabla c_i \tag{5.6}$$

The proportionality constant is often called the diffusivity or diffusion constant $D_{i,j}$ which is the diffusivity of species i through species j. In the bulk evaporation model, diffusion is only considered in the gas phase. As such partial pressures are used instead of concentrations in the gradient term. Further, CO_2 is assumed to make up most of the gas phase, to bring the total pressure inside the vapor chamber to atmospheric pressure. Therefore, a simplifying assumption was to determine the diffusivity of MeOH or water through CO_2 instead of the mixture as a whole. Last, because it was assumed that diffusion only occurs in a very thin stagnant layer, the constant gradient can be replaced by a slope over the thickness of the film where the partial pressure at the liquid interface is subtracted from the partial pressure in the bulk vapor chamber. It is assumed that liquid phase and vapor phase are always in equilibrium at the liquid–vapor interface because the limiting process is diffusion. These assumptions transform eq. (5.6) into

$$N_{l,i} = \frac{D_{i,CO_2}}{RTd_{film}}(x_i\gamma_i P_{i,vap} - y_i P) \tag{5.7}$$

Notice also that the maximum rate of mass transport is controlled by the difference in partial pressures and that a partial pressure of zero in the vapor chamber will yield a finite value. Estimating values for the diffusivity $D_{i,j}$ is a complex procedure in and of itself. There are several available equations available which describe different mixtures of gases. For this thesis, an equation proposed by Brokaw [130] as a correlation to the Chapman–Enskog equation [128] was used. This equation is fitted expressly for combinations of polar gases. The reader is referred to these two sources for further details.

$$N_{l,i} = \frac{Perm_i}{d_{mem}}(x_i\gamma_i P_{i,vap} - y_i P) \tag{5.8}$$

Transport through the dense membrane as stated in eq. (5.8) differs somewhat from bulk evaporation. The so–called solution–diffusion model is accepted by many membrane researchers [131–133]. It is still based on the principle of flux being proportional to the gradient in concentration, or the difference in partial pressures. The distinguishing feature is the replacement of the diffusivity by the permeability, $Perm_i$. $Perm_i$ is a convenient term which encompasses many physical characteristics of the membrane and the transported species. Among others, it includes the degree of solvation of the transported species by the membrane fibers (itself a function of many properties including polarity and size of the transported species and size of the polymer molecule), the drag of one transported species on the other, and the mass transfer resistance of the membrane. Literature is available to estimate this parameter [134, 135]. In the context of this work, these interactions were lumped into the permeability coefficient which was then fit to experimental data.

Balances

The last portion of the vapor chamber models are the mass and heat balances. Since MeOH and water exist in both the vapor chamber and the liquid reservoir, there must be four different balances to account for these two species. In addition, CO_2 requires another balance for just the gas phase. All balances observe the conservation of mass. Expressed in terms of known and differential variables, the balance for the liquid phase is given as:

$$\frac{\delta M_{i,l}}{\delta t} = -N_{i,l} \cdot M_{i,amu} \cdot A \tag{5.9}$$

For the gas phase, the balance is given as:

$$\frac{\delta M_{i,l}}{\delta t} = (N_{i,l} - N_{i,g}) \cdot M_{i,amu} \cdot A \tag{5.10}$$

Here A is the total area and $M_{i,amu}$ the molar mass of species i. The CO_2 balance is expressed as no change in the total pressure of the gas phase. That is, CO_2 is allowed to enter or leave as long as the pressure remains at atmospheric pressure.

$$\frac{\delta P}{\delta t} = 0 \tag{5.11}$$

The gas phase flux variable, $N_{i,g}$, is considered to be constant and set by the total current of the fuel cell, itself a constant.

5.1.2 Membrane parameters

Both phase separation boundaries have a single fitting parameter. For the dense membrane and bulk evaporation this parameter is the permeability and stagnant film thickness, respectively. Both of these parameters were calibrated against experimental evidence in two similar experiments.

Dense membrane:
The experimental setup for the dense membrane positioned the dense membrane between the liquid reservoir and the open atmosphere with a silicone sealant to maintain a liquid–impermeable connection between the membrane and the apparatus. Once the liquid reservoir was filled with pure MeOH and the membrane attached, the apparatus was flipped to maintain hydrodynamic pressure on the membrane. The convective airflow in the vapor chamber again assured a MeOH

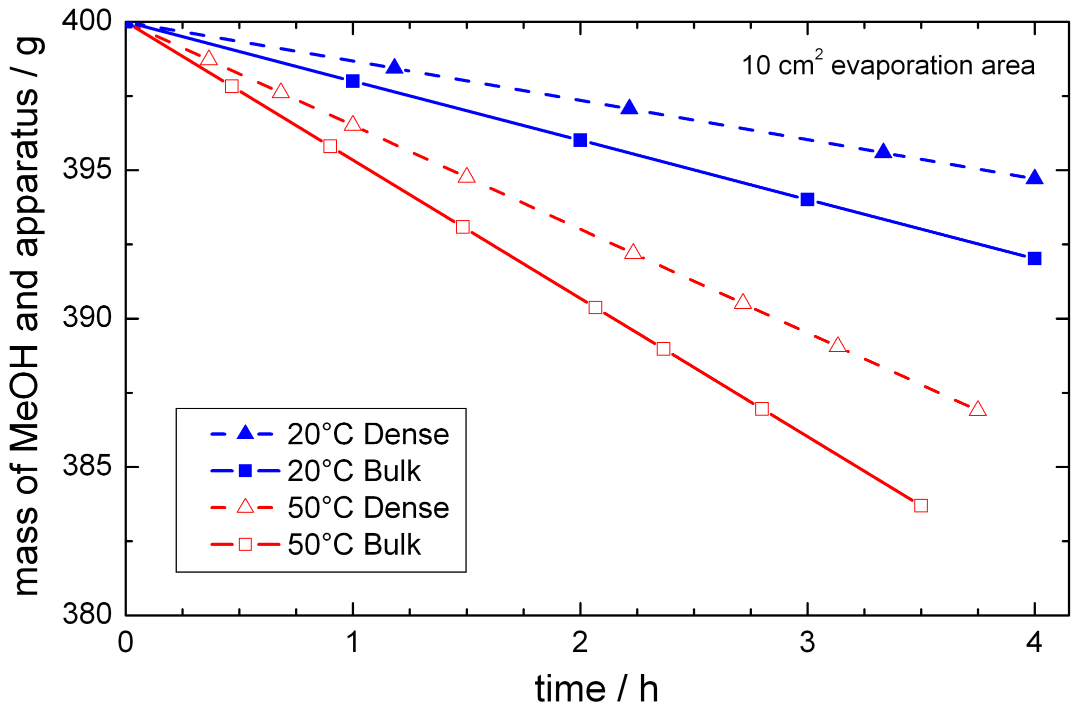

Figure 5.3: Measurements of the change in mass for bulk evaporation and dense membrane evaporation as a MeOH vapor delivery system at different temperatures.

partial pressure of approximately zero during the experiment and thus provided the maximum driving force for evaporation. The results from this experiment can be seen in Fig. 5.3 as well. During the first two hours the rate of evaporation is highest before it slows down to a constant rate. This effect might be the result of swelling within the membrane during the first two hours. After two hours, the rate of evaporation slows to a steady state value. A linear curve fit, neglecting the first two hours, identified the gradient and thus the permeability of the membrane could be calculated.

Bulk Evaporation:
The experiment for bulk evaporation was similar in concept to that for the dense membrane. However, without a real vapor-liquid separation membrane, this experiment simply allowed MeOH to evaporate out of a receptacle while the mass was recorded as a function of time. Convective airflow within the climate chamber maintained a MeOH partial pressure of approximately zero maximizing the evaporative driving force. The results from this experiment can be seen in Fig. 5.3. Linear–curve fitting identified the gradient and thus the thickness of the stagnant film assumed in the model could be determined.

The rate of evaporation for the bulk case is roughly $50\,\%$ higher than for the dense membrane which intuitively makes sense. Bulk evaporation offers a larger vapor–liquid interface than a dense membrane where liquid MeOH molecules must share space with the membrane fibers.

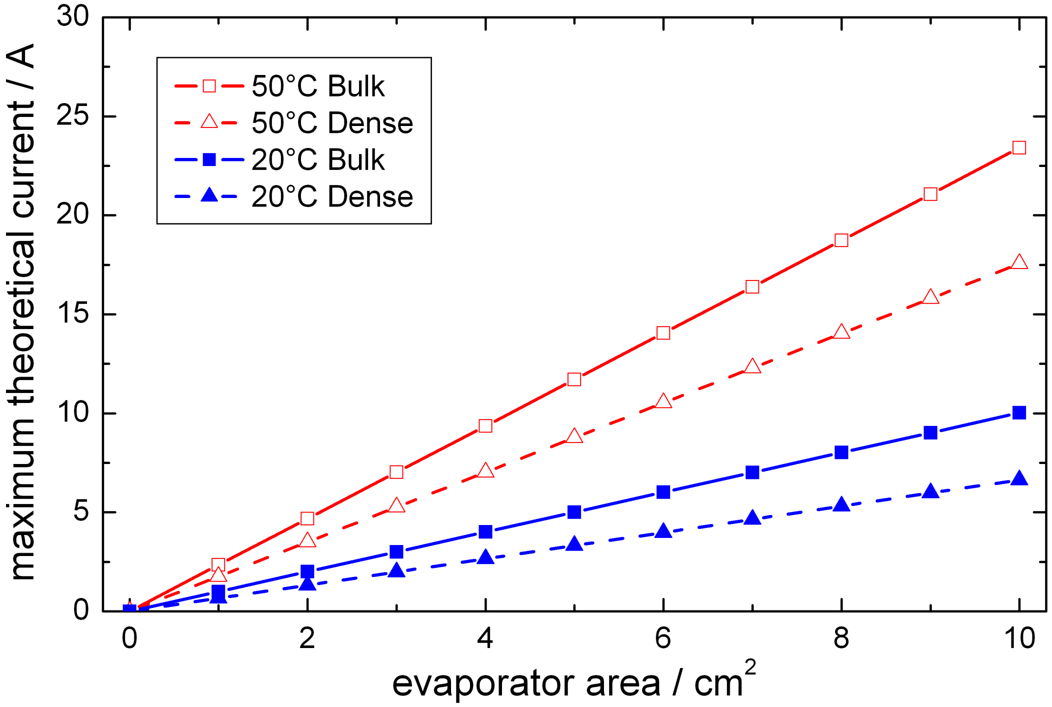

Figure 5.4: Maximum theoretical current densities at different temperatures and evaporator ares that could be achieved. Model parameters for the evaporation rate are derived from Fig. 5.3.

To gain an engineering perspective on the potential of both methods of MeOH evaporation, Fig. 5.4 shows theoretical currents according to MOR. This figure uses the maximum evaporative rate determined from Fig. 5.3 and converts that flux to a current using Faraday's law. This calculation makes no consideration of losses caused by MeOH crossover and assumes that every evaporated MeOH molecule is immediately converted to electric current. However, this graph is useful to find a rough dimensioning estimate for a fuel cell of known performance. At a working point of the fuel cell of $200\,\mathrm{mV}$ at $50\ ^{\circ}\mathrm{C}$ and a power density of $50\,\mathrm{mW/cm^2}$, the area of the evaporator is $1/8$ for the dense membrane and $1/10$ for bulk evaporation compared to the the active area of the fuel cell.

5.1.3 Vapor chamber in equilibrium

The establishment of vapor–liquid equilibrium (VLE) is important because evaporation is simply a system moving toward VLE. In all cases, equilibrium between vapor and liquid phases was assumed at the boundary between liquid reservoir and vapor chamber. The system in question is a binary mixture of water and MeOH. For such binary systems, it is convenient to express equilibrium in an x-y diagram, which is shown in Fig. 5.5 for the MeOH/water binary system.

The x and y axes show the mole fraction of MeOH in the liquid and gas phases respectively. The curve reflects the actual behavior of the two components and matches very closely to the

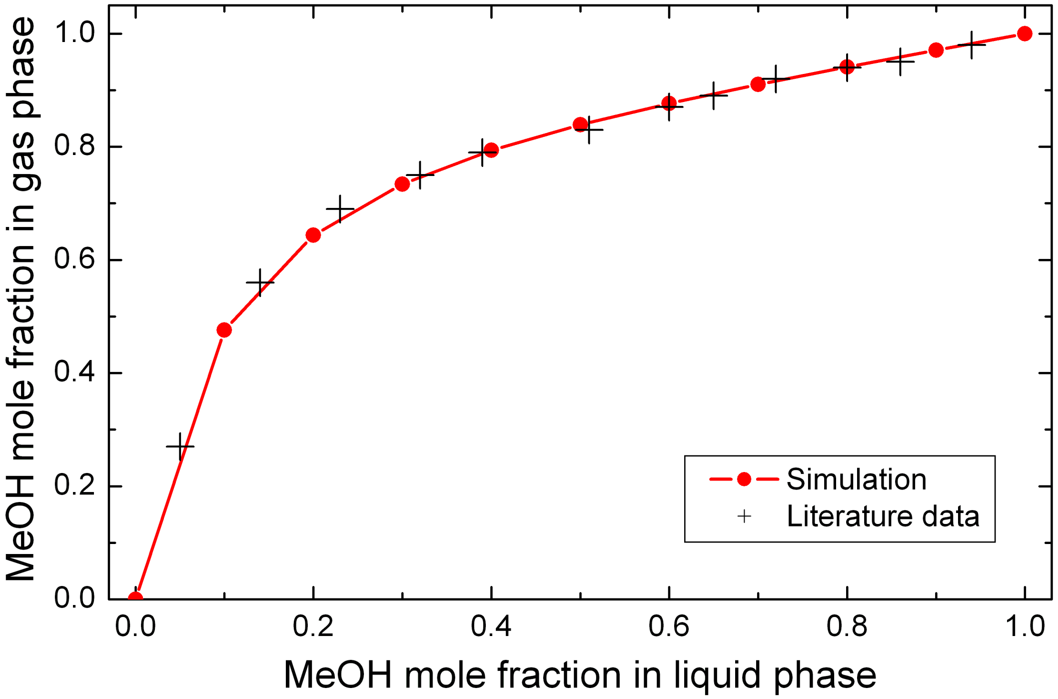

Figure 5.5: Vapor–liquid equilibrium for a MeOH/water system at 50 °C and different molar fractions. Interactions between the two species are taken into account according to eq. (5.5) and compared to [129].

literature data provided in [129]. The curve represents vapor–liquid equilibrium when factors such as different vapor pressures and intermolecular interactions are taken into account.

5.1.4 Vapor chamber in pseudo–equilibrium

The system only reaches equilibrium when the fuel cell is not drawing MeOH and water from the vapor chamber for reaction. As soon as the fuel cell begins consuming these reactants, the equilibrium is disrupted and the concentration of MeOH and water in the vapor chamber decreases until a new pseudo–equilibrium is established. The establishment of the new pseudo–equilibrium for $50\,\mathrm{wt\%}$ of MeOH and water at $50\,^{\circ}\mathrm{C}$ can be observed in Fig. 5.6 after approximately $30\,\mathrm{s}$.

The system starts at equilibrium. At time zero, the fuel cell begins drawing enough MeOH and water to run at $0.75\,\mathrm{A/cm^2}$ (assuming that the active area of the active fuel cell area is 10-times larger than the evaporative area). As the fuel cell draws off MeOH and water, the concentration in the gas phase decreases until a new steady state is reached, the pseudo–equilibrium. At this point, the flux of MeOH and water into the fuel cell is equal to the rate that it is being replenished by evaporation from the liquid reservoir.

As already stated, evaporation is proportional to $(x_i \gamma_i P_{i,vap} - P_i)$. When the system is in equilibrium, the rate of evaporation is zero and thus $x_i \gamma_i P_{i,vap} = P_i$. However, to make the rate of

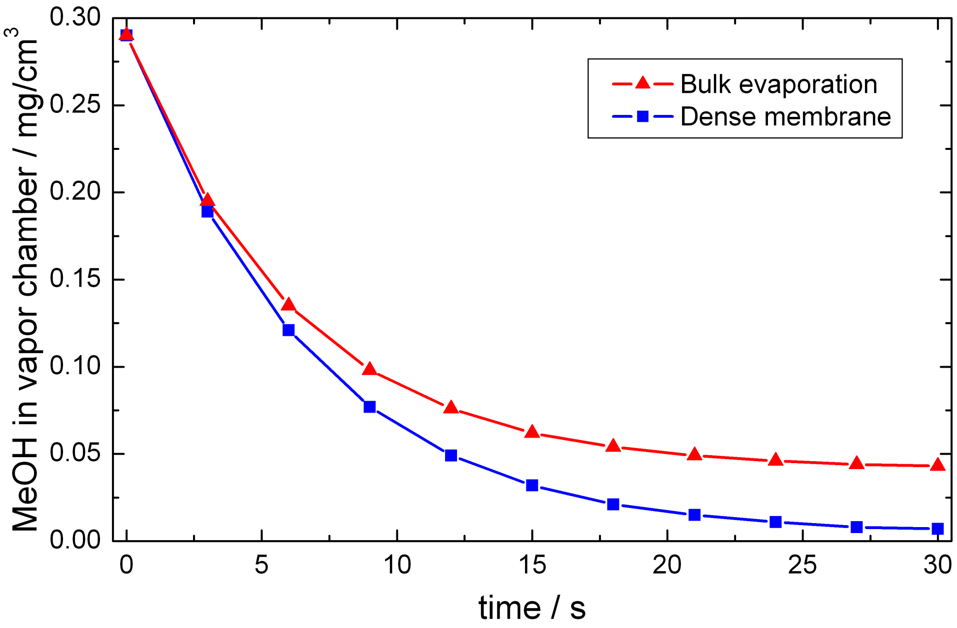

Figure 5.6: Simulation results of the establishment of pseudo–equilibrium over time when a cell current density of $0.75\,A/cm^2$ *was drawn from the fuel cell. A constant liquid phase composition of* $50\,wt\%$ *MeOH and* $50\,wt\%$ *water at* $50\,°C$ *is assumed. The active fuel cell area was 10-times larger than the evaporation area.*

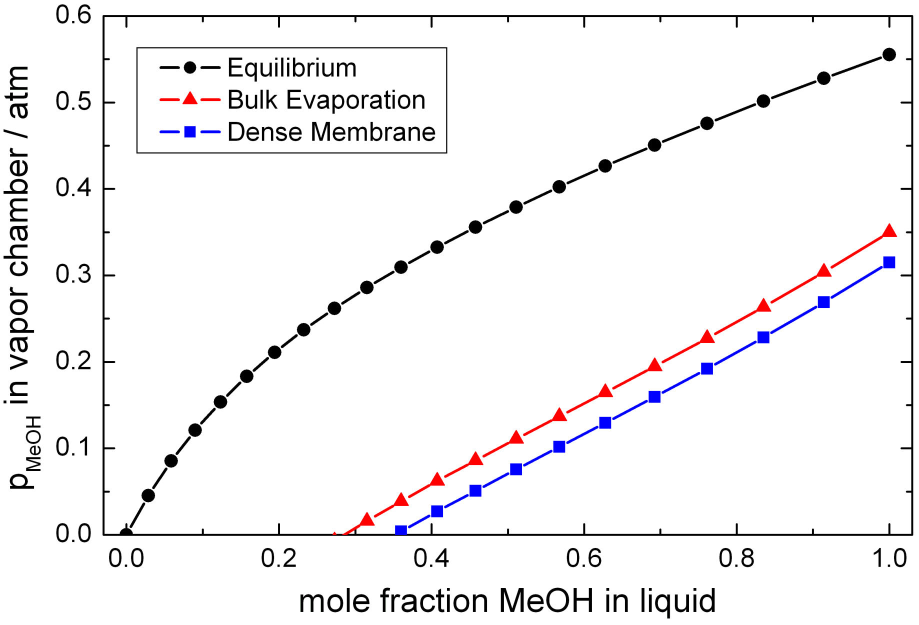

Figure 5.7: Model results of equilibrium and pseudo–equilibrium for bulk evaporation and dense membrane evaporation at different MeOH mole fractions when a cell current density of $0.75\,A/cm^2$ *was drawn from the fuel cell. The active fuel cell area was 10-times larger than the evaporation area.*

evaporation non–zero, the condition $x_i \gamma_i P_{i,vap} > P_i$ must be fulfilled. Hence, the partial pressure in the vapor chamber falls until the condition of pseudo–equilibrium, consumption equals evaporation, is met. How much the partial pressure must fall before pseudo–equilibrium has been established is a function of the diffusivity, permeability, and thickness of the phase separation boundary where systems that do not offer much resistance to mass transfer have minimal offsets from equilibrium and vice versa.

To find the pseudo–equilibrium for a variety of liquid phase conditions, Fig. 5.7 may be used. The x-axis is the mole fraction of MeOH in the liquid reservoir which covers all potential binary combinations of water and MeOH. The lines labeled "bulk evaporation" and "dense membrane" show pseudo–equilibrium values. If a pseudo–equilibrium value is zero, the rate of evaporation is not able to keep up with the rate of consumption. In all cases, $0.75\,\mathrm{A/cm^2}$ and an area that was 10-times larger for the fuel cell as for the evaporator was assumed.

Also noteworthy in both Fig. 5.6 and Fig. 5.7 is that the performance of the dense membrane and the bulk evaporation are similar. This is the result of an identical thermodynamic driving force which motivates evaporation.

5.2 Parameter study

The impact of operating conditions and structural parameters on the performance as well as on polarization and concentration losses of a VDMFC was studied. The connected NHE was used to assess losses individually. A PDMS membrane at an opening ratio of $6.8\,\%$ was used to evaporate a $50\,\mathrm{wt\%}$ solution of MeOH in deionized water into the vapor chamber. Dry air was supplied to the cathode flow channel. A minimum air flow rate of $40\,\mathrm{sccm}$ was set before switching to a stoichiometry of 2 at a current density of $0.11\,\mathrm{A/cm^2}$. Hydrogen, which was humidified inside a washing bottle at ambient conditions, was fed to one electrode of the NHE. The other electrode of the NHE was flooded with deionized water to guarantee a stable reference potential as mentioned in Appendix A. The temperature of the cell was kept constant at $50\,°\mathrm{C}$. A SIGRACET® 31AA GDL was used on both the anode and the cathode side. For the CCM, Nafion® 1135 being screenprinted with $3\,\mathrm{mg/cm^2}$ Pt/Ru at the anode and $1\,\mathrm{mg/cm^2}$ Pt at the cathode was used. The clamping force on the cell was set to $3450\,\mathrm{N}$, which results in a pressure of $345\,\mathrm{kPa}$ on the GDL. These standard conditions were applied unless stated otherwise in the text.

5.2.1 Structural parameters of the MEA

The influence of two different membrane thicknesses and catalyst loadings on the electric properties of the VDMFC were studied. Besides the commonly used Nafion® 117, which had a high Pt/Ru catalyst loading of $3\,\mathrm{mg/cm^2}$ at the anode electrode for this work and provided low crossover at sufficiently high current densities, thinner Nafion® 1135 and low anode loadings of $1\,\mathrm{mg/cm^2}$ were also studied.

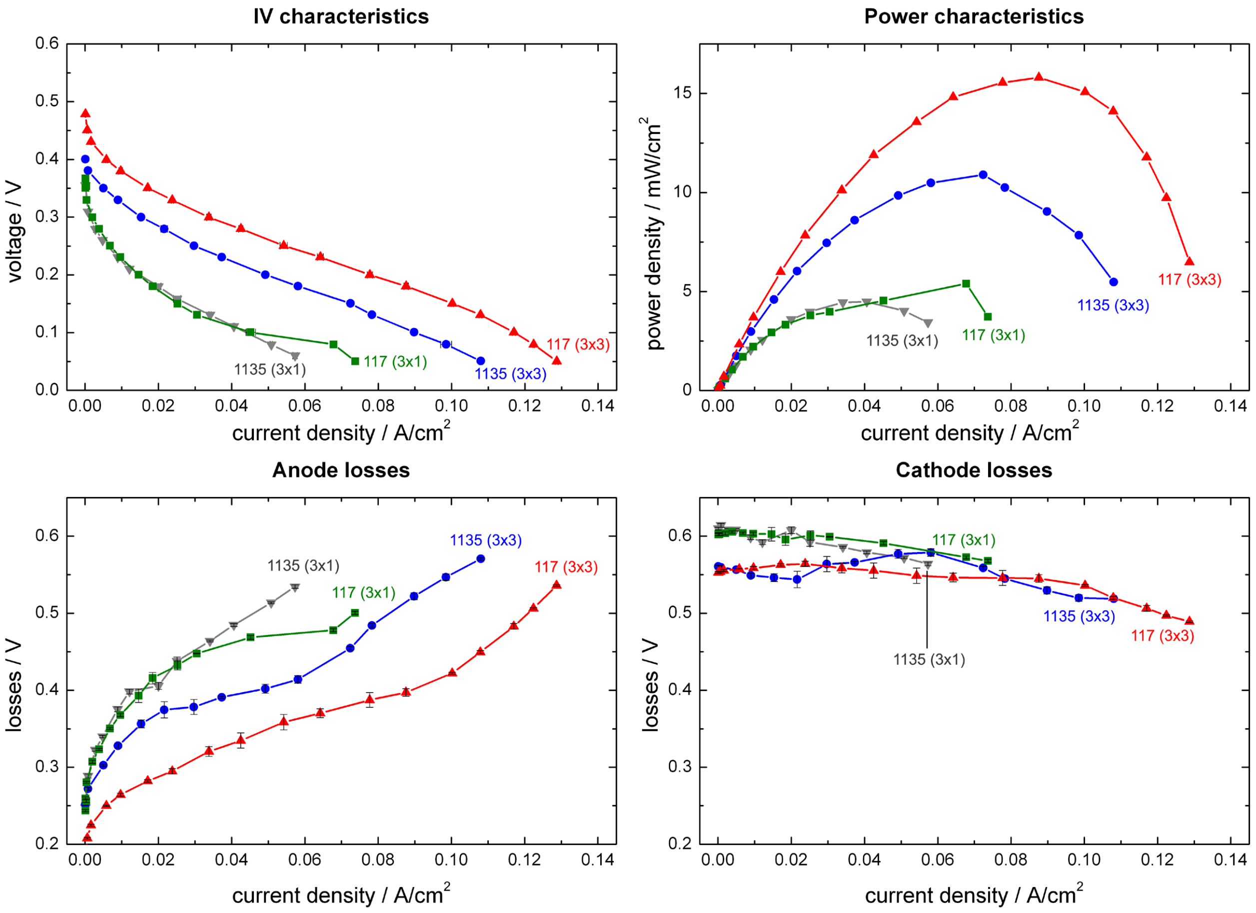

Figure 5.8: Electric properties of a VDMFC for different membranes and catalyst loadings. Anode and cathode polarization losses were calculated using a connected reference NHE. The temperature was 50 °C, the cathode air stream 40 sccm/λ 6, the evaporator opening ratio 6.8 % and MeOH concentration 75 wt%.

The following CCMs were investigated:

- Nafion® 117 screen–printed 3 times using HiSPEC 11100 at the cathode electrode (equal to 1 mg/cm^2 Pt) and 3 times using HiSPEC 6000 at the anode electrode (equal to 3 mg/cm^2 Pt/Ru)
- Nafion® 117 screen–printed 3 times using HiSPEC 11100 at the cathode electrode (equal to 1 mg/cm^2 Pt) and once using HiSPEC 6000 at the anode electrode (equal to 1 mg/cm^2 Pt/Ru)
- Nafion® 1135 screen–printed 3 times using HiSPEC 11100 at the cathode electrode (equal to 1 mg/cm^2 Pt) and 3 times using HiSPEC 6000 at the anode electrode (equal to 3 mg/cm^2 Pt/Ru)
- Nafion® 1135 screen–printed 3 times using HiSPEC 11100 at the cathode electrode (equal to 1 mg/cm^2 Pt) and once using HiSPEC 6000 at the anode electrode (equal to 1 mg/cm^2 Pt/Ru)

Results of this characterization can be found in Fig. 5.8. It is obvious that the CCMs having a high anode catalyst loading outperformed the others. It can also be observed that Nafion® 117 had a slightly better performance compared to the thinner Nafion® 1135. Looking at the individual electrode polarization losses, it is interesting to note that the thickness of the membrane did not seem to affect cathode losses, which reflected MeOH crossover among other effects. This is especially obvious at OCV, when no MeOH was consumed and the electroosmotic drag vanished. The catalyst loading at the anode had a much higher impact on the crossover as the thicker anode electrode offered a higher mass transfer resistance to the MeOH. Besides these effects, better anode performance at high catalyst loadings is displayed.

The different IV characteristics between the two membranes were caused on the anode side. Nafion® 117 displayed lower anode losses. This is surprising as back diffusion of product water from the cathode, which greatly influences anode performance as will be shown later, should be higher at thinner membranes. Apparently water transport was enhanced by Nafion® 117, especially at higher current densities.

5.2.2 Methanol Concentration

Experiments with different MeOH solutions in deionized water at 25, 50 and $75\,\mathrm{wt\%}$ and pure MeOH were conducted to study the impact of MeOH concentration on a VDMFC. All other operational and structural parameters were kept constant.

The IV characteristics and the electrode losses are depicted in Fig. 5.9. It should be mentioned that these results are valid only for an opening ratio of the evaporator of $6.8\,\%$ and will change when the opening ratio is varied. Optimal performance for the given conditions was achieved by having a $50\,\mathrm{wt\%}$ solution of MeOH; it decreased for higher and lower concentrations. Two opposing effects could be studied on the anode and the cathode. Crossover increased with MeOH concentration and consequently cathode losses increased as shown. The great difference between pure MeOH and the three solutions indicated a much higher crossover, probably combined with partial flooding of the cathode.

Anode losses decreased as expected with increasing MeOH concentration. Besides having higher partial pressures of MeOH at the anode electrode, resulting in higher anodic current densities according to eq. (2.20), the water concentration at the anode also greatly influenced the electrode losses. In the **Evaporator** section of this chapter, it was shown that the amount of evaporated water is only a fraction of the evaporated MeOH, depending on the MeOH concentration. Because one mole of water is needed to oxidize one mole of MeOH, the lack of water is slowing down the MOR.

As already mentioned, high MeOH concentrations result in a high crossover rate. Usually most of this cathodic MeOH is oxidized to $\mathrm{CO_2}$ and water. Thus, the water concentration at the cathode increases with crossover and back diffusion of water to the anode is enforced because of a large concentration gradient between the anode and the cathode. This assumption is validated by the

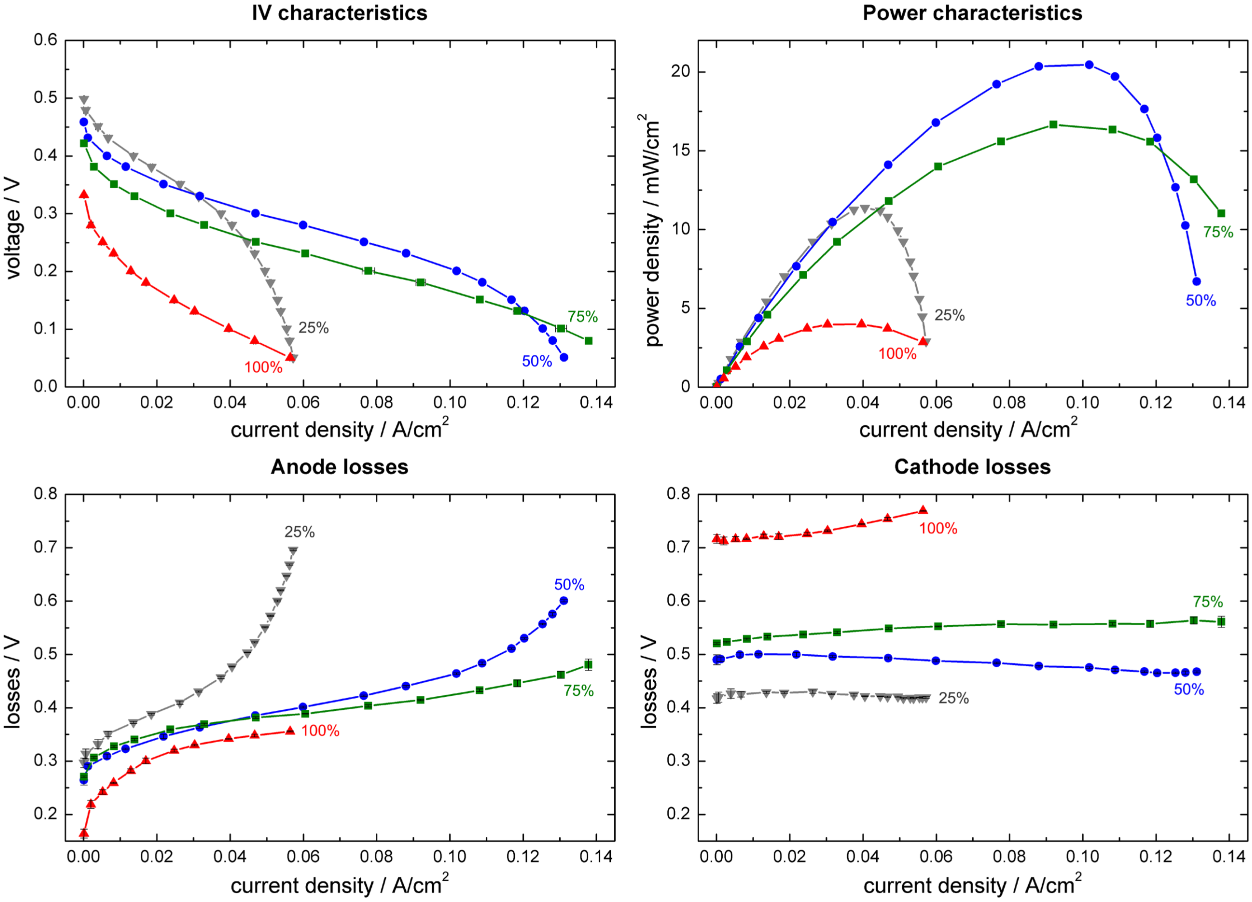

Figure 5.9: Electric properties of a VDMFC for different MeOH concentrations. Anode and cathode polarization losses were calculated using a connected reference NHE. The temperature was 50 °C, the cathode air stream 40 sccm/λ 2 and the evaporator opening ratio 6.8 %.

electrode losses of pure MeOH, where high cathode losses indicate high crossover and thus high water concentration that hinders oxygen access to the CCL. The anode electrode for pure MeOH performed slightly better than at 50 wt% and 75 wt% and much better than at 25 wt%.

This conclusion was supported by examining the ohmic high frequency resistances at 1 kHz for all cases, as shown in Fig. 5.10. The membrane resistance is a major part of the overall ohmic resistance, which therefore strongly correlates with the water content of the membrane. The ohmic resistance decreases with increasing water saturation of the ionomer [90] and thus reveals information about the humidification of the membrane. It can be noted that for a 25 wt% solution of MeOH, the resistance was much higher than for pure MeOH. This clearly indicated less water saturation inside the ionomer at lower MeOH concentrations due to lower crossover. Therefore the water concentration at the cathode and back diffusion of water to the anode was reduced as well. Effects of these mass transport problems could be seen in the anode losses. For pure methanol, the membrane resistance was only slightly smaller than for 75 wt%, and it can be concluded that

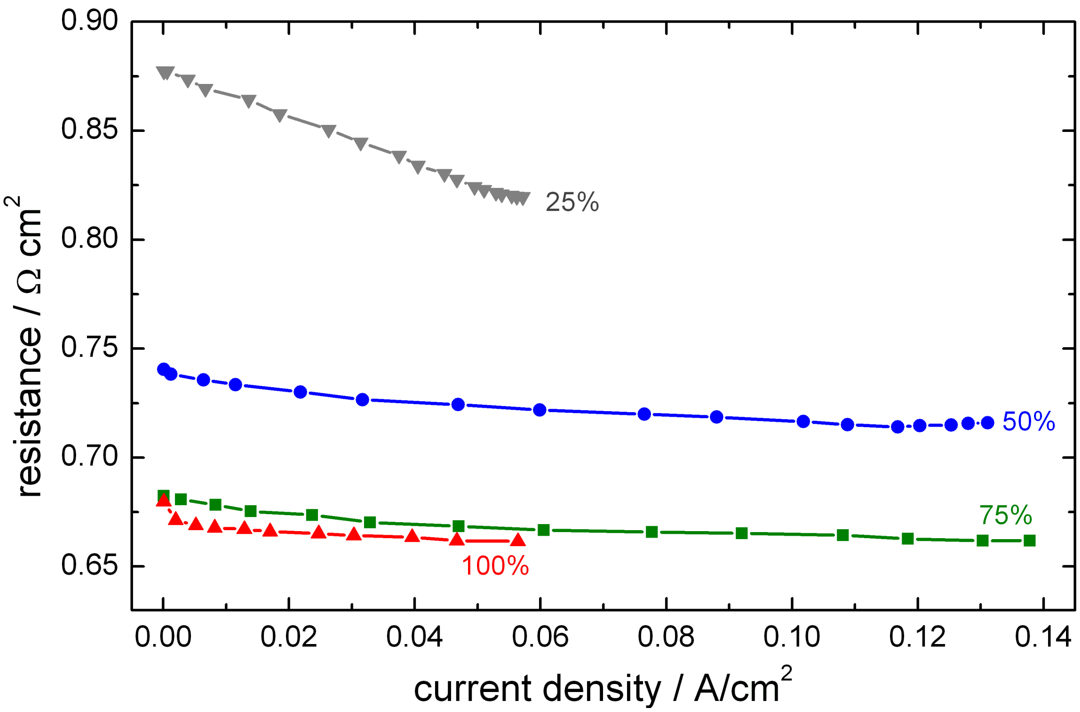

Figure 5.10: Ohmic resistance of the VDMFC versus current density. The temperature was 50 °C, the cathode air stream 40 sccm/λ 2 and the evaporator opening ratio 6.8 %. The MeOH concentration in the storage tank was varied.

product water at the cathode was no longer uptaken significantly by the ionomer. Thus flooding at the cathode, reflected by high cathode losses, occurred and water back diffusion to the anode increased, lowering the anode losses.

5.2.3 Cathode stoichiometry

The cathode flow rate was varied during this parameter study. Air was forced through the cathode flowfield at stoichiometries of 2, 4 and 6.

Results of this study can be seen in Fig. 5.11. A sharp drop at higher current densities indicating high concentration losses was found in the IV plots for all stoichiometries. Surprisingly the performance of the VDMFC declines with increasing air flow rate. For LDMFCs, the performance increases when the cathode stoichiometry is increased, which is described in Chapter 4. Here flooding can be prevented at higher stoichiometries and the impact of the parasitic MeOH oxidation at the cathode electrode can be reduced because of higher oxygen partial pressures. Lower cathode losses at higher flow rates were also found for the VDMFC, having the same cause as in the liquid-fed case.

The reason for the sharp drop in the IV curve could be found at the anode electrode. The maximum current density decreased from $130\,\mathrm{mA/cm^2}$ at an air stoichiometry of 2 to only $60\,\mathrm{mA/cm^2}$ at

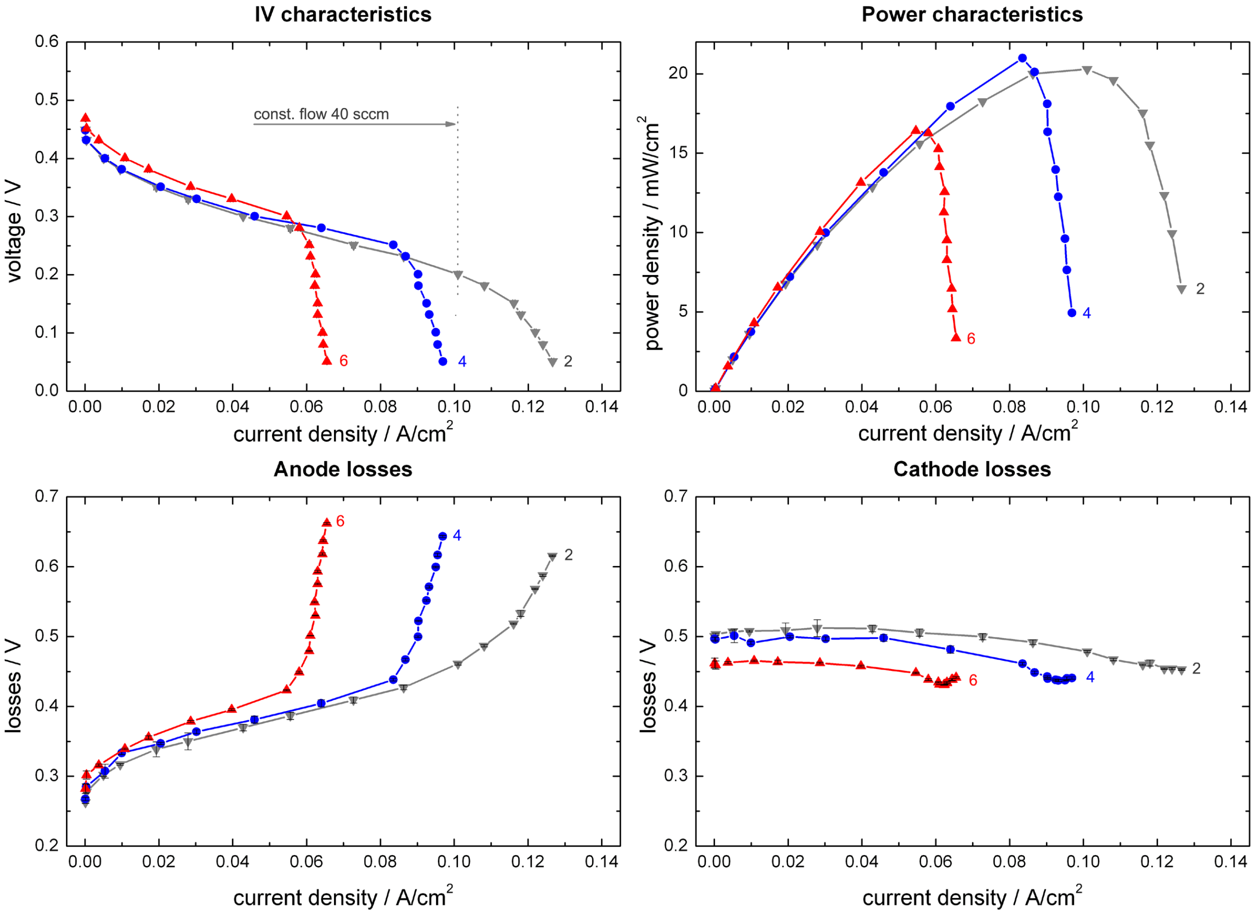

Figure 5.11: Electric properties of a VDMFC for different cathode air stoichiometries. Anode and cathode polarization losses were calculated using a connected reference NHE. The temperature was 50 °C, the cathode air stream 40 sccm/λ 2 and the evaporator opening ratio 6.8 %.

an air stoichiometry of 6. The sharp drop of the anode losses further implied limited access to one of the reactants of the MOR. As the evaporator of MeOH was not changed in this series of experiments the water concentration within the anode and thus the limiting current densities were changed at different stoichiometries. At lower cathode flow rates, less product water could be transported away from the cathode. The concentration gradient between the cathode and the anode increased as most water molecules at the anode were consumed during the MOR. Thus, back diffusion of water to the anode increased at lower stoichiometries.

5.2.4 Phase–separation membrane

In the given set–up, a phase–separation membrane guaranteed that no liquid MeOH had access to the anode electrode and that the evaporation rate of MeOH was high enough to enable stable operation of the VDMFC. Two different concepts were investigated: a dense membrane where

MeOH molecules were transported in the matrix of the membrane and a porous membrane with a highly hydrophobic surface and/or very small pore sizes that could not be wetted by MeOH. MeOH was held back in the pores by capillary forces.

Two different dense membranes were evaluated:

- PDMS on a porous polyacryl nitrile substrate
- Nafion® 115

For the $125 – 250\,\mu\mathrm{m}$ thick porous membranes, a specially treated polymer from Pall[1] that is highly hydrophobic was investigated along with $1\,\mathrm{mm}$ thick porous ceramics:

- Pall Versapor R $900\,\mathrm{nm}$
- $\mathrm{TiO_2}$ $5\,\mathrm{nm}$ on an α-$\mathrm{Al_2O_3}$ support
- NF (Nanofiltration membrane, $\mathrm{ZrO_2}$ $3\,\mathrm{nm}$ on an α-$\mathrm{Al_2O_3}$ support, hydrophobized)
- $\mathrm{TiO_2}$ $0.9\,\mathrm{nm}$ on an α-$\mathrm{Al_2O_3}$ support

The characterization of these materials can be seen in Fig. 5.12, with graphs for porous membranes on the left and for dense membranes on the right side of the figure. The use of the porous Versapor membrane and the $5\,\mathrm{nm}$ ceramic as evaporators led to the lowest anode losses and highest cathode losses. Parasitic oxidation of crossover MeOH at the cathode and flooding of the cathode electrode increased cathode losses. Especially the Versapor membrane with its 100-times greater pore size caused high MeOH crossover and probably severe flooding of the cathode electrode with water. Conversely, with increasing water concentration at the cathode, the back diffusion of water to the anode was enforced and anode losses were decreased.

Cathode losses of the NF ceramic were practically the same as for the $5\,\mathrm{nm}$ $\mathrm{TiO_2}$. Thus back diffusion of water to the anode should be the same. Conversly, high anode losses suggested increased concentration losses because of the ceramic's hydrophobized structure. $\mathrm{TiO_2}$ with a pore size of $0.9\,\mathrm{nm}$ caused the lowest cathode losses for the porous membranes. High anode losses at the same time caused by the limited supply of MeOH and water to the anode led to poor performance for given operating and structural parameters.

One problem in handling porous membranes is their tendency to leak, especially when clamping forces or the hydraulic pressure of MeOH on the membrane are high. The uptake of water for Nafion® is higher if the ionomer has access to liquid instead of gaseous water, known as Schroeder's Paradox [136, 137]. Therefore MeOH crossover across the membrane increases. High cathode losses, in particular for the Versapor membrane, indicated liquid MeOH and water at the anode electrode.

---

[1] http://www.pall.com/

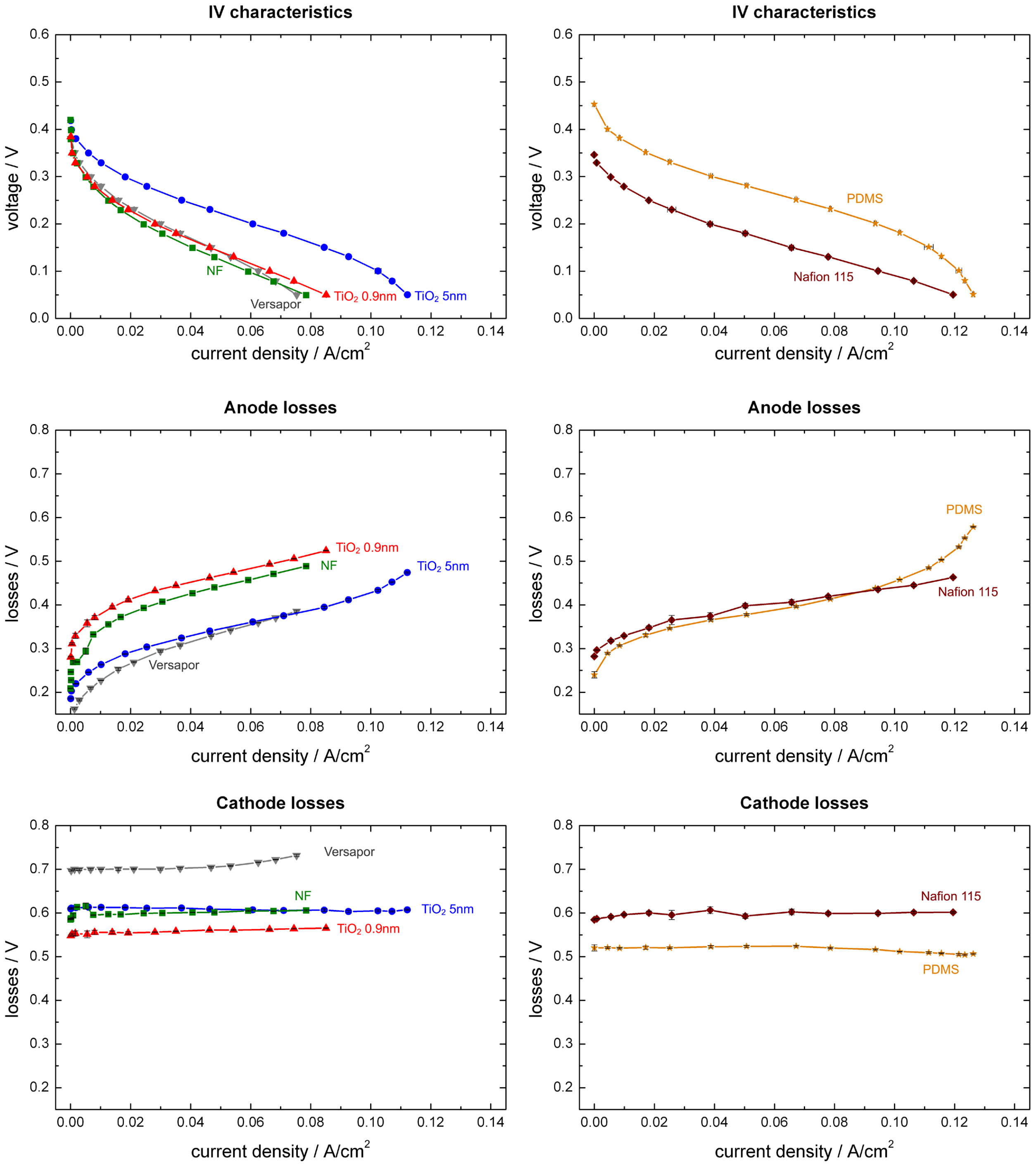

Figure 5.12: Electric properties of a VDMFC for different phase–separation membranes. Anode and cathode losses were calculated using a connected reference NHE. The temperature was 50 °C, the cathode air stream 40 sccm/λ 2 and the evaporator opening ratio 6.8 %. Porous membranes are depicted on the left side, dense membranes on the right side of the figure.

Leakage of liquid MeOH can be avoided if dense membranes are used. Chemical affinity between molecules of the liquid and the membrane cause sorption and solution of water and MeOH in the matrix of membrane. Desorption on the permeate side takes place in the vapor phase. The driving force between the liquid and gaseous sides is a difference of the fugacities, often expressed as chemical potentials. This separation technology is also known as pervaporation [124]. Transport and evaporation at dense membranes is studied in detail in the **Evaporator** section.

It can be observed in the IV plot of Fig. 5.12 that in particular the PDMS membrane exhibited better performance compared to the porous membranes. Nafion® 115 and the PDMS polymer as phase separation membranes lead to similar anode losses of the VDMFC. For the PDMS membrane, anode losses dominate close to the limiting current density, a phenomenon which did not appear for Nafion® 115. Cathode losses when using Nafion® 115 as an evaporator were $80\,\mathrm{mV}$ larger than for PDMS. Consequently the flux of MeOH to the cathode was elevated and more water was produced at the cathode. Increased water back diffusion for Nafion® 115 could cope with the demand of water for the MOR, whereas the PDMS membrane displayed significant concentration losses.

Comparing the porous $5\,\mathrm{nm}$ ceramic and the Versapor to the two dense membranes, anode losses close to OCV were higher for the dense membranes and equalized at $100\,\mathrm{mA/cm^2}$. It seemed very likely that for the dense membranes at high cell voltages, the water concentration at the anode was lower and reduced the kinetics of the MOR. This conclusion agrees well with the educated guess that the $5\,\mathrm{nm}$ ceramic and the Versapor membrane would tend to leak.

5.2.5 Temperature

The large thermal masses of the test cell that could be thermostatted externally allowed isothermal operation of the VDMFC. The impact of temperature was studied at 30, 50 and $70\,^\circ\mathrm{C}$ and results are shown in Fig. 5.13. In Chapter 4, it was shown that the performance of LDMFCs increases with temperature. For the VDMFC, the performance increases significantly between $30\,^\circ\mathrm{C}$ and $50\,^\circ\mathrm{C}$ and then stays stable, reaching an MPP of $20\,\mathrm{mW/cm^2}$, whereas the limiting current density increases further. The cause therefore can again be found at the cathode electrode. Higher temperatures facilitate crossover, which was also found for liquid-fed DMFCs, and thus yield increased cathode losses. Conversely, higher crossover increases water production at the cathode and back diffusion of water to the anode electrode is enhanced.

Temperature influenced several effects on the anode side that can be noticed in the anode losses. First, more MeOH was evaporated from the liquid reservoir at higher temperatures, as was determined in the **Evaporator** section of this chapter. The partial pressure of MeOH at the anode increased, causing a higher current production. Second, MeOH oxidation is a highly temperature–dependent reaction, especially in the given temperature range. This was also demonstrated in Chapter 4 for diluted MeOH in LDMFCs. Here, the anode losses were significantly decreased going from $30\,^\circ\mathrm{C}$ to $50\,^\circ\mathrm{C}$ so that the limiting current density could be doubled. This effect holds

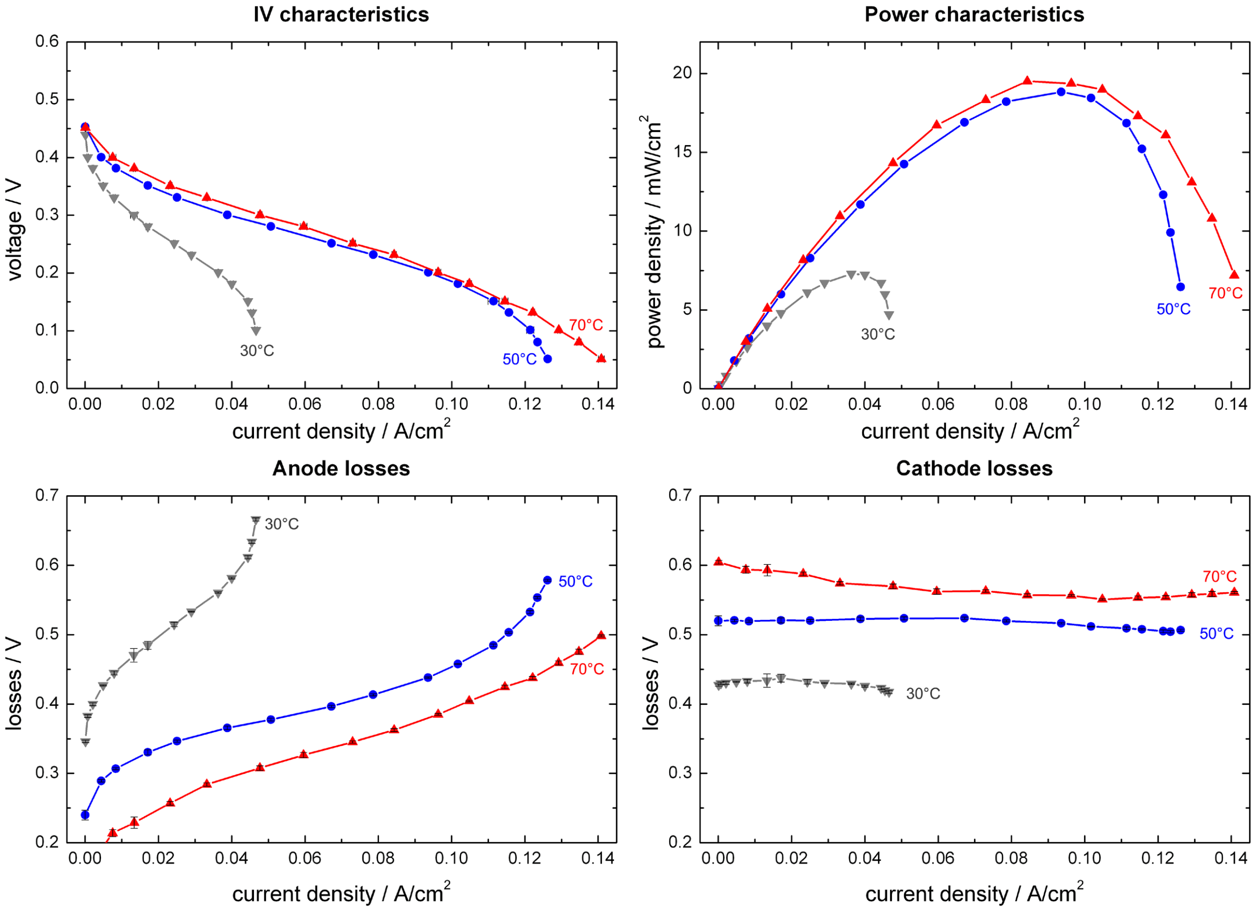

Figure 5.13: Electric properties of a VDMFC for different temperatures. Anode and cathode polarization losses were calculated using a connected reference NHE. The temperature was 50 °C, the cathode air stream 40 sccm/λ 2 and the evaporator opening ratio 6.8 %.

true for the VDMFC as well and the limiting current density could be tripled. Third higher back diffusion of water from the cathode improves the kinetics of the MOR. This is apparent at 30 °C and 50 °C where a steep rise of the anode losses close to limiting current occurs, which cannot be seen at 70 °C.

5.2.6 Gas diffusion layer

SIGRACET® 35 Series GDLs were used at different PTFE loadings with and without a microporous layer. Adding PTFE increases the hydrophobicity of the material. Four different GDLs were prepared and each was studied for both the anode and the cathode at the same time:

- GDL 35 AA (not modified)
- GDL 35 BA (5 wt% PTFE)

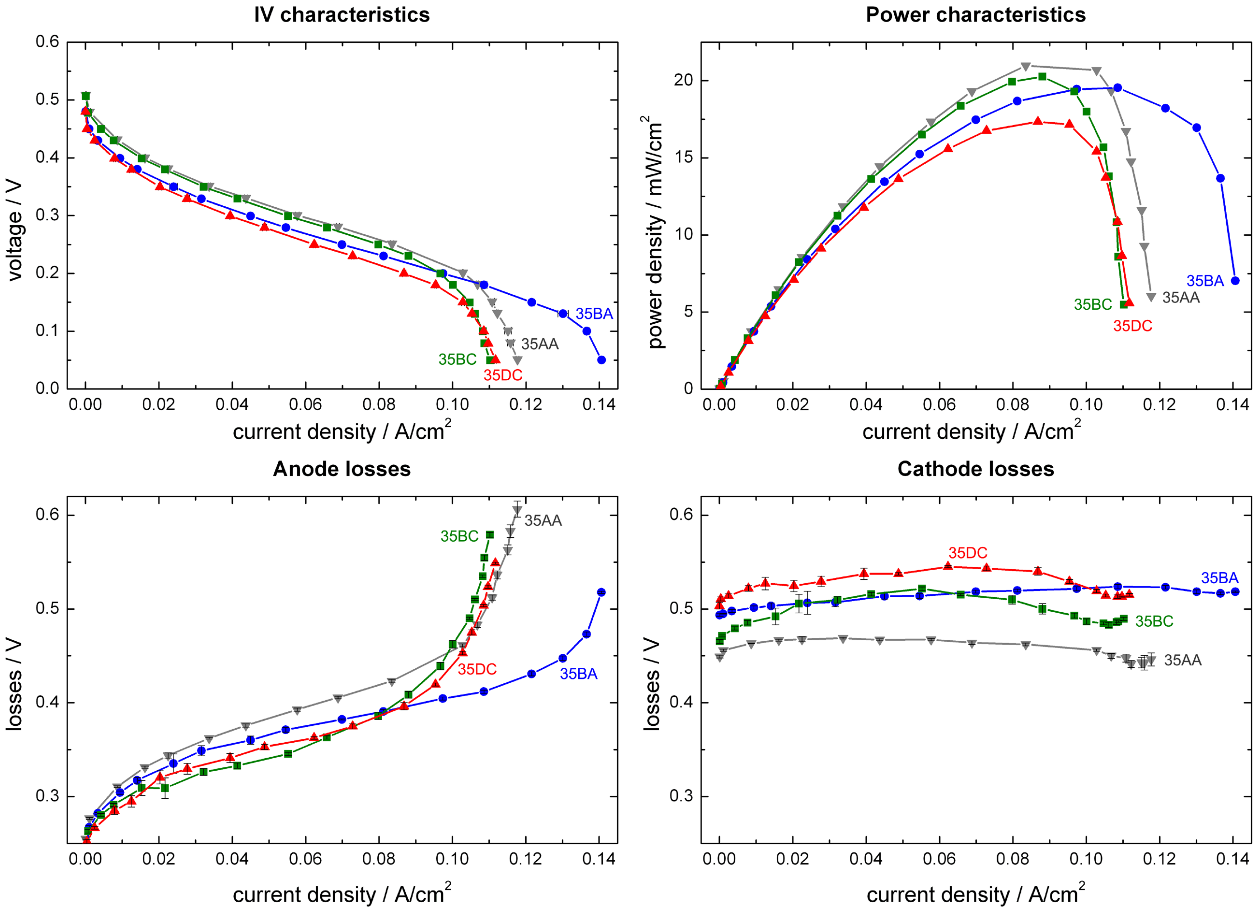

Figure 5.14: Electric properties of a VDMFC for different GDL parameters. Anode and cathode polarization losses were calculated using a connected reference NHE. The temperature was 50 °C, the cathode air stream 40 sccm/λ 2 and the evaporator opening ratio 6.8 %.

- GDL 35 BC (5 wt% PTFE including a microporous layer)
- GDL 35 DC (20 wt% PTFE including a microporous layer)

Experimental results for this study are shown in Fig. 5.14. The performance for all GDLs under investigation was quite similar. Significant deviations could be seen only close to limiting current density. The cathode losses were least when the unmodified GDL was mounted on both sides. Treatment of the GDL with PTFE slightly decreases pore sizes and hydrophobizes the material. Therefore flooding is expected to be smallest for unmodified GDLs, which was supported by the low cathode losses. A microporous layer on the cathode does not seem to influence cathode losses considerably.

On the anode, a large difference between GDL 35 BA without and 35 BC with a microporous layer can be noticed. The limiting current density was increased by 40 mA/cm^2 without the microporous layer. Similar behavior occurred for unmodified GDLs and hydrophobized GDLs having 5 wt% of

Experiment	MeOH Conc.	Temperature	Opening ratio	Air stoichiometry
Pas25_Act2	25 wt%	50 °C	27.2 wt%	2 (min. 40 sccm)
Pas100_Act2	100 wt%	50 °C	1.7 wt%	2 (min. 40 sccm)
Pas25_Pas	25 wt%	50 °C	27.2 wt%	-
Pas100_Pas	100 wt%	50 °C	1.7 wt%	-

Table 5.1: Structural parameters and operating conditions of the comparison between air breathing operation and forced air flow at the cathode.

PTFE. For unmodified GDLs, large amounts of product water could leave the cathode electrode, reducing back diffusion to the anode. A lack of water at the anode caused high concentration losses at high current densities. Hydrophobic GDLs improved the back diffusion of water, as can be seen for GDL 35 BA. The microporous layer that caused slightly lower anode losses at low current densities exhibited high concentration losses at higher current densities. Probably transport of MeOH to the anode electrode was limited by the higher mass transfer resistance of the microporous layer, reducing current generation.

5.2.7 Air–breathing cathode

Besides concepts for passive fuel delivery to the ACL, concepts for the cathode have to be examined with regard to complete passive operation of a VDMFC. The concept of air breathing operation is most commonly used. In this approach, the cathode plate has openings to the surrounding air and oxygen is transported to the CCL by diffusion only. The open cathode plate that was used for this experiments is described in Chapter 3.

A comparison between air–breathing operation and forced air flow at the cathode can be seen in Fig. 5.15. Nafion® 117 was used to minimize MeOH crossover. All other deviations from standard conditions are given in Table 5.1. The notation Pas(xx)_Act(y) is used throughout this section. The methanol concentration (xx) at the anode in wt% and the cathode air stoichiometry (y) is included in the notation. The air–breathing cathode is denoted as _Pas.

It can be noted that active operation of the cathode outperformed air–breathing operation. While anode losses were similar except close to short circuit, the reason for the difference in performance can be seen in the cathode losses. During air–breathing operation, product water at the cathode can only be removed by thermodynamically driven evaporation into the surrounding atmosphere and back diffusion to the ACL. Accumulation of water within the pores of the catalyst layer and the GDL hindered oxygen transport to catalyst sites and thus increased concentration losses.

One interesting result of the experiments was the fact that close to limiting current densities, a forced air flow at the cathode tremendously increased anode losses, which cannot be seen for air–breathing operation. Water supply to the ACL driven by back diffusion from the cathode cannot meet the increased demand at higher current densities, as water was constantly removed

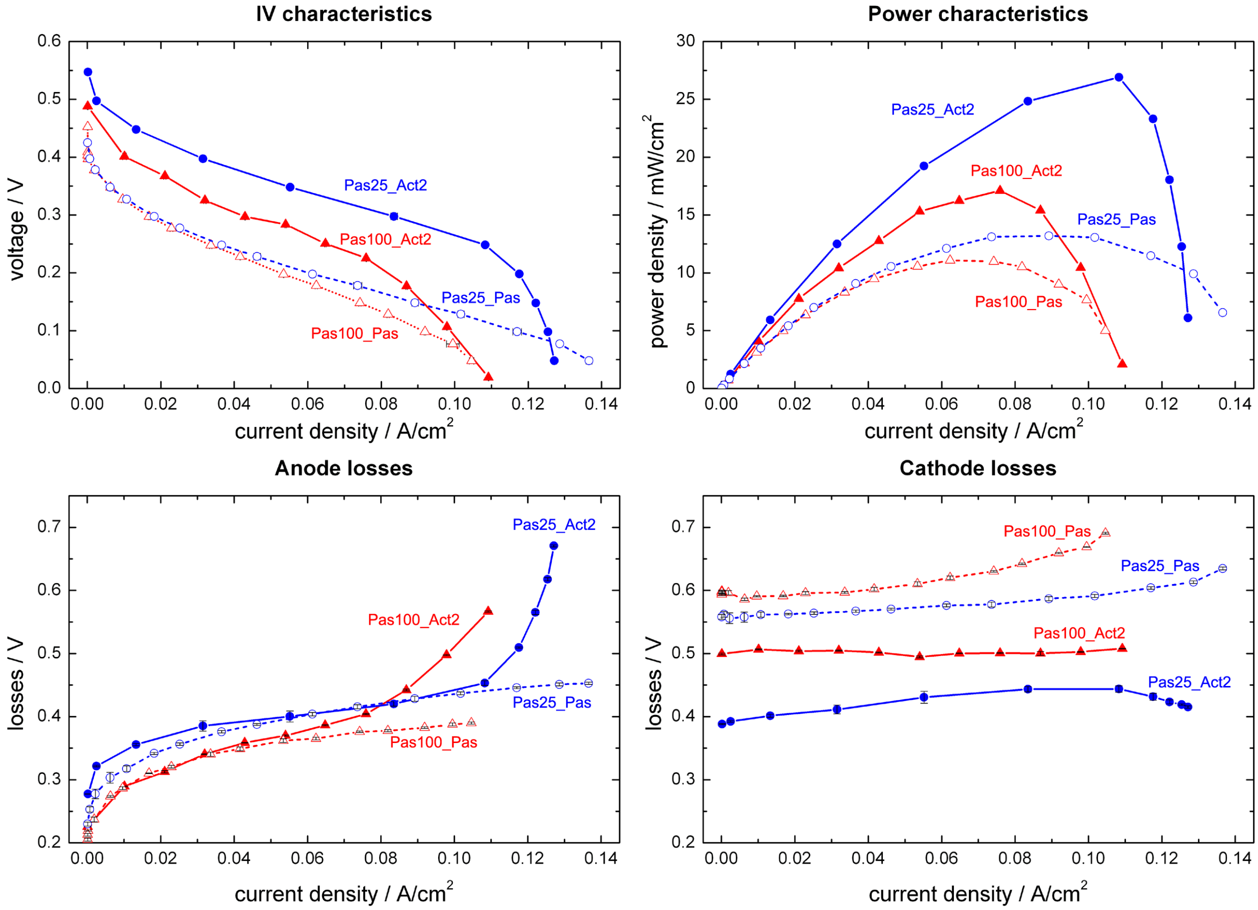

Figure 5.15: Electric properties of a VDMFC with Nafion® 117 for forced air flow and air–breathing operation at the cathode side. Experimental conditions can be found in Table 5.1. Anode and cathode losses were calculated using a connected reference NHE.

by the forced gas stream at the cathode. Accordingly, this phenomena was less pronounced for air breathing operation, which on the other hand led to increased flooding of the cathode.

The lower anode losses for a higher anode concentration of $100\,\mathrm{wt}\%$ are noteworthy as well. According to the theory described above, crossover increases with the concentration of MeOH. Higher crossover increases water production at the cathode because of the parasitic cathodic MOR, a fact that is apparent on analyzing the cathode losses. Thus, water back diffusion was increased and the concentration losses of the anodic MOR were lowered.

5.2.8 Evaporator Opening Ratio

The concentration of MeOH inside the vapor chamber at different current densities is inherently coupled with geometric and material properties of the evaporator as well as with MeOH concentration in the storage tank. Inlays with five different opening ratios of 1.7, 3.4, 6.8, 13.6 and $27.2\,\%$

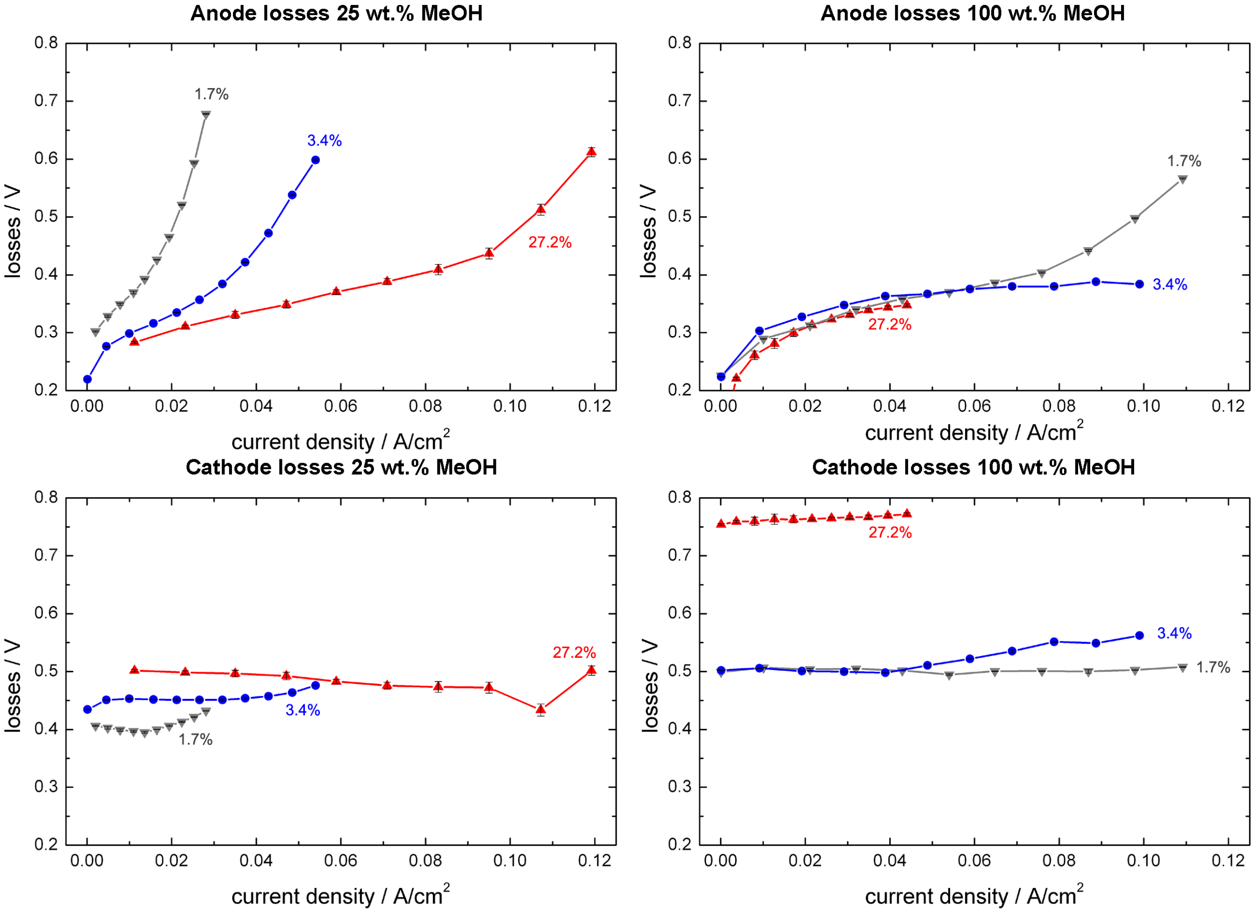

Figure 5.16: Anode losses and cathode losses of a VDMFC for different MeOH concentrations and evaporator opening ratios. Anode and cathode losses were calculated using a connected reference NHE. The temperature was 50 °C and the cathode air stream 40 sccm/λ 2.

were manufactured to study the influence of the opening ratio. Four different MeOH solutions of 25, 50 and 75 wt% in deionized water and pure MeOH were used throughout the epxeriments. Nafion® 117 was used as a membrane throughout these experiments.

The dependence of anode and cathode losses of the fuel cell on three different opening ratios of 1.7, 3.4 and 27.2 % at a MeOH concentration of 25 wt% and 100 wt% is illustrated in Fig. 5.16. Two different behaviors at the two MeOH concentrations can be noted. Anode losses for the 25 wt% MeOH solution decreased with increasing opening ratio. This behavior can be attributed to concentration losses of MeOH and water at the anode electrode. Cathode losses increased with increasing opening ratios. Therefore MeOH concentration in the vapor chamber and consequently MeOH crossover from anode to cathode increased at higher opening ratios, a fact that will be discussed later in this section. Water production at the cathode electrode was facilitated at higher leakage currents and water back diffusion to the anode increased, which minimized water concentration losses of the MOR.

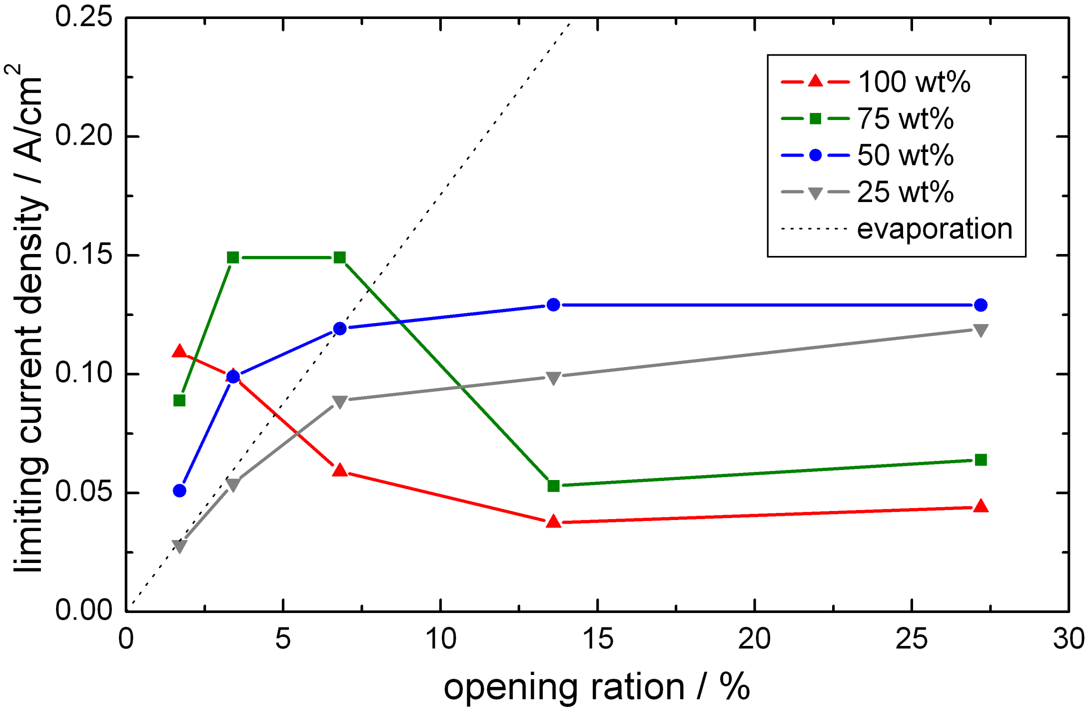

Figure 5.17: Influence of different MeOH concentrations and evaporator opening ratios on the limiting current density. The temperature was 50 °C and the cathode air stream 40 sccm. "Evaporation" is the product of the opening ratio and the evaporative flux for a dense membrane at 50 °C derived from Fig. 5.3.

Anode losses for the 100 wt% MeOH solution did not change significantly with different opening ratios except close to limiting current density for an opening ratio of 1.7 % where concentration losses occured. Polarization losses for this opening ratio were similar to polarization losses of the 25 wt% MeOH solution at 27.2 % opening ratio, which reckoned same partial pressures of MeOH within the vapor chamber. Cathode losses at the highest opening ratio were extremly large at values of 750 mV vs. NHE, indicating large flooded areas because of a high MeOH crossover.

It can be concluded from the polarization plots that MeOH crossover increased with opening ratio as well as with MeOH concentration. Partial pressures of MeOH in the vapor chamber increased with MeOH concentration as already shown in Fig. 5.7 of the **Evaporator** section of this chapter. At high partial pressures the concentration gradient of MeOH between anode and cathode rose and crossover was enlarged.

The complex interaction between opening ratio and MeOH concentration on the limiting current density is depicted in Fig. 5.17. The partial pressure of water and MeOH in the vapor chamber, which influenced MeOH crossover to the cathode and water back diffusion from the cathode, greatly affected the maximal current density. It is interesting to note that the current densities that were achieved exceeded the maximal current densities that could be achieved when multiplying the opening ratio to the evaporative flux for a dense membrane at 50 °C (the active area of the fuel cell equaled the active area of the evaporator). The values determined in the **Evaporator** section

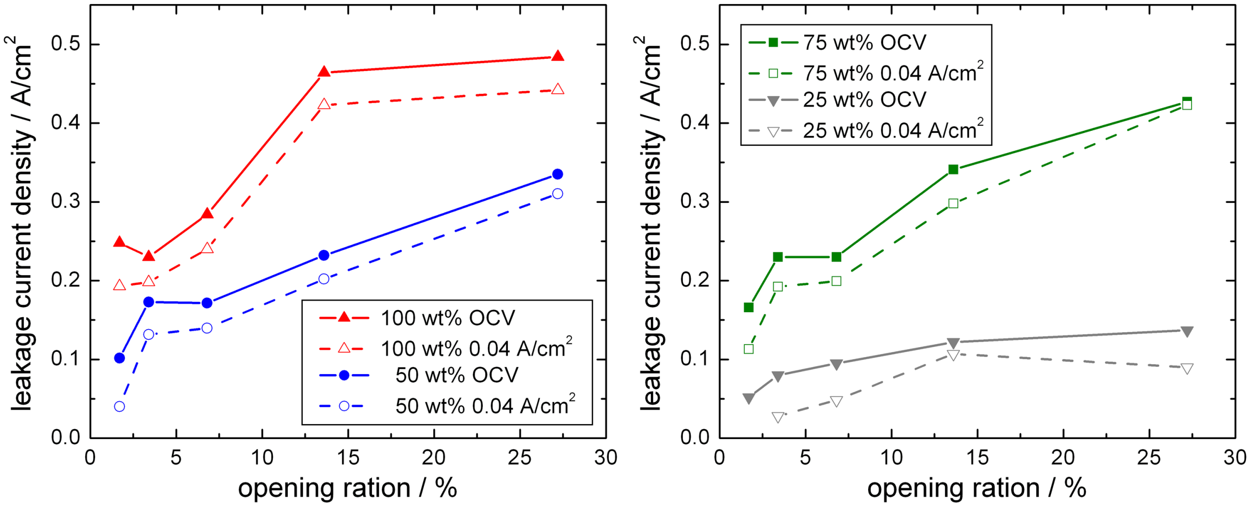

Figure 5.18: Influence of different MeOH concentrations and evaporator opening ratios on the MeOH crossover at OCV and 0.04 A/cm^2. The temperature was 50 °C and the cathode air stream 40 sccm/λ 2.

(Fig. 5.4) were multiplied by the opening ratio and introduced in Fig. 5.17 as a dotted line. Thus it is not evaporation, but diffusion or adsorption in the dense membrane that was the rate limiting step for the mass transport. The relation between opening ratio and evaporative flux into the vapor chamber is not necessarily linear as it depends e.g. on geometric properties of the opening ratio plate.

It was already mentioned that MeOH crossover was greatly affected by changing opening ratios and MeOH concentrations. Fig. 5.18 depicts leakage current densities at OCV and $0.04\,\mathrm{A/cm^2}$. The leakage current density decreased for all conditions when current was drawn from the cell which indicates that diffusion was the dominating transport process inside the membrane. At larger opening ratios the leakage current density increased due to higher MeOH partial pressures in the vapor chamber and thus enlarged the MeOH crossover.

5.3 Water management

One conclusion of the parameter study was that especially at high current densities, fuel cell performance decreased because of a lack of water at the anode electrode. It was shown that high crossover of MeOH led to higher water concentrations at the cathode which increased membrane humidification and decreased membrane resistance. Anode losses close to the limiting current density dropped compared to experiments with lower crossover. A higher back diffusion of water from the cathode to the anode could cope with stoichiometric water consumption during the MOR. As a consequence, higher water concentrations at the cathode electrode seem to be favorable for a VDMFC.

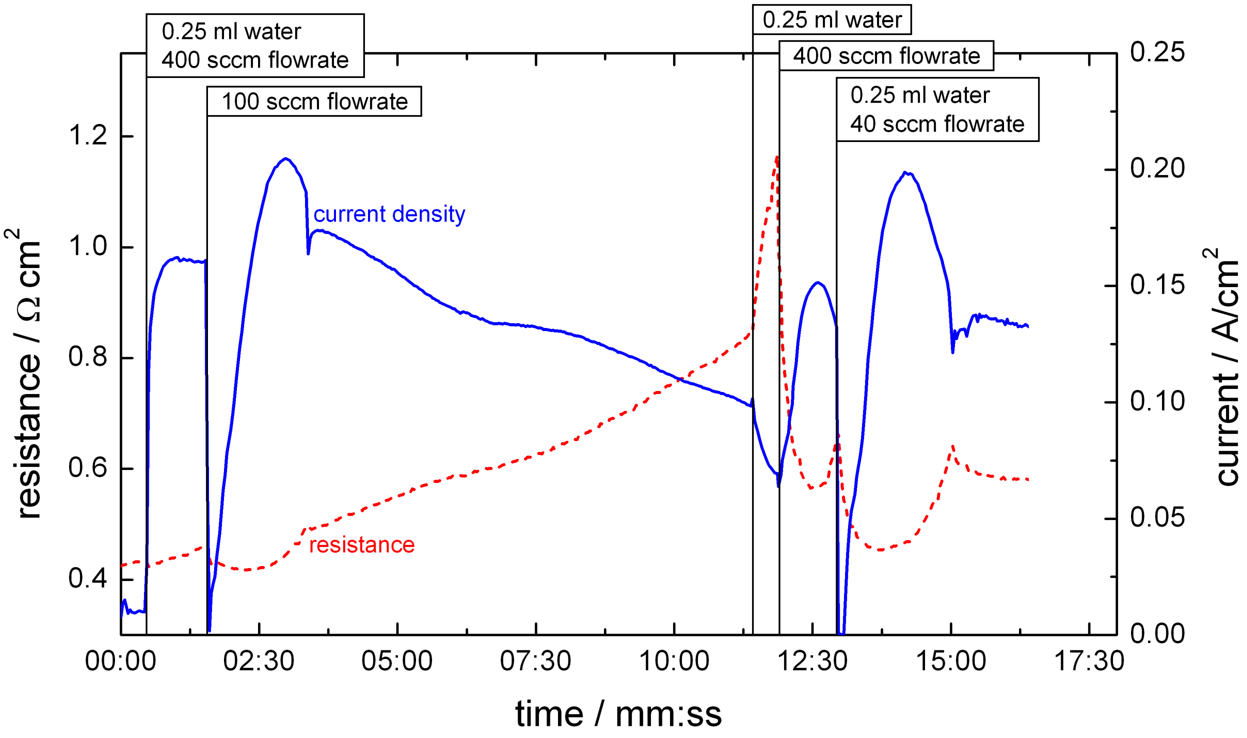

Figure 5.19: Influence of several actions to the cathode air stream on the performance and the ohmic resistance of a VDMFC. The cell voltage was kept constant at 250 mV.

Elevated crossover of MeOH decreases Faradaic efficiency of the fuel cell and additionally raises the risk of flooding within the pores of the cathode electrode and GDL. Therefore active supply of water to the cathode electrode was investigated along with a micro–structured cathode electrode that facilitated water back diffusion.

5.3.1 Active supply of water

Performance of a VDFMC at increased cathodic water concentrations was evaluated by actively injecting liquid deionized water into the air supply of the cathode. Most of the conditions from the **Parameter study** section of this chapter were applied: PDMS membrane with an evaporator opening ratio $6.8\,\%$, $50\,°\mathrm{C}$, SIGRACET® GDL 35AA and changing air flow rates at the cathode. Nafion® 117 with an Pt/Ru anode loading of $3\,\mathrm{mg/cm^2}$ and a Pt cathode loading of $1\,\mathrm{mg/cm^2}$ was used instead of Nafion® 1135 because of its better performance. Instead of using $50\,\mathrm{wt\%}$, the MeOH concentration was raised to $100\,\mathrm{wt\%}$.

The response of the fuel cell to several actions is shown in Fig. 5.19. The cell voltage was kept constant at $250\,\mathrm{mV}$ throughout this experiment. After injecting $0.25\,\mathrm{ml}$ of water into an air stream of $400\,\mathrm{sccm}$, the current increased significantly. When the air stream was reduced to $100\,\mathrm{sccm}$, flooding inside the cathode electrode occurred. Flooding decreased after some seconds and current

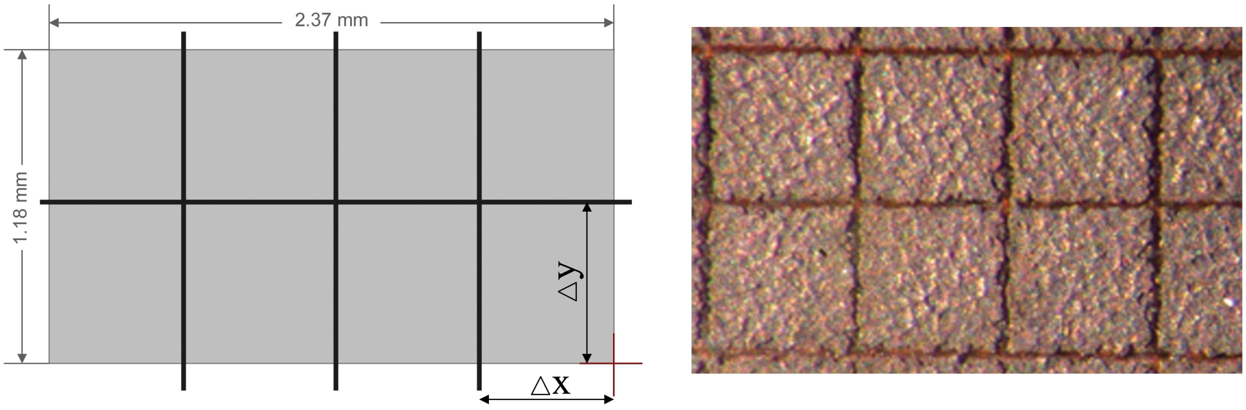

Figure 5.20: Segmentation of the CCL to increase water back diffusion from cathode to anode. a) Schematic drawing of the path of the laser beam. b) Magnification of an ablated CCL.

reached its maximum of more than $0.2\,\mathrm{A/cm^2}$. Injection of water at $100\,\mathrm{sccm}$ caused severe flooding, which was relieved when the flow rate was increased to $400\,\mathrm{sccm}$ again. The improvement in performance was reproducible, also for lower air flow rates of $40\,\mathrm{sccm}$. The crossover current density responded as expected to cathodic flow rates. It increased with flow rate because more MeOH molecules inside the cathode were consumed during parasitic oxidation. Adding liquid water to the air stream did not have any effect on the crossover current density.

5.3.2 Cathode geometries for increased water back diffusion

For completely passive operation, it is convenient to use water which is produced at the cathode to supply the MOR at the anode. For such a VDMFC system, pure MeOH can be used and energy densities for a complete system are increased. Furthermore, performance can be increased, as shown in the previous section.

The CCL and the membrane act as mass transport barriers and reduce water back diffusion. A partial ablation of the CCL can decrease this mass transport barrier. It was achieved by laser ablation of the catalyst layer, a process which is described in Chapter 3. The laser optics was focused on top of the CCL. Therefore in particular the cathode side was ablated and the ACL remained mostly unsegmented. The actual pattern is shown in Fig. 5.20 with dimensions of $\Delta x = 571\,\mu\mathrm{m}$ and $\Delta y = 577\,\mu\mathrm{m}$ for each rectangle. The line width was limited by the laser optic and had a thickness of $30\,\mu\mathrm{m}$. The active area of the CCL was reduced by $10\,\%$ by the applied reticule.

Experiments having an unsegmented cathode, a segmented cathode and a segmented cathode with externally applied water were performed. Pure MeOH within the storage tank was used with an opening ratio for the PDMS–membrane evaporator of $1.7\,\%$ to keep crossover small. Air was supplied to the cathode at a stoichiometry of 2 with a minimum flow rate of $40\,\mathrm{sccm}$. For

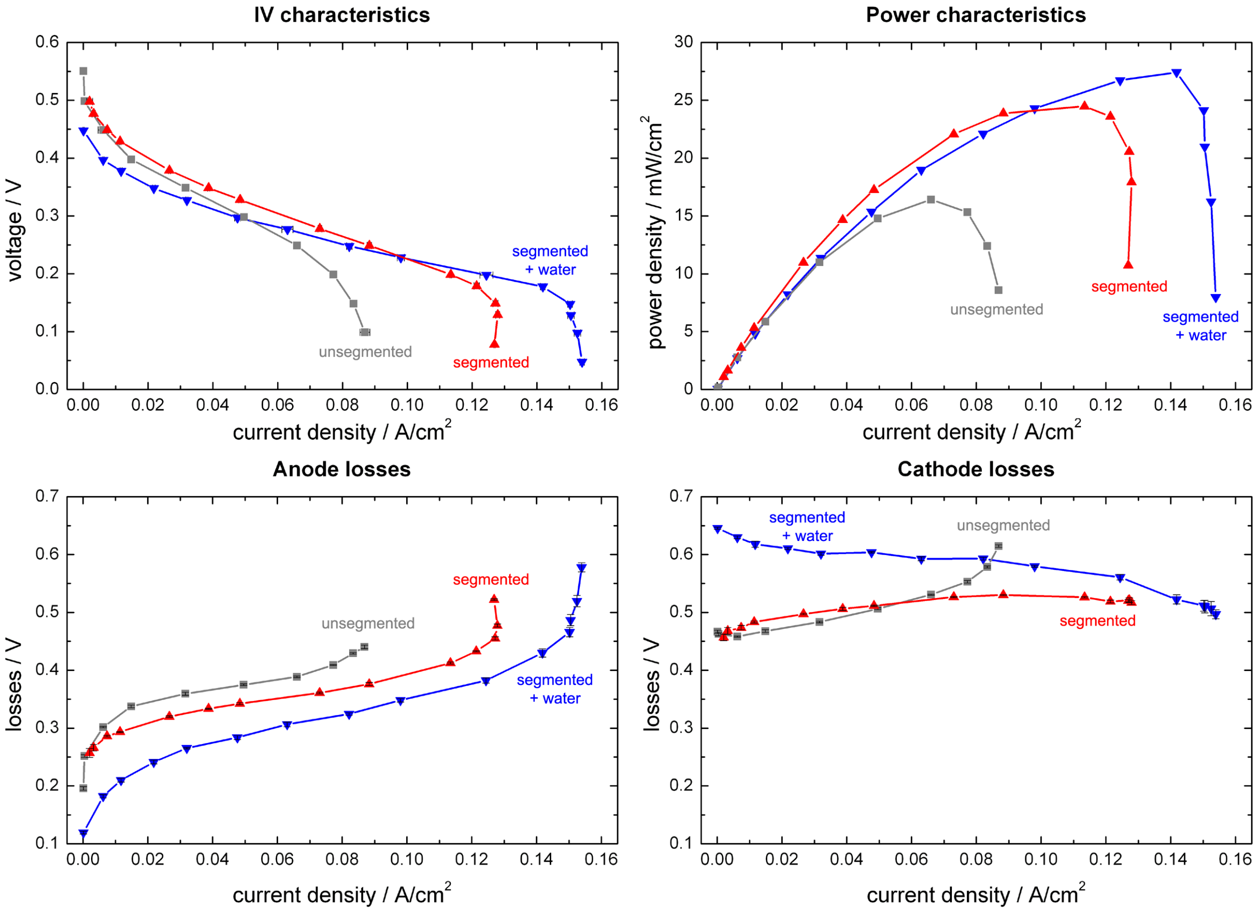

Figure 5.21: Electric properties of a VDMFC for unsegmented and segmented CCLs and pure MeOH in the storage tank. Additional 0.5 ml of water was injected into the cathode air stream for "segmented + water". Anode and cathode polarization losses were calculated using a connected reference NHE. The temperature was 50 °C, the cathode air stream 40 sccm/λ 2 and the evaporator opening ratio 6.8 %.

these experiments the hydrophobic GDL 35 DC (20 wt% PTFE including a microporous layer) was assembled on the cathode side to keep water inside the electrode while 35 AA was used as the anode GDL.

The three cases are compared in Fig. 5.21. Performance between the unsegmented and the segmented CCLs increased significantly and the limiting current density nearly doubled. It can be seen that anode losses of the unsegmented and the segmented CCL differ by 50 mV, a fact caused by higher water concentrations within the ACL. This conclusion was verified when additional 0.5 ml of water was injected into the segmented CCL and anode losses dropped further. On the other hand water injection into the cathode partially flooded the cathode and cathode losses raised. During the measurement water concentration at the CCL declined with time. Mass transfer of oxygen to the CCL improved and cathode losses decreased. At the same time water back diffusion to the anode diminished and anode losses raised.

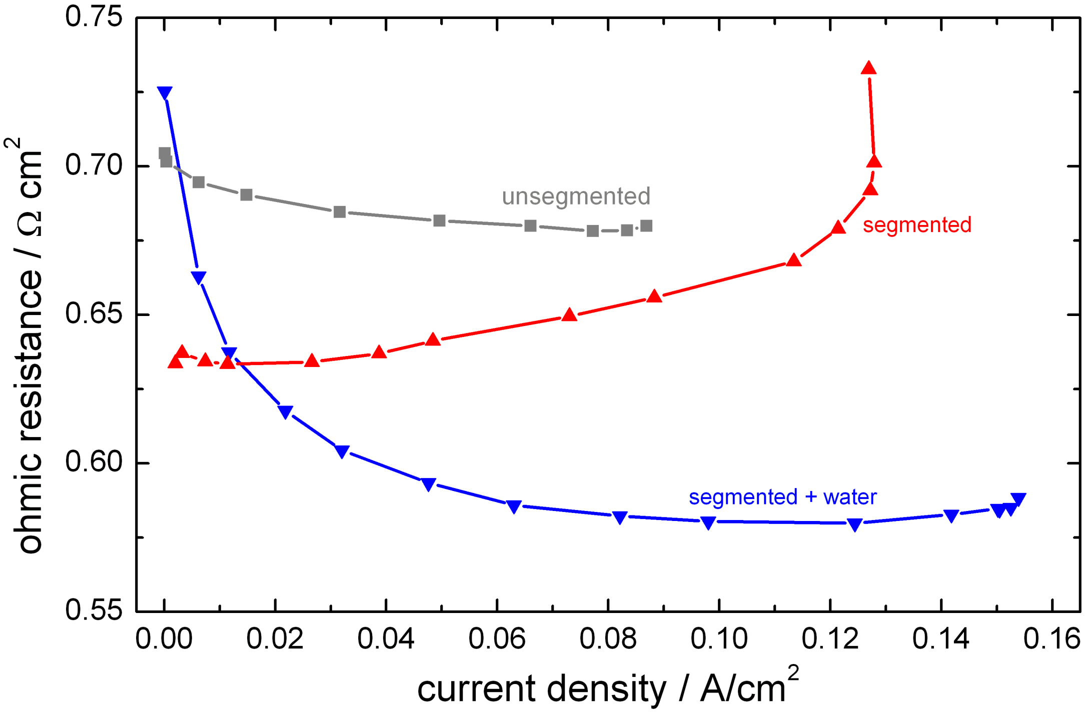

Figure 5.22: Ohmic resistance of the VDMFC versus current density for unsegmented and segmented CCLs. Additional 0.5 ml of water was injected into the cathode air stream for "segmented + water". The temperature was 50 °C, the cathode air stream 40 sccm/λ 2 and the evaporator opening ratio 6.8 %.

The ohmic high frequency resistance at 1 kHz and which is related to the water content of the membrane is depicted in Fig. 5.22. As expected from the electric properties, the resistance was lower for the segmented CCLs and decreased further when water was added to the cathode. A sharp increase of the ohmic resistance was recorded for the segmented CCL at $0.13\,\mathrm{A/cm^2}$. Here less water could diffuse into the membrane than was consumed at the ACL and consequently the membrane was drying up. During the consecutive experiment when water was added to the segmented CCL it took some time for the membrane to get into a well humidified state again.

It can be concluded that water management is the critical issue for a VDMFC. Excess water at the cathode limits the oxygen mass transport to the CCL. Low cathodic water concentrations reduce water back diffusion to the ACL, a fact that reduces performance significantly when operating the VDMFC at high MeOH concentrations.

5.4 Efficiency

The efficiency of a fuel cell system is a convenient parameter to make comparison to other electrochemical systems, e.g. primary or secondary batteries. In this section heat production of a VDMFC is looked at. Additionally, Faradaic and voltage efficiencies are evaluated for different structural parameters and operating conditions.

5.4.1 Heat losses

During the electrochemical reactions, MOR at the anode and ORR at the cathode, heat is generated. The common convention that heat production has a negative sign and heat consumption a positive sign, is used for this thesis. The enthalpy change is calculated according to eq. (2.3) with values of Table 2.1 ($\Delta H_{DMFC} = -726.51\,\mathrm{kJ/mol}$).

$$-q_{DMFC} = -i\left(\frac{\Delta H_{DMFC}}{nF} + U\right) \tag{5.12}$$

An additional term has to be added that accounts for MeOH crossover which is parasitically oxidized at the cathode. It equals Faradaic losses in the case of a VDMFC with a closed fuel cartridge. For simplicity it is assumed that all MeOH at the cathode is electrochemically oxidized with a 6 electron transfer process as described in eq. (2.3).

$$-q_{CO_2} = -i_{leak}\frac{\Delta H_{DMFC}}{nF} \tag{5.13}$$

The leakage current density i_{leak} describes the equivalent current density of MeOH crossover. Using eq. (5.12) and eq. (5.13) the total heat output can be calculated.

$$-q_{tot} = -q_{DMFC} - q_{CO_2} = -i\left(\frac{\Delta H_{DMFC}}{nF} + U\right) - i_{leak}\frac{\Delta H_{DMFC}}{nF} \tag{5.14}$$

Among other effects, MeOH crossover is highly dependent on the fuel cell temperature. Fig. 5.23 shows power densities and heat losses of the fuel cell and MeOH crossover for three different temperatures. A screen–printed CCM having Nafion® 117 as a membrane with $3\,\mathrm{mg/cm^2}$ Pt/Ru at the anode and $1\,\mathrm{mg/cm^2}$ Pt at the cathode attached to SIGRACET® 35AA GDLs was used. Cathode stoichiometry was 2 with a minimum air stream of $30\,\mathrm{sccm}$. A $75\,\mathrm{wt\%}$ solution of MeOH was evaporated through a PDMS membrane with an opening ration of $1.7\,\%$.

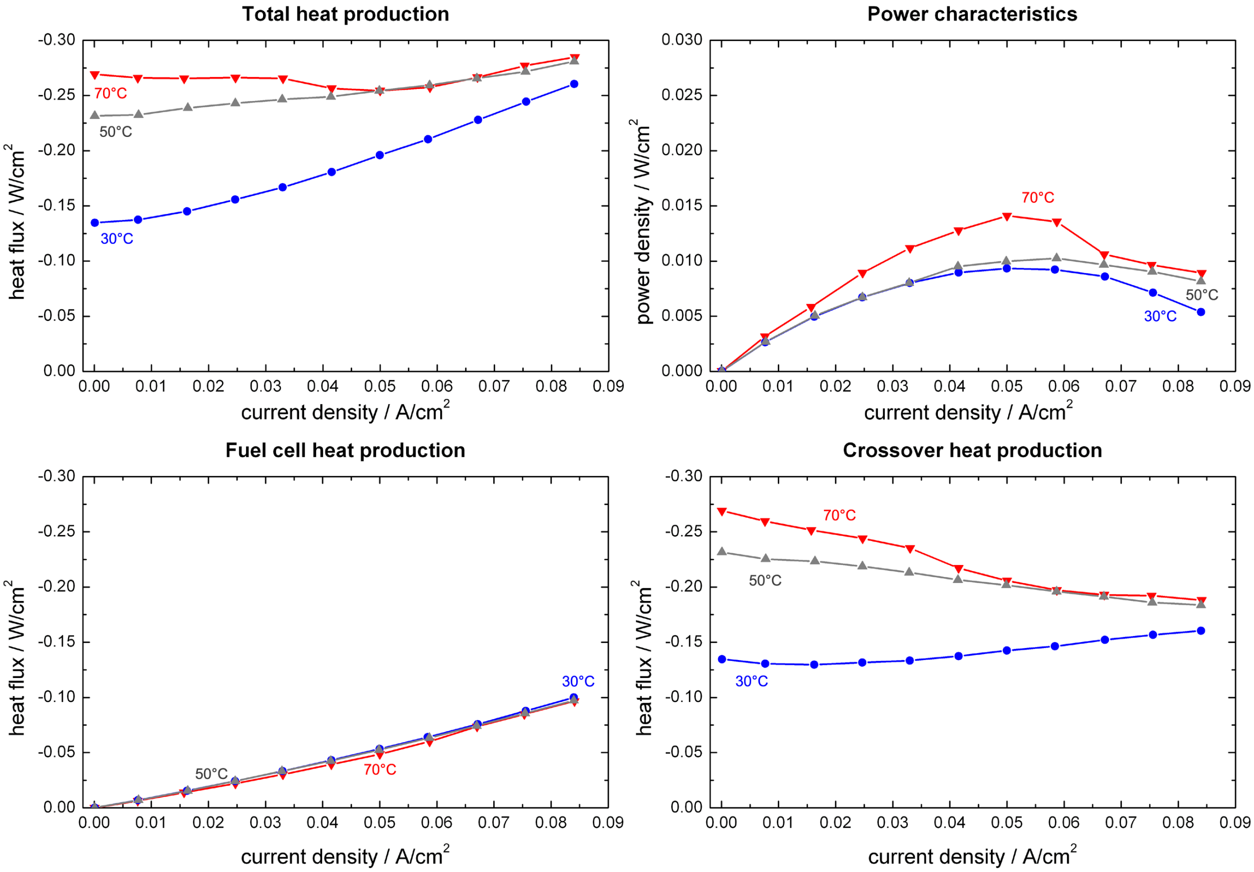

Figure 5.23: Heat fluxes and power densities of a VDMFC for different temperatures. The cathode air stream was 40 sccm/λ 2 and the evaporator opening ratio 6.8 % with a 75 wt% solution of MeOH.

It can be noted in the graph that the highest difference in heat production between the temperatures was gained at OCV, when heat production of the fuel cell is least. Crossover of MeOH across the membrane causes a heat production that is significantly higher than the heat of the fuel cell losses. Therefore even for 30 °C, a heat output of $140\,\mathrm{mW/cm^2}$ remained at OCV. This means that a large amount of fuel is consumed while the fuel cell is on “Standby”. Consequently, a mechanical separation between the storage and the anode vapor chamber has to be considered for VDMFC systems.

On the other hand, heat production can be of advantage for non–isothermal operation of a VDMFC system. As can be seen in the graph heat production at 70 °C remained relatively constant at different current densities. While fuel cell losses increased with current density MeOH crossover declined so that the superposition of these two heat sources according to eq. (5.14) stabilized. It was shown in the **Parameter study** section of this chapter that temperatures between 50 °C and 70 °C increase the performance drastically compared to ambient conditions. Heat production can be used to keep a VDMFC system at elevated temperatures. This would also decrease the risk of freezing at temperatures below freezing point for outdoor applications.

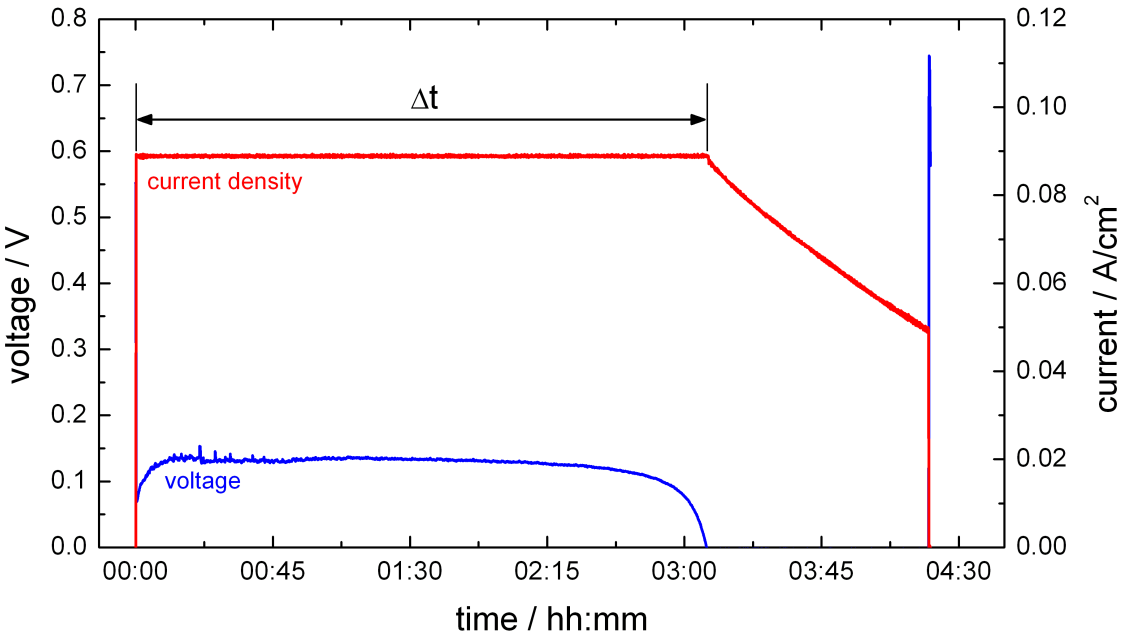

Figure 5.24: Operation time Δt of a VDMFC with limited fuel supply as mentioned as Exp. No. 1 in Table 5.2. The fuel cell was operated galvanostatically at 50 °C with a cathode air stream of 40 sccm.

5.4.2 Total efficiency

Extended–duration experiments at a constant current were performed to gain knowledge about system efficiencies of the VDMFC test cell. Most conditions of the **Parameter study** section of this chapter were applied: PDMS–membrane, $50\,°\mathrm{C}$ and SIGRACET® 35AA GDL. Nafion® 117 with an Pt/Ru anode loading of $3\,\mathrm{mg/cm^2}$ and a Pt cathode loading of $1\,\mathrm{mg/cm^2}$ was used instead of Nafion® 1135 because of its better performance. Thermodynamic efficiency according to eq. (2.6), voltage efficiency according to eq. (2.26) and Faradaic efficiency according to eq. (2.27) were used to calculate the total efficiency η_{tot}. Table 5.2 summarizes structural parameters, operating conditions and total operation times for the different experiments.

$$\eta_{tot} = \eta_i \cdot \eta_u \cdot \eta_{th} \tag{5.15}$$

The current and voltage response of the VDMFC over time during experiment no. 1 can be seen in Fig. 5.24. A $25\,\mathrm{wt\%}$ solution of MeOH in deionized water was used for this experiment with air–breathing cathode conditions. The opening ratio of the evaporator was $27.2\,\%$. The external load drew a constant current of $90\,\mathrm{mA/cm^2}$ from the fuel cell. After a time $\Delta t \approx 3\,\mathrm{h}$ voltage dropped to zero and no power could be drawn from the cell. Averaging current and voltage in this period the Faradaic, voltage und total efficiencies could be obtained.

Faradaic, voltage and total efficiencies for the four experiments can be seen in Fig. 5.25. Fuel crossover, fuel losses through the outlet vent for $\mathrm{CO_2}$ and residual concentrations caused a Faradaic efficiency of only $60\,\%$ and below.

The OCV of a DMFC is strongly reduced compared to its theoretical value, mostly because of the mixed potential at the cathode electrode. At the working point, if MeOH is not totally consumed inside the ACL during the MOR, crossover occurs and the same mechanism that reduces OCV leads to smaller cell potentials. Therefore the voltage efficiency is usually quite low for DMFCs. This conclusion is also valid for the given conditions of the VDMFC, and the voltage efficiencies are slightly above $10\,\%$.

In conclusion, MeOH crossover strongly affects both, Faraday and voltage efficiency. Working points where most of the MeOH is consumed at the anode electrode in addition to membrane materials that reduce crossover flux of MeOH are needed to increase system efficiencies.

Exp. No.	MeOH Conc.	Opening ratio	Liquid vol.	Working point	Δt
`Air-breathing conditions:`					
1	25 wt%	27.2 %	5 ml	$90\,\mathrm{mA\,cm^{-2}}$	11309 s
2	50 wt%	6.8 %	2.5 ml	$90\,\mathrm{mA\,cm^{-2}}$	11702 s
3	100 wt%	1.7 %	2 ml	$62\,\mathrm{mA\,cm^{-2}}$	12949 s
`Cathode air flow 30 sccm:`					
4	50 wt%	6.8 %	2 ml	$90\,\mathrm{mA\,cm^{-2}}$	10140 s

Table 5.2: Structural and operating conditions of experiments to the study system efficiency of a VDMFC. The oeration time Δt is obtained as mentioned in the text.

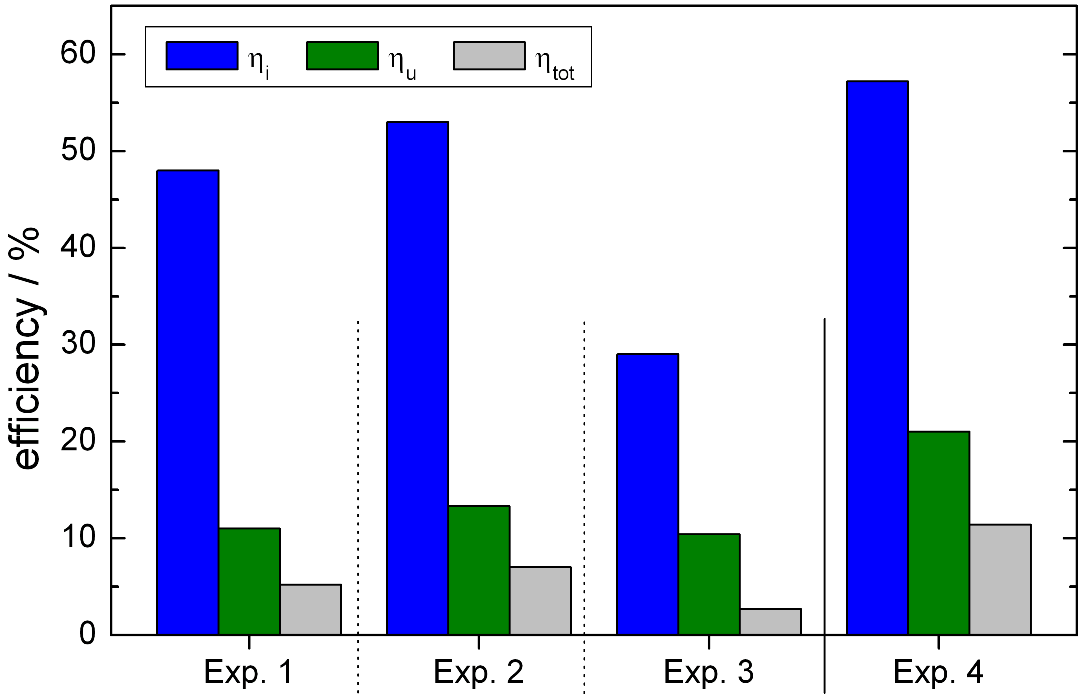

Figure 5.25: Faraday, voltage and total efficiency of different VDMFCs. If values differ from standard values defined in the Parameter study section, structural parameters and operating conditions are summarized in Table 5.2.

Chapter 6

Liquid-Phase Operation versus Vapor-Phase Operation

In this chapter, experimental results for the LDMFC (Chapter 4) are compared to results for the VDMFC (Chapter 5). Four combinations are evaluated with respect to electric performance and two with respect to MeOH crossover.

- actively pumped liquid MeOH supply and actively forced cathode flow (Act_Act)
- actively pumped liquid MeOH supply and passive air–breathing cathode (Act_Pas)
- passive vapor MeOH supply and actively forced cathode flow (Pas_Act)
- passive vapor MeOH supply and passive air–breathing cathode (Pas_Pas)

The given notation is used throughout this chapter. Additionally, the methanol concentration (xx) at the anode in M for the LDMFC and $\mathrm{wt\%}$ for the VDMFC and the cathode air stoichiometry (y) is included in the notation: Act(xx)_Act(y) for the LDMFC and Pas(xx)_Act(y) for the VDMFC. The air–breathing cathode is denoted as _Pas.

Standard conditions, which are described in the **Parameter study** section of the respective chapter, were applied. Instead of Nafion® 1135, the thicker Nafion® 117 was used throughout all experiments to minimize crossover. For the VDMFC results displayed in Fig. 6.2, a SIGRACET® GDL 35 DC was chosen on the cathode side instead of 35 AA, which was used otherwise. Further different operating conditions and structural properties that were chosen for each experiment are summarized in Table 6.1.

6.1 Electric performance

A comparison between an actively pumped liquid MeOH supply to the anode at $0.5\,\mathrm{M}$ and a passive evaporation supply of gaseous MeOH at $50\,\mathrm{wt\%}$ is made. Additionally, the cathode was

Experiment	**MeOH Conc.**	**Pump rate**	**Opening ratio**	**Stoichiometry**
`Liquid-fed operation:`				
Act0.5_Act6	0.5 M	$1\,\mathrm{ml\,min^{-1}}$	-	6 (min. 30 sccm)
Act0.5_Pas	0.5 M	$1.5\,\mathrm{ml\,min^{-1}}$	-	-
Act1.5_Act6	0.5 M	$3\,\mathrm{ml\,min^{-1}}$	-	6 (min. 30 sccm)
`Vapor-fed operation:`				
Pas25_Act2	25 wt%	-	27.2 %	2 (min. 40 sccm)
Pas50_Act2	50 wt%	-	6.8 %	2 (min. 40 sccm)
Pas50_Pas	50 wt%	-	6.8 %	-
Pas75_Act2	75 wt%	-	6.8 %	2 (min. 40 sccm)
Pas100_Act2	100 wt%	-	1.7 %	2 (min. 40 sccm)

Table 6.1: Structural parameters and operating conditions of the experiments which differ from the standard conditions as described in the text.

either air–breathing or was supplied with an air stream with stoichiometry 6 for the LDMFC and 2 for the VDMFC as displayed in Fig. 6.1. The higher cathode air stream for the LDMFC was chosen to prevent flooding of the cathode electrode. For the VDMFC, the cathode stoichiometry was low to increase water back diffusion to the anode electrode. It is shown in Chapter 5 that a low water concentration at the anode electrode decreases the limiting current density for a vapor-fed DMFC.

The LDMFC with a forced cathode air flow and stoichiometry 6 resulted in the best performance of $45\,\mathrm{mW/cm^2}$. The peak power density of the VDMFC with a forced cathode flow reached $20\,\mathrm{mW/cm^2}$, a value that was often gained for the vapor-fed operation (see Chapter 5). Passive air–breathing operation at the cathode resulted in the poorest performance of $13\,\mathrm{mW/cm^2}$ at MPP for both LDMFC and VDMFC. The electrode polarization losses will be used for a detailed discussion of the different phenomena:

Anode polarization losses:
The anode polarization losses for the LDMFC in both cathode operation modes (air–breathing and forced flow) were practically identical, as shown in Fig. 6.1. Apparently the cathode operation mode did not affect the MOR at the anode electrode for the LDMFC. For the VDMFC, a strong dependence of the anode electrode polarization losses on the cathode operation mode was obtained. The different behaviors for the LDMFC and VDMFC between the two cathode operation modes can be attributed to different water concentration profiles inside the fuel cell.

Excess water exists at the anode electrode for the LDMFC due to a highly diluted feed of MeOH in water. Additionally, the water uptake of the membrane is much greater when in contact with a liquid instead of a gas, a fact that is known in the literature as Schroeder's paradox [136–138]. Therefore, the anode electrode was always well humidified. Changes at the cathode did not limit the water concentration at the anode and thus the anode polarization losses did not change.

For the VDMFC, a lower vapor pressure for water compared to the one for methanol caused a low partial pressure of water inside the vapor chamber. Consequently, the water concentration

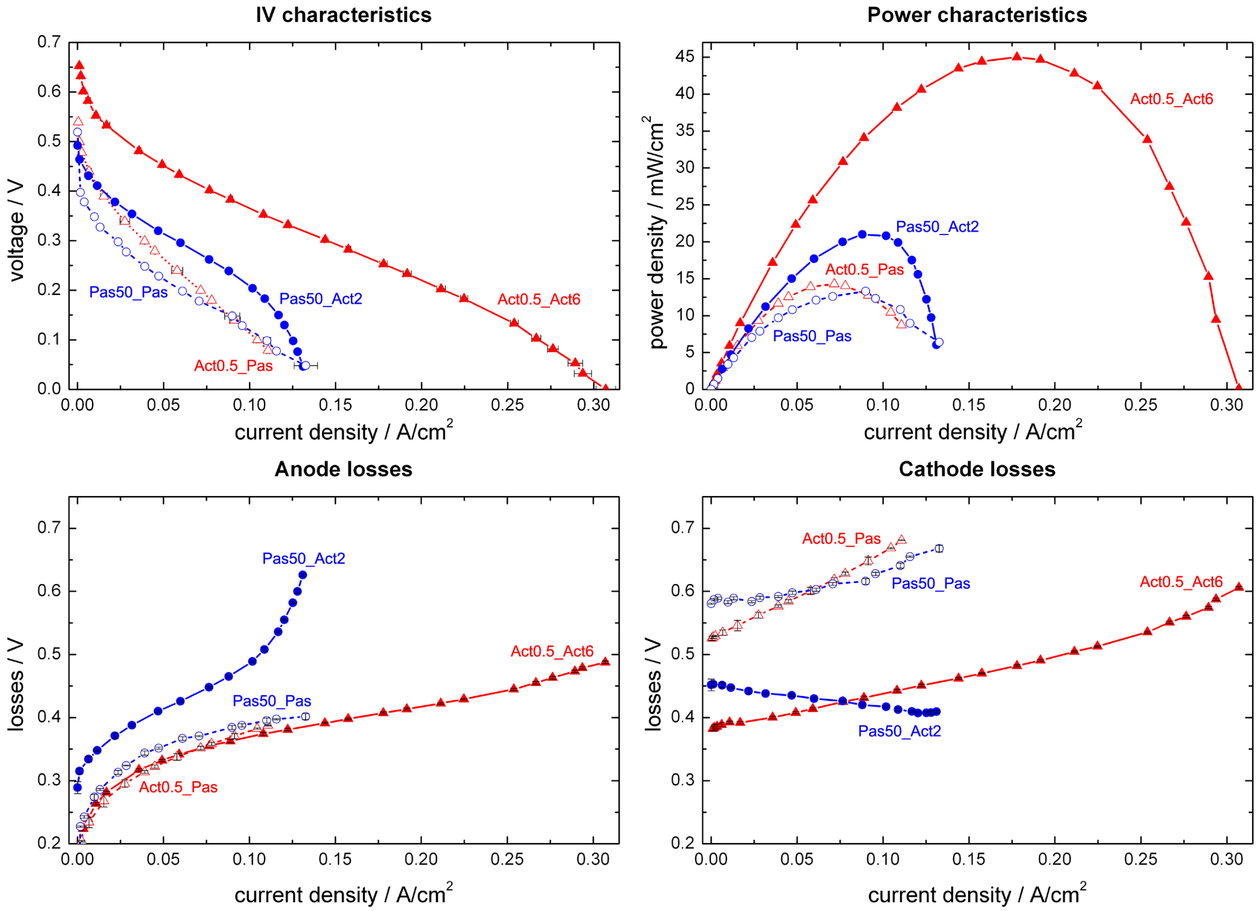

Figure 6.1: Electric properties of a LDMFC and a VDMFC for different structural parameters and operating conditions as given in Table 6.1. Anode and cathode losses were calculated using a connected reference NHE. Nafion® 117 was used as the membrane and the temperature was set to 50 °C.

at the anode electrode depended mainly on the water gradient between the anode and cathode. It can be seen in Fig. 6.1 that the anode polarization losses for the VDMFC under air–breathing conditions were much lower than for the forced air flow. The constant air flow at the cathode removed a large amount of product water from the electrochemical ORR. The water concentration gradient between the cathode and anode was lowered and less water diffused back to the anode. As a result, the MOR was hindered due to the limited water supply and the anode electrode polarization losses increased.

Cathode polarization losses:

The cathode polarization losses that are presented in Fig. 6.1 showed noticeable differences between forced cathodic flow and air–breathing conditions for both the LDMFC and the VDMFC. Under air–breathing conditions, less product water could be removed from the cathode electrode, a fact that is well known and discussed in literature [30, 40, 87]. Accordingly, the excess water for the air–breathing cathode blocked pores of the electrode and the GDL. Oxygen transport to the CCL was hindered and the cathode polarization losses increased.

The cathode polarization losses increased significantly with current density for the LDMFC. Consequently flooding of the cathode electrode was high at high current densities. The almost linear increase of the cathode polarization losses at both cathode operation modes (air–breathing and forced air flow) indicates that this phenomenon should be attributed to the electroosmotic drag of water and MeOH inside the membrane, which rises linearly with current density [94, 139].

The results were different for the VDMFC. Cathode polarization losses decreased at forced cathodic flow with increasing current density. As already mentioned, the water uptake of the membrane is much higher when in contact with a liquid than with a gas. Therefore the humidification of the membrane was much lower for the vapor-fed operation and the contribution of the electroosmotic drag on the concentration profiles of water and MeOH in the fuel cell diminished. More water was consumed inside the ACL at higher current densities. Hence, flooding effects at the cathode were minimized due to increased back diffusion of water to the anode electrode combined with higher air flow rates at the cathode due to the stoichiometric control. Cathode polarization losses for the air–breathing cathode increased slightly with current density due to equilibrium–limited evaporation of water at the cathode electrode into the surrounding air.

Given the fact that cathode losses for both air–breathing and forced cathodic flow were lower for the VDMFC than for the LDMFC at high current densities, the VDMFC could outperform the LDMFC if anode losses were comparable. Therefore the partial pressure of water inside the ACL has to be raised to minimize concentration losses for the VDMFC.

6.2 Micro–structured cathode

The most natural approach to increase the water concentration at the ACL for the VDMFC uses product water from the cathode. The laser segmentation process of only the CCL to facilitate water back diffusion to the anode electrode was presented in the **Water management** section of Chapter 5. The partial ablation of the electrode reduced the mass transfer resistance of the CCL and resulted in a better water uptake of the membrane. Consequently the flux of water to the anode electrode was higher.

Fig. 6.2 presents a comparison of anode losses for a standard LDMFC, a standard VDMFC and a VDMFC with a segmented CCL. Operating conditions were set according to the introduced notation. For the VDMFC with the segmented CCL ("segmented"), an additional measurement was performed where $0.5\,\mathrm{ml}$ of deionized water was injected into the cathode air stream ("segmented + water"). It can be noted in the graph that the anode performance of the VDMFC experiments improved for the segmented CCL and further improved when additional water was added at the cathode. Thus it can be concluded that the water concentration at the anode was highest for the segmented CCL experiment with additional cathodic water and lowest for the unsegmented CCL.

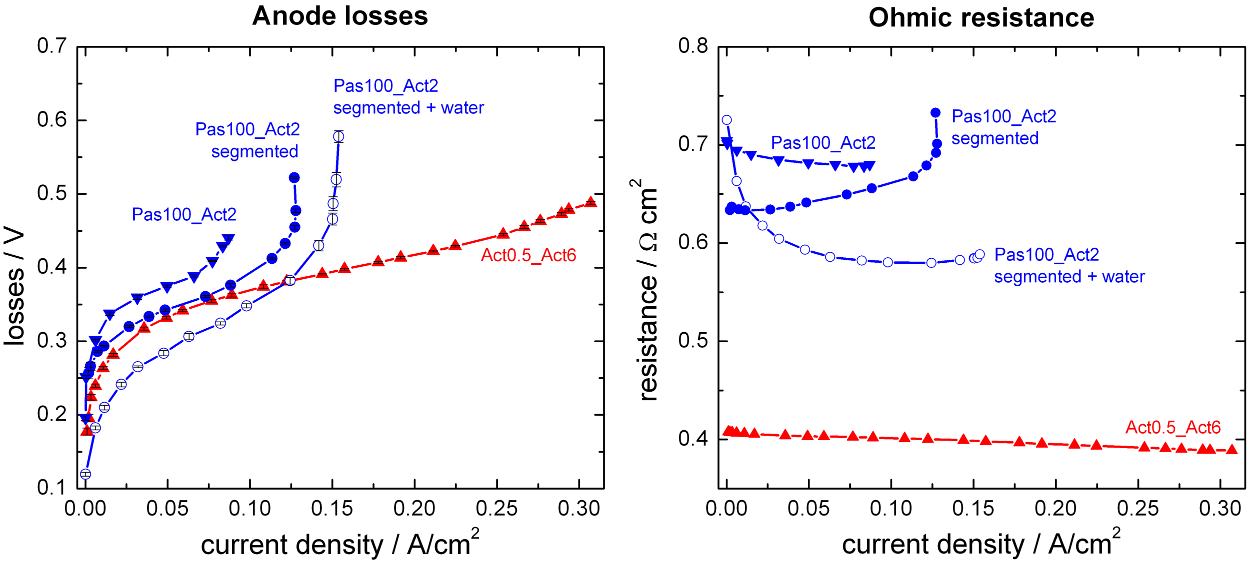

Figure 6.2: Anode polarization losses and ohmic resistances of a LDMFC, a VDMFC and a VDMFC with a segmented CCL for different structural parameters and operating conditions as given in Table 6.1. Extra 0.5 ml of water was added to the cathode air stream for the "segmented + water" experiment. The anode losses were calculated using a connected reference NHE. Nafion® 117 was used as the membrane and the temperature was set to 50 °C.

Anode polarization losses for the VDMFC with a segmented CCL were already comparable to the LDMFC up to a certain cell current density, where high concentration losses due to a lack of water occurred. With additional water added to the cathode, the VDMFC even outperformed the LDMFC with respect to anode polarization losses under the given operating conditions. Nevertheless, the limiting current densities of a VDMFC were still only half of those for a LDMFC and good water management of a VDMFC continues to be a major challenge.

Ohmic parts of the high frequency resistances at $1\,\mathrm{kHz}$ are given in Fig. 6.2 on the right. In addition to ohmic losses due to fuel cell components such as connectors, current collectors, flowfields etc., the ohmic resistance of the membrane accounts for most of the total ohmic losses. The ohmic resistance is a good parameter to measure the water content of the membrane as the membrane resistance for Nafion® greatly depends on the state of humidification [140]. The ohmic resistance of $0.7\,\Omega\,\mathrm{cm}^2$ for the VDMFC was almost twice the resistance for the LDMFC at $0.4\,\Omega\,\mathrm{cm}^2$, which supports the conclusion that the water uptake of the membrane is higher when in contact with a liquid. The ohmic resistance for the VDMFC was lowered by using the micro–structured CCL, due to a better water uptake at the cathode. The sharp increase close to the limiting current density reflects a drying of the membrane as the water consumption of the anodic MOR exceeded water back diffusion. Ohmic resistances of the segmented VDMFC further decreased when additional water was added to the cathode air stream. The gradual improvement of the ohmic resistance suggests that the membrane was in a dry state at the beginning and humidification took about one minute before a stable membrane resistance was established. The duration of this experiment

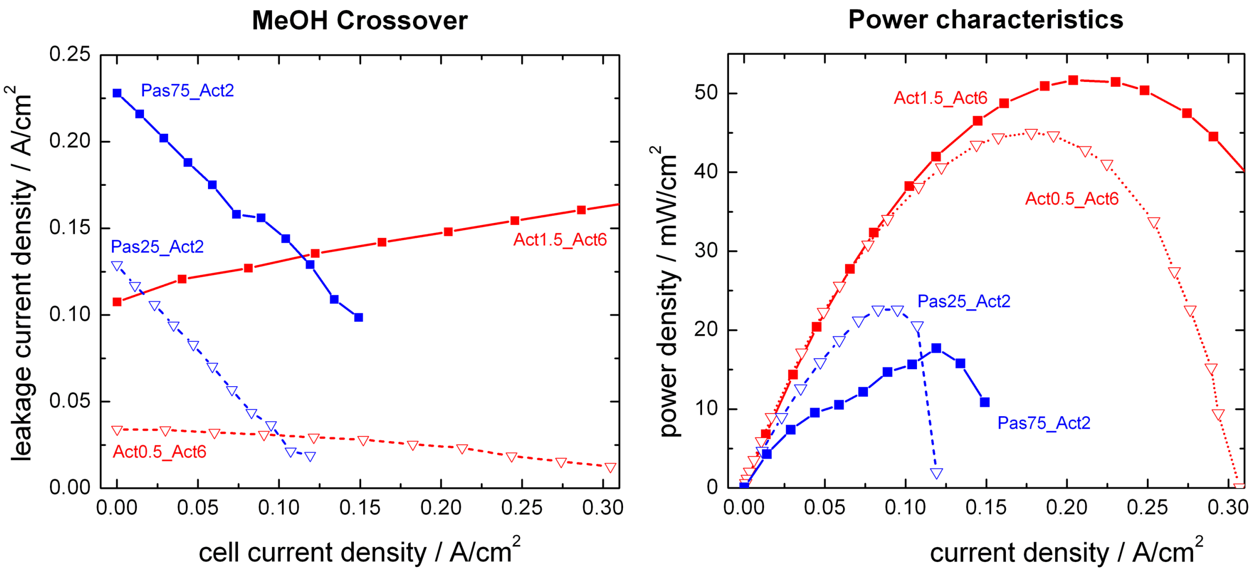

Figure 6.3: Leakage current densities and power densities of a LDMFC and a VDMFC for different structural parameters and operating conditions as explained in Table 6.1. Nafion® 117 was used as the membrane and the temperature was set to 50 °C.

can be derived from the experimental details, as measurements started at OCV and the voltage was reduced by $25\,\mathrm{mV}$ every $20\,\mathrm{s}$ as stated in Chapter 3. This means that every data point in the graph represents $20\,\mathrm{s}$.

6.3 Methanol crossover

The driving force for MeOH crossover from the anode to the cathode side across the membrane differs between liquid-fed and vapor-fed operation of a DMFC. While diffusion due to a concentration gradient between the anode and cathode is the major mechanism for VDMFCs, contributions of the electroosmotic drag are significant and cannot be neglected for LDMFCs, as described in the **Methanol crossover** section of Chapter 4. Additionally, methanol crossover is much smaller for the VDMFC, a fact also found by Kallo et al. [121].

Leakage current densities at $50\,^\circ\mathrm{C}$ for a LDMFC and two methanol concentrations of $0.5\,\mathrm{M}$ and $1.5\,\mathrm{M}$ are compared to a VDMFC at $25\,\mathrm{wt\%}$ and $75\,\mathrm{wt\%}$ in Fig. 6.3 along with the respective power densities. It should be noted that the methanol feed concentration for the VDMFC was much higher (e.g. $75\,\mathrm{wt\%} \mathrel{\widehat{=}} 19.5\,\mathrm{M}$ and $1.5\,\mathrm{M} \mathrel{\widehat{=}} 5\,\mathrm{wt\%}$). Further structural parameters and operating conditions are given in Table 6.1 and the **Parameter study** section of the respective chapter.

The different behavior of the leakage current densities between vapor-fed operation and liquid-fed operation is apparent in the graph. The MeOH crossover decreased linearly for the VDMFC with increasing cell current density. The linear decrease can be attributed to two effects. First, the methanol concentration inside the ACL decreases with current density, as more MeOH is needed for the anodic MOR. Second, humidification of the membrane was lowered at higher current densities due to the high consumption of water at the anode electrode. It is a valid assumption that methanol crossover decreases due to a decreased amount of water in the membrane [121]. For the LDMFC, the contribution of the electroosmotic drag changed the slope of the leakage current density and rose with cell current density. A liquid film of methanol solution inside the cathode electrode (see **Methanol crossover** section of Chapter 4) affecting the concentration gradient of methanol between anode and cathode and therefore the diffusive flux could have further changed the slope of the leakage current density. At a MeOH concentration of $1.5\,\mathrm{M}$, the MeOH crossover increased with cell current density for the LDMFC.

Usually the working point of a DMFC is chosen to be at MPP, which was $0.09\,\mathrm{A/cm^2}$ and $0.13\,\mathrm{A/cm^2}$ for the VDMFC and $0.18\,\mathrm{A/cm^2}$ and $0.22\,\mathrm{A/cm^2}$ for the LDMFC in the given case. MeOH crossover and thus leakage current densities for the LDMFC experiment with a $0.5\,\mathrm{M}$ solution of MeOH and air stoichiometry 6 and for the VDMFC experiment with a $25\,\mathrm{wt\%}$ solution of MeOH and air stoichiometry 2 were similar for the given cell current density at MPP. For the $1.5\,\mathrm{M}/\lambda\,6$ liquid-fed and the $75\,\mathrm{wt\%}/\lambda\,2$ vapor-fed experiments, the VDMFC had a significantly lower crossover of MeOH at MPP.

In a comparison between liquid-fed and vapor-fed operation, the water uptake of Nafion® is much lower for a VDMFC and crossover of MeOH is reduced, which was also found by Ren et al. [139]. Additionally, the electroosmotic drag plays a minor role for a VDMFC. The evaporative flux of MeOH from a highly concentrated MeOH solution in the storage tank can be controlled by additional mass transfer resistances. As a consequence, MeOH crossover during vapor-phase operation is drastically reduced compared to liquid-phase operation.

Chapter 7

Summary and Outlook

The object of this thesis was to investigate new approaches to passively operate direct methanol fuel cells and to compare these passive concepts to existing technology. A reference electrode was used as a tool to distinguish between anode and cathode losses. Two different methods have been pursued to achieve passive operation, one applying liquid methanol at ambient temperatures to a micro–structured anode that facilitated bubble removal and the other using methanol in the vapor-phase inside the anode compartment.

7.1 Summary

Data for active operation had to be obtained first in order to evaluate the passive concepts that are presented in this thesis. Literature values for active operation differ greatly as a variety of catalyst loadings, precursors, preparation methods and operating conditions are used. In addition reliable data for quantifying polarization losses of the anode and cathode electrode are seldom found. Therefore, a liquid-fed direct methanol fuel cell, including a methanol pump at the anode, flowing gas at the cathode and a heating system, was thoroughly characterized.

Results of this characterization are shown in Chapter 4. The influence of operating conditions was studied in detail, and the effect on polarization losses of the anode and cathode electrode was identified. In addition, passive air–breathing operation at the cathode side was investigated. Another focus was on quantifying crossover of methanol from the anode to the cathode through the membrane. A one–dimensional, steady–state model including methanol crossover was refined and validated with experimental data. It revealed contributions of electroosmotic drag and diffusion under different operating conditions. It was shown that especially for small cathodic flow rates, crossover methanol at the cathode was not completely oxidized.

One problem in having liquid methanol as the fuel is the formation of CO_2 bubbles due to the electrochemical reaction at the anode, resulting in a two–phase system. In the liquid-fed and pumped direct methanol fuel cell, these bubbles were either dissolved in the liquid or driven out by a constant flow of methanol inside the flowfield. If methanol is supplied passively or only pumped intermittently, these bubbles grow within the flowfield and consequently block the reactant access to the anode electrode. A flowfield configuration was introduced that removed the gas bubbles by capillary forces only. It also improved the fuel cell system's efficiency since continuous convective flow was not required for operation. Successful bubble removal was demonstrated visually in transparent cells. The long term behavior of a discontinuously pumped and hydrostatically fed direct methanol fuel cells under isothermal conditions, including the proposed micro–structure, confirmed advantages over commonly used channel structures. Better performance compared to continuously pumped direct methanol fuel cells, due to higher temperatures and thus better kinetics at the anode, was demonstrated for non–isothermal operation.

Two–phase problems can be avoided if methanol is delivered to the anode as a gas. Usually methanol is heated above boiling point to guarantee vapor-phase operation. An alternative concept for the passive approach was pursued in Chapter 5. Instead of using heated evaporators, thermodynamically driven evaporation at ambient temperatures was utilized. Therefore membranes were used as phase barriers between the liquid and gaseous methanol.

A model for evaporation of methanol inside the vapor chamber was developed. The model was validated against evaporation experiments, and predicted the gas composition including the transient behavior inside the vapor chamber. During experiments with a vapor–fed direct methanol fuel cell, several structural parameters were studied along with operating conditions. Water concentration at the anode electrode was found to be a major factor that influenced performance of a vapor-fed direct methanol fuel cell significantly. Water transport to the anode electrode was mainly caused by a large concentration gradient between the anode and the cathode. Therefore all actions that reduced water concentration at the cathode, such as increased air flow rates at the cathode or decreased methanol concentrations at the anode resulting in lower methanol crossover, limited the performance and especially the limiting current density of the fuel cell.

The effective evaporation area was identified to be an important factor that interacts with the methanol concentration in the liquid reservoir, fuel cell performance and crossover of methanol across the membrane. It was shown that operation with pure methanol was possible, as product water from the cathode diffused back through the ionomer to the anode as a reactant. As already mentioned, water supply to the anode electrode is a critical issue for vapor-fed direct methanol fuel cells. Back diffusion of cathodic product water was enhanced by introducing hydrophobic layers at the cathode side and by partial ablation of the cathode catalyst layer. Faraday and voltage efficiencies including heat production by the parasitic methanol oxidation at the cathode were determined under various operating conditions.

Active and passive operation modes of liquid-fed and vapor-fed direct methanol fuel cells are compared and discussed in Chapter 6. Passive air–breathing operation at the cathode resulted in comparable performance for both liquid-fed and vapor-fed direct methanol fuel cells. Good water management for the vapor-fed operation resulted in similar or even smaller polarization losses for the anode electrode than for liquid-fed operation. MeOH crossover for liquid-fed operation was recognized as a superposition of electroosmotic drag and diffusion across the membrane. For vapor-fed operation, the contribution of electroosmotic drag was negligible and MeOH crossover dropped faster with increasing cell current density.

Passive operation of a fuel cell causes various loss mechanism on the anode or cathode side which overlap in the IV characteristics. Air–breathing conditions at the cathode for example reduce the partial pressure of oxygen inside the catalyst layer and consequently reduce performance. In order to distinguish these effects, it is necessary to separate losses into cathodic and anodic contributions. Reference electrode measurement is one tool to identify polarization losses of the anode and cathode electrode separately.

One major obstacle in using a reference cell on a very thin substrate, such as a direct methanol fuel cell , is a misalignment of the electrodes. Errors in the results of the reference cell measurement can be significant due to an asymmetrical potential distribution inside the membrane. The equipotential line sensed by the reference cell can be driven from the center of the electrolyte beyond the physical boundaries of the system because of the resistance of the overlapping electrode. Therefore a post–processing method, as introduced in Chapter 3, was developed and evaluated which used laser ablation of both catalyst layers simultaneously to minimize the misalignment of the electrodes considerably.

Various other effects can influence the symmetry of the equipotential lines inside the ionomer as well. A displaced gasket for example can block direct access of the reactants through the GDL to one electrode. Completely blocked areas in proximity to the reference electrode impede the reactant flux to the electrode and thus lead to asymmetrical potential distributions and significant errors. Besides structural parameters, operating conditions influence the potential distribution. Low cathodic flow rates provoke inhomogeneously distributed hydrogen evolution at the anode which significantly changes the symmetry of the potential distribution inside the ionomer. Additionally, water droplets forming at the cathode locally influence the potential distribution. The stability of the normal hydrogen electrode itself was revealed to be dependent on the humidification of the gases. All of these factors that caused a disturbance in the symmetric potential distribution were studied in Appendix A along with their relative significance. Knowledge about the reliability of the reference cell measurements is mandatory to gain not only qualitative but also quantitative data about anode and cathode polarization losses.

7.2 Outlook

For passive operation of a direct methanol fuel cell, the approach applying vapor-fed operation seems to be preferable to liquid-fed operation. Water management to provide sufficient water for the methanol oxidation reaction at the anode is still challenging. Back diffusion of water from the cathode to the anode is an elegant method to meet the two demands of a passive direct methanol fuel cell: high water concentrations at the anode electrode and release of product water at the cathode. Various additional geometries for the patterned cathode catalyst layer should be evaluated in combination with hydrophobic and hydrophilic gas diffusion layers to achieve an increase in the back diffusion of water.

Exhaust gas treatment of the anode side of a vapor-fed direct methanol fuel cell is another big issue in terms of safety and fuel efficiency. Besides CO_2, gaseous methanol leaves the vapor chamber through the anodic outlet vent as well. Catalytic burning of gaseous methanol in the exhaust stream is one possible solution and can heat a passive system and therefore improve the kinetics of the methanol oxidation reaction.

A two–dimensional, spatially resolved model of a vapor-fed direct methanol fuel cell can help to optimize the channel design and the vapor chamber at the anode. In addition, the complex dependence of back diffusion of water on structural parameters and operating conditions could be included in the model. This would allow for new design rules given by model predictions. Furthermore, control strategies for steady–state operation or dynamic operation of a vapor-fed direct methanol fuel could be derived.

Appendix A

Reliability of reference electrode measurements

Reference electrode measurement is a powerful tool that is commonly used in electrochemistry to assess overpotentials of electrodes. For fuel cells this technique can be used to separate total losses into their anodic and cathodic contributions. In the case of a DMFC a reference electrode can either be connected using a salt bridge or be printed directly on the same ionomer as the working electrode. Several effects disturb the symmetrical potential distribution of the working electrode inside the membrane, thereby affecting the reference readings in this set–up. Thus the difficulty in using working electrodes with connected reference electrodes for DMFCs is the need to know where the equipotential line sensed by the reference electrode is geometrically located within the ionomer.

If the kinetics on both sides of the electrodes are equally fast and the working electrodes are perfectly aligned, the potential distribution within the electrolyte is symmetric and the reference electrode senses an equipotential line located in the middle of the ionomer. If additionally the ohmic drop of the fuel cell is known, half of the ohmic losses can be deducted on each side and the total losses can be split into anode and cathode polarization losses. It is important to confirm that no boundary effects influence the potential distribution inside the ionomer. Otherwise, additional electrode polarization losses in the lateral direction might occur and influence the potential distribution significantly. The reliability of a connected reference electrode, which is described in Chapter 3, is studied in this chapter both by experiment and modeling. Electrode polarization losses derived from half–cell experiments are compared to losses derived from reference readings and the results are discussed.

One prerequisite for an accurate measurement including a connected reference cell is a perfectly symmetric potential distribution in the proton–conducting phase of the membrane — or at least knowledge of the different contributions of the ohmic drop of the fuel cell on the electrode polarization losses. To investigate the impact of an asymmetric potential that might be caused by a misalignment between the anode and the cathode, a simple mathematical model of a DMFC was

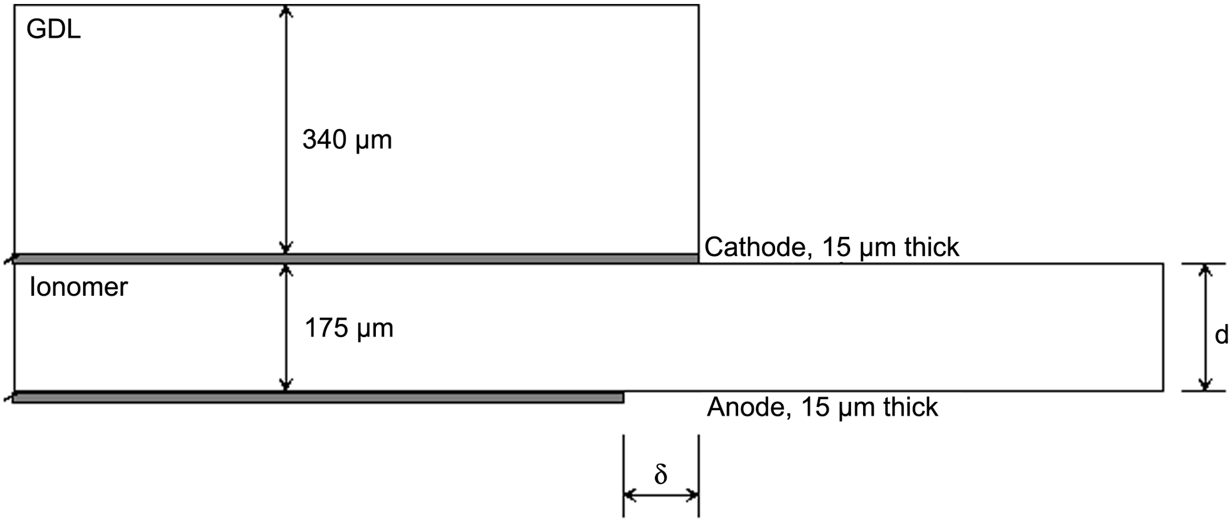

Figure A.1: Model geometry and dimensions used for the simulations. A misalignment δ was introduced between the anode and cathode electrode.

developed. Two different aspects of potential errors during an experiment will be discussed: a misalignment of the electrodes and boundary effects due to a partial change in the diffusivity of the GDL or changing boundary conditions. For the misalignment, a misalignment factor (MAF) is defined according to [70].

$$MAF = \frac{\delta}{d} \tag{A.1}$$

Here d is the thickness of the membrane and δ the absolute geometric misalignment between the edges of the electrodes.

A.1 Model description

The two–dimensional model is isothermal and steady–state. The model geometry of the fuel cell with its geometric properties is shown in Fig. A.1. The boundaries and the four model domains are shown in Fig. A.2. The model describes the transport of protons in subdomains $\Omega_{2,3,4}$ as well as the transport of electrons in subdomains $\Omega_{2,4}$. Diffusion of oxygen is modeled in subdomain $\Omega_{1a,1b}$ on the cathode side. Transport of methanol to the anode is neglected. The electrochemical reactions are described by the Butler–Volmer equation. Crossover of methanol from the anode to the cathode side and the occurrence of mixed potentials is neglected as these phenomena are not essential for drawing conclusions. All model parameters can be found in Table A.1.

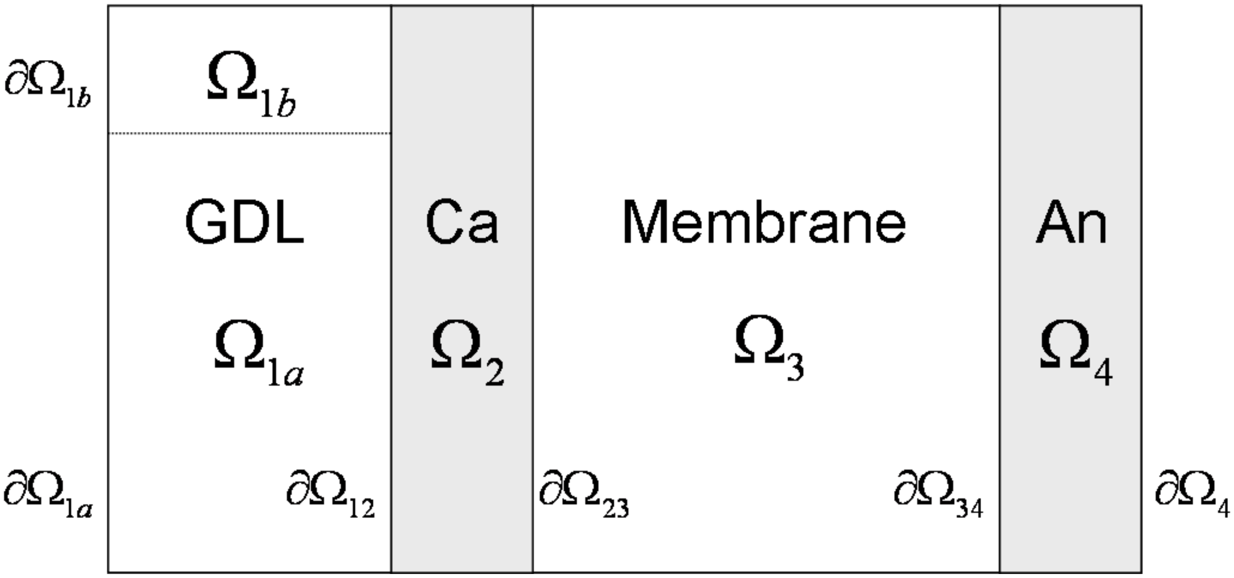

Figure A.2: The figure shows the geometry of the model domain. The model consists of a GDL on the cathode side, cathode (Ca) and anode (An) catalyst layer and the membrane. Subdomains are denoted as Ω_k, boundaries of the subdomains are denoted as $\partial\Omega_k$ or $\partial\Omega_{k,k+1}$.

Parameter	Value	Unit	Ref.
Anode exchange current density	$j_{0,an} = 3 \cdot 10^{-1}$	$\mathrm{A\,m^{-2}}$	fitted
Anode charge transfer coefficient	$\alpha_{an} = 0.9$		fitted
Anode equilibrium potential	$\Phi_{eq,\Omega_4} = 0$	V	
Cathode exchange current density	$j_{0,ca} = 4 \cdot 10^{-1}$	$\mathrm{A\,m^{-2}}$	fitted
Cathode charge transfer coefficient	$\alpha_{ca} = 0.2$		[141]
Cathode equilibrium potential	$\Phi_{eq,\Omega_2} = 1.21$	V	
Temperature	$T = 323$	K	
Protonic conductivity of membrane	$\sigma_{p,mem} = 13$	$\mathrm{S\,m^{-1}}$	[90]
Protonic conductivity of electrodes	$\sigma_p = 5$	$\mathrm{S\,m^{-1}}$	assumed
Electronic conductivity of electrodes	$\sigma_{el} = 3 \cdot 10^2$	$\mathrm{S\,m^{-1}}$	[142]
Inner surface are	$a = 1 \cdot 10^5$	$\mathrm{m^2\,m^{-3}}$	[110]
Oxygen diffusion coefficient of GDL	$D_{O_2} = 1.8 \cdot 10^{-5}$	$\mathrm{m^2\,s^{-1}}$	[6]
Porosity of GDL	$\epsilon = 0.4$		[143]
Tortuosity of GDL	$\tau = 2.6$		[143]
Reference pressure	$p_{ref} = 1.013 \cdot 10^5$	Pa	
Molar fraction of oxygen at inlet	$y_{O_2} = 0.21$		

Table A.1: Model parameters used for the charge transport and the mass transport in the DMFC model.

A.1.1 Charge transport

The governing equation for the transport of protons in the MEA, which occurs in subdomain $\Omega_{2,3,4}$, is the Poisson equation.

$$-\nabla \cdot \sigma_{p,k} \nabla \Phi_p = Q_p \tag{A.2}$$

Here $\sigma_{p,k}$ denotes the proton conductivity of subdomain k, and Φ_p the potential of the proton–conducting phase. Q_p is a source or sink term that describes the electrochemical reactions.

$$Q_p = \begin{cases} j_{0,an} \cdot a \cdot \left(e^{\frac{(1-\alpha_{an})6F}{RT} \cdot \eta_{an}} - e^{\frac{(-\alpha_{an})6F}{RT} \cdot \eta_{an}} \right) & \text{in } \Omega_4 \\ 0 & \text{in } \Omega_3 \\ -j_{0,ca} \cdot a \cdot \left(\frac{p_{O_2}}{p_{O_2,0}} \right) \cdot \left(e^{\frac{(1-\alpha_{ca})2F}{RT} \cdot \eta_{ca}} - e^{\frac{(-\alpha_{ca})2F}{RT} \cdot \eta_{ca}} \right) & \text{in } \Omega_2 \end{cases} \tag{A.3}$$

The methanol oxidation takes place inside the catalyst layer of the anode, subdomain Ω_4, . It can be represented as shown by Kauranen et al. [144].

$$\begin{aligned} \mathrm{CH_3OH} &\longrightarrow \mathrm{CO_{ads}} + 4\mathrm{H}^+ + 4\mathrm{e}^- \\ 2\mathrm{H_2O} &\longrightarrow 2\mathrm{OH_{ads}} + 2\mathrm{H}^+ + 2\mathrm{e}^- \\ \mathrm{CO_{ads}} + 2\mathrm{OH_{ads}} &\longrightarrow \mathrm{CO_2} + \mathrm{H_2O} \end{aligned} \tag{A.4}$$

A single rate determining step is assumed in the model. This step is the reaction of $\mathrm{CO_{ads}}$ and $\mathrm{OH_{ads}}$ on the catalytic sites [145]. Thus, a simple Butler–Volmer approach is used to describe the charge generation rate. The electrode has an active surface area per unit volume a due to its porosity. The anodic exchange current density is denoted as $j_{0,an}$. The anode overvoltage η_{an} is defined as the difference between the potential of the electron conductor Φ_{el} and the potential of the proton conducting phase Φ_p. As the reference equilibrium potential Φ_{eq,Ω_4} for the methanol oxidation is very small, it is neglected for the simulations.

$$\eta_{an} = \Phi_{el,\Omega_4} - \Phi_{p,\Omega_4} - \Phi_{eq,\Omega_4} \approx \Phi_{el,\Omega_4} - \Phi_{p,\Omega_4} \tag{A.5}$$

A zero flux boundary condition is applied at the boundary $\partial\Omega_4$.

$$-\sigma_{p,k} \nabla \Phi_p \cdot \vec{n} = 0|_{\partial\Omega_4} \tag{A.6}$$

Here $\vec{n}$ is the outward–pointing normal vector. The continuity of the protonic current holds at the interface $\partial\Omega_{34}$ between the membrane and the anode.

$$\sigma_{p,\Omega_3}\nabla\Phi_{p,\Omega_3} = \sigma_{p,\Omega_4}\nabla\Phi_{p,\Omega_4}|_{\partial\Omega_{34}} \tag{A.7}$$

No generation or consumption of protons is assumed to happen in the membrane, subdomain Ω_3. Oxygen is reduced to water inside the catalyst layer of the cathode electrode, domain Ω_2.

$$\mathrm{O_2} + 4\mathrm{H}^+ + 4\mathrm{e}^- \rightarrow 2\mathrm{H_2O} \tag{A.8}$$

Again a Butler–Volmer approach is used to model the sink term for protons on the cathode side. In addition to Ω_4 a term for the depletion of oxygen from the reference state $p_{O2,0}$ is added in eq. (A.3). The cathode overpotential η_{ca} is defined as follows:

$$\eta_{ca} = \Phi_{el,\Omega_2} - \Phi_{p,\Omega_2} - \Phi_{eq,\Omega_2} \tag{A.9}$$

The equilibrium potential Φ_{eq,Ω_2} equals the reversible cell voltage defined by eq. (2.5). The boundary conditions are likewise set to zero flux at $\partial\Omega_{12}$ and to continuity at $\partial\Omega_{23}$.

The electronic potential Φ_{el,Ω_4} is assumed to be zero at $\partial\Omega_4$. The resistance of the GDL and contact resistances are neglected.

$$U_{cell} = \Phi_{el,\Omega_2}|_{\partial\Omega_{12}} - \Phi_{el,\Omega_4}|_{\partial\Omega_4} = \Phi_{el,\Omega_2}|_{\partial\Omega_{12}} \tag{A.10}$$

The protonic and the electric potentials of the electrodes are coupled through eq. (A.3), (A.5) and eq. (A.3), (A.9). The electronic conductivity of the electrode is orders of magnitudes higher than the protonic conductivity. Thus, electronic resistances are neglected in the electrodes.

A.1.2 Mass transport

Mass transport limitations are taken into account on the cathode side. Since one purpose of this model is to show the influence of inhomogeneous GDLs on the potential sensed by a reference electrode it is not necessary to include both diffusion layers. Thus the anode GDL is neglected in the model. Diffusion through a porous GDL is modeled in Ω_{1a} and Ω_{1b} using Fick's law of diffusion.

$$\nabla \cdot (-\frac{\epsilon}{\tau} D_{O_2} \nabla y_{O_2}) = Q_m \tag{A.11}$$

Here ϵ and τ describe the porosity and the tortuosity of the GDL, whereas D_{O_2} is the diffusion coefficient of oxygen. The molar fraction of oxygen is described by y_{O_2}. Oxygen is consumed inside the porous catalyst on the cathode side. The Faraday law couples the charge transfer rate and the consumption rate of oxygen Q_m.

$$Q_m = \frac{Q_{p,\Omega_2}}{4F} \cdot \frac{RT}{p_{ref}} \tag{A.12}$$

The charge transfer rate Q_{p,Ω_2} is given by eq. (A.3). Continuity of flux is applied at the interface between the GDL and the cathode catalyst layer $\partial\Omega_{12}$.

$$N_{O_2,\Omega_{1a,1b}}\big|_{\partial\Omega_{12}} = N_{O_2,\Omega_2}|_{\partial\Omega_{12}} \tag{A.13}$$

No diffusion of oxygen is allowed through the boundary $\partial\Omega_{23}$.

$$\partial N_{O_2} \cdot \vec{n} = 0 \ |_{\partial\Omega_{23}} \tag{A.14}$$

At the outer boundaries, $\partial\Omega_{1a}$ and $\partial\Omega_{1b}$, the molar fractions of ambient air are used unless stated otherwise in the text.

$$y_{O_2} = y_{in,O_2} \ |_{\partial\Omega_{1a,1b}} \tag{A.15}$$

A.2 Experimental details

Half–cell measurements were used as a tool to evaluate the quality of the reference readings. The CCMs were prepared by the screen printing method. Nafion® 117 with a catalyst loading of $1\,\mathrm{mg/cm^2}$ Pt at the cathode electrode and $3\,\mathrm{mg/cm^2}$ Pt/Ru at the anode electrode was used throughout all experiments. The CCMs were post–processed by the laser ablation process described in Chapter 3 unless stated otherwise. Centering pins aligned the CCMs in the fuel cell assembly. One side of the reference electrode was flooded with deionized water to guarantee a good humidification of the other side that acted as a NHE.

For all half–cell experiments a $0.5\,\mathrm{M}$ solution of methanol diluted in deionized water was pumped to the anode flowfield at a flow rate of $1.5\,\mathrm{ml/min}$. Hydrogen was supplied to the cathode flowfield at a rate of $25\,\mathrm{sccm}$. The cathode electrode acted as a DHE in this measurement set–up. Hence the anode polarization losses could be determined by both the working electrode and the reference electrode simultaneously. Comparing these two values a relative error could be calculated. It was assumed that due to the large area and the laser segmentation of the working electrode boundary effects could be neglected and the measurement results of the DHE could be trusted. The relative error ϵ_r was defined according to Brondstejn [146], without the absolute value.

$$\epsilon_r = \frac{x - \tilde{x}}{x} \tag{A.16}$$

Here x is the true value and $\tilde{x}$ the biased value. Unless stated otherwise in the text, the losses derived from the DHE are taken as x and the losses derived from the reference readings as $\tilde{x}$.

A.3 Results and Discussion

The causes of a disturbance in the symmetric potential distribution was studied along with their relative significance. Therefore several effects were investigated experimentally and the findings were combined with simulation work. Besides investigations in measurement errors caused by experimental configurations and operating conditions, the stability of the reference cell itself and differences between half–cell operation and full–cell operation on the reference readings were looked at.

Fig. A.3 depicts the results of a half–cell experiment using a post–processed MEA. Special care was taken in minimizing potential error sources by applying a laser ablated CCM, a homogeneous pressure, fixing the membrane by centering pins and humidifying the reference electrode. These steps are described in detail in Chapter 3. The experiments were conducted at half–cell operation and $30\,^\circ\mathrm{C}$. No deviations between the anode losses determined by the reference electrode and the losses determined by the working electrode were observed. The relative error was well below $1\,\%$,

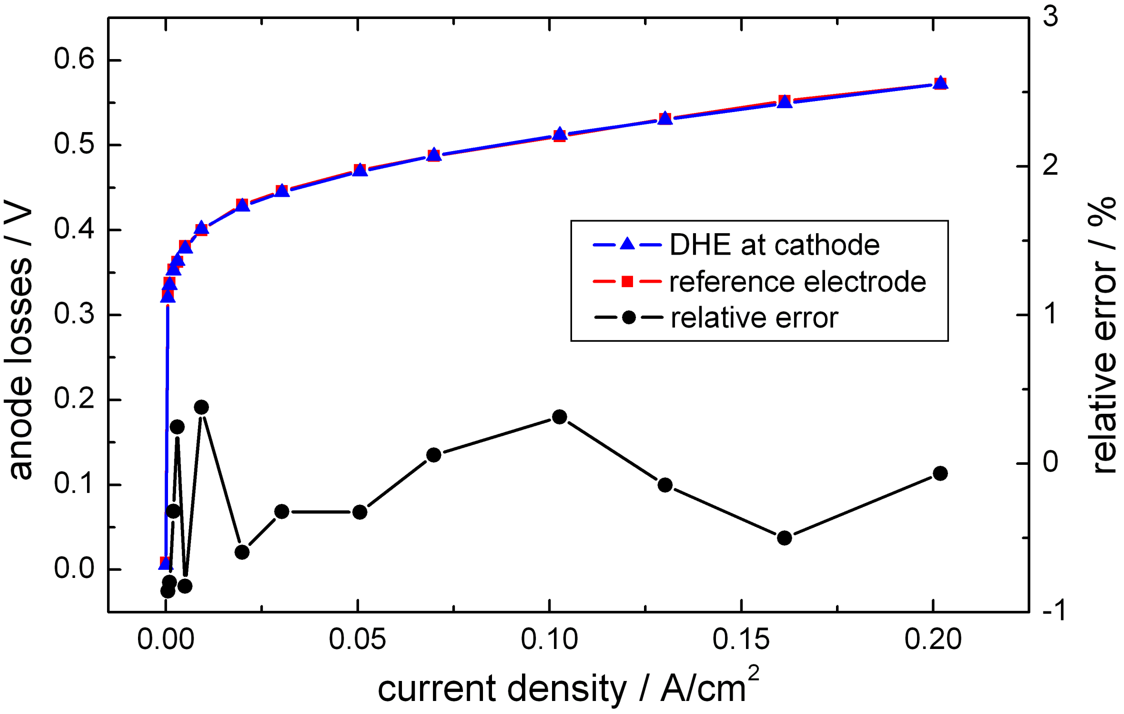

Figure A.3: Measurement results of a half–cell experiment of a DMFC. The cathode was flushed with hydrogen. The anode polarization losses were determined with both the DHE at the cathode and the reference electrode. The relative error was calculated as mentioned in the text.

indicating that the experimental effort to guarantee a symmetric potential inside the ionomer led to tolerable deviations.

A.3.1 Experimental error sources

Various physical phenomena can lead to an inhomogeneous potential distribution inside the membrane. Along with a misalignment of the anode and the cathode electrode, dissimilar flowfields with respect to the resistance, inhomogeneous pressures inside the cell and obstructed parts of the GDL can lead to different contributions of the ohmic drop of the membrane to the electrode polarization losses. As a result, significant measurement errors can be made when using a reference electrode.

Several experiments were performed to study the impact of different effects. If possible, only one source of error was applied to the experiment in order to separate the effects. The reference cell is said to sense a potential that is located in the middle of the membrane. Thus, half of the ohmic loss was subtracted from the electrode readings to get the electrode polarization losses. Additionally, simulations were carried out to study some effects in more detail.

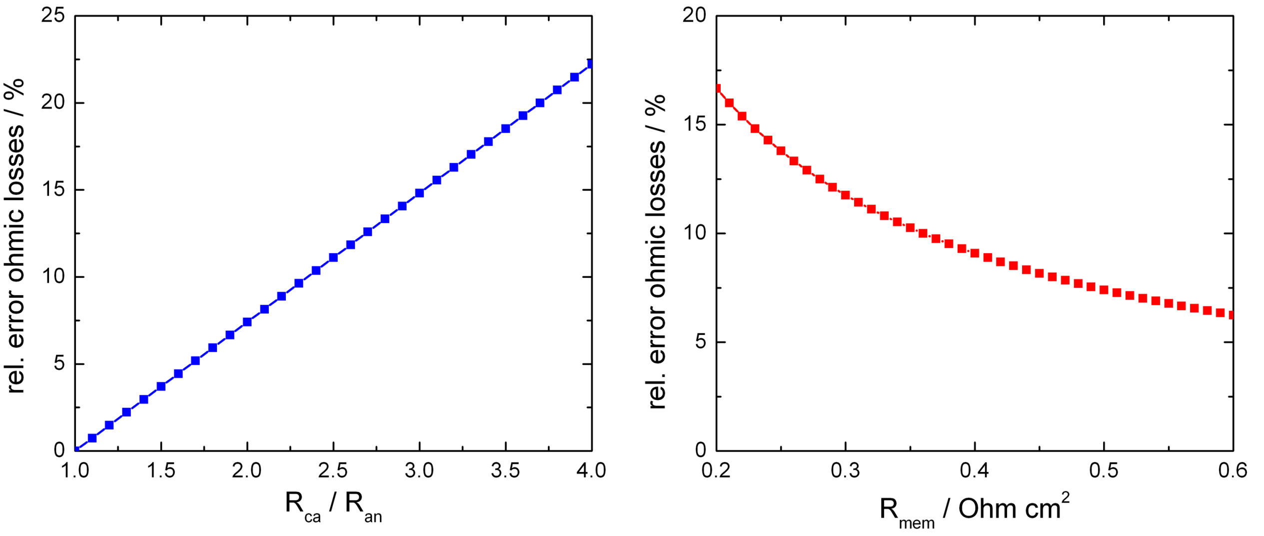

Figure A.4: Relative errors of the ohmic losses caused by different anode and cathode flowfield resistances. For the left graph, R_{mem} *was fixed to* $500\,m\Omega\,cm^2$*. For the right graph,* R_{ca}/R_{an} *was fixed to* 2 *with* $R_{an} = 2\,m\Omega$*.*

Different flowfield resistances

Fig. A.4 depicts errors that occur when the ohmic resistances of the anode and cathode flowfields are not identical. Different geometries, dimensions or materials of the flowfields can lead to different resistances. Furthermore, contact resistances differ for each assembled cell. Typical experimental values were chosen for the calculations. The left graph shows the relative error with respect to the symmetric case as a function of the ration of cathode to anode flowfield resistances R_{ca}/R_{an}. The ohmic resistance was fixed at $500\,\mathrm{m\Omega\,cm^2}$ with an assumed active area of $10\,\mathrm{cm^2}$. The anode flowfield resistance was set to $2\,\mathrm{m\Omega}$. A current density of $0.1\,\mathrm{A/cm^2}$ was assumed. The cathode flowfield resistance was varied between $2\,\mathrm{m\Omega}$ and $8\,\mathrm{m\Omega}$. For these parameters a relative error of the ohmic contributions was calculated. The ohmic losses for the anode $\eta_{ohm,an}$ and cathode $\eta_{ohm,ca}$ were determined by adding half of the membrane losses to the respective ohmic flowfield losses.

$$\left|\epsilon_r^{ohm}\right| = \frac{\eta_{ohm,an} - \eta_{ohm,ca}}{\eta_{ohm,an}} \tag{A.17}$$

It can be seen that the relative error has a linear dependence and is already significant for small deviations between the two flowfield resistances.

For the right graph of Fig. A.4, the anode flowfield resistance is fixed at $2\,\mathrm{m\Omega}$ and the cathode flowfield resistance at $4\,\mathrm{m\Omega}$. The relative error was calculated as described above. Again a current density of $0.1\,\mathrm{A/cm^2}$ was assumed. The membrane resistance R_{mem} was varied, showing a much more pronounced relative error for smaller resistances.

Considering the results of these calculations, it is obvious that one has to make sure that both flowfields have the same resistance at the point of voltage measurement. This is especially true when reactions with negligible polarization resistances, such as the hydrogen evolution reaction, take place at one electrode. Further resistances occur when copper plates are used to collect the current and to sense the voltage. These contact resistances between the flowfield and the copper plate should also be the same on both sides. Alternatively the voltage can be sensed directly at the electrodes.

Misalignment of the electrodes

Several papers have been published on the impact of a misalignment of the electrodes, using simulation as the method of investigation [61,62,70,147]. One of their conclusions was that due to the different kinetics of the reactions on the anode and the cathode, even electrodes in perfect alignment have some deviations from the symmetric case [61,70]. Different anode and cathode kinetics lead to different charge transfer rates as described in eq. (A.3). In consequence, the electrode polarization losses differ and the symmetric potential distribution inside the ionomer is disturbed. In the case of a DMFC, the polarization losses of anode and cathode electrode are of the same order of magnitude. Therefore, the effect of different kinetics on the potential distribution should be small. Fig. A.5 shows relative errors for the anode and cathode overpotentials determined from simulation results. The effects of different kinetics and a misalignment can be studied in the graph.

The “Anode kinetics” and “Cathode kinetics” curves depict the relative error according to eq. (A.16) determined by the true overpotentials η and the overpotentials calculated from the reference readings without a misalignment $\tilde{\eta}$. The true polarization losses of the anode and cathode electrode have been calculated by subtracting the electronic potential Φ_{el} from the protonic potentials at the ionomer/electrode interfaces $\partial\Omega_{23}$ and $\partial\Omega_{34}$.

$$\eta_{ca} = \Phi_{el} - \Phi_p|_{\Omega_{23}} \tag{A.18}$$

$$\eta_{an} = \Phi_{el} - \Phi_p|_{\Omega_{34}} \tag{A.19}$$

The interface is chosen because the protonic polarization losses of the electrodes are maximal at this position. The electronic potential inside the electrodes is considered to be constant as mentioned in the modeling section. The modeled reference potentials are extracted at a point where the potential inside the membrane is stabilized in a region of constant potential as depicted in Fig.

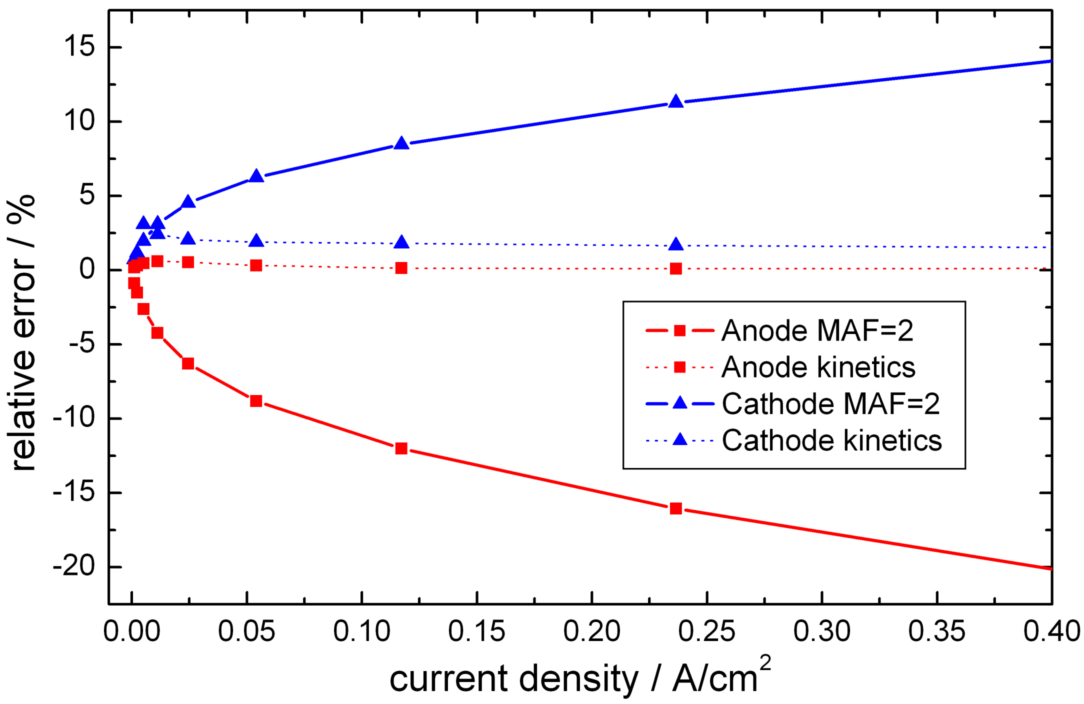

Figure A.5: Errors calculated from simulation results. Deviations of the symmetric potential distribution for a DMFC appeared because of different anode MOR and cathode ORR kinetics and because of a misalignment of $350\,\mu m$ *of the cathode electrode (MAF=2).*

2.7. Using the electronic potentials of the electrodes, the simulated reference cell readings from the reference electrode to the working anode can be calculated.

$$U_{ref\_an-we\_an} = \Phi_{el,\Omega_4}|_{\partial\Omega_4} - \Phi_{ref} \tag{A.20}$$

Here Φ_{ref} denotes the potential of the reference electrode, which is $0\,V$ for the NHE. The voltage losses of the electrodes $\tilde{\eta}$ are calculated according to eq. (2.31) and eq. (2.32). It can be seen in the figure that the deviations due to different kinetics of the MOR and the ORR are negligible, especially for the anode readings.

"Anode MAF=2" and "Cathode MAF=2" depict the relative errors determined by simulated reference readings without and reference readings with a misalignment. The electrode polarization losses are calculated for each of the two model geometries. Results from the well aligned model are taken as the true value, results from the misaligned model as the biased value and thus the relative error can be calculated. The misalignment factor (MAF) as introduced in eq. (A) was set to 2; hence the cathode overlap was twice the thickness of the ionomer in the misaligned model. The potentials of the reference electrode were extracted for both cases, one with a perfect alignment

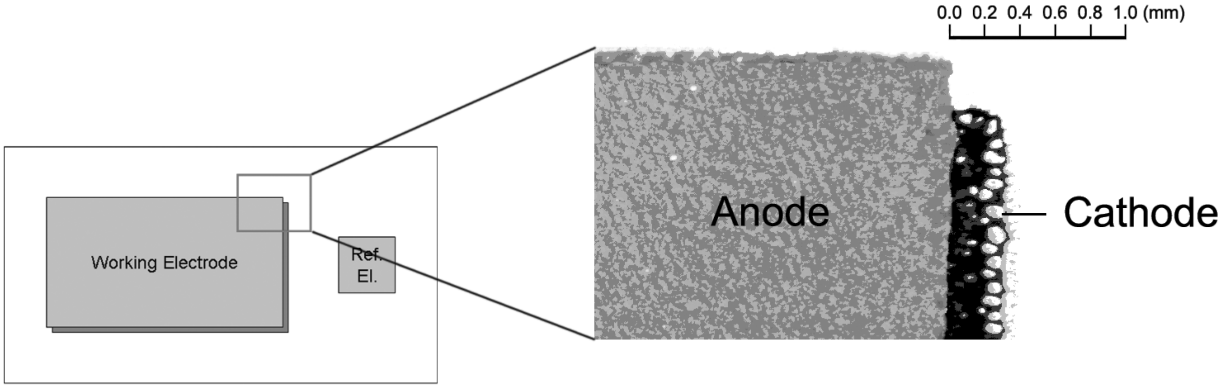

Figure A.6: Top view showing the misalignment of the anode and cathode electrode of a CCM after the preparation process. The transparent ionomer is masked.

and one with an overlapping cathode electrode of $350\,\mu\mathrm{m}$, with the same set of parameters. They were evaluated in a region of constant potential, far away from the cathode electrode. Applying eq. (A.20), $U_{ref\_an-we\_an}$ and consequently the anode polarization losses could be calculated according to eq. (2.31). The voltage drop of the cathode electrode was calculated using eq. (2.32). The relative error displays a dependence on the current in an order of magnitude that cannot be neglected, even for low current densities.

Experiments were conducted to verify the results predicted by the model. A CCM after the preparation step can be seen in Fig. A.6. There was a large geometric deviation between the anode and cathode of approximately $350\,\mu\mathrm{m}$, which was twice the thickness of the membrane. It can be noted that the edge was slightly frayed and did not seem to be very homogeneous. The reference electrode was connected to the right side of this set–up. In this case, the post processing with the laser ablation process was not applied so that the impact of the misalignment could be investigated experimentally. This half–cell experiment was performed at $50\,^{\circ}\mathrm{C}$. The readings were disturbed by the misalignment of the two working electrodes.

Results of this experiment can be seen in Fig. A.7. As indicated by the simulation results of Fig. A.5, the extension of the cathode beyond the anode leads to an overestimation of the anode overpotential. This effect increased with increasing current density. Therefore, the relative error rose at higher currents. In a direct comparison between experiment and simulation, the model showed much higher relative errors than the experiment. The frayed edge of the CCM appeared to decrease the error. In addition, the two electrodes were distorted and the misalignment decreased from top to bottom.

Nevertheless, a misalignment of the electrodes had a considerable effect on the reference readings in both experiment and simulation and severe errors influenced the different losses deducted from measurement results. Thus, it is apparent that the electrodes in proximity to the reference electrode must be well aligned, e.g. by using the proposed laser ablation process.

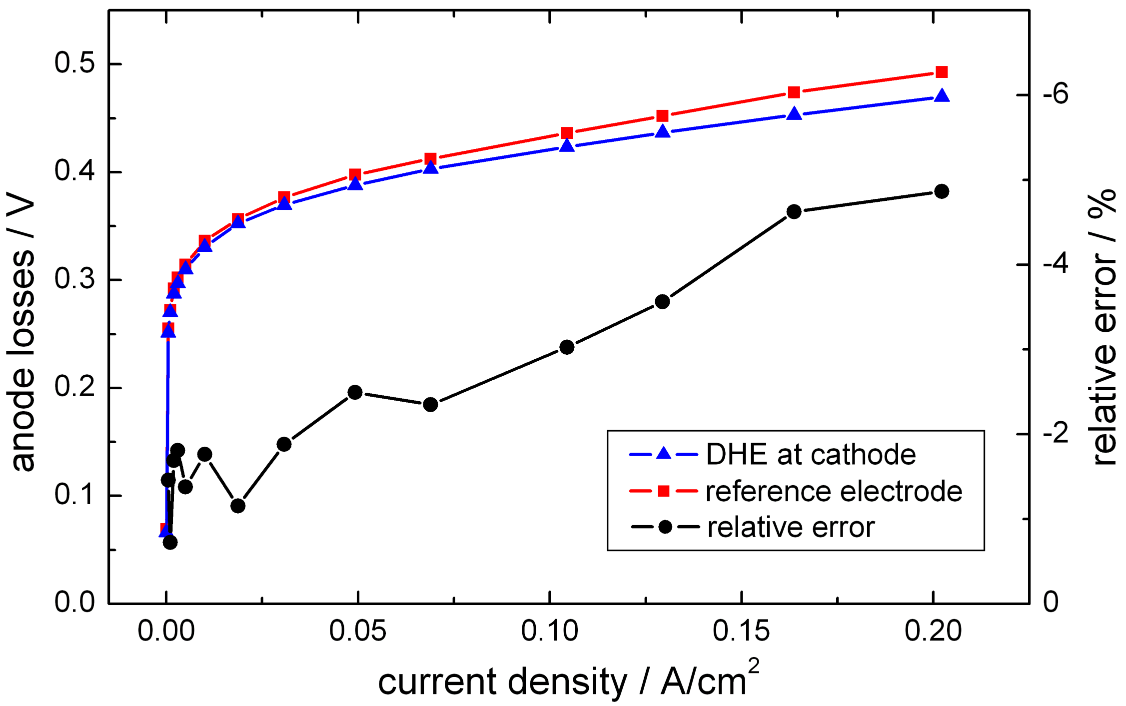

Figure A.7: Half–cell measurements using the misaligned electrodes of Fig. A.6. The voltage drop of the anode electrode was determined by both the DHE at the cathode and the reference electrode.

Inhomogeneous pressure on the cell

The influence of inhomogeneous pressure on the cell leading to deviations in the potential distribution was studied experimentally. In one experiment, the force applied to the side where the reference electrode had been printed was $3760\,\mathrm{N}$. The clamping force on the opposite site was $1966\,\mathrm{N}$. In all other experiments, a force of $2553\,\mathrm{N}$ was applied on both sides. A half–cell experiment at $50\,^{\circ}\mathrm{C}$ with hydrogen on the cathode side and methanol on the anode side was performed to study the impact of these inhomogeneities. The pressure distribution inside the cell, and specifically on the GDL, was not measured. Hence the results shown in Fig. A.8 are to be regarded qualitatively. A relative error which increased for current densities up to $0.15\,\mathrm{mA/cm^2}$ and then decreased again for higher current densities was calculated from measurement results. The parabolic form of the relative error versus the current density indicated that several effects overlap.

A second experiment was performed to study only the influence of different diffusivities of the GDL. GDLs that vary in thickness, porosity, or mechanical strength can cause different diffusivities. A small piece of GDL having a width of $2\,\mathrm{mm}$ and the same thickness and length as the cathode GDL was appended on the cathode side. It was aligned with the edge of the cathode GDL on the side of the reference electrode where higher pressure reduced the porosity. The experiment was performed with the same operating conditions at $50\,^{\circ}\mathrm{C}$. No relative error exceeding the deviations of the perfectly aligned and homogeneously pressurized case displayed in Fig. A.3

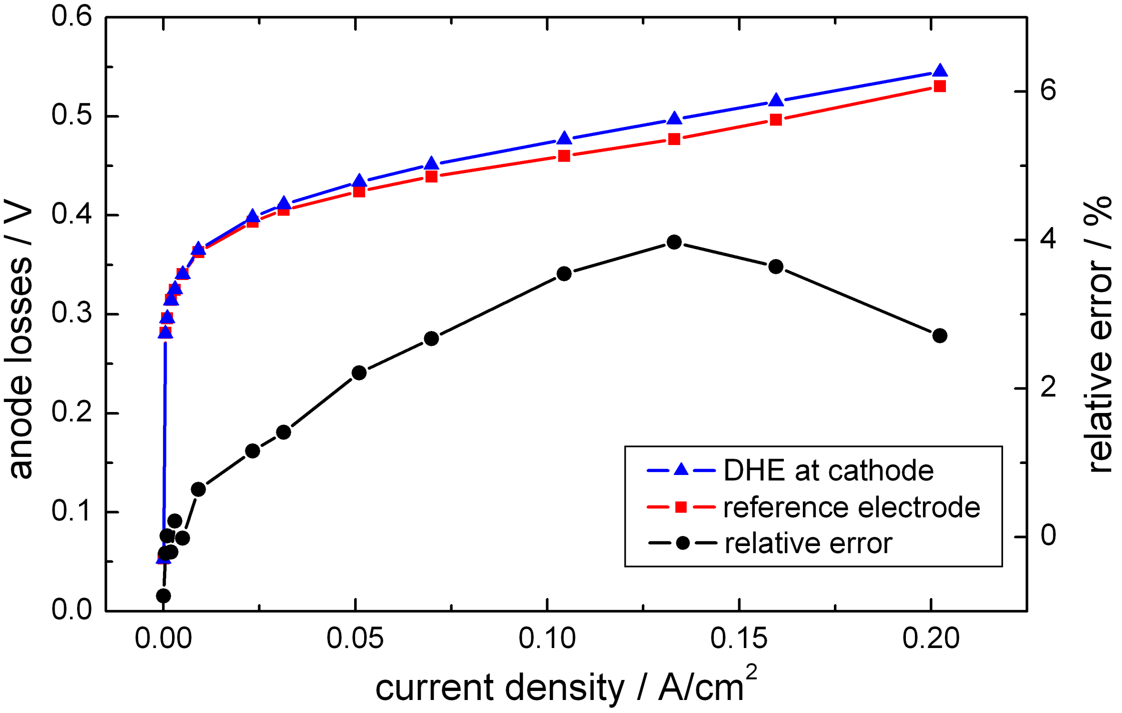

Figure A.8: Anode polarization losses deducted from the two readings of half–cell measurements with an inhomogeneous pressure applied to the cell. The side of the reference electrode was subjected to greater compression than the opposite side.

could be found. Therefore, either errors due to this kind of disturbance are negligible or the additional GDL on the cathode side also decreased the porosity of the anode GDL resulting again in a symmetric potential. Conversely, the compression might have been too weak to change the symmetry in the potential distribution. Simulations were carried out to study the influence of the porosity in more detail.

Fig. A.9 depicts simulation results for the relative error between a reference electrode sensing the middle of a symmetric potential distribution and a reference electrode sensing a non-symmetric potential due to different porosities inside the GDL. The potentials of the reference electrode were determined with the same set of parameters, except for the changing porosity of model domain Ω_{1b}. They were evaluated at a region of constant potential, far away from the disturbed cathode electrode. The voltage between the reference electrode and anode electrode, $U_{ref\_an-we\_an}$, was calculated according to eq. (A.20) and corrected for half of the ohmic drop of the fuel cell to obtain the anode electrode overpotentials. The porosity ϵ in model domain Ω_{1b} was varied from $12.5\,\%$ to $50\,\%$ of the value given in Table A.1; the domain Ω_{1b} was $300\,\mu\mathrm{m}$ long. No such influence was added to the anode side. Simulation results of anode overpotential where the porosity had the same value in Ω_{1a} and Ω_{1b} were taken as the reference case x. Anode polarization losses determined with a different porosity were taken as $\tilde{x}$ and the relative errors were calculated. It can

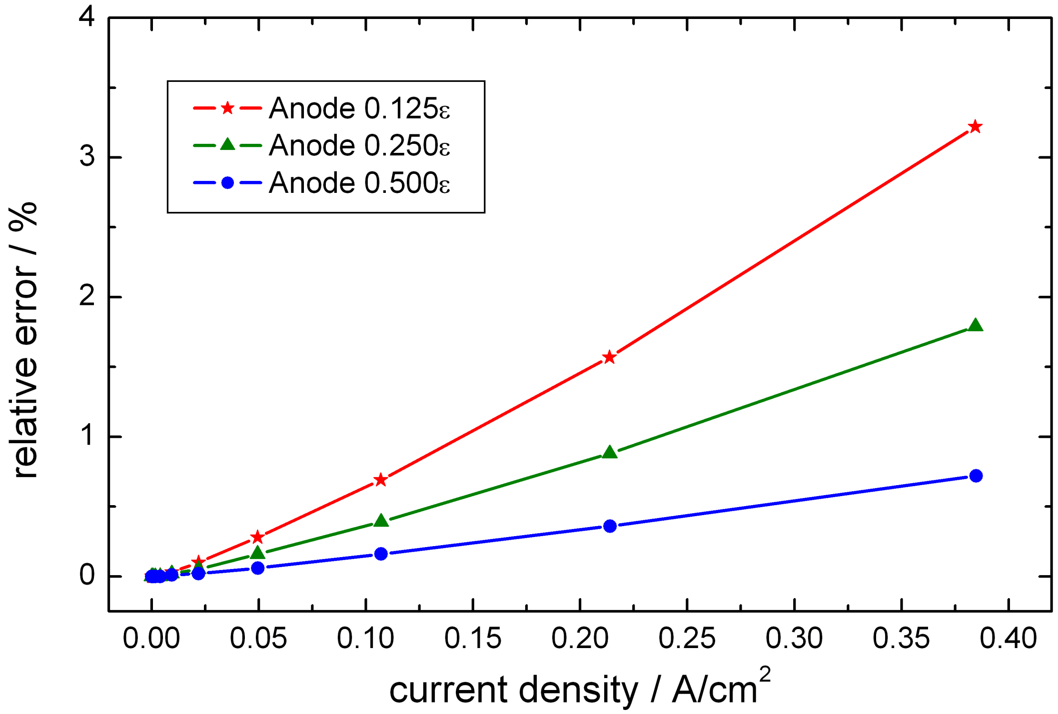

Figure A.9: Simulation results of different degrees of compressions of the GDL in model domain Ω_{1b}. *The relative errors of the anode polarization losses were calculated with respect to the symmetric potential distribution.*

be seen in the graph that significant relative errors occur only for very high additional compression of the GDL which greatly reduces porosity.

The effect of a changing porosity over a certain range is regarded to be minor because simulation results as well as experimental results do not show a great impact on the relative error. This conclusion is valid as long as areas are not completely blocked, as discussed in the following paragraph.

Obstruction of the GDL

Another difficulty in performing a measurement with a connected reference cell might occur when some parts of the GDL, especially at the interface to the reference electrode, are obstructed or blocked. Local flooding of the GDL can be one reason for this effect. Another more systematic effect can be induced during the assembly process, when the gasket is not fixed to the flowfield and moves onto the GDL. Assuming the case when the anode is perfectly assembled but the gasket on the cathode side is shifted onto the cathode GDL, two effects occur. First, the GDL is more compressed in this region due to the higher pressure. It has been shown in the previous section that this does not affect the reference readings considerably. Second, the GDL is obstructed with

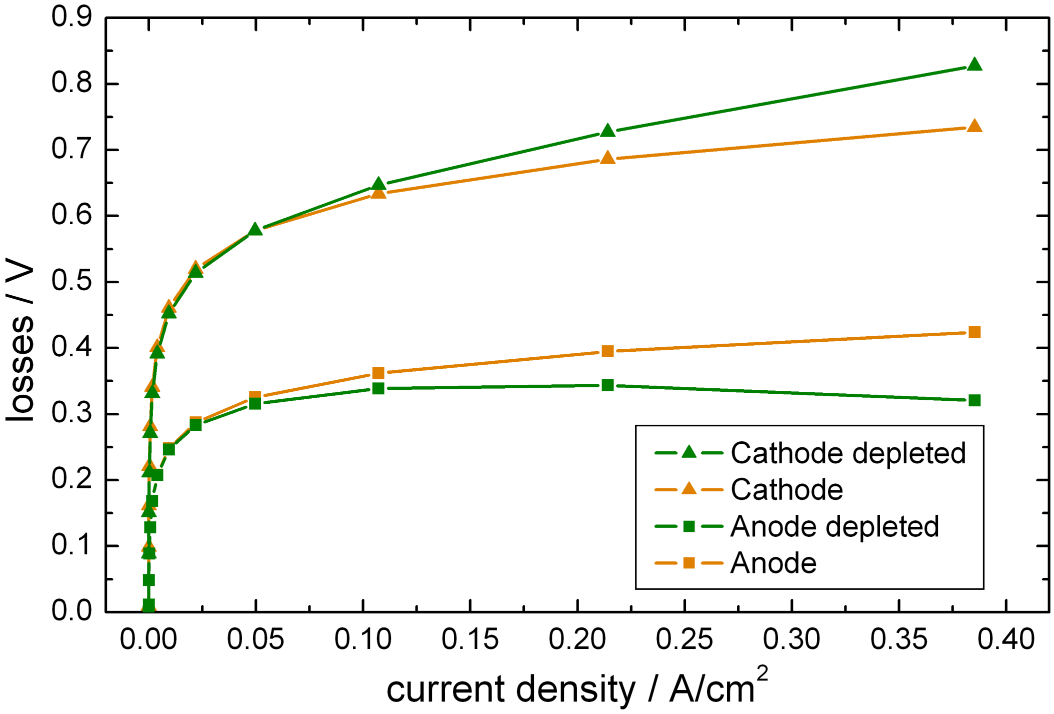

Figure A.10: Comparison of simulated anode and cathode overpotentials with and without an oxygen depletion at the boundary $\partial\Omega_{1b}$. This boundary had a length of 2 mm.

respect to the flowfield and oxygen can only diffuse in plane to the cathode electrode in this region. This leads to highly asymmetric potential distributions inside the membrane.

Fig. A.10 shows simulation results for anode and cathode polarization losses with and without oxygen depletion at the edge of the reference electrode. In the model it is assumed that the boundary $\partial\Omega_{1b}$ is impermeable for gases. Therefore it is set to zero flux conditions,

$$\partial N_{O2} \cdot \vec{n} = 0|_{\partial\Omega_{1b}} \tag{A.21}$$

The boundary $\partial\Omega_{1b}$ has a length of $2\,\mathrm{mm}$. Exposure to air is assumed at boundary $\partial\Omega_{1a}$, the molar fraction y_{O_2} is given in Table A.1. As mentioned in the previous section, the potentials of the reference electrode are determined at a region of constant potential far away from the (disturbed) cathode electrode. The voltage drops of the anode and cathode are calculated using eq. A.18–A.20. It can be seen that the anode polarization losses are highly underestimated and the cathode polarization losses highly overestimated with respect to the case without oxygen depletion.

The relative errors resulting from this deviation can be seen in Fig. A.11. Loss of anode potential without obstruction are taken as the true value x, results including obstructed areas as $\tilde{x}$. The relative error for the anode overpotential is depicted for different lengths of $\partial\Omega_{1b}$. As shown,

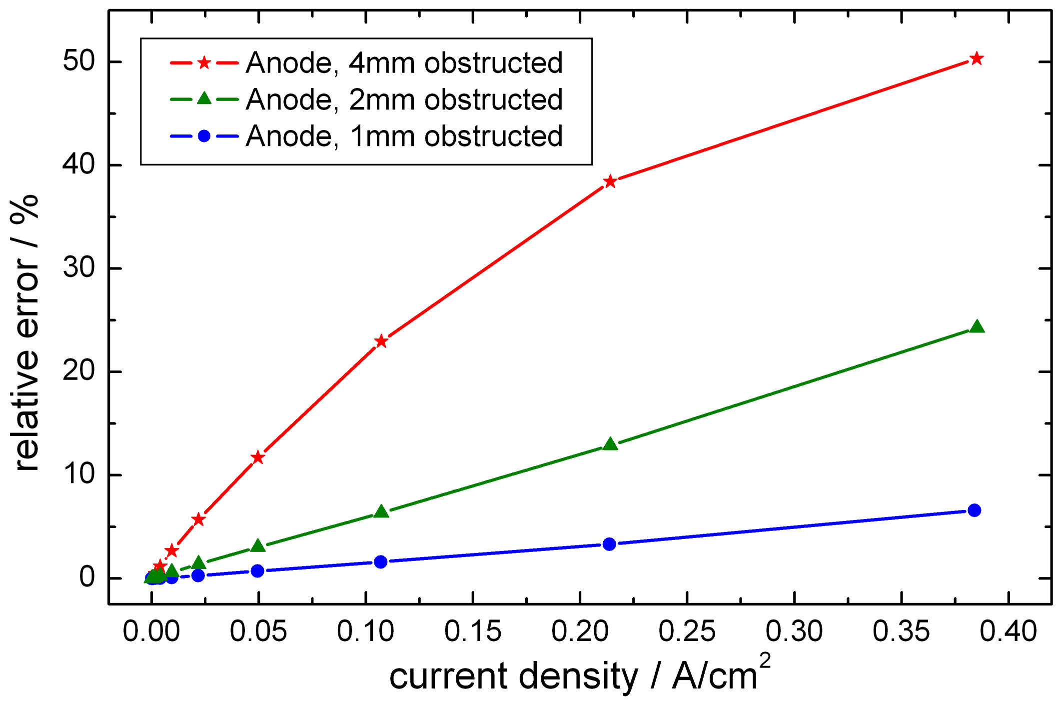

Figure A.11: Simulated relative errors compared to the symmetric case for the anode overpotential when the GDL was obstructed over different lengths at boundary $\partial\Omega_{1b}$.

obstruction of the cathode GDL of only $2\,\mathrm{mm}$ results in severe relative errors exceeding $10\,\%$ at $0.2\,\mathrm{A/cm^2}$. These errors are a result of the oxygen depletion in this area which leads to lower current densities as can be seen in the concentration–dependent term in eq. (A.3). Consequently the equipotential lines lose their symmetry inside the membrane. Larger obstructed areas lead to stronger deviations from the symmetric potential disribution resulting in larger errors when using the reference readings.

Experiments were performed to verify the model predictions. A small piece of sealing material was placed on the cathode GDL next to the gasket at the side of the reference electrode. It had a width of $4\,\mathrm{mm}$, a thickness of $1\,\mathrm{mm}$ and the same length as the GDL. After assembling the cell, this part of the GDL was obstructed due to the extra sealing material and no oxygen could diffuse perpendicularly to or from the cathode flowfield. Additionally the GDL was more compressed due to the thickness of the sealing material and the porosity was lowered because of a higher pressure in this region. Results of a half–cell experiment performed at $50\,^\circ\mathrm{C}$ can be seen in Fig. A.12. A great deviation between the measurements of the DHE at the cathode electrode and the connected reference electrode can be seen. The relative error is very high and exceeds $20\,\%$ at $0.2\,\mathrm{mA/cm^2}$ as predicted in the simulation results.

Obstructing parts of the GDL, thereby preventing the reactants from diffusing perpendicularly to the electrodes, can cause considerable changes in the potential distribution. If this happens at the boundary to the reference electrode, e.g. because of a shifted gasket, the reference readings cannot

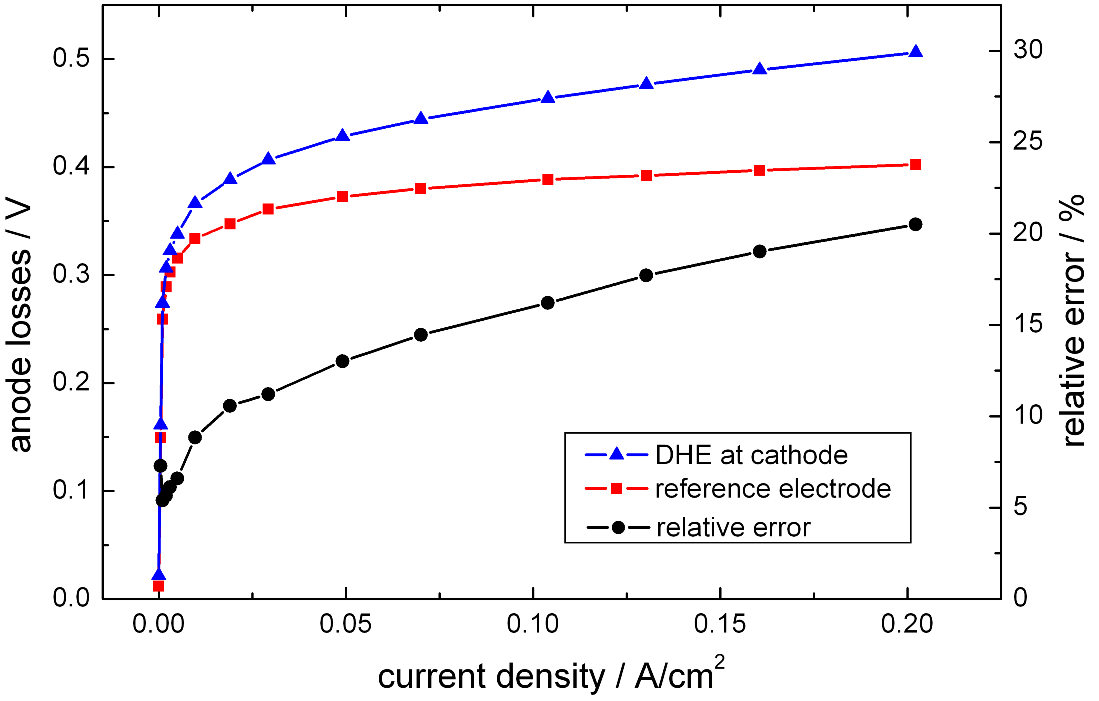

Figure A.12: Depletion of oxygen and an inhomogeneous contact pressure due to a piece of sealing material on the GDL in a half–cell experiment. The relative errors derived from anode polarization losses were calculated using the cathodic DHE and the reference electrode.

be corrected for half of the ohmic losses. Otherwise large overestimations or underestimations of the anode and cathode polarization losses respectively will be made. As a consequence of these results, one can conclude that the anode and cathode flowfields should have the same dimensions to prevent boundary effects due to different rib positions. Additionally it must be ensured that no flooding on the cathode side occurs, e.g. by using sufficiently high stoichiometries for the air flow rate.

A.3.2 Stability of the reference electrode

Besides errors due to an inhomogeneous potential distribution at the working electrode, a drift or an instability of the reference electrode potential itself can cause errors in calculating the overpotentials of the working electrode. Unlike the DHE, the NHE used for the reference cell usually does not show a drift over time. Experiments were performed to check the stability of the reference cell. Hydrogen was supplied to the cathode during half–cell operation so that the cathode working electrode acted as a DHE. On comparing these values to the reference readings, it was observed that the reference cell displayed unstable behavior.

Results of these half–cell measurements at different cell temperatures can be seen in Fig. A.13. Hydrogen for the reference cell was humidified using a vapor liquid equilibrium chamber at ambient

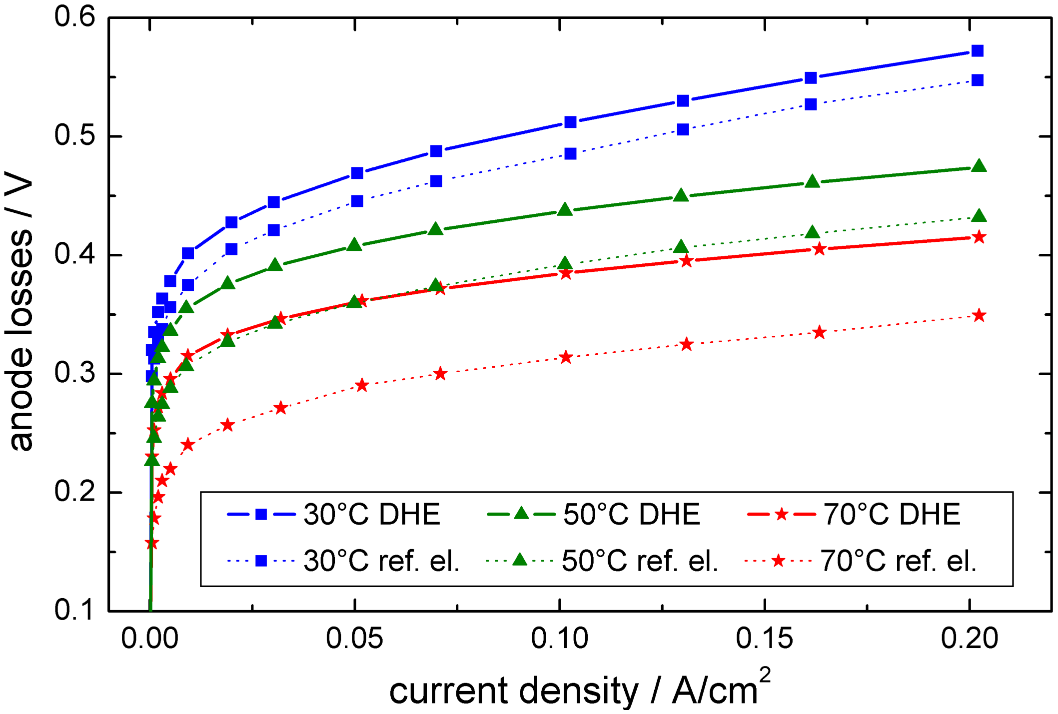

Figure A.13: Anode polarization losses determined by the DHE of the cathode and the reference electrode during half–cell operation at different cell temperatures. A 0.5 M solution of methanol was fed at 1.5 ml/min to the anode.

temperatures. The anode polarization losses were determined by both the DHE and the reference electrode. A temperature–dependent offset of the overpotentials was seen that was determined by the reference cell and increased with temperature. This offset did not change with current and displayed only a temperature dependence. Additional experiments were performed to study these phenomena in detail.

The fuel cell was heated to $50\,^\circ\mathrm{C}$ and a small current of $10\,\mathrm{mA}$ was imprinted using the external power supply to guarantee a constant coverage of the cathode catalyst with hydrogen during the half–cell operation. The hydrogen supply of the reference cell was connected to a temperature–controlled gas humidifier. The connection to the reference cell was heated $5\,^\circ\mathrm{C}$ above the humidifier temperature to prevent condensation inside the tubes. Fig. A.14 depicts the difference between the DHE and the reference electrode for different temperatures of the humidifier. The difference decreased with increasing humidifier temperature. Thus the potential of the reference electrode appeared to be dependent on the humidification of the supplied hydrogen. This was also found by Stähler [148]. He proposed an equilibrium reaction at the hydrogen electrode.

$$2\mathrm{H_3O^+} + 2\mathrm{e^-} \longleftrightarrow \mathrm{H_2} + 2\mathrm{H_2O} \tag{A.22}$$

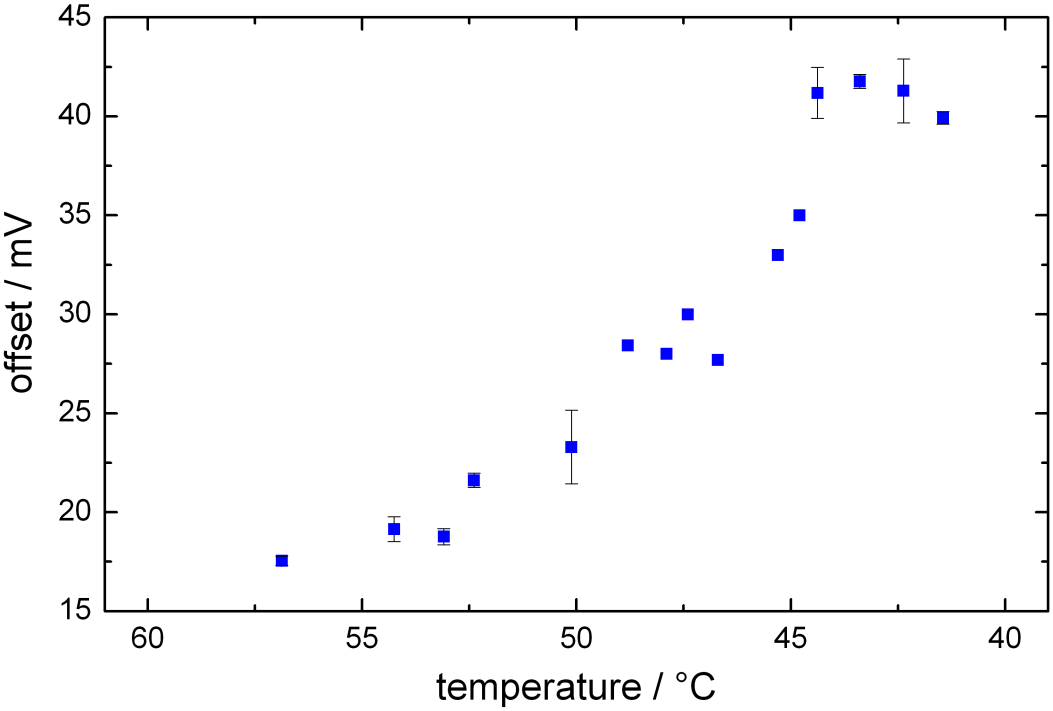

Figure A.14: Difference between the values of the cathode DHE and the reference cell. Hydrogen supplied to the reference cell was humidified at different temperatures. The fuel cell temperature was 50 °C, a 0.5 M solution of methanol was fed to the anode at 1.5 ml/min.

The Nernst equation at a thermodynamically equilibrated mixture of hydrogen and water predicts that the partial pressure of water and the proton activity within the ionomer phase will both influence the potential of the reference electrode.

The DHE on the cathode side during half–cell measurements did not show a drift at different cell temperatures. The membrane was well humidified as it was in contact with a liquid methanol solution at the anode. This concept was transferred to the reference cell. One side was flooded with distilled water and hydrogen was supplied to the other side. The difference between the DHE and the reference electrode vanished and the reference cell potential remained stable when the fuel cell temperature was changed.

A.3.3 Full–cell operation

In order to separate the different losses of a DMFC, half–cell experiments are often used to determine the anode polarization losses [63, 64, 68, 149]. Full–cell experiments are performed additionally to get the complete polarization plots. When the ohmic resistances are known as well, the cathode polarization losses can be calculated according to eq. (2.29). There are several obstacles in determining the voltage drops of the electrodes using this method. Since the anode overpotential and the cathode overpotential are determined in two consecutive experiments, the conditions in-

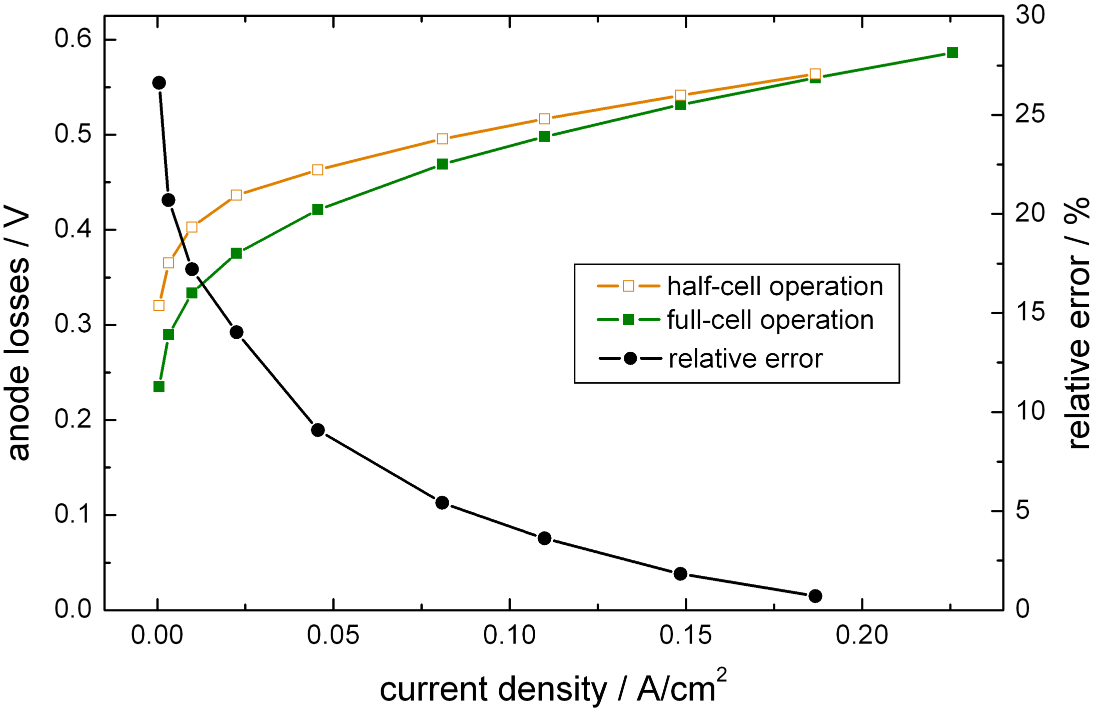

Figure A.15: Anode polarization losses determined by the DHE of a half–cell experiment in comparison to anode polarization losses determined with the reference electrode in full–cell operation. The fuel cell temperature was 30 °C, a 0.5 M solution of methanol was fed to the anode at 1.5 ml/min.

side the fuel cell may have changed between the first and the second experiment. If this happens, the calculated voltage drop of the cathode can differ considerably from the real values. Additionally, since only steady–state experiments can be conducted, the dynamic behavior of the electrode polarization losses cannot be studied.

Experiments for both half–cell and full–cell operation were performed. The anode overpotentials were calculated for each in order to see whether deviations between the two operating conditions occur. The cell temperature was kept constant at $30\,^\circ$C. In full–cell operation, ambient air was supplied to the cathode at a stoichiometry of 6. The relative error was calculated using eq. (A.16). The polarization losses determined by half–cell measurements were taken as the true value x, the polarization losses determined by full–cell operation as the biased values $\tilde{x}$.

A large error in the anode overpotentials can be seen in Fig. A.15 for small current densities, up to $25\,\%$ at OCV. The error function decreases exponentially with increasing current density. Thus, one must be very careful when drawing conclusions about electrode polarization losses when only half–cell measurements are available.

One uncertainty regarding this method is the extent to which half–cell operation of a DMFC can be compared to a full–cell operation. With respect to half–cell experiments, hydrogen can cross over from the cathode to the anode side. This phenomenon was studied by Tapan et al. [65]. He found

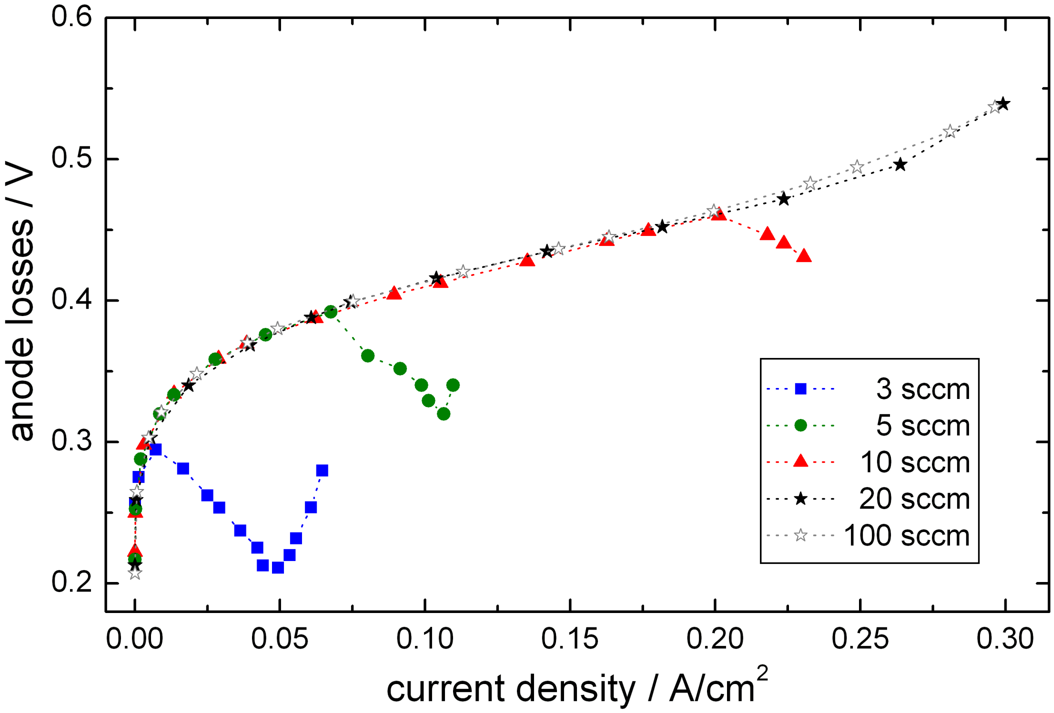

Figure A.16: Anode overpotentials determined by a reference electrode at different cathode oxygen flow rates. A 0.5 M solution of methanol was fed to the anode at 1.5 ml/min. The fuel cell was heated to 50 °C.

a deviation of $50\,\mathrm{mV}$ at $0.22\,\mathrm{A/cm^2}$ between half–cell experiments with hydrogen and with argon supplied to the cathode flowfield. Taking the argon experiment as the true value, this corresponds to a relative error of approximately $8.5\,\%$, which cannot be regarded as insignificant. However, the paper did not study in detail whether this deviation could also be a result of the DHE at the cathode electrode not being completely covered with hydrogen. During full–cell operation, crossover of oxygen to the anode can also occur, changing the MOR. Additionally, a hydrogen evolution reaction at the anode appears at low current densities and low oxygen flow rates [150, 151]. Electrolysis takes place at parts of the cell that are depleted of oxygen. This electrolysis is driven by the local fuel cell voltage at oxygen–rich parts of the cell [152]. Hydrogen that is produced at the anode might lead to a potential of hydrogen or a mixed potential of hydrogen and methanol at the electrode and thus influence the anode polarization.

Experiments were carried out to investigate these additional effects. Hydrogen or oxygen were mixed with the methanol stream before it entered the anode compartment during half–cell experiments. The gases with a flow rate of $3\,\mathrm{sccm}$ were added to the methanol stream with a flow rate of $1.5\,\mathrm{ml/min}$ via a y–connector. No deviation of the anode overpotentials compared to normal half–cell operation was found for either gas. Gas crossing over within a working fuel cell is in close proximity to the catalyst layer and can interact with the catalyst sites. This could not be guaranteed during these experiments.

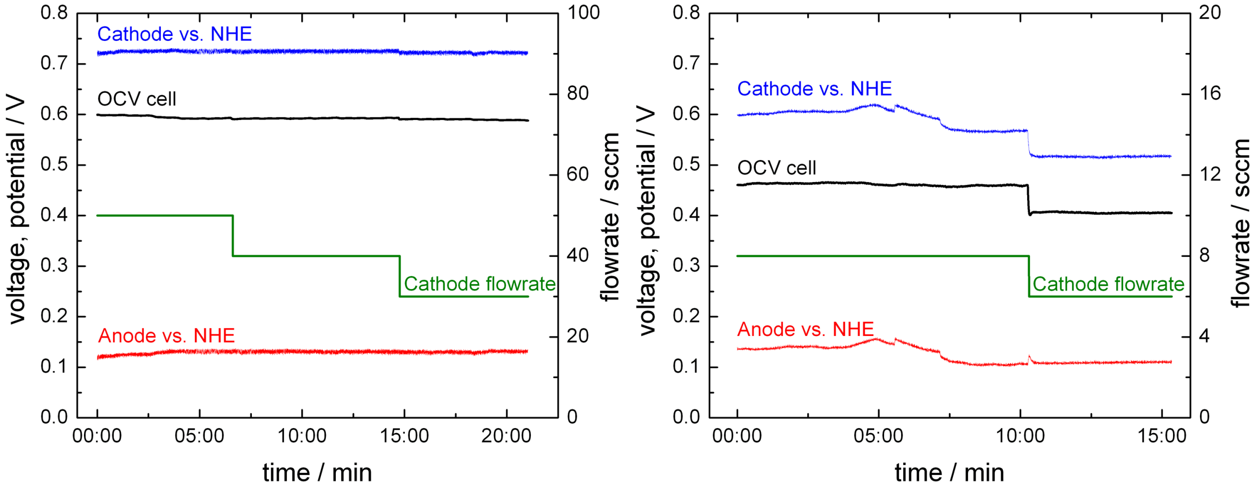

Figure A.17: OCV and reference readings of the anode and cathode electrode over time at different cathode air flow rates. The cell was kept at 50 °C, a 0.5 M solution of methanol was supplied at 1.5 ml/min to the anode.

The evolution of hydrogen inside the anode catalyst layer was forced in another experiment during full–cell operation of the DMFC. A $0.5\,\mathrm{M}$ solution of methanol was fed to the anode at $1.5\,\mathrm{ml/min}$. The fuel cell was heated to $50\,^\circ\mathrm{C}$. Dry oxygen was supplied to the cathode at low flow rates and varied between $3\,\mathrm{sccm}$ and $100\,\mathrm{sccm}$. The anode overpotentials at different cathode flow rates can be seen in Fig. A.16. At a certain cell current density, a decline of the voltage drop of the anode can be seen for 3, 5 and $10\,\mathrm{sccm}$. The current density, where the decline begins, increases with flow rate. At these current densities, formation of bubbles within the anode outlet stream can be observed. At cathode streams greater than $20\,\mathrm{sccm}$ no such effects can be observed. The anode polarization losses also stay the same for a 5-times higher air flow rate of $100\,\mathrm{sccm}$. It can be concluded that the formation of hydrogen, especially formation close to the reference electrode, greatly affects the potential distribution and thus the calculated anode polarization losses. As the hydrogen evolution was not homogeneously distributed over the whole anode catalyst layer, one must be very careful in quantitatively evaluating the reference readings.

Results displayed in Fig. A.17 reveal another effect at low cathode flow rates. Here the OCV of a DMFC for changing cathode air flow rates is displayed over time. Again the cell was kept at $50\,^\circ\mathrm{C}$ and a $0.5\,\mathrm{M}$ solution of methanol was supplied at $1.5\,\mathrm{ml/min}$ to the anode. The scale for the cathode flow rates is shown by the right axes of the graph. It can be seen in the left graph that decreasing the cathode air supply did not affect the cell potential and the reference readings down to an air flow of $30\,\mathrm{sccm}$. The right graph depicts the OCV and the reference readings at very low flow rates of $8\,\mathrm{sccm}$ and $6\,\mathrm{sccm}$. At approximately $5\,\mathrm{min}$, an unstable increase and decrease of the reference readings can be seen. This occurred simultaneously for the anode and cathode readings and in the same direction. Since the OCV of the fuel cell was constant during that time, it can be concluded that the symmetric potential distribution at the working electrodes was disturbed during that time. Most likely a water droplet was forming at the cathode electrode close to the reference cell, as no bubbles in the anode outlet stream indicated a hydrogen evolution reaction within the fuel cell. The droplet locally influenced the potential of the working electrode and thus changed the reference readings. Also, a drift of both reference readings toward lower values was noted. At 10 min, the air flow rate was reduced to 6 sccm, which lowered the cathode potential and consequently the OCV dropped. Here the reference readings were working correctly again but yielded an offset of 20 mV. This demonstrates that at low cathode flow rates, a symmetric potential distribution within the ionomer cannot be guaranteed.

List of Tables

List of Figures

Bibliography

[1] Frost&Sullivan. World Micro Fuel Cell Markets for Consumer Portable Devices. Market engineering research, Frost & Sullivan 2400 Geng Road, Suite 201 Palo Alto, CA 94303-3331 USA, 05.10.2006 2006.

[2] A. Heinzel, C. Hebling, M. Muller, M. Zedda, and C. Muller. Fuel cells for low power applications. *Journal of Power Sources*, 105(2):250–255, 2002.

[3] A. Schmitz, M. Tranitz, S. Wagner, R. Hahn, and C. Hebling. Planar self-breathing fuel cells. *Journal of Power Sources*, 118:162–171, 2003.

[4] www.HFPeurope.org. European Hydrogen & Fuel Cell Technology Platform: Strategic Research Agenda. Technical report, 2005.

[5] D. Linden and T. B. Reddy. *Handbook of batteries*. McGraw-Hill, New York, 3rd edition, 2002.

[6] P. Atkins. *Physical chemistry*. Oxford University Press, 3. ed. edition, 1986.

[7] R. Dillon, S. Srinivasan, A. Arico, and V. Antonucci. International activities in DMFC R&D: status of technologies and potential applications. *Journal of Power Sources*, 127:112–126, 2004.

[8] J.-H. Wee. Which type of fuel cell is more competitive for portable application: Direct methanol fuel cells or direct borohydride fuel cells? *Journal of Power Sources*, 161(1):1–10, 2006.

[9] W. Qian, D. Wilkinson, J. Shen, H. Wang, and J. Zhang. Architecture for portable direct liquid fuel cells. *Journal of Power Sources*, 154(1):202–213, 2006.

[10] S. K. Kamarudin, W. R. W. Daud, S. L. Ho, and U. A. Hasran. Overview on the challenges and developments of micro-direct methanol fuel cells (DMFC). *Journal of Power Sources*, 163(2):743–754, 2007.

[11] R. Edinger, G. Isenberg, and B. Hoehlein. Methanol from fossil and renewable resources. In W. Vielstich, H. Gasteiger, and A. Lamm, editors, *Handbook of fuel cells - Fundamentals, Technology and Applications*, volume 3, pages 39–48. John Wiley & Sons, Ltd., 2003.

[12] M. Specht, A. Bandi, E. Mennenkamp, K. Schaber, and T. Weimer. Liquid fuels from hydrogen and atmospheric CO2, a climate-neutral energy concept. In *11th World Hydrogen Energy Conference*, volume 2, pages 1311–1315, Stuttgart, Germany, 1996. DECHEMA.

[13] E. Peled, T. Duvdevani, A. Aharon, and A. Melman. A direct methanol fuel cell based on a novel low-cost nanoporous proton-conducting membrane. *Electrochemical and Solid-State Letters*, 3(12):525–528, 2000.

[14] N. Miyake, J. S. Wainright, and R. F. Savinell. Evaluation of a sol-gel derived Nafion/silica hybrid membrane for polymer electrolyte membrane fuel cell applications II. Methanol uptake and methanol permeability. *Journal of the Electrochemical Society*, 148(8):A905–A909, 2001.

[15] L. Li, J. Zhang, and Y. Wang. Sulfonated poly(ether ether ketone) membranes for direct methanol fuel cell. *Journal of Membrane Science*, 226(1-2):159–167, 2003.

[16] T. Ioroi, K. Kuraoka, K. Yasuda, T. Yazawa, and Y. Miyazaki. Surface-modified nanopore glass membrane as electrolyte for DMFCs. *Electrochemical and Solid-State Letters*, 7(11):A394–A396, 2004.

[17] H. Kim, H. Kim, Y. Shul, and H. Han. Nafion-Nafion/polyvinylidene fluoride-Nafion laminated polymer membrane for direct methanol fuel cells. *Journal of Power Sources*, 135(1-2):66–71, 2004.

[18] W. Harrison, M. Hickner, Y. Kim, and J. McGrath. Poly(arylene ether sulfone) copolymers and related systems from disulfonated monomer building blocks: Synthesis, characterization, and performance - a topical review. *Fuel Cells*, 5(2):201–212, 2005.

[19] R. Thangamuthu and C. Lin. DBSA-doped PEG/SiO(sub 2) proton-conducting hybrid membranes for low- temperature fuel cell applications. *Solid State Ionics, Diffusion & Reactions*, 176(5-6):531–538, 2005.

[20] R. Wycisk, J. Lee, and P. Pintauro. Sulfonated polyphosphazene-polybenzimidazole membranes for DMFCs. *Journal of the Electrochemical Society*, 152(5):A892–898, 2005.

[21] P. Kalappa and J.-H. Lee. Proton conducting membranes based on sulfonated poly(ether ether ketone)/TiO2 nanocomposites for a direct methanol fuel cell. *Polymer International*, 56(3):371–375, 2007.

[22] B. Lee, d. Junga, and Y. Kob. Analysis of DMFC/battery hybrid power system for portable applications. *Journal of Power Sources*, 131:207–212, 2004.

[23] C. Xie, J. Bostaph, and J. Pavio. Development of a 2W direct methanol fuel cell power source. *Journal of Power Sources*, 136(1-2):55–65, 2004.

[24] A. Oedegaard and C. Hentschel. Characterisation of a portable DMFC stack and a methanol-feeding concept. *Journal of Power Sources*, 158(1):177–187, 2006.

[25] J. Bostaph, R. Koripella, A. Fisher, D. Zindel, J. Hallmark, J. Neutzler, and L. Bai. Microfluidic fuel delivery system for 100 mW DMFC. In *Direct Methanol Fuel Cells. Proceedings of the*

International Symposium, volume 2001, viii+350, pages 274–285, Narayanan, 2001. Electrochemical Society Proceedings.

[26] J. Pavio, J. Bostaph, A. Fisher, J. Hallmark, B. Mylan, and X. Chenggang. LTCC fuel cell system for portable wireless electronics. *Advancing Microelectronics*, 29(5):8–11, 2002.

[27] N. Nakagawa and Y. Xiu. Performance of a direct methanol fuel cell operated at atmospheric pressure. *Journal of Power Sources*, 118:248–255, 2003.

[28] M. Abdelkareem and N. Nakagawa. DMFC employing a porous plate for an efficient operation at high methanol concentrations. *Journal of Power Sources*, 162(1):114–123, 2006.

[29] W.-J. Kim, H.-G. Choi, Y.-K. Lee, J.-D. Nam, S. M. Cho, and C.-H. Chung. Hydrogels in methanol fuel cartridge used as a diffusion-rate-controlling agent suppressing the methanol crossover in passively operated flat-pack type DMFCs. *Journal of Power Sources*, 157(1):193–195, 2006.

[30] C. Chen and P. Yang. Performance of an air-breathing direct methanol fuel cell. *Journal of Power Sources*, 123:37–42, 2003.

[31] T. Shimizu, T. Momma, M. Mohamedi, T. Osaka, and S. Sarangapanic. Design and fabrication of pumpless small direct methanol fuel cells for portable applications. *Journal of Power Sources*, 137(2):277–283, 2004.

[32] G. Q. Lu, P. C. Lim, F. Q. Liu, and C. Y. Wang. On mass transport in an air-breathing DMFC stack. *International Journal of Energy Research*, 29(12):1041–1050, 2005.

[33] J. G. Liu, T. S. Zhao, Z. X. Liang, and R. Chen. Effect of membrane thickness on the performance and efficiency of passive direct methanol fuel cells. *Journal of Power Sources*, 153(1):61–67, 2006.

[34] T. Yen, N. Fang, X. Zhang, G. Lu, and C. Wang. A micro methanol fuel cell operating at near room temperature. *Applied Physics Letters*, 83(9):4056–4058, 2003.

[35] G. Lu, C. Wang, T. Yenb, and X. Zhangb. Development and characterization of a silicon-based micro direct methanol fuel cell. *Electrochimica Acta*, 49(5):821–828, 2004.

[36] K. Wozniak, D. Johansson, M. Bring, A. Sanz-Velasco, and P. Enoksson. A micro direct methanol fuel cell demonstrator. *Journal of Micromechanics and Microengineering*, 14(9):59–63, 2004.

[37] Y. Jiang, X. Wang, X. Qiu, L. Zhong, Y. Zhou, Z. Wang, and L. Liu. Design, fabrication, and testing of a silicon-based air-breathing micro direct methanol fuel cell. In *PowerMEMS 2005, 5th International Workshop on Micro and Nanotechnology for Power Generation and Energy Conversion Applications, Technical Digest*, volume 5, pages 120–123, Tokyo, JP, 2005.

[38] S.-C. Yao, X. Tang, C.-C. Hsieh, Y. Alyousef, M. Vladimer, G. K. Fedder, and C. H. Amon. Micro-electro-mechanical systems (MEMS)-based micro-scale direct methanol fuel cell development. *Energy (Amsterdam, Netherlands)*, 31(5):636–649, 2006.

[39] J. Han and E. Park. Direct methanol fuel-cell combined with a small back-up battery. *Journal of Power Sources*, 112(2):477–483, 2002.

[40] B. Bae, B. K. Kho, T.-H. Lim, I.-H. Oh, S.-A. Hong, and H. Y. Ha. Performance evaluation of passive DMFC single cells. *Journal of Power Sources*, 158(2):1256–1261, 2006.

[41] T. S. Zhao and Q. Ye. A natural-circulation fuel delivery system for direct methanol fuel cells. *Journal of Power Sources*, 147(1-2):196–202, 2005.

[42] Z. Guo and A. Faghri. Miniature DMFCs with passive thermal-fluids management system. *Journal of Power Sources*, 160(2):1142–1155, 2006.

[43] K. Kordesch and G. Simader. *Fuel cells and their applications*. VCH, Weinheim, 1996.

[44] J. Larminie and A. Dicks. *Fuel cell systems explained*. J. Wiley, New York, 2nd edition, 2003.

[45] W. Vielstich, A. Lamm, and H. A. Gasteiger. *Handbook of fuel cells : fundamentals, technology, and applications*. Wiley, Chichester, England ; New York, 2003.

[46] L. J. M. J. Blomen and M. N. Mugerwa. *Fuel cell systems*. Plenum Press, New York, 1993.

[47] J. Kallo, J. Kamara, W. Lehnert, and R. Helmolt. Cell voltage transients of a gas-fed direct methanol fuel cell. *Journal of Power Sources*, 127:181–186, 2004.

[48] S. Swathirajan and Y. M. Mikhail. Electrochemical oxidation of methanol at chemically prepared platinum-ruthenium alloy electrodes. *Journal of the Electrochemical Society*, 138(5):1321–6, 1991.

[49] S. Wasmus and A. Kuver. Methanol oxidation and direct methanol fuel cells: a selective review. *Journal of Electroanalytical Chemistry*, 461(1,2):14–31, 1999.

[50] A. Hamnett. Direct methanol fuel cells (DMFC). In Wolf Vielstich, Arnold Lamm, and Hubert A. Gasteiger, editors, *Handbook of fuel cells : fundamentals, technology, and applications*, volume 1, pages 305–322. Wiley, Chichester, England ; New York, 2003.

[51] V. S. Bagotzky, Y. B. Vassiliev, and O. A. Khazova. Generalized scheme of chemisorption, electrooxidation and electroreduction of simple organic compounds on platinum group metals. *Journal of Electroanalytical Chemistry*, 81(2):229–238, 1977.

[52] T. Iwasita-Vielstich. Progress in the Study of Methanol Oxidation. In H. Gerischer and C. Tolias, editors, *Advances in Electrochemical Science and Engineering*, pages 127–170. 1990.

[53] C. Lamy, J.-M. Leger, and S. Srinivasan. Direct methanol fuel cells: From a twentieth century electrochemist's dream to a twenty-first century emerging technology. *Modern Aspects of Electrochemistry*, 34:53–118, 2001.

[54] H. Wang, T. Loffler, and H. Baltruschat. Formation of intermediates during methanol oxidation: a quantitative DEMS study. *Journal of Applied Electrochemistry*, 31(7):759–765, 2001.

[55] C. H. Hamann, A. Hamnett, and W. Vielstich. *Electrochemistry*. Wiley-VCH, Weinheim ; New York, 1998.

[56] J. Kallo. *Untersuchung der stationaeren und dynamischen Eigenschaften einer gasfoermig versorgten Direkt Methanol Brennstoffzelle*. Dissertation, Universitaet Ulm, 2003.

[57] K. J. Vetter. *Electrochemical kinetics : theoretical and experimental aspects*. Academic Press, New York, 1967.

[58] A. Kuever, I. Vogel, and W. Vielstich. Distinct performance evaluation of a direct methanol SPE fuel cell. A new method using a dynamic hydrogen reference electrode. *Journal of Power Sources*, 52(1):77–80, 1994.

[59] X. Ren, T. Springer, and S. Gottesfeld. Water and Methanol Uptakes in Nafion Membranes and Membrane Effects on Direct Methanol Cell Performance. *Journal of the Electrochemical Society*, 147(1):92–98, 2000.

[60] G. Li and P. Pickup. Measurement of single electrode potentials and impedances in hydrogen and direct methanol PEM fuel cells. *Electrochimica Acta*, 49(24):4119–4126, 2004.

[61] W. He and T. Nguyen. Edge Effects on Reference Electrode Measurements in PEM Fuel Cells. *Journal of The Electrochemical Society*, 151(2):A185–A195, 2004.

[62] S. Adler, B. Henderson, M. Wilson, D. Taylor, and R. Richards. Reference electrode placement and seals in electrochemical oxygen generators. *Solid State Ionics, Diffusion & Reactions*, 134(1-2):35–42, 2000.

[63] B. Gurau and E. Smotkin. Methanol crossover in direct methanol fuel cells: a link between power and energy density. *Journal of Power Sources*, 112(2):339–352, 2002.

[64] J. Amphlett, B. Peppley, E. Halliop, and A. Sadiq. The effect of anode flow characteristics and temperature on the performance of a direct methanol fuel cell. *Journal of Power Sources*, 96(1):204–213, 2001.

[65] N. Tapan, W. Mustain, B. Gurau, G. Sandi, and J. Prakash. Investigation of methanol oxidation electrokinetics on Pt using the asymmetric electrode technique. *Journal of New Materials for Electrochemical Systems*, 7(4):281–286, 2004.

[66] C. L. Green and A. Kucernak. Determination of the Platinum and Ruthenium Surface Areas in Platinum-Ruthenium Alloy Electrocatalysts by Underpotential Deposition of Copper. I. Unsupported Catalysts. *Journal of Physical Chemistry B*, 106(5):1036–1047, 2002.

[67] J. Diard, N. Glandut, P. LandaudÂ´, B. Le Gorrec, and C. Montella. A method for determining anode and cathode impedances of a direct methanol fuel cell running on a load. *Electrochimica Acta*, 48(5):555–562, 2003.

[68] A. Oedegaard. Characterisation of direct methanol fuel cells under near-ambient conditions. *Journal of Power Sources*, 157(1):244–252, 2006.

[69] K. Wippermann, B. Richter, K. Klafki, J. Mergel, G. Zehl, I. Dorbandt, P. Bogdanoff, S. Fiechter, and S. Kaytakoglu. Carbon Spported Ru-Se as Methanol Tolerant Catalysts for DMFC Cathodes. Part II: Preparation and Characterization of MEAs. *Journal of Applied Electrochemistry*, online, 2007.

[70] Z. Liu, J. Wainright, W. Huang, and R. Savinell. Positioning the reference electrode in proton exchange membrane fuel cells: calculations of primary and secondary current distribution. *Electrochimica Acta*, 49(6):923–935, 2003.

[71] F. Meier, S. Denz, A. Weller, and G. Eigenberger. Analysis of direct methanol fuel cell (DMFC)-performance via FTIR spectroscopy of cathode exhaust. *Fuel Cells*, 3(4):161–168, 2003.

[72] W. Vielstich, V. A. Paganin, F. H. B. Lima, and E. A. Ticianelli. Nonelectrochemical pathway of methanol oxidation at a platinum-catalyzed oxygen gas diffusion electrode. *Journal of the Electrochemical Society*, 148(5):A502–A505, 2001.

[73] H. Dohle, J. Divisek, J. Mergel, H. Oetjen, C. Zingler, and D. Stolten. Recent developments of the measurement of the methanol permeation in a direct methanol fuel cell. *Journal of Power Sources*, 105(2):274–282, 2002.

[74] Z. Qi and A. Kaufman. Open circuit voltage and methanol crossover in DMFCs. *Journal of Power Sources*, 110(1):177–185, 2002.

[75] A. Kuever and W. Vielstich. Investigation of methanol crossover and single electrode performance during PEMDMFC operation: a study using a solid polymer electrolyte membrane fuel cell system. *Journal of Power Sources*, 74(3):211–218, 1998.

[76] S. Song, W. Zhou, W. Li, G. Sun, Q. Xin, S. Kontou, and P. Tsiakaras. Direct methanol fuel cells: methanol crossover and its influence on single DMFC performance. *Ionics*, 10(5-6):458–462, 2004.

[77] P. Gravesen, J. Branebjerg, and O. Soendergaard Jensen. Microfluidics - a review. *Journal of Micromechanics and Microengineering*, 3(4):168–82, 1993.

[78] K. Scott, W. M. Taama, and P. Argyropoulos. Material aspects of the liquid feed direct methanol fuel cell. *Journal of Applied Electrochemistry*, 28(12):1389–1397, 1998.

[79] J. Ge and H. Liu. Experimental studies of a direct methanol fuel cell. *Journal of Power Sources*, 142:56–69, 2005.

[80] V. Paganin, E. Sitta, T. Iwasita, and W. Vielstich. Methanol crossover effect on the cathode potential of a direct PEM fuel cell. *Journal of Applied Electrochemistry*, 35(12):1239–1243, 2005.

[81] J. Cowart. An experimental and modeling based investigation into the high stoichiometric flow rates required in direct methanol fuel cells. *Journal of Power Sources*, 143:30–35, 2005.

[82] J. Shim, H. Y. Ha, S.-A. Hong, and I.-H. Oh. Characteristics of the Nafion ionomer-impregnated composite membrane for polymer electrolyte fuel cells. *Journal of Power Sources*, 109(2):412–417, 2002.

[83] M. Wilson, D. DeCaro, N. J., C. Zawodzinski, and S. Gottesfeld. Air-breathing fuel cell stacks for portable power applications. In *Fuel Cell Seminar*, volume xxvi+794, pages 331–334, Washington, DC, USA, 1996. Courtesy Associates.

[84] T. Hottinen, O. Himanen, and P. Lund. Effect of cathode structure on planar free-breathing PEMFC. *Journal of Power Sources*, 138(1-2):205–210, 2004.

[85] S. U. Jeong, E. A. Cho, H.-J. Kim, T.-H. Lim, I.-H. Oh, and S. H. Kim. A study on cathode structure and water transport in air-breathing PEM fuel cells. *Journal of Power Sources*, 159(2):1089–1094, 2006.

[86] J. Liu, G. Sun, F. Zhao, G. Wang, G. Zhao, L. Chen, B. Yi, and Q. Xin. Study of sintered stainless steel fiber felt as gas diffusion backing in air-breathing DMFC. *Journal of Power Sources*, 133(2):175–180, 2004.

[87] B. Kho, B. Bae, M. Scibioh, J. Lee, and H. Ha. On the consequences of methanol crossover in passive air-breathing direct methanol fuel cells. *Journal of Power Sources*, 142:50–55, 2005.

[88] G.-B. Jung, F.-b. Weng, A. Su, C.-C. Chung, C.-H. Tu, and S.-H. Chan. Design and performance analysis of innovative bipolar direct methanol fuel cell stacks with 2D planar configuration. *Journal of Fuel Cell Science and Technology*, 3(1):8–12, 2006.

[89] G. Q. Lu and C. Y. Wang. Development of high performance micro DMFCS and a DMFC stack. *Journal of Fuel Cell Science and Technology*, 3(2):131–6, 2006.

[90] A. Z. Weber and J. Newman. Transport in polymer-electrolyte membranes. II. Mathematical Model. *Journal of the Electrochemical Society*, 151(2):A311–A325, 2004.

[91] T. F. Fuller and J. Newman. Experimental determination of the transport number of water in Nafion 117 membrane. *Journal of the Electrochemical Society*, 139(5):1332–7, 1992.

[92] Jr. Zawodzinski, T. A., C. Derouin, S. Radzinski, R. J. Sherman, V. T. Smith, T. E. Springer, and S. Gottesfeld. Water uptake by and transport through Nafion 117 membranes. *Journal of the Electrochemical Society*, 140(4):1041–7, 1993.

[93] J. Wang, S. Wasmus, and R. Savinell. Real-time mass spectrometric study of the methanol crossover in a direct methanol fuel cell. *Journal of the Electrochemical Society*, 143(4):1233–1239, 1996.

[94] J. Cruickshank and K. Scott. The degree and effect of methanol crossover in the direct methanol fuel cell. *Journal of Power Sources*, 70(1):40–47, 1998.

[95] A. Heinzel and V. Barragan. A review of the state-of-the-art of the methanol crossover in direct methanol fuel cells. *Journal of Power Sources*, 84(1):70–74, 1999.

[96] V. Gogel, T. Frey, Z. Yongsheng, K. Friedrich, L. Joerissen, and J. Garche. Performance and methanol permeation of direct methanol fuel cells: dependence on operating conditions and on electrode structure. *Journal of Power Sources*, 127:172–180, 2004.

[97] S. Ma, M. Odgaard, and E. Skou. Carbon dioxide permeability of proton exchange membranes for fuel cells. *Solid State Ionics*, 176(39-40):2923–7, 2005.

[98] A. Siebke. *Modellierung und numerische Simulation der Direktmethanol-Brennstoffzelle*. Dissertation, Univ. Stuttgart, 2003.

[99] B. L. Garcia, V. A. Sethuraman, J. W. Weidner, R. E. White, and R. Dougal. Mathematical model of a direct methanol fuel cell. *Journal of Fuel Cell Science and Technology*, 1(1):43–48, 2004.

[100] B. L. Garcia. *Kinetics and Mass Transfer in a Direct Methanol Fuel Cell*. Dissertation, University of South Carolina, 2007.

[101] J. P. Meyers and J. Newman. Simulation of the direct methanol fuel cell: II. Modeling and Data Analysis of Transport and Kinetic Phenomena. *Journal of the Electrochemical Society*, 149(6):A718–28, 2002.

[102] K. T. Jeng and C. W. Chen. Modeling and simulation of a direct methanol fuel cell anode. *Journal of Power Sources*, 112(2):367–75, 2002.

[103] A. Kulikovsky. The voltage-current curve of a direct methanol fuel cell: "exact" and fitting equations. *Electrochemistry Communications*, 4(12):939–946, 2002.

[104] Z. Wang and C. Wang. Mathematical Modeling of Liquid-Feed Direct Methanol Fuel Cells. *Journal of the Electrochemical Society*, 150(4):A508–A519, 2003.

[105] H. Dohle and k. Wippermann. Experimental evaluation and semi-empirical modeling of U/I characteristics and methanol permeation of a direct methanol fuel cell. *Journal of Power Sources*, 135(1-2):152–164, 2004.

[106] G. Rosenthal. *Modellierung einer Direkt-Methanol-Brennstoffzelle mit Hilfe eigens bestimmter Parameter*. Dissertation: Fortschritt-berichte vdi, reihe 3: Verfahrenstechnik * band 791, TU Clausthal, Clausthal-Zellerfeld, 2003.

[107] T. Schultz and K. Sundmacher. Mass, charge and energy transport phenomena in a polymer electrolyte membrane (PEM) used in a direct methanol fuel cell (DMFC): Modelling and experimental validation of fluxes. *Journal of Membrane Science*, 276(1-2):272–285, 2006.

[108] K. Scott, W. Taama, and J. Cruickshank. Performance and modeling of a direct methanol solid polymer electrolyte fuel cell. *Journal of Power Sources*, 65(1-2):159–171, 1997.

[109] M. Ise, K. D. Kreuer, and J. Maier. Electroosmotic drag in polymer electrolyte membranes: an electrophoretic NMR study. *Solid State Ionics*, 125(1-4):213–223, 1999.

[110] J. Divisek, J. Fuhrmann, K. Gartner, and R. Jung. Performance modeling of a direct methanol fuel cell. *Journal of the Electrochemical Society*, 150(6):A811–825, 2003.

[111] S. Ge, B. Yi, and P. Ming. Experimental Determination of Electro-Osmotic Drag Coefficient in Nafion Membrane for Fuel Cells. *Journal of the Electrochemical Society*, 153(8):A1443–A1450, 2006.

[112] S. Hikita, K. Yamane, and Y. Nakajima. Influence of cell pressure and amount of electrode catalyst in MEA on methanol crossover of direct methanol fuel cell. *JSAE Review*, 23(1):133–135, 2002.

[113] D. Hongli and R. T. Wilkie. A Fourier transform infrared spectroscopy based protocol for measuring direct methanol fuel cell methanol crossover. *Journal of the Electrochemical Society*, 153(3):A521–6, 2006.

[114] J. Kohnle, G. Waibel, R. Cernosa, M. Storz, H. Ernst, H. Sandmaier, T. Strobelt, and R. Zengerle. A unique solution for preventing clogging of flow channels by gas bubbles. In *IEEE International Conference on Micro Electro Mechanical Systems*, pages 77–80, Las Vegas, NV, United States, 2002.

[115] C. Litterst, J. Kohnle, H. Ernst, S. Messner, H. Sandmaier, R. Zengerle, and P. Koltay. Mobility of Gas Bubbles in CHIC-type Flow Channels. In H. Borgmann, editor, *ACTUATOR*, pages 541–544, Bremen, 2004.

[116] A. Shukla, P. Christensen, A. Hamnett, and M. Hogarth. A vapour-feed direct-methanol fuel cell with proton-exchange membrane electrolyte. *Journal of Power Sources*, 55(1):87–91, 1995.

[117] A. Arico, P. Creti, R. Mantegna, P. Antonucci, N. Giordano, and V. Antonucci. Analysis of the electrochemical characteristics of a direct methanol fuel cell based on a Pt-Ru/C anode catalyst. *Journal of the Electrochemical Society*, 143(12):3950–3959, 1996.

[118] M. Hogarth, P. Christensen, A. Hamnett, and A. Shukla. The design and construction of high-performance direct methanol fuel cells. 2. Vapour-feed systems. *Journal of Power Sources*, 69(1-2):125–136, 1997.

[119] H. Fukunaga, T. Ishida, N. Teranishi, C. Arai, and K. Yamada. Impedance of vapor feed direct methanol fuel cells - polarization dependence of elementary processes at the anode. *Electrochimica Acta*, 49:2123–2129, 2004.

[120] K. Furukawa, F. Kaga, K. Okajima, and M. Sudoh. Generation performance of gas-feed direct methanol fuel cell. *International Journal of Green Energy*, 1(1):123–135, 2004.

[121] J. Kallo, W. Lehnert, and R. von Helmolt. Conductance and methanol crossover investigation of nafion membranes in a vapor-fed DMFC. *Journal of the Electrochemical Society*, 150(6):A765–769, 2003.

[122] L. Fuqiang, L. Guoqiang, and W. Chao Yang. Low crossover of methanol and water through thin membranes in direct methanol fuel cells. *Journal of the Electrochemical Society*, 153(3):A543–53, 2006.

[123] N. Nakagawa, M. A. Abdelkareem, and K. Sekimoto. Control of methanol transport and separation in a DMFC with a porous support. *Journal of Power Sources*, 160(1):105–115, 2006.

[124] X. Feng and R. Y. M. Huang. Liquid Separation by Membrane Pervaporation: A Review. *Industrial & Engineering Chemistry Research*, 36(4):1048–1066, 1997.

[125] H. Kim. Passive direct methanol fuel cells fed with methanol vapor. *Journal of Power Sources*, 162(2):1232–1235, 2006.

[126] W. K. Lewis and W. G. Whitman. Principles of gas absorption. *Journal of Industrial and Engineering Chemistry (Washington, D. C.)*, 16:1215–20, 1924.

[127] J. M. Prausnitz, R. N. Lichtenthaler, and E. G. d. Azevedo. *Molecular thermodynamics of fluid-phase equilibria*. Prentice-Hall international series in the physical and chemical engineering sciences. Prentice Hall PTR, Upper Saddle River, N.J., 3rd edition, 1999.

[128] R. H. Perry, D. W. Green, and J. O. Maloney. *Perry's chemical engineers' handbook*. McGraw-Hill, New York, 7th edition, 1997.

[129] J. Gmehling, U. Onken, and W. Arlt. *Vapor-liquid equilibrium data collection*. Chemistry data series ; v. 1. Dechema ; Distributed by Scholium International, Frankfurt/Main Flushing, N.Y., 1977.

[130] R. S. Brokaw. Predicting transport properties of dilute gases. *Industrial & Engineering Chemistry Process Design and Development*, 8(2):240–53, 1969.

[131] T. Kataoka, T. Tsuru, S. Nakao, and S. Kimura. Membrane transport properties of pervaporation and vapor permeation in ethanol-water system using polyacrylonitrile and cellulose acetate membranes. *Journal of Chemical Engineering of Japan*, 24(3):334–9, 1991.

[132] T. Kataoka, T. Tsuru, S. Nakao, and S. Kimura. Permeation equations developed for prediction of membrane performance in pervaporation, vapor permeation and reverse osmosis based on the solution-diffusion model. *Journal of Chemical Engineering of Japan*, 24(3):326–33, 1991.

[133] J. G. Wijmans and R. W. Baker. The solution-diffusion model: a review. *Journal of Membrane Science*, 107(1-2):1–21, 1995.

[134] J. Crank and G. S. Park. *Diffusion in polymers*. Academic Press, London, New York, 1968.

[135] M. H. Mulder. *Basic principles of membrane technology*. Kluwer Academic, 2. ed., repr. edition, 2000.

[136] P. Schroeder von. Ueber Erstarrungs- und Quellungserscheinungen von Gelatine. *Physikalische Chemie*, 45:75–117, 1903.

[137] A. Z. Weber and J. Newman. Transport in polymer-electrolyte membranes. I. Physical model. *Journal of the Electrochemical Society*, 150(7):A1008–A1015, 2003.

[138] C. M. Gates and J. Newman. Equilibrium and diffusion of methanol and water in a Nafion 117 membrane. *AIChE Journal*, 46(10):2076–2085, 2000.

[139] X. Ren, W. Henderson, and S. Gottesfeld. Electro-osmotic drag of water in ionomeric membranes. New measurements employing a direct methanol fuel cell. *Journal of the Electrochemical Society*, 144(9):L267–L270, 1997.

[140] S. Gottesfeld and T. A. Zawodzinski. Polymer electrolyte fuel cells. *Advances in Electrochemical Science and Engineering*, 5:195–301, 1997.

[141] S. Gojkovic, S. Zecevic, and R. Savinell. O2 Reduction on an Ink-Type Rotating Disk Electrode Using Pt Supported on High-Area Carbons. *Journal of The Electrochemical Society*, 11:3713–3720, 1998.

[142] P. Gode, F. Jaouen, G. Lindbergh, A. Lundblad, and G. Sundholm. Influence of the composition on the structure and electrochemical characteristics of the PEFC cathode. *Electrochimica Acta*, 48(28):4175–4187, 2003.

[143] T. Springer, T. Zawodzinski, M. Wilson, and S. Gottesfeld. Characterization of polymer electrolyte fuel cells using AC impedance spectroscopy. *Journal of the Electrochemical Society*, 143(2):587–599, 1996.

[144] P. Kauranen and E. Skou. Mixed methanol oxidation/oxygen reduction currents on a carbon supported Pt catalyst. *Journal of Electroanalytical Chemistry*, 408(1-2):189–198, 1996.

[145] K. Scott and P. Argyropoulos. A one dimensional model of a methanol fuel cell anode. *Journal of Power Sources*, 137(2):228–238, 2004.

[146] I. j. N. Bronstejn. *Taschenbuch der Mathematik*. Thun; Frankfurt am Main, 5., ueberarb. u. erw. aufl., unveraend. nachdr. edition, 2001.

[147] S. Chan, X. Chen, and K. Khor. Reliability and accuracy of measured overpotential in a three-electrode fuel cell system. *Journal of Applied Electrochemistry*, 31(10):1163–1170, 2001.

[148] M. Staehler. *Die Normal-Wasserstoffelektrode als Bezugselektrode in der Direkt- Methanol-Brennstoffzelle*. Dissertation, Forschungszentrum Juelich, 2006.

[149] K. Scott, A. K. Shukla, C. L. Jackson, and W. R. A. Meuleman. A mixed-reactants solid-polymer-electrolyte direct methanol fuel cell. *Journal of Power Sources*, 126(1-2):67–75, 2004.

[150] Q. Ye and T. S. Zhao. Abrupt decline in the open-circuit voltage of direct methanol fuel cells at critical oxygen feed rate. *Journal of the Electrochemical Society*, 152(11):A2238–45, 2005.

[151] A. A. Kulikovsky, H. Schmitz, K. Wippermann, J. Mergel, B. Fricke, T. Sanders, and D. U. Sauer. DMFC: Galvanic or electrolytic cell? *Electrochemistry Communications*, 8(5):754–760, 2006.

[152] Q. Ye and T. Zhao. Electrolytic hydrogen evolution in DMFCs induced by oxygen interruptions and its effect on cell performance. *Electrochemical and Solid-State Letters*, 8(4):A211–A214, 2005.